Analysis of defects in additively manufactured lattice structures

by

Ifeanyichukwu Echeta

Manufacturing Metrology Team
Advanced Manufacturing Technology Research Group
Department of Mechanical, Materials and Manufacturing Engineering
Faculty of Engineering
University of Nottingham

Submitted to The University of Nottingham for the degree of
Doctor of Philosophy

Supervisors: Dr Samanta Piano, Professor Richard Leach

Analysis of defects in additively manufactured lattice structures

Ifeanyichukwu Echeta

First submission: 30th March 2022

Final submission: 25th April 2023

Abstract

Additive manufacturing is a popular area of research because it greatly increases design opportunities, allowing for significantly more geometric freedom than in more established manufacturing methods, such as machining, casting and forming. A relatively small set of additive manufacturing processes are consistently used for the manufacturing of lattice structures, and these processes produce characteristic defects and geometric deviations within lattice structures.

In this thesis, a modelling approach is presented for the generation of surface models of strut-based lattice structures into which defects and geometric deviations can be added. Conversion of the surface models into tetrahedral meshes for finite element (FE) analysis is also demonstrated. Signed distance functions (SDFs) form the foundation of the model and can be used to create surfaces of ideal lattice structures. The thesis demonstrates how modification of the signed distance function allows for the inputting of geometric deviations—namely, waviness, radius variation and elliptical cross sections. Surface defects are modelled by defining an additional function that applies displacements to the surface produced by the signed distance function. To understand the limitations of the proposed modelling approach, a sensitivity study is performed wherein the underlying parameters of the approach are modified to observe their impact on three quantities: SDF error, meshing error and mesh quality.

X-ray computed tomography (XCT) was used for obtaining original data on geometric deviations and surface defects in lattice structures, more specifically, a BCCZ lattice structure. Cross sectional measurements of the struts was performed, as well analysing the strut surfaces to observe locations of increased surface defects. Comparisons were made between the design's vertical struts and inclined struts. The XCT results showed the inclined struts to be significantly more prone to geometric deviations; radius variation, waviness and texture bias all showed greater deviations in the inclined struts. The cross sectional data, grouped by strut orientation, was fitted to probability density functions (PDFs) which were used in subsequent stages for generating lattice structures with geometric deviations statistically equivalent to the XCT measurement.

The BCCZ lattice structures were also subjected to compression testing for determining the Young's modulus of the design, which was determined to be 984.1 MPa. The proposed modelling approach was then configured, using the PDFs derived from the XCT data to generate a model of a lattice structure with geometric deviations applied. Upon the application of the geometric deviations, the simulated Young's modulus reduced from 4148 MPa to 4023 MPa, suggesting that the introduction of geometric deviations does indeed reduce stiffness, however, these results are a significant overestimation of the experimentally determined Young's modulus. A number of areas could be explored to improve this disparity, in particular, the updating of the material model used in the analysis.

In summary, the work in this thesis demonstrates the versatility of SDFs for the modelling of strut-based lattice structures. The XCT results showed strong trends between strut overhang angle and the exacerbation of geometric deviations and surface defects. The cross sectional data from the XCT measurement was well described by the PDFs; the simulated data showed very strong agreement to the XCT data. The FE modelling requires further investigation to improve its agreement with experimental data.

Acknowledgements

Firstly, I would like to thank my supervisors, Dr Samanta Piano and Professor Richard Leach, for accepting me for this position and supervising me throughout this project. I also acknowledge my industrial supervisor Dr Ben Dutton for funding and support through The Manufacturing Technology Centre. I also acknowledge the University of Nottingham's Augusta High Performance Computing service which was used for producing some of my results. I thank my internal and external assessors—Professor Ian Ashcroft and Dr Paul Bills, respectively—for providing many insights during my viva voce and thus helping me to produce a much stronger thesis. I must also thank Professor John Durodola, of Oxford Brookes University, for his support and encouragements both before and during my PhD. I am also grateful to Dr Armando Coco, my MSc project supervisor at Oxford Brookes University, for helping me begin my journey with academic research.

I thank my friends and fellow PhD students, George Gayton, Kieran Smith, Christopher Strong and Matthew Thomas, for their friendship, support, insights, and many jokes throughout all the unique experiences and challenges that a PhD presents.

I must also thank the many dear friends I have made through joining Cornerstone Church Nottingham, all of which have been a great support. This list includes and, of course, is not limited to: Rupert and Vicky Akhalu; David and Liz Faminu; Alexis Crown; Ben Cheong; John and Catherine (and Edith and Florence!) Russell; Jim and Helen Watkin; Ed and Charlie Tyrrell; Paul and Amy Smith; Jo and Ed Upcott; Roo and Esther Miller; Sam and Kat Payne; Mark and Claire Collins; Phil and Gill Moore; Paul and Hannah Wilkins; Jacob and Leah Locke; Luke and Helena Edis; Matt and Lerato Dixon; Matryn Dunning.

Outside of Nottingham, I thank my friends of many years for supporting me through my PhD by simply being great company. Special mention goes to Kent Francisco; Elise Beer; Prince Jacob; Samuel Herklots and his brother, Peter; Josh Mejia.

I thank my family—Mum, Dad, Chinedum and Chiamaka—for supporting me throughout all aspects of my life. Any attempts to explain the vast support of my family would always do it a disservice. Lastly, as a Christian, I thank God for his provision of all the above.

Contents

Abstract v

Acknowledgements vii

Contents ix

Declaration xv

List of figures xvii

List of tables xxiii

List of abbreviations xxv

Chapter 1 – Introduction 27

1.1 Motivation 28

1.2 Aim and objectives 33

1.3 Overview of work and novelty 34

1.4 Structure of thesis 36

Chapter 2 – Background and State of the art 39

2.1 Cellular solids 40

2.2 Strut-based lattice structures 43

2.3 Additive manufacturing 47

  2.3.1 Powder bed fusion 48

  2.3.2 Process parameters 51

  2.3.3 Powder bed fusion: defect formation mechanisms 53

2.4 Lattice structure defects 55

2.4.1 Geometric deviations 56

2.4.2 Surface texture variations 59

2.4.3 Porosity 61

2.4.4 Post processing 62

2.5 Measurement techniques 63

2.6 X-ray computed tomography 66

2.6.1 Principles of X-ray computed tomography 66

2.6.2 Measurement procedure 67

2.6.3 Data processing 69

2.6.4 Measurement parameters 71

2.6.5 Metrology considerations 73

2.7 Finite element modelling 75

2.7.1 Tetrahedral elements 76

2.7.2 Beam elements 79

2.8 Discussion and conclusion 81

2.9 Summary 85

Chapter 3 – Methodology 87

3.1 Overview 88

3.2 Manufacture 89

3.3 Measurement 91

3.3.1 X-ray computed tomography 91

3.3.2 Data processing 92

3.3.3 Dimensional analysis 99

3.4 Mechanical testing 102

3.5 Incorporation of deviations into model 103

3.6 Finite element analysis 104

Chapter 4 – SDF-based modelling of strut-based lattice structures 109

4.1 Implicit surfaces 110

4.1.1 Implicit functions 110

4.1.2 Signed distance functions 111

4.2 Surface modelling 115

4.2.1 Lattice strut 115

4.2.2 Unit cell and lattice structure 117

4.2.3 Defects and geometric deviations 119

4.3 Tetrahedral modelling 127

4.4 Discussion and conclusion 130

4.5 Summary 131

Chapter 5 – Sensitivity study of the proposed modelling approach 133

5.1 Outputs 134

5.2 Inputs 137

5.2.1 Functional input parameters 138

5.2.2 Geometrical input parameters 140

5.2.3 Surface defect parameters 145

5.2.4 Summary 146

5.3 Study #1: SDF error sensitivity 148

5.3.1 Sphere 148

5.3.2 Strut 149

5.3.3 Strut intersection 154

5.3.4 Radius deviation 156

5.3.5 Key findings 157

5.4 Study #2: Meshing error sensitivity 158

5.4.1 Sphere 158

5.4.2 Strut 159

5.4.3 Strut intersection 161

5.4.4 Radius deviation 162

5.4.5 Surface defects 163

5.4.6 Key findings 164

5.5 Study #3: Mesh quality sensitivity 165

5.5.1 Sphere 166

5.5.2 Strut 167

5.5.3 Strut intersection 168

5.5.4 Radius deviation 171

5.5.5 Surface defects 171

5.5.6 Key findings 174

5.6 Discussion and conclusion 174

5.7 Summary 175

Chapter 6 – Results: XCT, experiments, modelling and simulations 177

6.1 XCT 178

6.1.1 Cross sectional analysis 178

6.1.2 Texture bias and surface unwrapping 180

6.1.3 Influence factors 182

6.2 Compression testing 187

6.3 FEA 191

6.3.1 Modelling of geometric deviations 191

6.4 Conclusion 195

Chapter 7 – Discussions, conclusions and future work 197

7.1 Thesis summary 198

7.2 Discussion 201

7.3 Future work 204

References 207

List of publications and presentations 223

Appendix A – XCT settings 225

Appendix B – MATLAB code 227

Appendix C – Texture bias functions 235

Appendix D – Analytical calculation of lattice volumes 239

Declaration

I, Ifeanyichukwu Echeta, declare that this thesis – titled "Analysis of defects in additively manufactured lattice structures" – is my own work from the time of my PhD at the University of Nottingham under the supervision of Dr Samanta Piano and Professor Richard Leach, and that this thesis has never been previously submitted for the award of any degree, or any similar type of recognition.

List of figures

Figure 1.1. Example applications of lattice structures.____30

Figure 1.2. Dispersion curves for various unit cell designs. ____31

Figure 1.3. Flowchart showing the main stages of work in this thesis. ____36

Figure 2.1. Hierarchical display of the main types of cellular solids. ____42

Figure 2.2. Examples of bending-dominated and stretch-dominated unit cells, according to Maxwell's stability criterion.____43

Figure 2.3. Example compressive stress strain response of bending-dominated and stretch-dominated strut-based lattice structures. ____44

Figure 2.4. Diagram of the definition of the medial axis.____46

Figure 2.5. Diagram of the definition of cell size. ____46

Figure 2.6. Diagram of the definition of overhang angle____47

Figure 2.7. Bar chart showing various AM processes used for manufacturing lattice structures. ____49

Figure 2.8. Diagram of the laser melting AM process.____50

Figure 2.9. Diagram of an electron beam melting system. ____51

Figure 2.10. Examples of the defects which form in PBF processes. ____55

Figure 2.11. Example of strut orientation-dependency.____59

Figure 2.12. SEM micrograph showing strut waviness ____59

Figure 2.13. SEM micrographs showing stair-stepping defects.____61

Figure 2.14. XCT results showing increased porosity in the nodes of a lattice ____62

Figure 2.15. Diagram of an X-ray tube ____67

Figure 2.16. Diagram of an industrial cone-beam XCT system. ____68

Figure 2.17. Diagram of a sample platform and detector panel. ____68

Figure 2.18. Grey-value histogram showing the ISO50 value. ____ 70

Figure 2.19. An example of a beam hardening artefact. ____ 72

Figure 2.20. FE modelling of geometric deviations, using connected spheres. ____ 77

Figure 2.21. Modelling of defects using elliptical cross sections. ____ 79

Figure 2.22. Modelling and simulation of an octet-truss lattice structure, using beam elements. ____ 80

Figure 2.23. Results from a parametric study on strut waviness and radius variation ____ 81

Figure 2.24. BCC unit cell meshed using tetrahedral elements and beam elements. 84

Figure 3.1. Flowchart showing the main stages of work in this thesis (duplicate of Figure 1.3). ____ 88

Figure 3.2. BCCZ lattice structure, the design selected for manufacture. ____ 90

Figure 3.3. 4 x 4 x 4 BCCZ lattice manufactured by laser powder bed fusion. ____ 91

Figure 3.4. Flowchart of the XCT data processing stages. ____ 92

Figure 3.5. Illustration of surface determination. ____ 93

Figure 3.6. Fitting of geometry elements to determined surface. ____ 94

Figure 3.7. A unit cell ROI. ____ 95

Figure 3.8. Extraction of individual struts from point cloud data. ____ 98

Figure 3.9. Examples of extraction of the cylindrical section inclined and vertical struts. ____ 98

Figure 3.10. Extraction of strut cross sections from point cloud ____ 102

Figure 3.11. Illustration of the definition the parameters used for texture bias analysis ____ 102

Figure 3.12. Flowchart of FEA stages. ____ 104

Figure 3.13. Example mesh of a BCCZ lattice with cropped top and bottom faces. 106

Figure 4.1. The unit circle defined by an implicit function. 111

Figure 4.2. An illustration of a distance function. 112

Figure 4.3. An illustration of a signed distance function. 112

Figure 4.4. An example of modifying the signed distance function of a unit cell to increase geometric complexity, generating a petal-like structure. 114

Figure 4.5. A Boolean union of two distance fields. 114

Figure 4.6. Illustration of the locating of $\phi x = 0$ in a discrete distance field 115

Figure 4.7. A lattice strut generated using a signed distance function. 117

Figure 4.8. Boolean union performed to create the BCC unit cell. 118

Figure 4.9. Cropped surfaces created on the lattice structure 119

Figure 4.10. Illustration of the signed distance function used for modelling waviness. 120

Figure 4.11. Illustration of how radius variation is applied to the signed distance function. 122

Figure 4.12. Modelling a strut with an elliptical cross section. 123

Figure 4.13. Example of modelling porosity. 124

Figure 4.14. Diagram showing how the surface angle is defined. 126

Figure 4.15. Derivation of surface parameters and application of surface defects 127

Figure 4.16. Example conversion from surface mesh to tetrahedral mesh 129

Figure 4.17. Summary of the proposed modelling approach. 131

Figure 5.1. Triangulated surface mesh of a sphere geometry 135

Figure 5.2. Illustration of mesh quality calculation. 137

Figure 5.3. Expanded flowchart of proposed modelling approach. 138

Figure 5.4. Spheres generated from signed distance functions using different resolutions. 139

Figure 5.5. Examples of the effects of $radbound$ on the mesh of a sphere. 139

Figure 5.6. Examples of the effect of the $maxvol$ parameter on the mesh of a sphere. 140

Figure 5.7. Geometries considered representative of strut-based lattice structures and geometric deviations. 141

Figure 5.8. BCCZ unit cell showing examples of strut connections. 144

Figure 5.9. Illustrations of a strut intersection and radius deviation. 145

Figure 5.10. Relationship between SDF error for a sphere and the domain resolution. 149

Figure 5.11. Relationship between SDF error for a strut and domain resolution 151

Figure 5.12. Flowchart of Monte Carlo simulation steps. 153

Figure 5.13. Results of the Monte Carlo simulation. 153

Figure 5.14. Relationship between the SDF error and the displacement applied to the strut intersection. 155

Figure 5.15. Relationship between the SDF error and the varied radius applied to the radius deviation. 157

Figure 5.16. Relationship between the meshing error for a sphere and$radbound$. 159

Figure 5.17. Relationship between the meshing error and the strut length, plotted at different values of $radbound$ 160

Figure 5.18. Relationship between the meshing error and the displacement a applied to the strut intersection. 162

Figure 5.19. Relationship between the meshing error and the varied radius applied to the radius deviation 163

Figure 5.20. Relationship between the meshing error and the parameters of the surface defects function 164

Figure 5.21. Histogram showing how mesh quality is impacted by the parameter controlling element size 167

Figure 5.22. Histogram showing how mesh quality is impacted by strut length 168

Figure 5.23. Histogram showing how mesh quality is impacted by intersection angle 170

Figure 5.24. Histogram showing how mesh quality is impacted by the radius in the radius deviation 171

Figure 5.25. Influence of surface defects on the mesh quality of body and surface elements. 173

Figure 6.1. XCT cross section results for the vertical struts. 179

Figure 6.2. XCT cross section results for the inclined struts. 179

Figure 6.3. Plots of the average texture bias for vertical and inclined struts. 181

Figure 6.4. Results of the average unwrapped surface of the vertical and inclined struts 182

Figure 6.5. Texture bias plots using different settings for point cloud generation. 184

Figure 6.6. Convergence analysis for the vertical struts. 186

Figure 6.7. Convergence analysis for the inclined struts. 187

Figure 6.8. Average results from the compression tests. 188

Figure 6.9. Compression test results of sample 1. 189

Figure 6.10. Compression test results of sample 2. 189

Figure 6.11. Compression test results of sample 3. 190

Figure 6.12. Compression test results of sample 4. 190

Figure 6.13. Compression test results of sample 5. 191

Figure 6.14 Simulated cross sectional data for the radius and offset of vertical and inclined struts, using probability density functions fitted to the XCT data. 192

Figure 6.15. Example struts generated with deviations defined from probability density function fitted to XCT cross sectional data. ____________________194

Figure B.1. Pseudocode describing the point cloud import and segmentation script. 228

Figure B.2. Pseudocode describing the cross section analysis script. 229

Figure B.3. Pseudocode describing the signed distance function. 230

Figure B.4. Pseudocode describing the tessellation function. 231

Figure B.5. Pseudocode describing the cropping function. 232

Figure B.6. Pseudocode describing the surface analysis script. 233

Figure C.1. Example of using pseudorandom displacements used to apply texture bias. 236

Figure C.2. Examples of functions used to explicitly define the displacements applied to model surface defects. 238

Figure D.1. Volume calculation for the radius defect. 241

Figure D.2. Volume calculation for the strut intersection. 241

List of tables

Table 1. Observed deviations in strut diameters. 58

Table 2. Defect measurement methods 65

Table 3. X-ray computed tomography influence factors 75

Table 4 Lattice modelling parameters. 104

Table 5. Summary of input parameters used in the sensitivity studies. 147

Table 6. Minimum and maximum distances d for different settings used for point cloud generation. 185

Table 7 FEA results. 195

List of abbreviations

1D/2D/3D	One/two/three-dimensional
AM	Additive manufacturing
BCC	Body centred cubic
BCCZ	Body centred cubic with *z*-axis reinforcement
CAD	Computer aided design
CGAL	The Computational Geometry Algorithms Library
EBM	Electron beam melting
FE	Finite element
FEA	Finite element analysis
LM	Laser melting
MCS	Monte Carlo simulation
PBF	Powder bed fusion
PDF	Probability density function
RDT	Restricted Delaunay tetrahedralization
SDF	Signed distance function
SEM	Scanning electron microscopy
SLM	Selective laser melting
TPMS	Triply period minimal surface(s)
XCT	X-ray computed tomography

Chapter 1 – Introduction

This chapter provides an introduction and overview of the thesis. Section 1.1 discusses the motivations for this work, followed by the aim and objectives in Section 1.2. Next, Section 1.3 gives an overview of the stages of work and highlights the thesis' novel contributions. Lastly, Section 1.4 explains the structure of the remaining chapters of the thesis.

1.1 Motivation

Additive manufacturing (AM) is a popular area of research because it greatly increases design opportunities, allowing for significantly more geometric freedom than in more established manufacturing methods, such as machining, casting and forming. Within AM, a popular area of study is that of lattice structures—a unit cell tessellated in three axes. Lattice structures have many desirable properties, such as high specific strength, high surface area to volume ratio, and high impact energy absorption properties [1].

As shown in Figure 1.1, lattice structures have been studied for a range of applications, using various techniques. The study of lattice structures generally focuses on investigating lattice designs and documenting their mechanical properties (e.g. [2–7]) via mechanical testing (Figure 1.1a), or exploiting known lattice structure properties for specific applications, such as biomedical implants (Figure 1.1b) [8–12], heat exchangers/heat sinks (Figure 1.1c) [13–16] and sandwich structures for the lightweighting of engineering components [17,18].

The utility of lattice structures produced by AM extends to precision engineering, where the vibrational wave propagation properties of lattice structure designs have been investigated (e.g. [19–21]) and could be used for vibration attenuation applications. For example, vibration attenuating lattice structures could be incorporated into machine frames for reducing the noise in a measurement system. Figure 1.1d shows an experimental setup used for studying the vibrational properties of a lattice structure. Sources of vibration which are relevant to precision engineering include: moving stages; camera shutters; contact between tool and workpiece; rotary components, for example, spindles, cutting tools and electronic fans; nearby road traffic.

Figure 1.2 shows some numerical modelling results taken from the PhD thesis of Elmadih [22] in which several lattice structure designs—more specifically, unit cell designs—were studied for their vibrational wave propagation properties; these plots are known as dispersion curves. Although a full explanation of the terminology in

Figure 1.2 is beyond the scope of this section, a simplified interpretation of these results must be provided. To identify if a unit cell design is appropriate for vibration attenuation applications, it must possess "bandgaps"—that is, it must possess ranges of frequencies in which there is no wave propagation in any direction. In Figure 1.2, the y-axes denote "frequency" ($f \cdot L \cdot v^{-1}$) and the x-axes denote "wave vector" ($\Gamma, \mathrm{X}, \mathrm{R}, \mathrm{M}, \Gamma$) which can be considered as the direction of a vibration. Bandgaps can be seen in the plots in Figure 1.2a-b which show ranges of frequencies in which there are no data points i.e. no wave propagation in any of the directions of the wave vectors. This is a promising result which strongly supports the suitability of some lattice structure designs for vibration attenuation. For further introduction to the topic of dispersion curves, the reader is directed to Chapter 3 of Elmadih's thesis [22].

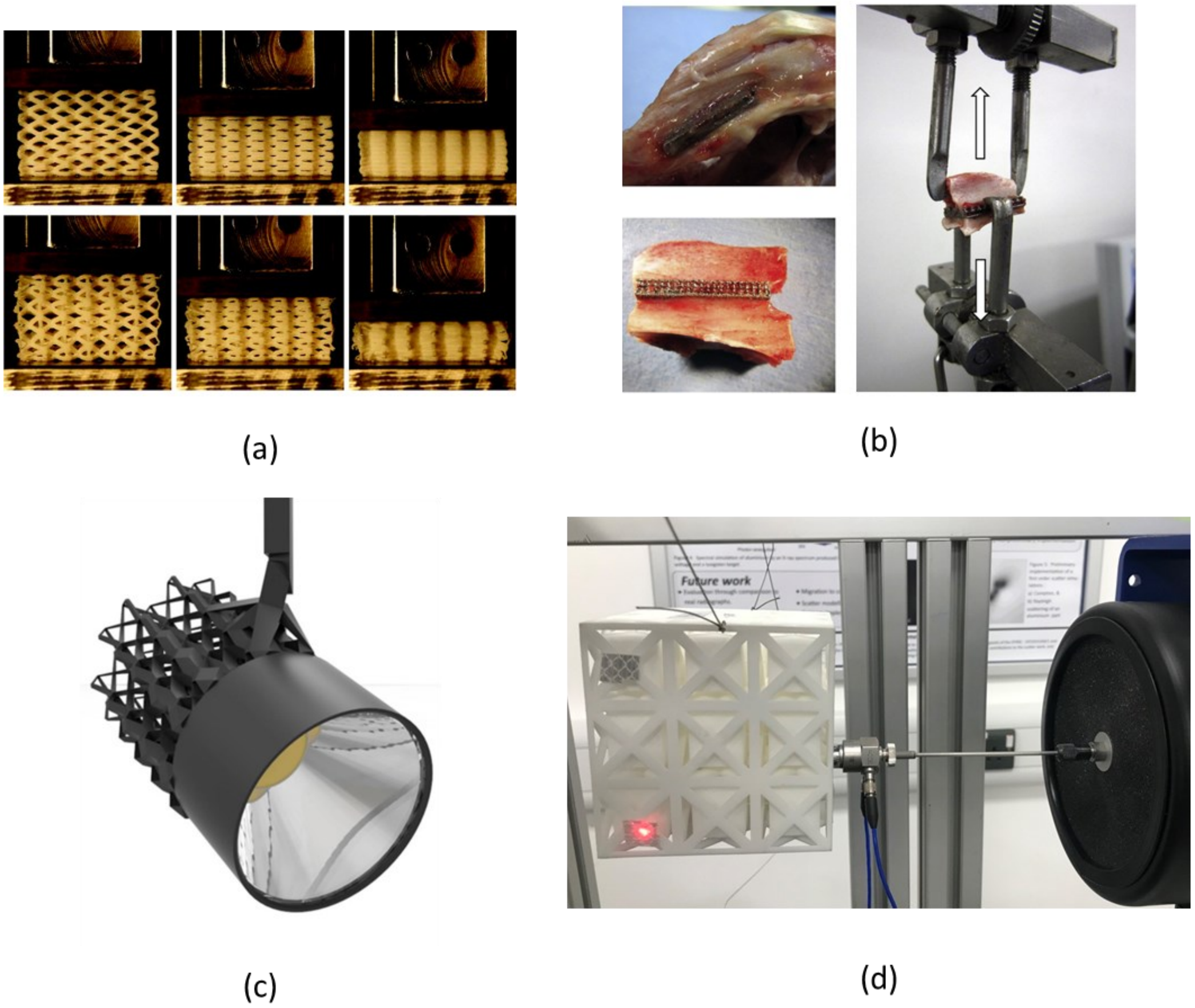

(a) (b)

(c) (d)

Figure 1.1. Example applications of lattice structures..(a) The study of compressive properties of lattice structures [4] (b) Testing the tensile strength of a lattice structure for use as a biomedical implant; the figure shows the implant inside a rabbit tibia [9]. (c) Concept design for a monolithic LED lamp unit including a lattice structure heat sink [15]. (d) A study on the vibrational properties of a lattice structure [23].

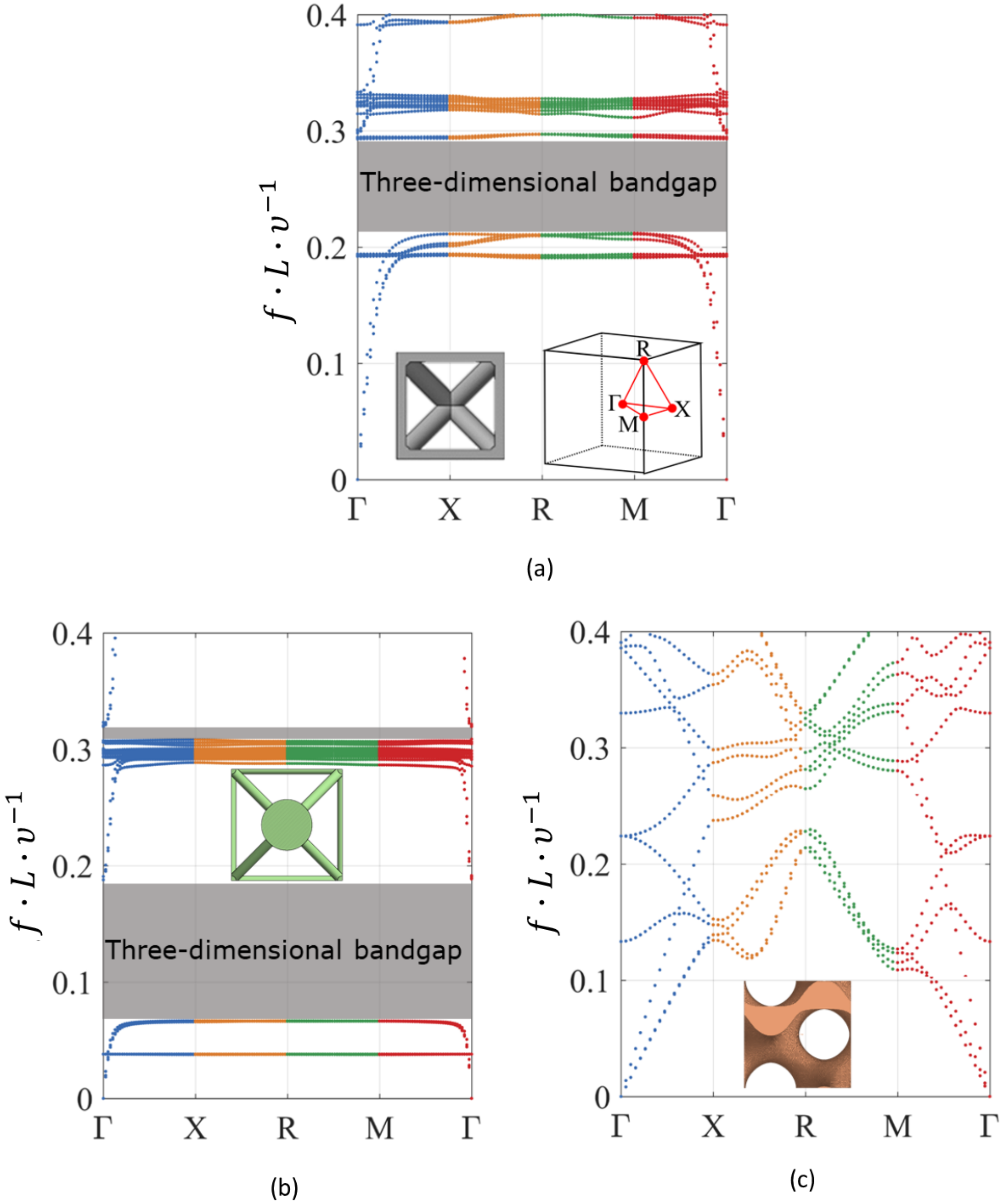

Figure 1.2. Dispersion curves for various unit cell designs. (a) A body centred cubic (BCC) unit cell, in which a bandgap is identified. (b) A BCC unit cell with an internal resonator, in which another bandgap is identified. (c) A gyroid unit cell, in which no bandgap is identified [22].

Within AM, there are "process categories" which are used to group subsets of AM processes which share similarities. The AM processes which are often used to manufacture lattice structures fall under the process category called "powder bed fusion" (PBF). All PBF processes are governed by similar types of parameters which must be optimised to improve the quality of manufactured parts. However, even with optimisation, there are distinct ways in which designs manufactured by PBF processes can deviate from their initial designs. The term "defect" can sometimes be used to broadly describe such deviations (e.g. [24–30]), although more specific and descriptive terms are also used and are defined later (see Chapter 2, § 2.3.3). Furthermore, a distinct set of defects also form among the features which are common in lattice structure designs (see Chapter 2, § 2.4).

The presence of defects in lattice structures is a potential issue in all fields in which lattice structures are studied, as defects have the potential to alter the behaviour of any design. In the case of lattice structures for vibration attenuation, defects may detrimentally alter the structural and vibrational properties of lattice structures. There are increasing numbers of studies investigating the impact of defects on the function of a lattice structure for a particular application (see Chapter 2).

A large of range of measurement techniques have been applied to lattice structures (see Chapter 2, § 2.5). Some of these techniques are destructive and potentially undesirable due to the destroying of the sample. For example, using a scanning electron microscope (SEM) to obtain cross-sectional measurement data requires prior sectioning of the sample. Additionally, the complicated geometries associated with lattice structures present line-of-sight limitations. For this reason, a measurement process not hindered by line-of-sight is desired. X-ray computed tomography (XCT) is an increasingly popular measurement method for lattice structures; XCT is not limited by line-of-sight and is able to obtain both internal and external images of a sample. However, a significant disadvantage of XCT is the measurement time; an XCT measurement can often take several times longer than the manufacturing and preparation of the sample. Additionally, the quality of XCT data can be difficult to interpret, due to the complex interactions between the X-rays and the samples, coupled with the vast range of interrelated parameters which must be configured for each measurement.

Modelling defects and simulating their impact is useful for understanding the potential influence of a defect on a particular lattice structure property. Additionally, models allow for the development of parametric studies, from which relationships can be drawn between a particular lattice structure property and a defect which is varied over a range of values. Modelling can aid the tolerancing process for lattice structures by allowing designers to discern whether the presence of a given defect is critical or negligible for a particular application. Finite element (FE) methods are often used for these modelling studies, in which the lattice structure is replaced by a representative mesh. These meshes can be generated using different “element types” (see Chapter 2, § 2.7); typically either tetrahedral elements or beam elements.

1.2 Aim and objectives

The aim of the work in this thesis is to develop a modelling method for investigating the impact of geometric deviations on the stiffness of lattice structures. This work is inspired by previous work in the field of precision engineering in which certain lattice structure designs were shown to possess three-dimensional bandgaps [22], as mentioned in Section 1.1. This thesis supports existing work in the field of vibration attenuating lattice structures and aims to provide a means for assessing the impact of defects on a lattice structure’s vibrational properties, for example, stiffness.

To pursue this aim, the following objectives are set:

1. Develop an approach for modelling lattice structure defects/geometric deviations and performing simulations via finite element (FE) modelling.
2. Perform a sensitivity study on the developed modelling approach to define limits on its underlying parameters.
3. Use X-ray computed tomography (XCT) to quantify manufacturing defects/geometric deviations in lattice structures and extract defect parameters which can be applied to the FE model.

4. Perform mechanical testing and validate the developed model using the experimental data.

The term "lattice structure" technically describes a large group of designs which can be split into two main categories, based on their common features: strut-based and surface-based (see Chapter 2 § 2.1). This thesis focuses strongly on the subset of lattice structures known as "strut-based lattice structures". A key reason for restricting the scope of this thesis in this way is found in the results of Elmadih's thesis [22]: certain strut-based lattice structures possess three-dimensional (3D) bandgaps whereas surface-based lattice structures do not. These observations are illustrated in Figure 1.2 in which the designs shown in Figure 1.2a-b are strut-based and possess3D bandgaps, whereas the design in Figure 1.2c is surface based and does not possess bandgaps. It must be noted, however, that one-dimensional (1D) bandgaps have indeed been observed in some surface-based lattice structures but a 1D bandgap is significantly less applicable to precision engineering applications which require 3D vibration attenuation. For further discussion on 1D and 3D bandgaps, the reader is referred to Chapter 6 and Chapter 7 respectively of Elmadih's thesis [22], supported by the following journal papers [31,32].

In line with the above objectives, publications were produced and are referred to in the thesis at the beginning of relevant chapters. A full list of the author's publications and conference presentations is given on page 223, List of publications and presentations.

1.3 Overview of work and novelty

The following paragraphs provide an overview of the work contained in each of the main stages of the thesis, explaining their novel contributions when required. The five stages into which the thesis' work is divided is shown in the flowchart in Figure 1.3.

In Stage 1, a modelling approach is proposed for generating surface models of lattice structures with manufacturing defects which can then be converted into tetrahedral meshes and used for finite element modelling. A fundamental part of the modelling approach is the use of signed distance functions (SDFs) for generating surfaces of lattice structure geometries. The novelty is found extending SDFs beyond modelling only ideal lattice structures and demonstrating how SDFs can be extended to also model a range of defects in lattice structures. It should also be noted that this SDF-based modelling approach can be applied to any strut-based lattice structure, since the model can adapt to any configuration of lattice struts.

Next, Stage 2 performs a sensitivity study on the proposed modelling approach, determining optimal parameters for modelling lattice structure geometries and defects. Although sensitivity studies are a common and necessary practice in numerical analysis, this sensitivity study can also be considered a novelty because it is in supporting the novel modelling work from Stage 1.

In Stage 3, a lattice structure design is selected for manufacture using laser powder bed fusion and measurements are performed using XCT. The measurement data provides quantitative information on a range of defects, and is required for Stage 5, in which the proposed model is configured to replicate the defects according to the measurement data.

In Stage 4, compression tests are performed on the manufactured lattice structure samples in order to calculate their stiffness. These mechanical tests are also required for Stage 5, in which the proposed model is used to predict lattice stiffness and is compared to the experimentally determined stiffness.

In Stage 5 and Stage 6, the proposed model is validated by first incorporating the measured defects and then predicting the stiffness of the lattice structure design selected in Stage 3, using FE analysis. To incorporate the defects into the model, statistical analysis is performed on the XCT measurement data, obtaining parameters which are used by the model to generate simulated defects which are statistically equivalent to the XCT measurement data. Again, although model validation is a common practice, Stage 5 is considered novel as is necessary for the completion of the proposed modelling approach, for making informed judgments on the model's suitability and for justifying further simulations. A potential additional novelty is found in the use of simulated defects which allow for fast generation of lattice structure surface models which statistical equivalence to real-world data. High quality simulated data has many potential applications, for example, the training of machine learning algorithms which require very large data sets. Additionally, the ability to model useful lattice structure surfaces from statistical parameters may reduce reliance upon slow XCT measurements. There are some modelling approaches—known as image-based methods—in which lattice structure properties are determined from the XCT data (e.g. [33–35]), for example via conversion into an FE mesh. Image-based methods bear a significant time cost.

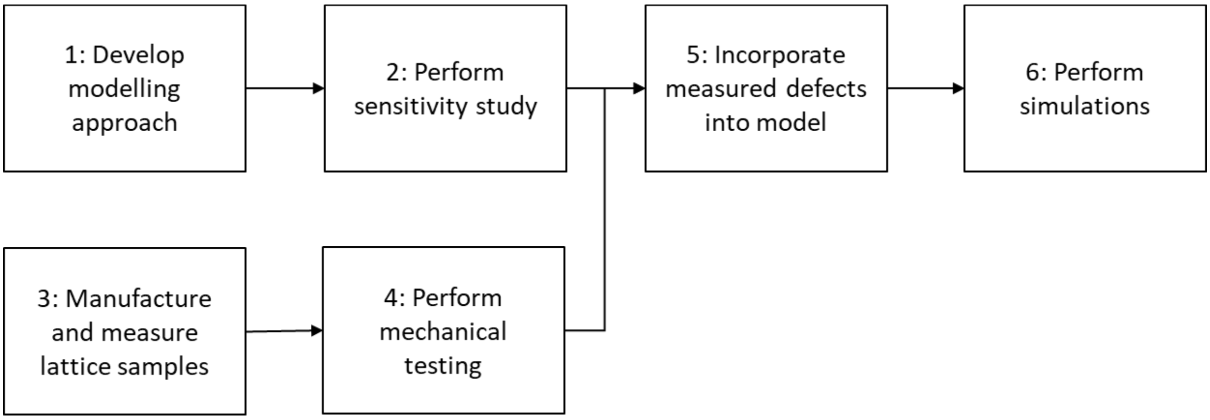
1: Develop modelling approach
2: Perform sensitivity study
5: Incorporate measured defects into model
6: Perform simulations
3: Manufacture and measure lattice samples
4: Perform mechanical testing

Figure 1.3. Flowchart showing the main stages of work in this thesis.

1.4 Structure of thesis

In Chapter 1, the motivation of the thesis is stated, alongside the aim and objectives and statements of novel contribution.

In Chapter 2, a review of the background and relevant literature is provided, on topics such as cellular solids, additive manufacturing, X-ray computed tomography and finite element modelling.

In Chapter 3, the methodology of the thesis is outlined, explaining the procedures used in obtain all the results.

In Chapter 4, the proposed modelling approach is explained in detail, demonstrating how existing mathematical tools—namely, signed distance functions—can be extended for modelling a range of defects in lattice structures.

In Chapter 5, a sensitivity study of the proposed modelling approach is performed, defining regions of stability.

In Chapter 6, the results of the procedures explained in the methodology are presented, namely, X-ray computed tomography results, compression testing and finite element analysis.

In Chapter 7, the conclusions of the thesis are provided, the aim and objectives are reviewed and suggestions for future work are made.

Chapter 2 – Background and State of the art

This chapter provides the background information for this thesis and reviews the state of the art in relevant fields. Section 2.1 introduces the more general form of lattice structures—cellular solids—before specifically describing strut-based lattice structures in more detail in Section 2.2; strut-based lattice structures are the focus of this thesis. Next, Section 2.3 discusses the basic principles of additive manufacturing, focusing on powder bed fusion and its process parameters and defect formation mechanisms. Section 2.4 reviews the literature and collates a range of observations on defects formation specifically within lattice structures. The literature on a large range of measurement techniques for lattice structures is reviewed in Section 2.5. Section 2.6 discusses X-ray computed tomography in more depth, due to its popularity in the literature and its use for this thesis. Section 2.7 reviews the literature on finite element modelling methods for lattice structure analysis. A discussion of the chapter is given in Section 2.8, followed by a summary in Section 2.9.

Reviewing these topics is necessary for achieving the aim (Chapter 1, § 1.2). This chapter provides the required information for understanding lattice structures and the processes by which defects are produces, as well methods for measuring the defects and modelling their impact.

Note that portions of this chapter were used in the publishing of a review paper, [30].

2.1 Cellular solids

Cellular solids are defined by Gibson and Ashby as “an interconnected network of solid struts or plates which form the edges and faces of cells” [1]. Cellular solids exist in many forms; Figure 2.1 shows the categories of the main types of cellular solids.

Based on their geometrical structure, cellular solids are grouped into two main categories: foams and lattice structures. Foams consists of a stochastic geometries generated through processes which hold little control over local features. Therefore, foams are more appropriately defined through their global properties, for example, density. An example foam manufacturing process is the introduction of a gas into a molten material; the amount of gas used will influence the foam’s density but specific geometric features will form stochastically. Conversely, lattice structures possess highly ordered geometries at both local and global scales. On a local scale, a lattice structure is defined by a unit cell which is then tessellated to create the global lattice structure. The ability of a lattice structure to be controlled via unit cell design allows for much greater control of its properties, in comparison to foams.

Continuing with Figure 2.1, lattice structures can be further categorised. Unit cells are generally grouped into two categories: strut-based and surface-based. Strut-based unit cells consist of a network of struts connected at nodes, analogous to a truss structure; the example in Figure 2.1 is a body centred cubic lattice structure. Surface-based unit cells are mathematically defined using a surface connecting set of points for which a given function has a constant value, that is, an isosurface (see Chapter 4, § 4.1.1 for further discussion on isosurfaces). The most common types of surface-based unit cells are called triply periodic minimal surfaces (TPMS). TPMS unit cells can be categorised according to the method by which the geometry is generated. If the unit cell geometry is generated through the thickening of its isosurface, this is considered as sheet/matrix-TPMS. However, if the geometry is generated through the the solidification of the volume enclosed by the thickened isosurface, this is called skeletal/network-TPMS. Examples of sheet/matrix and skeletal/network TPMS are the double gyroid and gyroid respectively.

An example TPMS lattice structure is called the gyroid, defined by the equation

$$\cos(k_x x)\sin(k_y y) + \cos(k_y y)\sin(k_z z) + \cos(k_z z)\sin(k_x x) - t \tag{2.1}$$

where the number of cells—that is, the periodicity—in each direction x, y and z is given by

$$k_i = 2\pi \frac{n_i}{L_i}. \tag{2.2}$$

n_i is the number of unit cell repetitions in the directions x, y and z, and L_i is the absolute length of the structure in those directions. The isosurface in Eq. (2.1) can be treated as the boundary between solid and void regions in the unit cell volume. t is a variable that can be used to control the relative density (as defined in the following paragraph) of the lattice structure.

A key property of a cellular solid is its relative density ρ / ρ_s , which is defined as the ratio of the density of the cellular solid ρ to the density of the material from which the lattice is made ρ_s. As relative density increases, more of the design space is filled with material. A value of $\rho / \rho_s = 1$ corresponds to the case where $\rho = \rho_s$, denoting that the design space is now completely full of material. The relative density of the unit cell is a design feature of key importance, largely controlling the mechanical properties of the structure.

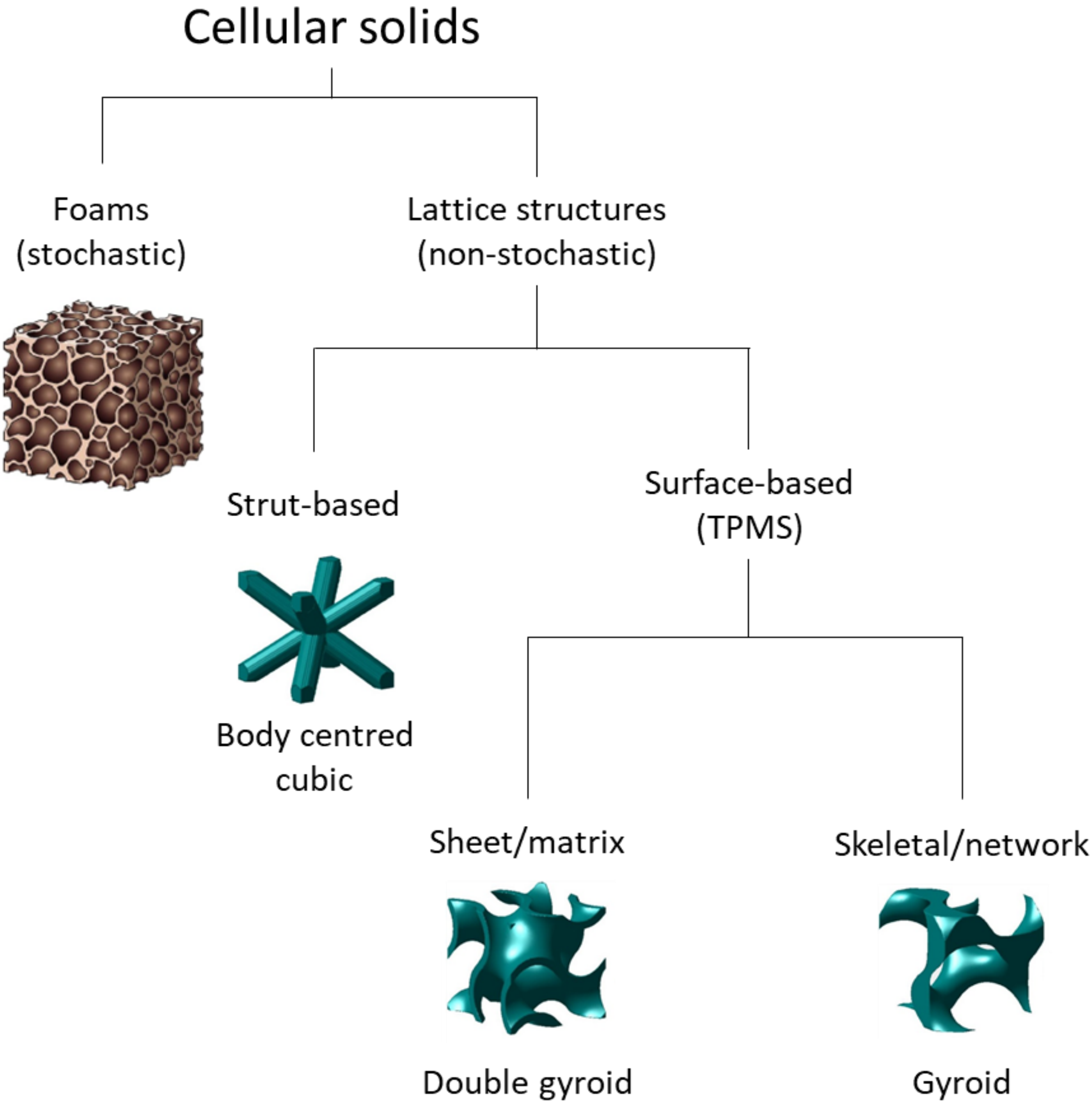
Cellular solids
Foams
(stochastic)
Lattice structures
(non-stochastic)
Strut-based
Surface-based
(TPMS)
Body centred
cubic
Sheet/matrix
Skeletal/network
Double gyroid
Gyroid

Figure 2.1. Hierarchical display of the main types of cellular solids. Note that the entire structure of the foam must be shown, due to its stochastic geometric structure [36]. Conversely, for the lattice structures, it is sufficient to only show images of the unit cells [37].

2.2 Strut-based lattice structures

Strut-based lattice structures are categorised into groups, based on their compressive stress-strain response which is controlled by the configuration of the lattice's struts and nodes. Two such categories are defined: bending-dominated and stretch-dominated [38]. To understand these categories, Maxwell's stability criterion must first be defined. Maxwell's stability criterion [39] states that for a frame consisting of b struts and j pin-jointed frictionless joints to be both statically and kinematically determinate in three dimensions, it must satisfy

$$M = b - 3j + 6 = 0. \tag{2.3}$$

If $M < 0$, the frame is a mechanism; it is not load-bearing and possesses one or more degrees of freedom in which displacements are allowed. However, lattice structures produced by additive manufacturing (AM) possess rigid joints, therefore if $M < 0$ then the struts will bend under load and the structure is classed as bending-dominated. If $M \geq 0$ then the structure is classified as stretch-dominated (for both pinned and rigid joints), as axial displacements will dominate the struts. Figure 2.2 shows examples of bending-dominated and stretch-dominated unit cells.

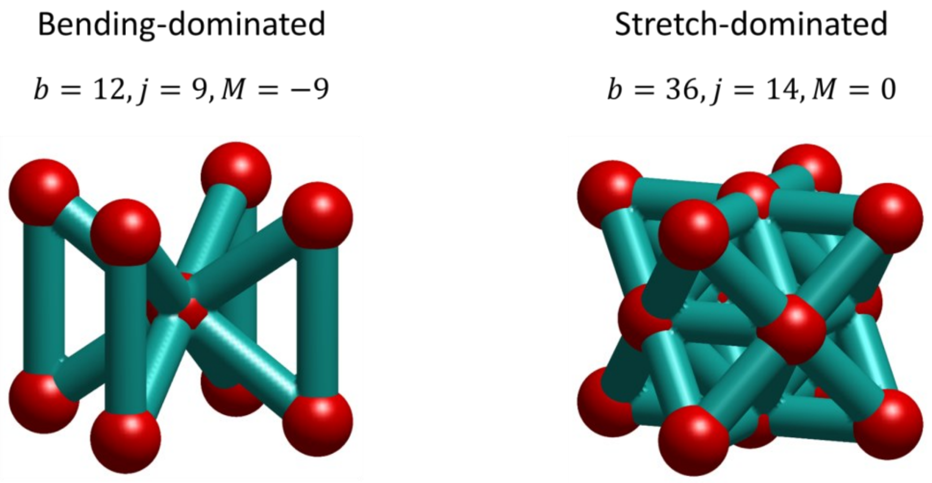

Figure 2.2. Examples of bending-dominated and stretch-dominated unit cells, according to Maxwell's stability criterion.

Figure 2.3 shows the characteristics of the compressive stress-strain response of bending-dominated and stretch-dominated structures. Both bending-dominated and stretch-dominated structures possess initial elastic deformation until the yield point and include a stage of plastic deformation at near constant "plateau stress", concluded by "densification" which occurs when the structure is nearly flattened and the crushed struts begin to make contact with each other. Stretch-dominated structures possess several unique characteristics: higher Young's modulus and yield strength, and a gradual decrease in stress after yield, called post-yield softening [38]. Bending-dominated structures are more suitable for applications where impact energy-absorption is desirable, due to its long plateau region. Stretch-dominated structures are more suitable for high load-bearing structural applications, due to the higher Young's modulus and yield strength [38].

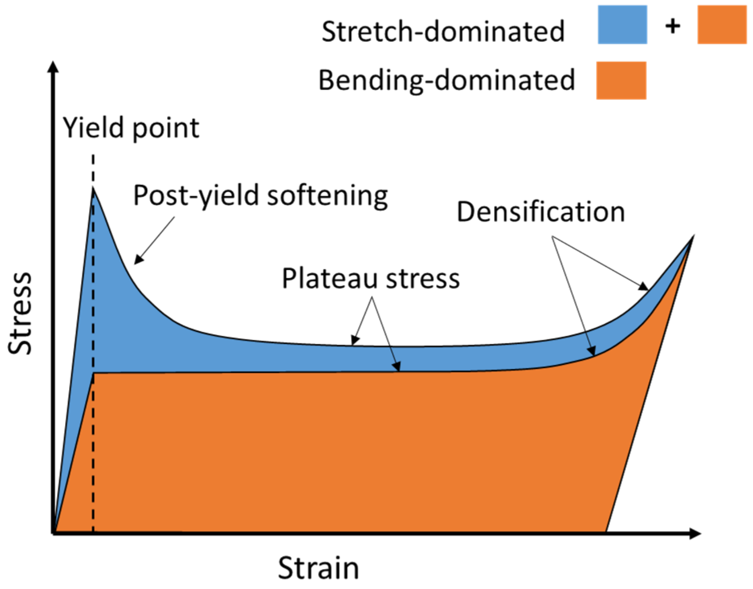

Figure 2.3. Example compressive stress strain response of bending-dominated and stretch-dominated strut-based lattice structures.

To conclude this section, the following paragraphs provide definitions of terms relating to lattice structures which are referred to throughout the thesis.

Medial axis

The mathematical definition of a medial axis for a planar shape is given as “the locus of the centres of a set of disks that maximally fit into the shape” [40]. Figure 2.4 shows an example of the medial axis of a planar shape. Extending the definition into three dimensions, the medial axis of a three-dimensional shape is defined as the locus of the centres of a set of spheres that maximally fit into the shape.

Cell size

The cell size of a unit cell defines the edge length of the bounding box which minimally encloses the medial axes of the unit cell’s struts, as shown in the example in Figure 2.5. Note that the bounding box must be cubic, such that the cell size can be derived from any edge length.

Overhang angle

In AM, overhangs refer to features which are not positioned perpendicular to the build bed (see § 2.3.1 for the definition of the build bed). Mathematically, a feature can be considered as an overhang if the surface normal of that region is not parallel to the build bed. Overhang angle θ, in degrees, defines the severity of the overhang. For a lattice strut, overhang angle θ is best visualised using Figure 2.6 which shows the right-angled triangle whose hypotenuse is the strut’s medial axis. This right-angled triangle is in a plane perpendicular to the xy plane. θ is determined using trigonometry. The maximum and minimum values of θ are, respectively, 90° and 0°, corresponding, respectively, to a strut whose medial axis is parallel or perpendicular to the build bed.

Tessellation

Tessellation refers to the duplication of a unit cell in up to three axes. A tessellation is notated as $a \times b \times c$ where a, b and c are integers denoting the number of unit cells in x, y and z respectively.

Porosity

Porosity is defined as any unintentional voids within the material of a lattice structure.

Designed porosity

Contrary to porosity, the term "designed porosity" will be used to refer to the enclosed void space intentionally designed into a given unit cell. Designed pores are of interest particularly to the biomedical implant industry, where the void space in a lattice structure has significant effect on bone ingrowth. The literature in the biomedical field often uses "porosity" to refer to "designed porosity" and therefore a distinction must be made here.

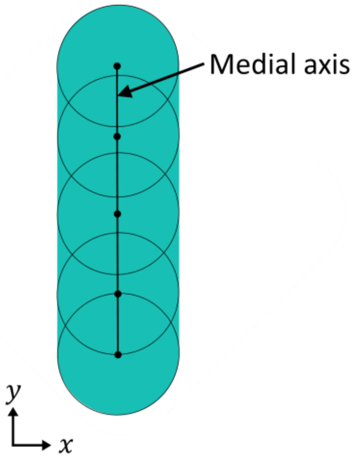

Figure 2.4. Diagram of the definition of the medial axis.

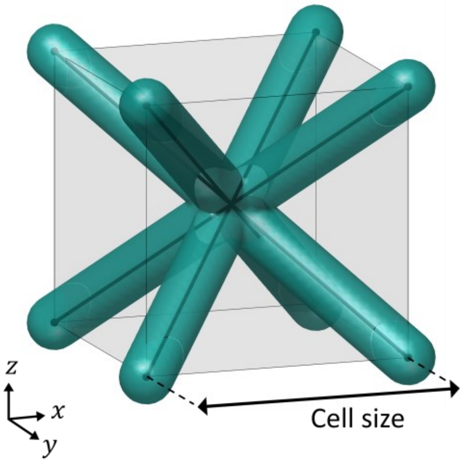

Figure 2.5. Diagram of the definition of cell size.

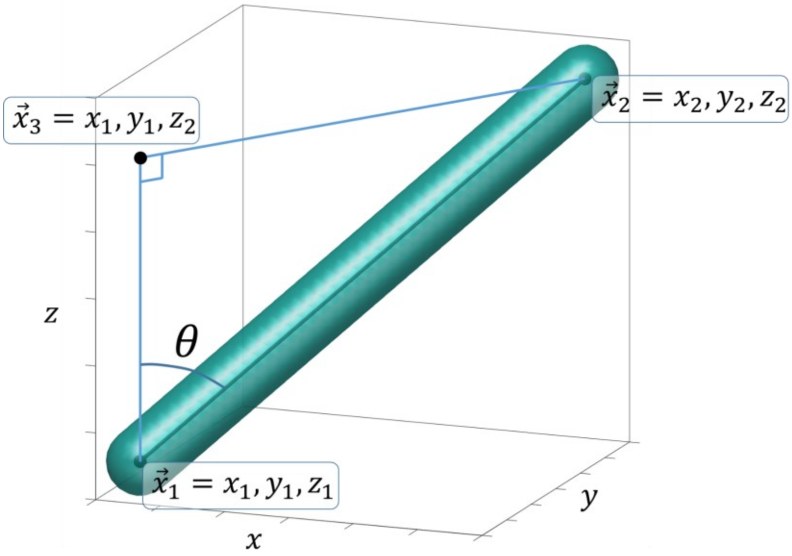
$\vec{x}_3 = x_1, y_1, z_2$
$\vec{x}_2 = x_2, y_2, z_2$
z
θ
$\vec{x}_1 = x_1, y_1, z_1$
y
x

Figure 2.6. Diagram of the definition of overhang angle θ.

2.3 Additive manufacturing

Due to the highly complex geometries present in lattice structures, AM methods are most often employed for their production (to the best of the author's knowledge). In this section, an overview of AM is provided, followed by additional discussion on specific AM processes most commonly used for the manufacturing of lattice structures.

Additive manufacturing (AM) is defined as the "process of joining materials to make parts from 3D model data, usually layer upon layer as opposed to subtractive manufacturing and formative manufacturing methodologies" [41]. In order to sort the vast range of AM methods, "process categories" are used to group AM methods according to similar process characteristics. There are seven process categories, listed in the following bullet points and accompanied by their definitions, according to [41]:

- Binder jetting: a liquid bonding agent is selectively deposited to join powder materials.
- Directed energy deposition: focused thermal energy is used to fuse materials by melting as they are being deposited.

- Material extrusion: material is selectively dispensed through a nozzle or orifice.
- Material jetting: droplets of build material are selectively deposited.
- Powder bed fusion: thermal energy selectively fuses regions of a powder bed.
- Sheet lamination: sheets of material are bonded to form a part.
- Vat photopolymerization: liquid photopolymer in a vat is selectively cured by light-activated polymerisation.

2.3.1 Powder bed fusion

From the author's own observations of the literature, powder bed fusion (PBF) appears to be the most commonly used process category for manufacturing lattice structures. This observation is further supported by a review paper from Nazir et al. [42], in which an attempt was made to count the frequency with which different AM methods were employed for lattice structure manufacture. Nazir's results found the majority of AM process to belong to the PBF process category, as shown in Figure 2.7, where SLM and EBM—selective laser melting and electron beam melting, respectively, both of which are PBF processes—form the majority (~50%). A similar observation on the dominance of PBF in the literature is made by a review by Helou and Kara [43]. Therefore, since PBF appears most relevant to lattice structures, further discussion of this process category will now be provided.

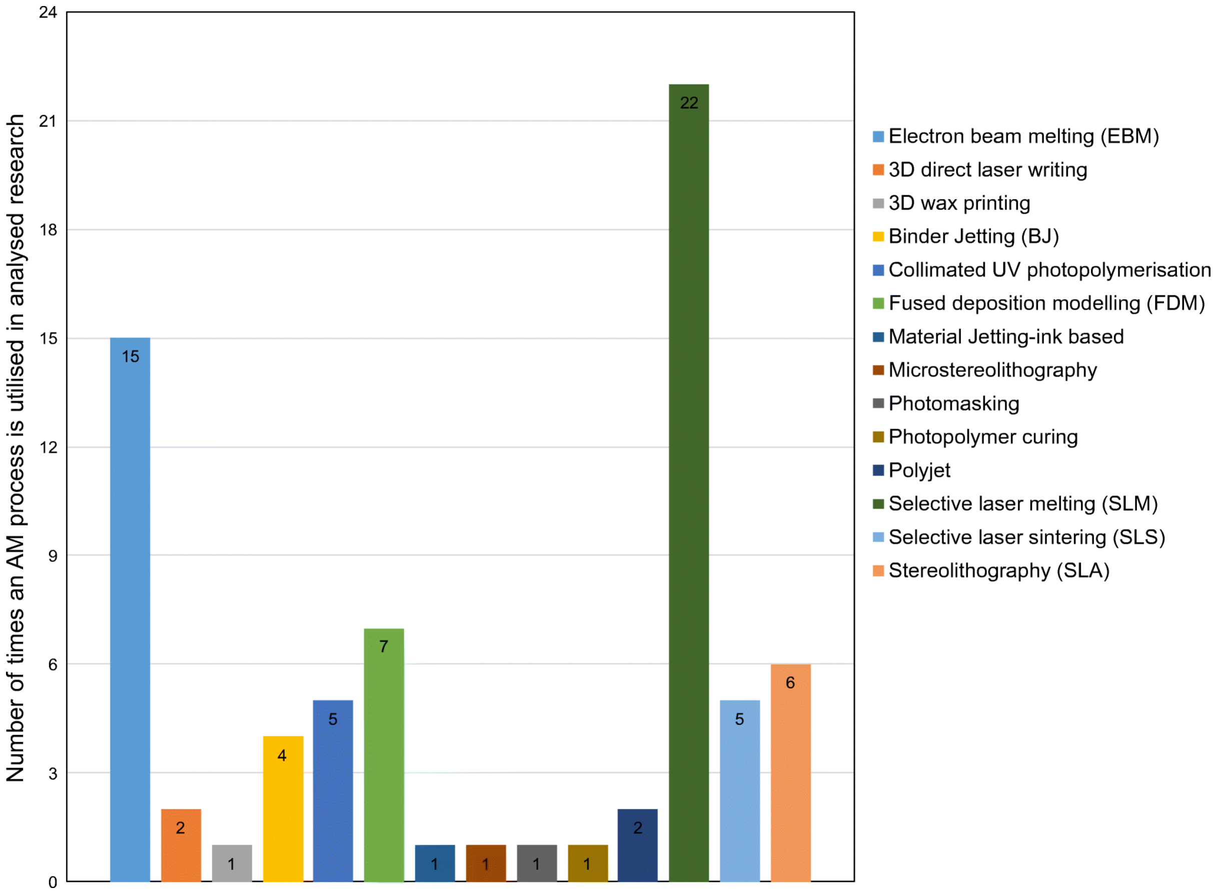

Figure 2.7. Bar chart showing various AM processes used for manufacturing lattice structures. [42]

Within PBF, there are four primary mechanisms by which the fusion of powder is performed: solid state sintering, chemically induced binding, liquid phase sintering and full melting—full melting is the predominant method for metal processing [44]. In full melting, the thermal energy is high enough to create a melt pool whose depth ensures the creation of well-bonded, high-density structures. There are two main methods which utilise full melting: laser melting (LM)—previously referred to as SLM—and electron beam melting (EBM). Figure 2.8 shows a diagram of the LM process, which is summarised in the following steps:

- A layer of powder is spread across the build bed using a recoating mechanism.
- A laser is focused onto the powder bed and fuses some regions of the layer of powder, according to a predefined laser scanning path.
- The build bed is lowered by one layer thickness.
- The process repeats until completion.

LM is performed in an enclosed chamber which is filled with an inert gas (e.g. argon) to minimize oxidation. Infrared heaters are used to maintain the powder material at a temperature just below its melting point. This raised temperature reduces the thermal gradients subjected to the powder upon interaction with the focused thermal energy source.

LM and EBM differ fundamentally in energy source, using a laser and electron beam respectively—this difference yields several effects such as a reduced feature resolution in EBM due to the defocusing of the beam to prevent a build-up of negative charge [44]. Figure 2.9 shows a diagram of an EBM system. The EBM manufacturing process follows the same steps as described for LM in the above bullet points, where "laser" should be substituted for "electron beam".

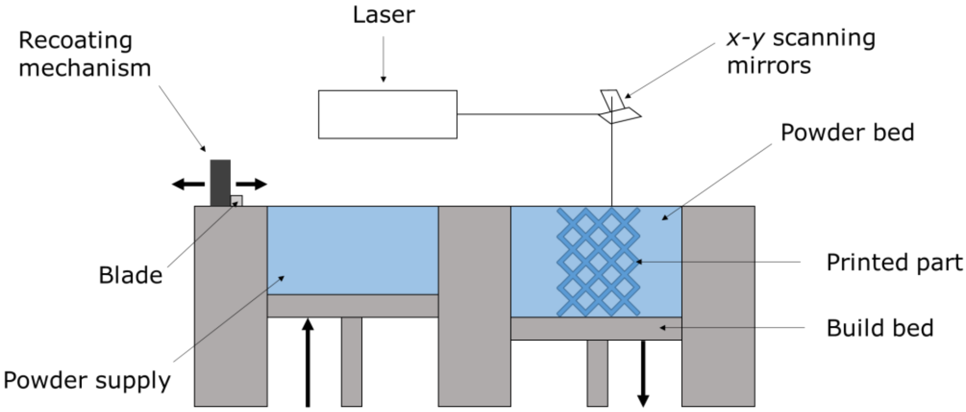
Laser
Recoating mechanism
x-*y* scanning mirrors
Powder bed
Blade
Printed part
Build bed
Powder supply

Figure 2.8. Diagram of the laser melting AM process.

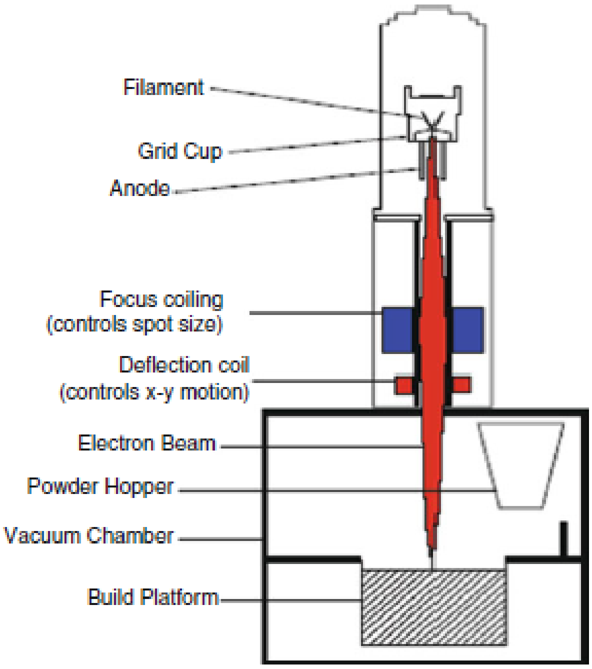
Filament
Grid Cup
Anode
Focus coiling
(controls spot size)
Deflection coil
(controls x-y motion)
Electron Beam
Powder Hopper
Vacuum Chamber
Build Platform

Figure 2.9. Diagram of an electron beam melting system. [44]

2.3.2 Process parameters

There are many process parameters which dictate the quality of an AM part. PBF process parameters can be grouped into four categories, according to [44]: thermal source parameters, scan parameters, powder parameters and temperature-related parameters. Thermal source parameters, such as laser/electron beam power, most directly control the fusing of powder material and, in the case of full melting, directly affect the melt pool characteristics. Higher powered energy sources tend to increase the size of the melt pool and thus produce denser parts. Scan parameters, for example scan speed and scanning patterns, control how the thermal energy is directed within the powder bed, which can control surface finish. The scanning of the energy source often occurs in two modes: contour mode and fill mode. Contour mode is often used to scan the perimeter of a cross section, often to increase accuracy and surface finish. The rest of the cross section is then scanned using a fill pattern. Example fill patterns include rastering, diagonal lines and random paths. Powder parameters such as powder size and layer thickness can control the thermal conductivity of the powder bed, powder bed density, powder spreading characteristics and the thickness of each layer. Finer powders have a higher overall surface area and absorb the energy source more efficiently than coarser powders. Temperature related parameters, such as powder bed temperature, can have a strong influence on the repeatability of the manufacturing process, where constant temperatures encourage uniformity throughout the build bed and between batches of production.

Many of these process parameters are strongly interdependent. For example, powder bed temperature, laser/electron beam power, scan speed and scan pattern all influence melt pool size, dimensional accuracy and surface finish. Keeping powder bed temperature uniform helps to achieve repeatable results. The combination of a higher-powered laser/electron beam and high powder bed temperature tends to produce dense parts but can also produce poorer dimensional accuracy—due to larger melt pools—than using a combination of a lower powered laser/electron beam and lower powder bed temperature. Higher laser/electron beam power also requires higher powder bed temperature in order to reduce warping due to residual stresses formed through the thermal gradients produced during melting. A lower powdered laser/electron beam requires lower scan speeds in order to ensure sufficient melting at each location. The spacing of scanning paths must also provide sufficient overlap to ensure good bonding between melted material in adjacent scanning paths.

The term energy density defines the relationship between key process parameters. Energy density is defined as:

$$Energy\ density = \frac{P}{vhf}, \tag{2.4}$$

where P is laser power, v is scan speed, h is hatch spacing (the spacing between scanning paths) and f is layer thickness [45]. These parameters are often used to investigate the effects of process parameters on print quality (for example [46,47]).

Lastly, a mention is given to support structures. Support structures are often manufactured alongside designs containing overhanging features which would otherwise distort under their own weight. Additionally, support structures are often required in metal PBF processes to prevent distortion from residual stresses induced through high thermal gradients[44]. Naturally, support structures must be removed from the design post-manufacture.

2.3.3 Powder bed fusion: defect formation mechanisms

The previously mentioned interrelated PBF process parameters (§ 2.3.2) have been shown to give rise to a range of defects in AM parts. In this section, a discussion is provided on the mechanisms by which different defects can form in parts produced by PBF. This section serves as the foundation for Section 2.4, in which the defects observed specifically in lattice structures will be discussed. As first mentioned in Section 1.1, the term "defect" can sometimes be used in a general sense to describe any aspect of a manufactured part which deviates from its initial design. However, in the following paragraphs in this section, more specific terms will be used to describe each defect more effectively. The following defects will be discussed: porosity, incomplete fusion, cracks, warping, balling, spatter and surface texture variations.

Porosity is defined by Zhang et al. [48] as approximately spherical voids with diameter typically less than 100 μm (Figure 2.10a). Pores can form in AM parts when gases within the melt pool are entrapped due to high cooling rates (up to 10^8 Ks^{-1}). The entrapped gases initially form either from gaps within the powder bed or through evaporation of lower melting point constituents within the powder material. Pores can also form through the use of hollow powder particles and through ridges formed in previous layers which impede the flow of the melt pool.

Incomplete fusion defects are explained by Zhang et al. [48] to occur mainly due to insufficient input energy and thus form irregular voids containing un-melted powders (Figure 2.10b). For easily oxidised materials, (for example $AlSi_{10}Mg$) the formation of oxide layers impedes melt pool flow and can cause additional incomplete fusion.

Cracks can form in parts produced by PBF, due to the residual stresses created through high thermal gradients which subject the part to rapid expansion and contraction [48]. Residual stresses can also cause shrinkage or warping in the AM part [49]. Cracking is more likely to occur in materials with low thermal conductivity and high coefficient of thermal expansion such as stainless steels and nickel-based superalloys [48]. Mercelis and Kruth [50] define two mechanisms through which residual stresses are induced. Firstly, the temperature gradient mechanism where, upon heating the part, expansion is hindered by the solidified material beneath, creating compressive residual stresses. Secondly, upon cooling of molten layers, contraction is hindered, creating tensile residual stresses. Mercelis and Kruth note that the temperature gradient mechanism does not require the material to be molten and can, therefore, occur in both solid state sintering and full meting processes, whereas the cooling mechanism requires the formation of a melt pool and thus only occurs in full melting processes.

Unstable melt pools can cause balling and spatter. Balling occurs when the melt pool solidifies into a sphere instead of spreading onto, i.e. "wetting", the underlying substrate to form a layer—wetting is mainly controlled by the length-to-width ratio of the melt pool, where a ratio < 2.1 is desirable [51] (Figure 2.10c). Spatter occurs at relatively high energy densities, where molten material is expulsed by the recoil pressure generated by evaporation within the melt pool (Figure 2.10d).

In PBF, the overall surface texture of a region will be strongly affected by orientation of that region in space. Regions of a surface possessing a surface normal which is directed towards the build bed—such regions are called down-skin surfaces—produce significantly more irregular surfaces than regions with surface normals facing away from the build bed—called up-skin surfaces. This discrepancy between down-skin and up-skin surfaces will be called a "texture bias". Texture bias is caused by the support powder which is a poor conductor of heat. Down-skin surfaces experience excess heating and poor cooling through the support powder, whereas up-skin surfaces cool faster via conduction through the solidified part underneath [49]. Note that the chosen convention here is that surface normals are directed outwards away from the part, not inwards.

Lastly, some consideration is given to the quality of the powder material which naturally has a fundamental effect on the quality of manufactured parts. In particular, powder recycling can have adverse effects on the quality of parts produced by PBF, these effects vary based on the material. To share some examples, He et al. [52]

observed porosity increases when using recycled powder in AM parts manufactured using laser melting of Hastelloy X (a nickel-based alloy). Similarly, porosity increases were observed by Ahmed et al. [53] when using recycled powder for laser melting of 17-4 PH stainless steel.

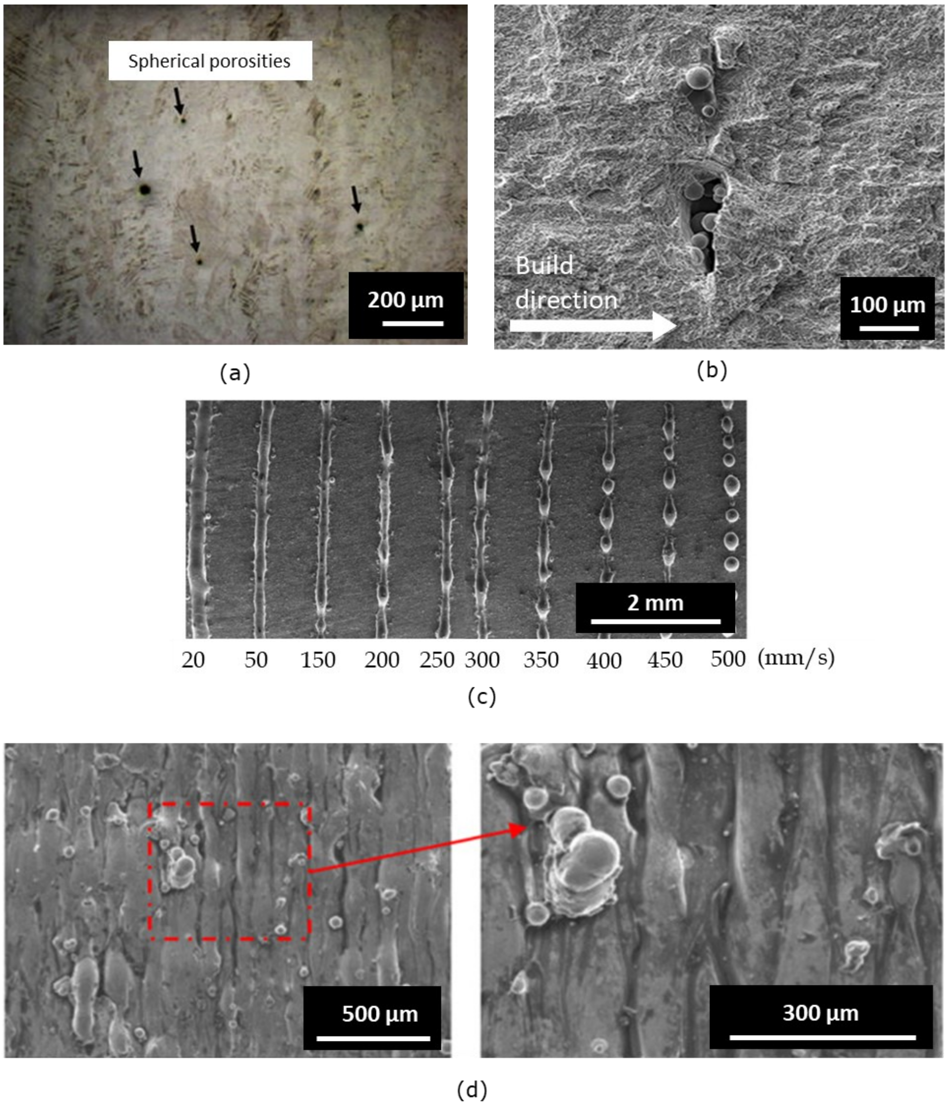
Spherical porosities
200 µm
(a)
Build direction
100 µm
(b)
2 mm
20 50 150 200 250 300 350 400 450 500 (mm/s)
(c)
500 µm
300 µm
(d)

Figure 2.10. Examples of the defects which form in PBF processes. (a) porosity [54] (annotations from [26]) (b) incomplete fusion [55] (c) balling occurring at higher scanning speeds [56] (d) spatter [57].

2.4 Lattice structure defects

This section discusses the range of defects commonly observed in lattice structures. Lattice structures possess numerous overhanging, often millimetre-scale, features which challenge the performance limits of PBF manufacturing systems, therefore, lattice structures are particularly prone to defects. Furthermore, the absence of the use of support structures in manufacturing lattice structures can increase defect formation; support structures cannot be used in lattice structures due to the unfeasibility of their removal post-manufacture. The defect formation mechanisms mentioned in Section 2.3.3 cause the formation of characteristic defects in lattice structures produced by PBF. Additionally, defects are more prevalent in metallic lattice structures produced by PBF, due to higher processing temperatures and therefore higher thermal gradients. Defects can significantly hinder the desired operating performance of AM parts, for example through the introduction of stress concentrations causing a reduction in fatigue strength [47].

As has been established in this thesis, the term "defect" is useful for general discussions regarding discrepancies between an initial design and the manufactured part, but more descriptive terms are appropriate for the following discussions. The following defects are discussed in the remainder of this section: geometric deviations, surface texture variations and porosity. Only defects in metal PBF lattices are discussed in this section, due to their prevalence in the literature. In this section, comparisons will be made between a manufactured lattice structure and its initial design; the terms "as-built" and "nominal" will be used to refer to the manufactured lattice structure and the initial design respectively.

2.4.1 Geometric deviations

Geometric deviations are a type of defect defined by deviations in the geometry of lattice structures which are on the scale of the dimensions / design features of a given lattice structure, for example, deviations in strut radius. This section discusses the geometric deviations which have been observed in the following lattice features: strut diameter, wall-thickness, cross section, medial axis, lattice nodes and designed pores.

Significant deviations have been observed between the nominal and as-built average diameter of lattice struts; both over-sizing and under-sizing has been observed in as-built lattice struts, as shown in Table 1. Cuadrado et al. [58] and Arabnejad et al.

[59] showed the relationship between as-built strut diameter and strut orientation, where vertically oriented struts (i.e. overhang angle of 0°) were under-sized by up to 45%, and horizontal struts (i.e. overhang angle of 90°) were over-sized by over 100%. Zhang et al. [60] observed similar orientation-dependent thickness variations in the surfaces of TPMS unit cells; the wall-thickness of horizontally oriented surfaces was larger than the nominal thickness, and vertically oriented surfaces were thinner than nominal. The cross sectional shape of as-built lattice struts has been shown to often deviate from its nominal circular shape and into an elliptical shape [59–61]. Arabnejad et al. [59] notes that this deviation is also dependent upon orientation, occurring the most in horizontally oriented struts, due to overmelting. Sercombe et al. [62] discuss some of the effects of diameter variations (Figure 2.11) and found horizontal struts to cause failure in lattice structures loaded under compression, due to the tensile load carried by the horizontal struts.

The term "waviness" is used to describe deviations between the as-built medial axis and the nominal medial axis. Melancon et al. [63] and Liu et al. [64] have both observed waviness (Figure 2.12) in lattice struts, where the waviness was present to a greater degree in horizontal struts. Liu et al. [64] found the maximum waviness—i.e. the maximum distance between as-built and nominal medial axes—to increase from approximately 8% to 17% of the nominal radius in diagonally oriented struts and horizontal struts respectively. Similarly, Melancon et al. [63] found the maximum waviness to increase from of 7% to 9% in diagonal and horizontal struts respectively. Similar observations on strut orientation dependency are also observed in [60,65–67].

Several defects have been observed at lattice nodes. Excess material accumulation—known also as mass agglomeration—at lattice nodes has been observed by Gümrük et al. [68]. Similar results were seen by Li et al. [69], where strut diameters increased by approximately 30% near the nodes. Al-Ketan et al. [70] compared several unit cell designs and found nodes to be smoother in surface-based unit cells in comparison to strut-based. Additional comments on geometric deviations around lattice nodes are made in references [71,72].

Hollander et al. [73] and Lin et al. [74] both observed mass agglomeration, referred to as "surface protrusions", in the designed pores (first defined in § 2.2) of lattice structures, the most severe of these extended across 0.3 mm (30%) of the diameter of the designed pore [73]. Surface protrusions form obstructions within designed pores which can impede bone ingrowth in lattice structures used for biomedical implant applications.

Table 1. Observed deviations in strut diameters.

	Designed strut diameter/mm	**Strut deviation/mm**
Sing et al. [75]	0.6 to 0.8	-0.5 to -0.2 Up to ~60%
Tancogne-Dejean et al. [71]	0.534	Average strut deviation -0.01 (~2%)
Choy et al. [76]	0.4 to 1.2	-0.138 to +0.156 (-10% to +40%)
Cuadrado et al. [58]	0.65	Vertical: 0.46 (-30%) Sloped: 0.36 (-45%) Horizontal: 1 (+54%)
Arabnejad et al. [59]	0.2	Vertical: 0.11 (-45%) Sloped: 0.26 (+30%) Horizontal: 0.45 (+128%)

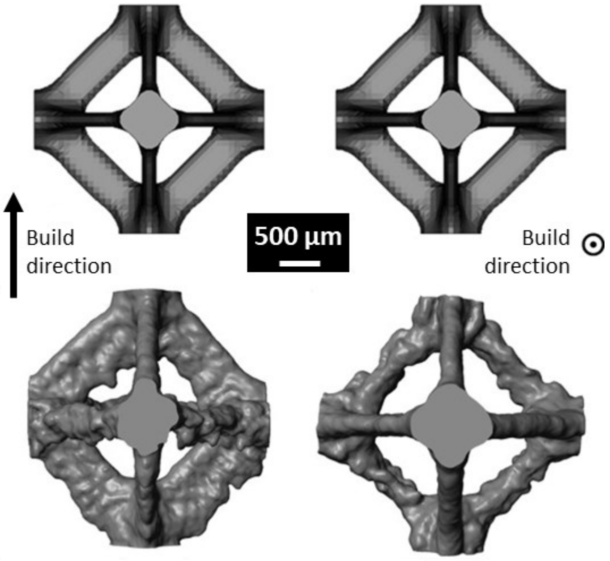

Figure 2.11. Example of strut orientation-dependency. Top row: CAD representation of unit cell. Bottom row: 3D rendering of XCT model. The geometry of the horizontal struts is shown to be highly irregular. The "build direction" labels on the left and right correspond to the left and right columns in the image [62].

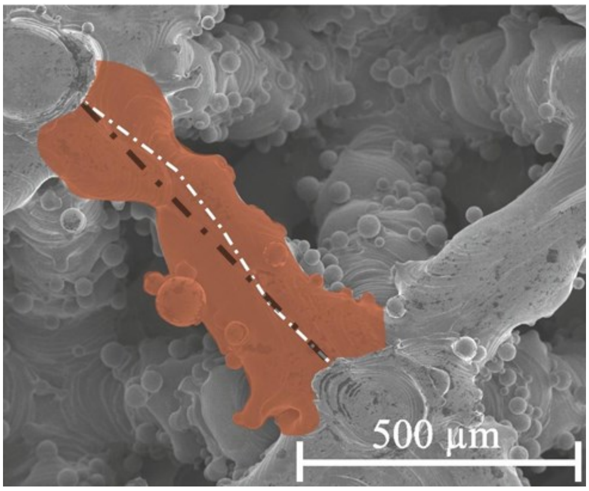

Figure 2.12. SEM micrograph showing strut waviness The nominal medial axis and as-built medial axis are shown in black and white respectively [63].

2.4.2 Surface texture variations

As previously mentioned, (§ 2.3.3) PBF processes produce parts with highly complex surfaces and undesirable surface texture variations can form due to melt pool instabilities. In this section, two surface texture variations are considered: texture bias and stair-stepping effects. Surface texture is considered at a scale much smaller than that of the dimensions of the lattice structure and exists at high spatial frequencies.

Texture bias can be clearly observed when comparing down-skin and up-skin surfaces of lattice struts. Lattice structures often possess many down-skin surfaces due to their many overhanging struts; these down-skin surfaces are subjected to local over-heating [34,62,69,70,77–79]. Pyka et al. [80] and Leary et al. [72] analysed up-skin and down-skin surfaces of lattice structures using surface roughness parameters, as defined by ISO 4287 [81]. Pyka et al. [80] examined the surfaces of lattice struts and found the *Ra* value of down-skin surfaces to be approximately twice that of up-skin surfaces. Leary et al. [72] calculated *Ra* and *Rz* values for down-skin and up-skin surfaces of struts with overhang angles of approximately 45° and 55°. Leary et al. showed that increasing the overhang angle of struts from 45° to 55° caused the *Ra* value of down-skin surfaces to increase by almost 200%. Similarly, the *Rz* values for down-skin surfaces showed significant increase upon increasing overhang angle. Conversely, for up-skin surfaces the *Ra* values showed little variation upon changing overhang angle. Although the parameters *Ra* and *Rq* provide insights on the surface texture of surfaces produced by AM, these parameters are particularly limiting because they are one-dimensional measurements i.e. profile measurements. Two-dimension—that is, areal—measurements have several distinct advantages over profile measurements, as discussed by Townsend et al. [82]. Firstly, because a measured surface is three-dimensional in nature, profile measurements provide ambiguous and/or incomplete descriptions of the measured surface. Due to the popularity of the *Ra* parameter, the areal parameter *Sa*—which is mathematically equivalent to *Ra* but extended into two dimensions—is commonly used for areal characterisation of surfaces produced by AM [82]. There are other areal parameters which provide more descriptive information on a given measured surface; areal parameters are defined in ISO 25178-2 [83]. For an example work in which a range of areal parameters are used on surfaces produced by AM, the reader is directed to Thompson et al. [84] in which areal surface characterisation is performed using a range of areal parameters on surfaces produced using various measurement instruments.

Stair-stepping defects have also been investigated in lattice structures. Stair-stepping defects are a natural by-product of the layer-wise PBF process, in which discontinuities form between successive layers. Al-Ketan et al. [70] compared the surfaces of strut-based and surface-based unit cells produced by laser-PBF of Maraging steel and observed the stair-stepping effect to be less severe in surface-based unit cells, an example of which is shown in Figure 2.13. The reduced stair-stepping effect in surface-based unit cells has been attributed to the fact that surface-based designs possess a continuous change in overhang angle. Other supporting comments on the surface texture of lattice surfaces can be found elsewhere [68,71,73,85–98].

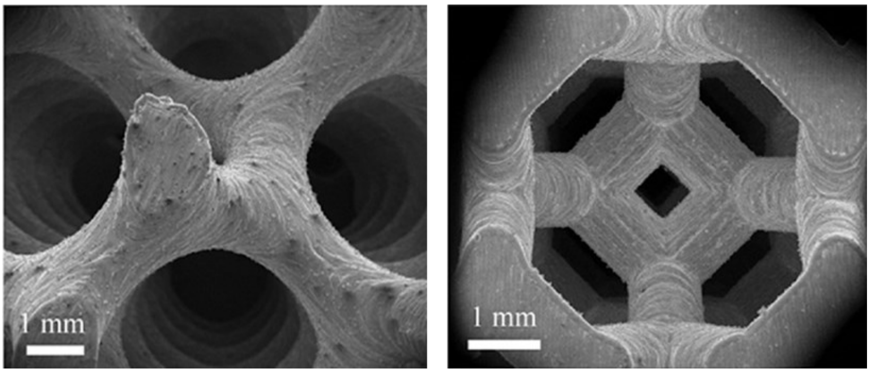

Figure 2.13. SEM micrographs showing stair-stepping defects. From left to right: gyroid (surface-based) unit cell and Kelvin structure (strut-based) unit cell. A more pronounced stair-stepping effect can be seen in the Kelvin structure [70].

2.4.3 Porosity

To the author's knowledge, there are few studies in the literature which study the relationship between specific lattice structure features and porosity formation. Yan et al. [99] investigated the effects of increasing unit cell size on porosity. Porosity was found to increase by up to approximately 10% upon increasing the size of gyroid unit cells from 2 mm to 8 mm. This porosity increase was attributed to the longer scanning paths required for the larger unit cells which in turn allows a greater period of time for pores to form in between adjacent scanning tracks; each unit cell was manufactured using the same process parameters. Yan et al. [99] highlight that further optimisation of the parameters depending on unit cell size should alleviate any increase in porosity. Amani et al. [33] also attribute scan strategy to an increase in porosity, where pore size was observed to increase at the nodes of lattices in comparison to the struts (Figure 2.14).

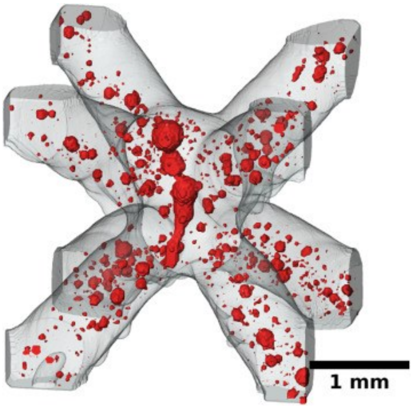

Figure 2.14. XCT results showing increased porosity in the nodes of a lattice [33].

2.4.4 Post processing

After the PBF manufacturing process is completed, post processing can be performed to improve the quality of the part. Post processing methods can be performed for many reasons, such as to reduce porosity, to alter grain structure or to modify surface texture. This section discusses post processing methods which have been employed for smoothening the surface texture of and reducing porosity in lattice structures.

To smoothen the surface texture of AM parts, mechanical surface treatment methods—such as sandblasting—are commonly used [73,93]. However, limited access to the internal features in lattice structures may prove difficult to treat, as highlighted by Hollander et al. [73]. Chemical etching has also been used in several studies to investigate its effect on the surface texture of Ti6Al4V lattice structures [78,80,100,101]. de Formanoir et al. [100] investigated the effect of hydrofluoric acid and nitric acid solutions on the surface texture of Ti6Al4V octet lattice structures. A clear decrease in attached particles was observed and a corresponding reduction in profile parameters (*Ra* and *Rt*) was calculated from XCT data of the lattice structure surface (the reader is referred to § 2.4.2 for discussions on profile and areal parameters). The etching process also caused the volume fraction to decrease by approximately 7%. Compression tests revealed a reduction in stiffness upon etching, with this reduction being proportional to the change in volume fraction. Chemical etching was also observed to reduce the discrepancies between experimentally determined and simulated stiffness values. This stronger agreement with simulation data was attributed to the removal of attached particles which allowed for a better representation of nominal, cylindrical struts.

To reduce the porosity in AM parts, hot isostatic pressing is commonly used, a process in which porous parts are subjected to high pressure and temperature [102–104]. Wu et al. [105] observed a significant improvement in fatigue properties upon hot isostatic pressing of Ti6Al4V lattice structures, quantified by an increased endurance ratio of approximately 80%. The improved fatigue properties were attributed to a phase change from brittle α'-martensite to tough $\alpha + \beta$ mixed phases causing an increase in toughness—the key material property for resisting crack propagation. A 20% and 30% reduction in hardness and yield strength respectively was also recorded. Hot isostatic pressing was also performed by Dutton et al. [106] on EBM and LM parts. It was observed that for LM parts, the high pressure caused the gas filled pores to compress into sharp edges. However, EBM parts were unaffected due to the evacuated chamber preventing gas filled pores from forming. Van Hooreweder et al. [107] studied the effects of stress relieving, hot isostatic pressing and chemical etching on the fatigue properties of Ti6Al4V lattice structures; the results showed all of these post processing methods to increase fatigue life. In particular, the combination of hot isostatic pressing and chemical etching produced the largest improvement in fatigue life.

2.5 Measurement techniques

As previously mentioned (Chapter 1, § 1.1), many studies of lattice structures involve the use of a measurement technique to assess the quality of manufacture parts and, in particular, to obtain quantitative data on a given defect. Table 2 lists various measurement methods used for observing different defects in lattice structures.

Regarding the measurement of geometric deviations, X-ray computed tomography (XCT) data can be aligned to the original CAD model for comparison against the nominal values. This alignment can be used to calculate the maximum or average deviation of the XCT data points [34,93,95]. Other methods using XCT include measuring the volume or surface area of the lattice structure, as demonstrated by Van Bael et al. [108,109] and Parthasarathy et al. [92]. For local strut measurements, Qiu et al. [94] and Melancon et al. [63] calculated strut diameter using fitting algorithms to inscribe circles within individual XCT slice images. Pyka et al. [80] and Heinl et al. [86] expand this into three dimensions (3D) by using sphere-fitting algorithms to measure the diameters of struts and designed pores respectively. Hrabe et al. [87] suggest that using the median value of inscribed sphere diameter is a more appropriate representation of the strut diameter. SEM [68,69,73,89,90,94,98,110–113] and optical microscopy [58,76,77,95,114–117] have also been used for measuring dimensions in lattice structures. It is also relatively common to use Vernier calipers for the measurement of outer dimensions (for example, lattice diameter, length, width) [75,112,114,118]. The lattice's mass has been used to calculate volume fraction, as performed by Al-Ketan et al. [70] and Wieding et al. [119].

For the measurement of surface texture variations, *Ra* values from profiles of strut surfaces have been calculated using XCT, by Kerckhofs et al. [78], Pyka et al. [80], and de Formanoir et al. [100], and using optical microscopy by Leary et al. [72]. Similarly, *Ra* was determined using the variation in strut cross-sectional area using XCT by Tancogne-Dejean et al. [71].

Porosity is often calculated using Archimedes' method wherein the mass of the lattice is weighed in two different fluids [76,93,99,120]. XCT has been used to calculate porosity [33,34,65,121]. Amani et al. [33] employ a stitching method with XCT, whereby small portions of the lattice are imaged at higher magnification and are stitched together. This enabled smaller voxel sizes to be achieved and a greater proportion of pores were detected. Optical microscopy was used by Qiu et al. [94] and Köhnen et al. [2] to calculate an average porosity from a select number of cross-sections. SEM has also been used by Tancogne-Dejean et al. [71] to view surface porosity.

Table 2. Defect measurement methods

Defect	Measurement system	Reference	Measurement technique
Geometric deviations	XCT	[27,28,33,34,59,62–64,71,72,74,80,86,87,92–95,108,109,122,123]	Comparison to CAD model Calculate total volume Analyse cross sectional shape
	SEM	[68,69,73,89,90,94,98,110–113]	Dimensional measurements (length, diameter, etc.) Infer relative density
	Optical microscopy	[58,76,77,95,114–117]	
	Vernier calipers	[75,112,114,118]	
	Weighing	[70,119]	Infer relative density
Surface texture variations	XCT	[34,71,74,78,80,94,100]	Calculate *Ra* value from strut profile or cross-sectional area
	Optical microscopy	[72,92,97,116]	*Ra* value from strut profile
	SEM	[68,69,80,85–89,93,96,98,115,117]	Qualitative analysis
Porosity	Archimedes' method	[76,93,99,120]	Infer porosity from weight in two fluids
	XCT	[33,34,65,121]	Calculate total porosity
	Optical microscopy	[2,94]	Average porosity determined from select cross sections
	SEM	[71]	Surface porosity

2.6 X-ray computed tomography

As demonstrated in the previous section, X-ray computed tomography (XCT) is commonly used for the measurement of lattice structures [30] due to its ability to image both external and internal geometries; XCT does not suffer from line-of-sight issues. For these reasons, XCT was used for all measurements of lattice structures in this thesis (see Chapter 3, § 3.3.1). This section will discuss the basic principles of XCT (§ 2.6.1), followed by explaining how measurement data is acquired (§ 2.6.2-2.6.4) and will conclude with a discussion on XCT metrology considerations (§ 2.6.5).

2.6.1 Principles of X-ray computed tomography

There are several methods by which X-ray production can be achieved [124], this section explains the method utilised by the XCT system in thesis (see Chapter 3, § 3.3.1): the X-ray tube. As shown in Figure 2.15, the main components of an X-ray tube are a cathode and anode inside an evacuated chamber. A voltage is applied to the cathode—often a tungsten filament—which is heated by the Joule effect. As the cathode temperature continues to rise, the kinetic energy of the electrons overcomes the attractive forces of the nuclei (i.e. the work function) and are released from the metal. Electron optics are then used to form an electron beam, which is accelerated towards the anode target—also often tungsten—forming a focal spot on the target. Incoming electrons interact with the atoms in the target causing emission of X-ray photons either through the deceleration of incoming electrons, by the refilling of vacancies in electron shells, or by colliding with the atoms' nuclei [124]. The X-ray beam is then shaped by passing through a beryllium window.

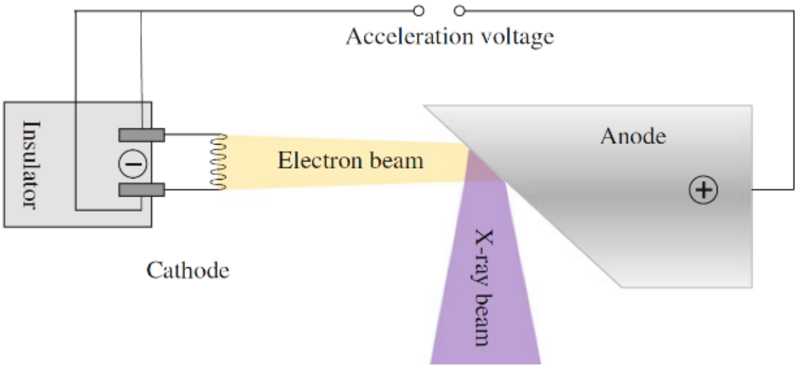

Figure 2.15. Diagram of an X-ray tube [124].

2.6.2 Measurement procedure

XCT imaging systems exist in many different configurations, each of which is designed to suit a specific set of needs. For the imaging of engineering components, industrial XCT systems are used. More specifically, only the industrial cone beam system will be considered here, as this is the system used in this thesis. Other XCT systems are discussed here [124].

Figure 2.16 shows a diagram of a typical industrial cone-beam XCT system, with further detail on select components provided in Figure 2.17. The three main components of this system are as follows: an X-ray source, the sample platform and an X-ray detector. The X-ray source produces the X-ray beam; the sample platform holds and rotates the sample during the scanning process; the detector, or solid-state detector, consists of a grid of scintillation crystals which are used in the conversion of the X-rays into an electric current.

To perform a measurement on a given sample, the sample is placed on the rotation stage and irradiated by a cone-shaped X-ray beam. Absorption of X-ray photons by the sample causes attenuation in the X-ray beam intensity. Individual pixels in the flat panel detector record the attenuated intensities, thus completing one cycle in the measurement i.e. one projection. The rotation stage then rotates the sample by a small increment θ_{proj} and the process restarts until the sample has been rotated by 360°.

For each projection, a slice is defined as the data recorded by one row of scintillation crystals in the detector. A sinogram is defined as the projection data for all rotations for a given slice. A sinogram is formed by stacking all of the projections acquired for a given slice. Raw XCT data is often stored in sinograms.

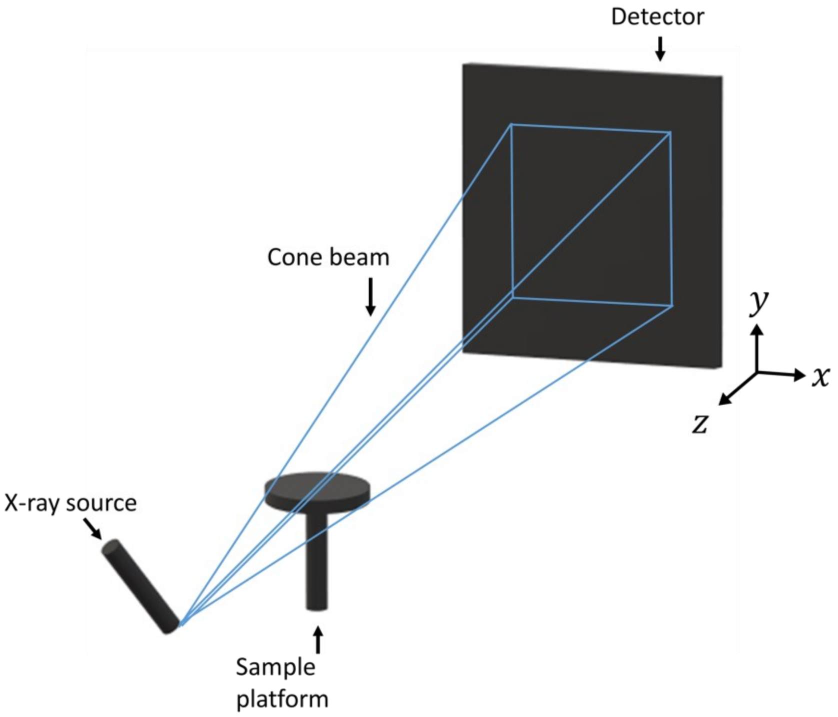
Detector
Cone beam
y
x
z
X-ray source
Sample platform

Figure 2.16. Diagram of an industrial cone-beam XCT system.

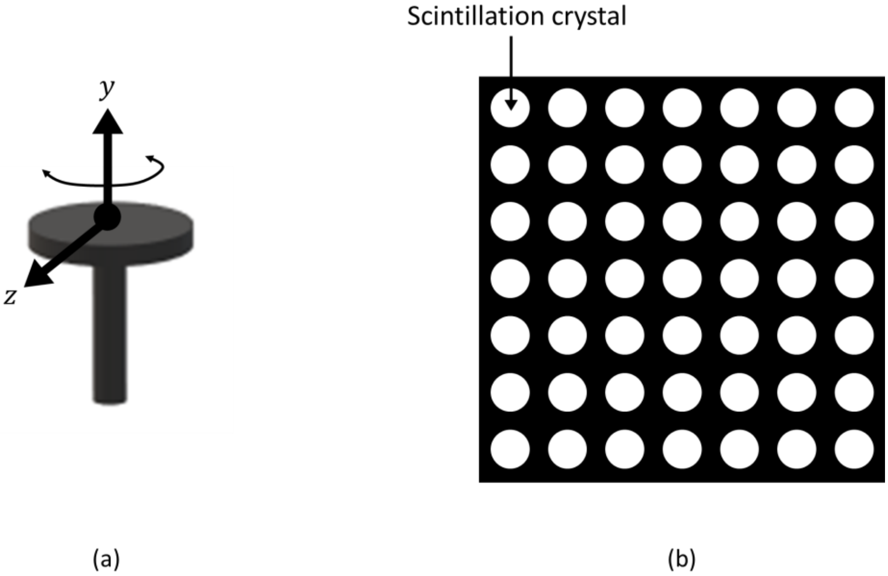
y
z
Scintillation crystal
(a)
(b)

Figure 2.17. Diagram of a sample platform and detector panel. (a) The sample platform moves via translations in z and rotations about y. (b) The detector uses scintillation crystals for conversion into electrical current.

2.6.3 Data processing

Reconstruction, the first step in XCT data processing, is the process of combining all of the data from each projection and converting it into a three dimensional scalar field of ‘grey-values’. The reconstruction processing is outside of the scope of this section; the reader is referred to [124] for further discussion. Each point in the grey-value scalar field corresponds to the amount of X-ray attenuation caused from that location in the scanning volume. The more dense the material is at a given point, the higher the grey-value. The points in a grey-value scalar field are equally spaced in all three dimensions; the term “voxel size” is used to define this spacing.

As shown in Figure 2.18, these grey-values can be represented in a histogram. Peaks in the histogram correspond to specific materials within the scanning volume. Figure 2.18 shows an example histogram for a mono-material sample; the higher grey-value peak corresponds to the sample material, the lower grey-value peak corresponds to the surrounding air (note that the surrounding air is itself a material). A histogram with three or more peaks suggests a multi-material sample.

Surface determination, the second step in XCT data processing, is the process of extracting a surface from the grey-value scalar field. This surface is extracted by first specifying a threshold value and then searching the grey-value scalar field for the coordinates of the threshold value—interpolating where necessary. The threshold value can be specified either globally or locally. The most common global thresholding method uses the mean grey-value of the material and air peaks in the histogram. This mean is commonly called ISO50, an example of which is in Figure 2.18. The static nature of ISO50 thresholding presents a number of limitations. ISO50 can be clearly unsuitable for some multi-material histograms, particularly in cases where grey-value distributions begin to overlap and thus fail to provide a distinct point between the materials. Additionally, imaging artefacts produce erroneous grey-values which may be undetected by a global threshold method. Therefore, ISO50 is prone to systematic errors. Local thresholding methods allow for the threshold value to vary within a small search distance of voxels, depending on the grey-value data within that region.

In each of these regions, a starting threshold (often ISO50) is compared to the grey-values in its region and the local threshold value is altered when deemed necessary by criteria defined in the thresholding algorithm. Local methods allow for more reliable results even in the presence of artefacts (which manifest as sudden local changes in grey-value).

After completing reconstruction and surface determination, the XCT data can be analysed. Analysis can be performed through manual selection of points on the surface—which can be used to calculate dimensions—or through fitting techniques such as the fitting of geometrical primitives (e.g. spheres, cylinders and planes) for use in geometric dimensioning and tolerancing (e.g. flatness and cylindricity). Internal porosity is also often calculated, which is particularly common for AM measurements [125,126]. The determined surface can also be aligned to the original CAD model to assess the deviations from the initial design. Examples of these types of analyses were discussed earlier in this chapter (§ 2.5).

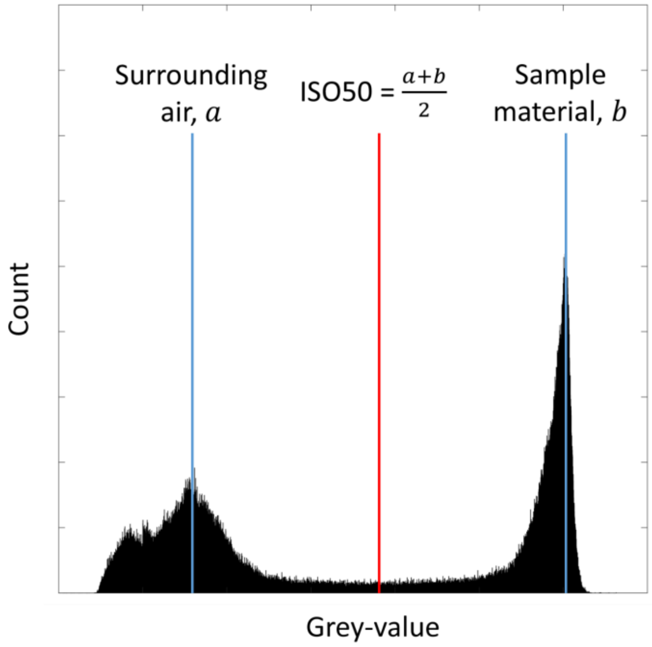

Figure 2.18. Grey-value histogram showing the ISO50 value.

2.6.4 Measurement parameters

There are many parameters to consider when setting up an XCT measurement. This section will define the following parameters:

- Voltage
- Current
- Filtering
- Number of projections
- Exposure time
- Images per projection
- Magnification

The voltage of an XCT system controls the speed at which the electrons are guided into the anode. Increasing the voltage of an XCT system will increase the average energy of the X-ray beam; this is required for imaging dense and highly attenuating materials.

The X-ray tube current controls the number of X-ray photons produced per unit time. Controlling the current can remove noise in the captured images. Changing the current does not change the energy of the X-ray beam.

A filter is a piece of metal, up to a few millimetres thick, placed in front of the X-ray source. Filtering of the X-ray beam can help to remove unwanted low-energy X-ray photons before the beam interacts with the sample. If filtering is not used, a sample may cause beam hardening to occur, which describes a scenario in which the sample absorbs low-energy X-ray photons and thus increases the average energy of the beam which passes through and is recorded by the detectors. Beam hardening can lead to erroneous pixel values in the images, known as “beam hardening artefacts”. An example of beam hardening can be seen in Figure 2.19a which shows an XCT projection of a spherical mono-material sample in which the grey values of the edge are incorrectly higher than the rest of the material. Note that same beam hardening artefacts can be removed using image processing algorithms; Figure 2.19b shows an example.

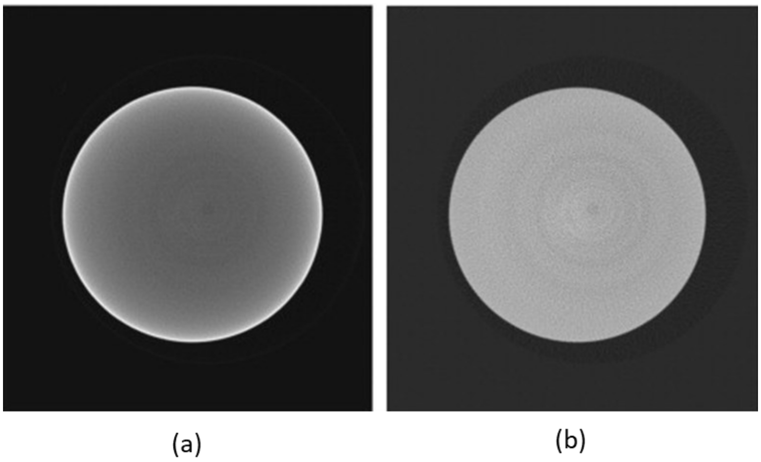

Figure 2.19. An example of a beam hardening artefact. (a) The beam hardening artefact causes the grey values of the edges of the material to be incorrectly higher that the rest of the material. (b) A result of an image processing algorithm used for removing beam hardening artefacts. [127]

The number of projections is best described by considering the angle θ_{proj} through which the sample is rotated during its one revolution in the scanning process (previously mentioned in Section 2.6.2). θ_{proj}, in degrees, is given by

$$\theta_{proj} = \frac{360}{Number\ of\ projections}. \tag{2.5}$$

The number of projections is inversely proportional to θ_{proj}. A high number of projections produces more accurate reconstructions, as the sinograms are built using more slices.

Exposure time describes the duration for which the sample is irradiated by the X-ray beam in each projection. The number of images per projection describes the number of times the sample is irradiated by the X-ray beam in each iteration. When using multiple images per projection, each pixel of the detector records the average intensity of the attenuated X-ray beam through all images per projection. This averaging method is useful for counteracting outliers during image acquisition.

Magnification describes the distance between the rotation stage and the X-ray source. The distance from the rotation stage and the X-ray source is labelled SRD; the distance between the X-ray source and the detector is labelled SDD. Magnification is given by

$$Magnification = \frac{SDD}{SRD}. \tag{2.6}$$

Increasing magnification results in a smaller voxel size and thus yields higher quality images.

2.6.5 Metrology considerations

The term "measurement uncertainty" is defined in the International Vocabulary of Metrology [128] as a "non-negative parameter characterizing the dispersion of the quantity values being attributed to a measurand, based on the information used". In other words: for a given measurement system, there is always some variation (i.e. dispersion) in a given set of repeat measurements (i.e. quantity values) of a given sample (i.e. measurand); this variation should be characterised (i.e. by a non-negative parameter). Calculating uncertainty in XCT measurements is a difficult task due to the complex relationships between influence factors [124]. In metrology, the term "influence factor" is used to describe anything that can cause variation in the output of a measurement system.

The VDI/VDE 2630-1.2 [129], provides an extensive list of XCT influence factors and the effects they may have on an XCT system. As shown in Table 3, provided by Stofi et al. [130], there is a wide range of influence factors for XCT measurements. An in-depth discussion on the full range of documented influence factors is beyond the scope of this section, nevertheless, some consideration will be given to influence factors which are commonly modified in XCT measurements.

The X-ray source is controlled by several sub-factors: the electron accelerating voltage, filament current, focal spot size and anode target material. Accelerating voltage and current affect the energy in the electron beam and ultimately the quality of the projections. Both voltage and current control the focal spot size of the electron beam which is susceptible to drifting in size, shape and location and thus affects the system's maximum resolution. In turn, the focal spot size controls the extent to which the target material is degraded during operation, and the target material controls the average X-ray photon energy.

The sample being measured can also have significant influence on the XCT measurement. The severity of beam hardening effects increases with the absorption and thickness of the sample. However, polymers cause a very low amount of beam hardening in comparison to metals, even at larger thicknesses. Beam hardening can affect measurements by decreasing inner dimensions (such as an inner diameter) and increasing outer dimensions (such as the height of a sample). According to Muller et al.[131], this effect may be because beam hardening modifies the inner and outer grey values of the surrounding background air, which influences the contrast and surface determination. As stated by Lifton et al. [132], beam hardening also causes greater measurement error for outer dimensions than for inner dimensions because the relationship between X-ray attenuation and thickness is non-linear for the first millimetres of material being penetrated.

Data processing methods are a very crucial part of obtaining XCT measurement data and therefore can have strong effects on a dataset. For example, surface determination has been shown to cause greater errors in edge-to-edge length measurements over sphere-centre distances [124]. Adding to previous discussions on global and local surface determination methods (§ 2.6.3), several comparisons between these surface determination methods have been conducted. Townsend et al. [133] compared areal parameters extracted from XCT and focus variation measurements of a Rubert plate, for the XCT measurements, several surface determination methods were used including ISO50 and a local iterative method. The results showed the local iterative method outperform ISO50 and achieved results significantly closer to those obtained using focus variation. Further issues with the ISO50 method have been identified, for example, Tawfik et al. [134] observed ISO50 to be unable to detect the contours of unfused powder in a AlSi10Mg sample produced by laser melting; pores filled with air were successfully detected, however.

Table 3. X-ray computed tomography influence factors [124]

Group	Influence factors
CT system	X-ray source Detector Positioning system
Data processing	3D reconstruction Threshold determination and surface generation
Workpiece	Material composition Dimension and geometry Surface texture
Environment	Temperature Vibrations Humidity
Operator	Workpiece fixturing and orientation Magnification X-ray source settings Number of projections and image averaging Measurement strategy

2.7 Finite element modelling

This section discusses a range of finite element (FE) modelling approaches used to study the impact of defects on the mechanical properties of lattice structures. This section focuses on reviewing studies in which a method has been developed for incorporating measurement data of lattice structures into the FE model. FE modelling approaches for lattice structures utilise either beam element or tetrahedral element meshes. Section 2.7.1 will discuss tetrahedral element modelling approaches and

Section 2.7.2 will discuss beam element modelling approaches. For a further discussion of FE modelling, additional studies can be found in a review by Dong et al. [135].

2.7.1 Tetrahedral elements

Ravari et al. [89] modelled the impact of radius variation and strut waviness on the compressive stress strain response of BCC and BCCZ lattice structures produced by LM of an NiTi alloy. These geometric deviations were implemented into a CAD model by modelling each strut using a connection of spheres (Figure 2.20a-b), where radius variation and strut waviness were applied to the strut by varying the radius and position respectively of each sphere. The FE meshes were then generated via conversion of the CAD model, using quadratic tetrahedral elements. Scanning electron microscopy (SEM) data of the lattice struts was used to determine the values for the geometric deviations in the CAD model. The diameter D of each sphere was given by

$$D = D_{min} + r \times (D_{max} - D_{min}) \tag{2.7}$$

where r is a randomly generated number between 0 and 1, and D_{min} and D_{max} are the minimum and maximum diameters of the struts measured via SEM. Similarly, the position of the spheres is varied by applying a displacement A_d to each sphere in a random direction

$$A_d = r \times A_d^{max} \tag{2.8}$$

where A_d^{max} is the maximum offset obtained from SEM data of lattice struts and r is as defined in Eq. (2.7).

Discussing one of several FE studies in this paper, Ravari et al. performed a compression test on a BCC lattice structure and compared the results to two FE models: one with no defects and one with the above defects implemented. The results showed the maximum error between simulated and experimental stress-strain response of BCC lattices to reduce from 53% to 27% upon incorporating defects into the FE model. These results are shown in Figure 2.20c, where the FE models of the lattice with and without defects are denoted by “MCD” and ”MC” respectively. The reader is referred to the full text [89] for further discussion of results.

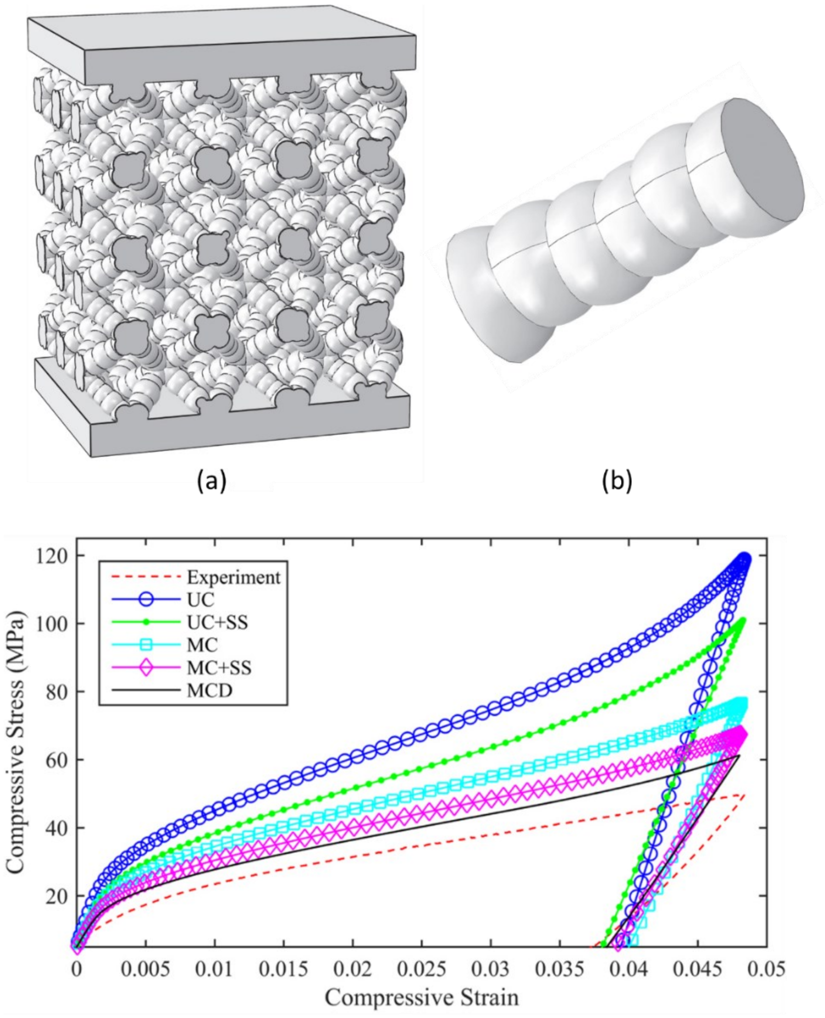

(a) (b)

(c)

Figure 2.20. FE modelling of geometric deviations, using connected spheres. (a) CAD model of lattice structure with strut waviness and radius variation (b) individual strut modelled using spheres of varied position and radius (c) a set of results comparing various simulation approaches to experimental data [89]. The labels “MCD” and “MC” describe simulations of lattice structures with and without defects respectively.

Lozanovski et al. [28] used X-ray computed tomography (XCT) to measure the form of the cross sections of lattice struts produced by LM of Inconel 625 (a nickel-based alloy). Ellipses were fitted to the cross sectional images of the struts (Figure 2.21a) and the data was used to compute probability density functions (PDFs) describing the cross sections. These PDFs were then used for creating CAD models of lattice struts with statistically similar cross sections (Figure 2.21b). The surface of the struts was generated by performing a loft operation over the cross sections. Linear tetrahedral elements were used to convert the CAD models into meshes. Compressive Young's modulus, yield strength and buckling studies were all performed, the results showed improved adherence to experimental data upon the inclusion of defects into the model.

Defects can also be incorporated into FE meshes by direct conversion of measurement data into an appropriate mesh; such an approach is often referred to as an image-based technique. Using a lattice structure produced by EBM of a titanium alloy (Ti-6Al-4V), Suard et al. [136] suggest an image-based FE technique by using XCT images of individual struts and converting them into tetrahedral meshes which are used to calculate the stiffness of individual struts. Suard et al. then suggest that future FE models could use struts of constant radius (i.e. no geometric deviations) but then modify the radius value of each strut such that its theoretical stiffness matches that which was calculated from the image-based method. This approach could potentially save significant computational power for any simulations performed after the image-based modelling, however, validation of this method via comparison to experimental data is yet to be performed. Additionally, though this method aims to increase efficiency of future simulations, the image-based portion of the work is nevertheless very computationally expensive. Furthermore, Suard et al. state that a mesh simplification had to be performed on the meshes converted from XCT data, bringing into question the integrity of the data.

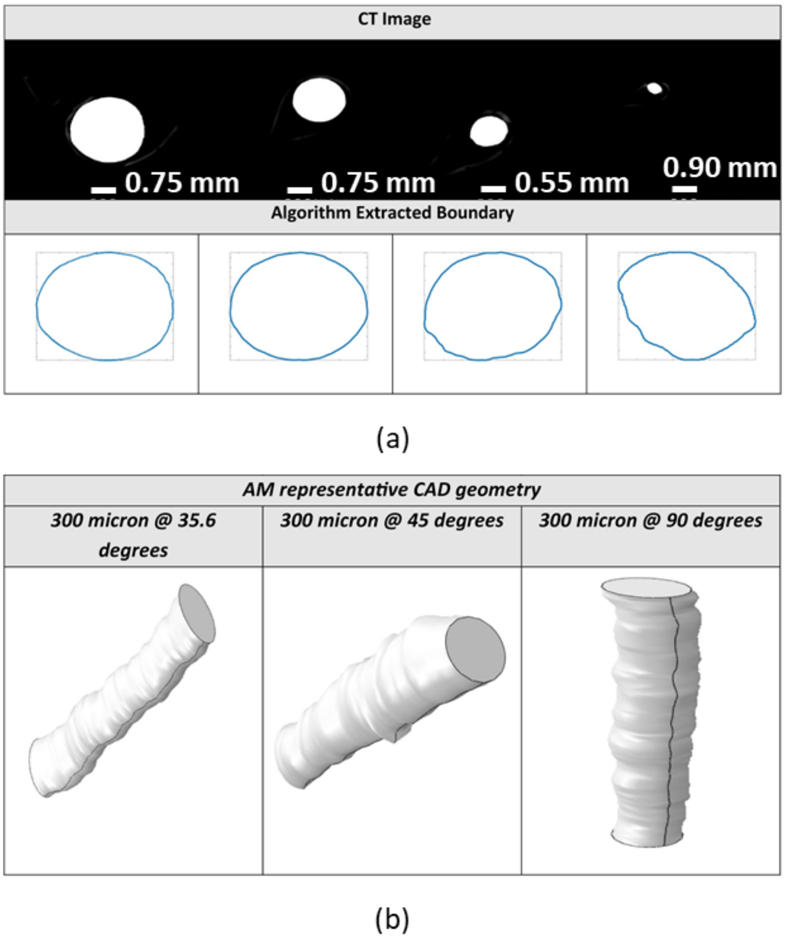
CT Image
0.75 mm
0.75 mm
0.55 mm
0.90 mm
Algorithm Extracted Boundary
(a)
AM representative CAD geometry
300 micron @ 35.6 degrees
300 micron @ 45 degrees
300 micron @ 90 degrees
(b)

Figure 2.21. Modelling of defects using elliptical cross sections. (a) elliptical cross sections of lattice struts (b) CAD models of struts at different overhang angles with defects implemented [28].

2.7.2 Beam elements

Beam elements are also often used to model geometric deviations in lattice struts. Due to their geometrical limitations, beam elements are generally only capable of modelling radius variation and strut waviness. Each strut is modelled using several beams; radius variation and strut waviness are modelled by varying the radius and location respectively of each element [61,64,137–141]. To give one example, Liu et al. [64] modelled the compressive stress-strain response of octet-truss lattices and rhombicuboctahedron lattices produced by LM of an aluminium alloy (AlSi10Mg). X-ray computed tomography was used to develop probability density functions for strut radius and centre position. Similar to Lozanovski et al. [28] (§ 2.7.1), beam element models were then generated using the statistical parameters from the probability density function (Figure 2.22a). Figure 2.22b shows the results of comparing the simulated stress-strain data of an octet-truss lattice to experimental data. The results showed that applying geometric deviations produces a significant reduction in the discrepancy between experiment and simulation; the model which used the as-designed geometry was proven highly inaccurate. Further examples of beam element models can be found in from [61,64,137–140].

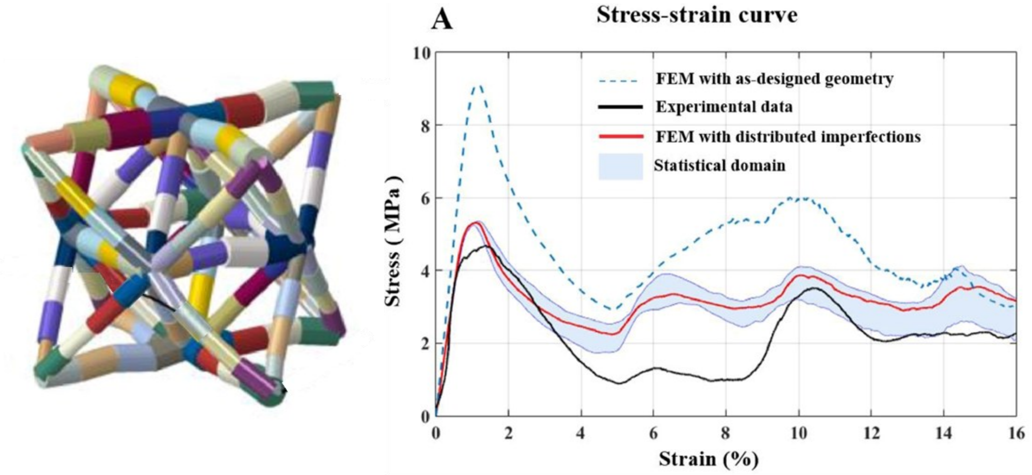

(a) (b)

Figure 2.22. Modelling and simulation of an octet-truss lattice structure, using beam elements. (a) Beam element model of an octet-truss unit cell with radius variation and strut waviness (b) results of comparing the simulated stress-strain data of an octet-truss lattice to experimental data. The “statistical domain” marks the full range of stress-strain data from multiple simulations.

A particularly powerful aspect of FE modelling is the ability to perform parametric studies wherein a specific deviation or defect can be controlled and analysed in depth. Parametric studies for defects in lattice structures can help quantify the unique impact of a specific defect (or combination of defects) on the mechanical properties of a given lattice structure. Several parametric studies have been performed for defects in lattice structures [29,64,137]. Discussing one example, Liu et al. [64] performed a parametric study on strut waviness and radius variation in octet-truss lattices. In the first simulation, Young’s modulus E_{z_o} of the model with no defects was calculated and used as a baseline, for comparison to future results. In subsequent simulations, strut waviness and radius variation were independently modified and the Young's modulus E_z was calculated. Figure 2.23 shows a result of this study, where the Young's modulus from each simulation has been normalised to the baseline E_{z_0}. Visual inspection of Figure 2.23 shows that the Young's modulus is more sensitive to strut waviness than radius variation; the Young's modulus decreases more rapidly upon increasing the strut waviness parameter. The reader is directed to [64] for a full explanation of the notation in Figure 2.23. Results like these are useful for determining the sensitivity of a design to specific defects and are crucial for designing defect-tolerant lattice structures.

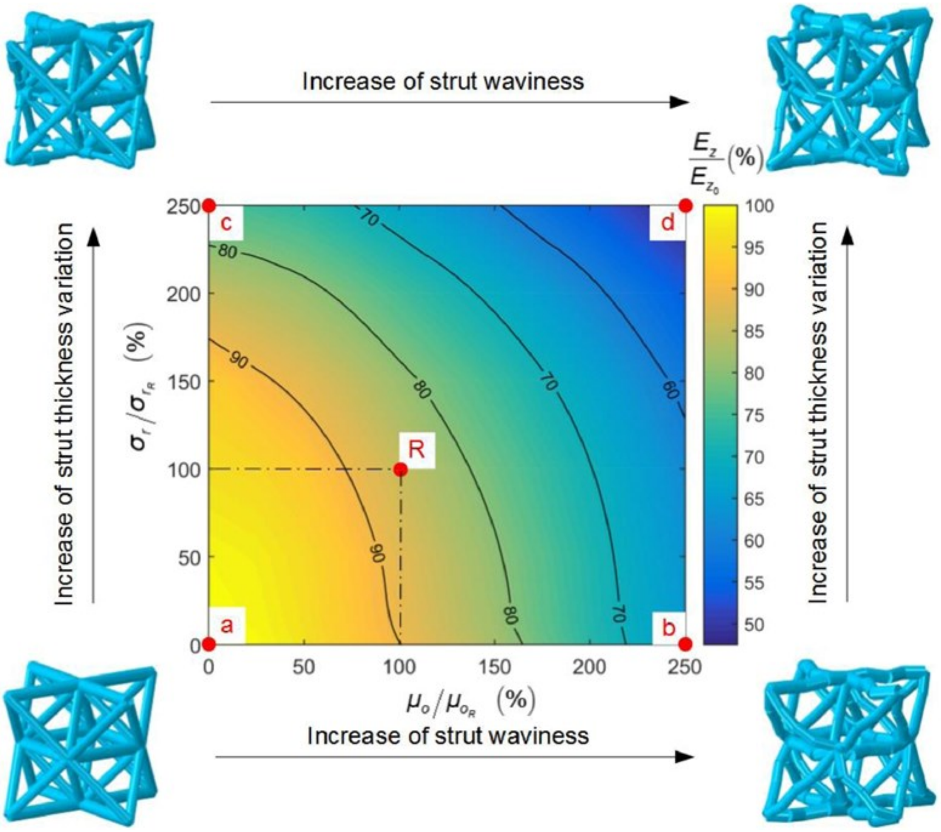

Figure 2.23. Results from a parametric study on strut waviness and radius variation [64].

2.8 Discussion and conclusion

Cellular solids exist in a vast range of forms. Strut-based lattice structures are of particular interest due to the significant control they provide over the structure's mechanical properties, in contrast to surface-based lattice structures which are less configurable. Furthermore, referring again to the thesis' motivation, strut-based lattice structures have been shown to possess 3D bandgaps, unlike surface-based lattice structures (Chapter 1, § 1.1-1.2). AM processes are commonly used for producing lattice structures, due to their highly complex geometries. Within AM, the most commonly used process category is PBF, this is likely due to its suitability for metal processing. Though there are other process categories which handle metals, such as directed energy deposition, these are likely less popular due to being inferior to PBF in terms of dimension accuracy and complexity of geometry [44,142,143]. There is a significant number of PBF process parameters, many of which are strongly interrelated and bear significant control over part quality. A stable melt pool is particularly crucial to high-quality AM parts; calculating energy density (Eq. (2.4)) is helpful for assessing melt pool stability. A stable melt pool can help reduce formation of defects such as porosity, balling and spatter. Defects such as texture bias and stair-stepping (the latter is more strictly a geometric deviation) can only at best be reduced, as these are natural by-products of the layer-wise process.

A range of defects have been observed in lattice structures, many of which—for example, geometric deviations and texture bias—are exacerbated by overhanging features, these can be overhanging struts or unit cell walls. Classification of defects in more specific terms—geometric deviations, surface texture variations and porosity—is useful for more accurately describing the features present in lattice structures produced by AM. In the literature on lattice structure defects (§ 2.4), it is design parameters that are often varied—for example strut overhang angle—whilst process parameters are kept constant. Additionally, it is often not stated if the chosen process parameters underwent optimisation. Therefore, it could be valuable for these studies to be extended by investigating the effects and optimisation of process parameters.

Many techniques have been employed for performing measurements on lattice structures. Significantly, XCT is most often used, due to its freedom from line-of-sight issues and its 3D capabilities. Unfortunately, XCT is controlled by a vast number of influence factors, and understanding the relationships between these factors is a highly complex problem, for which there is currently significant effort to solve. Incremental progress is being made and this enables the development of general measurement guidelines which can be helpful for optimising a particular measurement and more accurately interpreting the results. For example, since surface determination causes greater errors in edge-to-edge length measurements over sphere-centre distances (§ 2.6.5), the measurement of strut diameter may possess higher error than the measurement of the position of strut centres and node centres. Alignment of XCT and CAD data is effective for analysing the overall geometry of a lattice, however, segmentation of individual features is a more informative approach for analysing local deviations. Furthermore, large-scale deviations, such as shrinkage and warping, present a challenge during alignment of significantly dissimilar geometries. For porosity measurement, employing a stitching method [33] enables detection of smaller pores through the smaller voxel size, however, errors may form at the boundaries of reconstructed volumes [124].

FE modelling approaches have been developed for studying the impact of defects on lattice structure mechanical properties. FE meshes are generated using either tetrahedral elements or beam elements, each of which possess different advantages and disadvantages which can be described in their underlying mathematical formulations. In-depth information regarding FE formulations can be found at [144–148] (and many other sources).To summarise, tetrahedral elements are a type of "3D continuum element", which is often best suited for meshing very complex geometries. Meshing a geometry using tetrahedral elements often requires using many elements, and therefore these meshes bear a significant computational cost. Beam elements are a type of "structural element" best suited for meshing geometries whose size in one dimension is far greater than in the other two dimensions (i.e. a beam); beam elements are not well suited to complex geometries. Beam elements, however, have the advantage of being very computationally efficient. Figure 2.24 shows examples of a BCC unit cell which has been meshed using tetrahedral elements and beam elements. The higher node count for a tetrahedral mesh results in a much larger stiffness matrix—the central part of FE calculations [149–151])—which greatly increases the computation cost of tetrahedral elements. It is therefore important to consider which element type is most appropriate for a given modelling scenario and to justify the chosen element type.

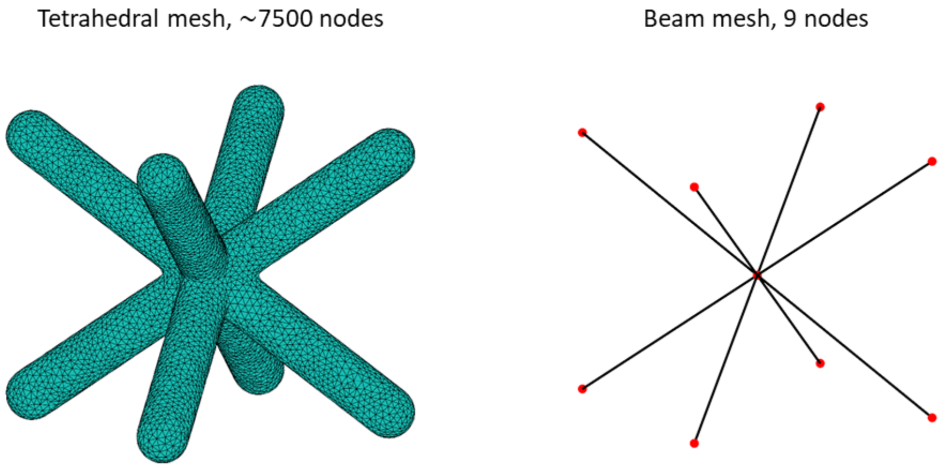

Figure 2.24. BCC unit cell meshed using tetrahedral elements and beam elements. Significantly more nodes are required to generate the tetrahedral mesh.

The reviewed studies demonstrated improvements upon model which do not include defects, however, it is not clear how adaptable these approaches are for the wide range of defects observed in the literature. The method by Ravari et al. [89] of modelling defects using a connection of spheres improves upon ideal models, but this method assumes a geometry which might not be an appropriate description of a lattice strut, due to the periodic geometry imposed by the connected spheres, which is not present in lattice structures. The method by Lozanovski et al. [28] appears to more appropriately describe lattice struts and the FE models demonstrated reduces lattice stiffness upon incorporating defects, however, the explicit definition of the elliptical cross sections, combined with the loft operation in CAD software may be difficult to modify for new geometrical features. Additionally, the modelling approaches in the literature do not include any sensitivity studies which are crucial for understanding the stability of the model under varied inputs. Furthermore, comments on mesh quality are lacking in these studies.

2.9 Summary

In this chapter, background information and a review of the state of the art were provided, supported with definitions where necessary. First, the topic of cellular solids was introduced, defining their main categories. Next, a subset of cellular solids, namely strut-based lattice structures, was discussed in further detail, providing classifications, characteristic mechanical properties and key terminology. Strut-based lattice structures are the focus of this thesis. The seven process categories of additive manufacturing were next discussed, followed by a review of the powder bed fusion (PBF) process category in more detail, due to its prevalence in the literature. Laser melting and electron beam melting processes were reviewed, as well and process parameters and defect formation mechanisms. Building on the more general information surrounding PBF, the literature on defects in lattice structures was reviewed, namely, geometric deviations, surface texture variations and porosity. Studies regarding attempts to reduce defects via post processing methods were also discussed. Next, the wide range of measurement techniques for lattice structure imaging was reviewed, identifying X-ray computed tomography (XCT) as the most commonly used technique. Given its common use, and its use in this thesis, XCT was further discussed, explaining its basic principles, procedures, parameters and influence factors. The last section of the review discussed the FE modelling approaches used for simulating the impact of defects on lattice structure mechanical properties. Tetrahedral element and beam element approaches were discussed, contrasting their strengths and weaknesses.

Chapter 3 – Methodology

In this chapter the methodology of the thesis is explained and justifications are provided for the decisions that were made. The methodology of this thesis is broad and is divided into several stages. Section 3.1 provides an overview of the methodology and subsequent sections provide further detail.

3.1 Overview

Figure 3.1 shows a flowchart of the six main stages of the methodology; this flowchart was first shown in Section 1.3. The first stage is the development of a modelling approach for strut-based lattice structures and a range of geometric deviations and defects, followed by a sensitivity study of the modelling approach in which regions of stability for the model's parameters are identified. These two stages are of considerable length and are therefore described in detail in their own dedicated chapters, Chapter 4 and Chapter 5. In the remainder of this chapter, references to Chapter 4 and Chapter 5 are made when necessary.

The remaining stages (three to six) serve as a case study for validating the proposed modelling approach through a comparison to experimental data. In Section 3.2 and Section 3.3 (stage three in Figure 3.1), a lattice structure sample is selected for manufacturing and measurement using X-ray computed tomography (XCT). Next, Section 3.4 describes the compression tests which were performed for obtaining stiffness values for the manufactured lattice structures (stage four). Section 3.5 describes how the XCT data is used in the proposed modelling approach to produce tetrahedral meshes of lattice structures which resemble the manufactured samples (stage five). Lastly, Section 3.6 (stage six) describes the configuring of the simulations of lattice structure stiffness using finite element (FE) analysis.

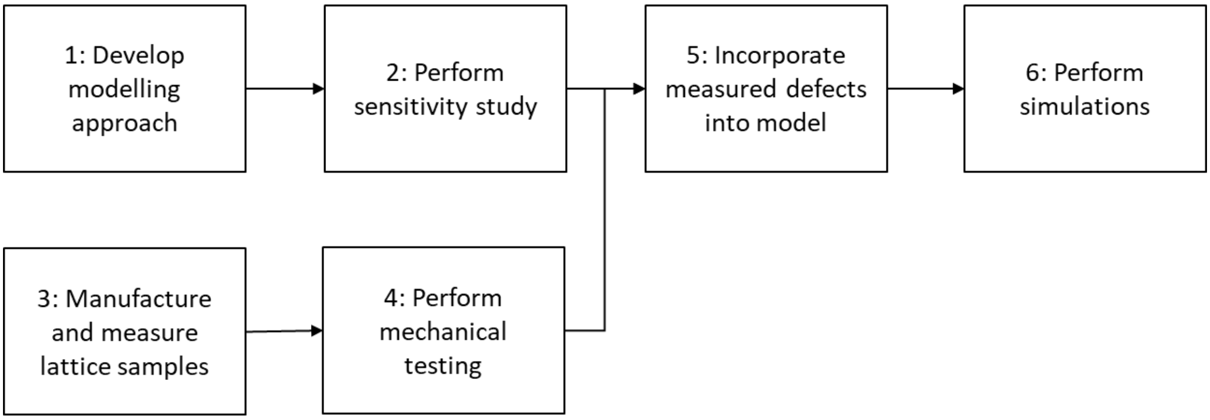
1: Develop modelling approach
2: Perform sensitivity study
5: Incorporate measured defects into model
6: Perform simulations
3: Manufacture and measure lattice samples
4: Perform mechanical testing

Figure 3.1. Flowchart showing the main stages of work in this thesis (duplicate of Figure 1.3).

3.2 Manufacture

The BCCZ (body centred cubic, with z-axis reinforcement) lattice design was chosen for study in this thesis because this design has been shown to have promising vibration attenuation properties (as observed by Elmadih et al, see Figure 1.2). Additionally, this design is generally prevalent in the literature. As shown in Figure 3.2a, the BCCZ unit cell contains 12 struts and 9 nodes, making it a bending-dominated structure, according to Maxwell's criterion ($M = -9$). The struts in the unit cell are grouped into two categories: vertical and inclined. The vertical struts are four outer struts which are positioned perpendicular to the xy plane i.e. overhang angle $\theta = 0°$. The remaining 8 struts are the inclined struts, with $\theta = 54.7°$. The chosen lattice dimensions are as follows:

- Strut radius: 0.5 mm
- Node radius: 0.75 mm
- Cell size: 7 mm
- Tessellation: 4 x 4 x 4.

The surface model of the lattice structure was generated using the signed distance function method described in Chapter 4[1]. As shown in Figure 3.2b, the lattice design includes the cropped faces first; the terms "top face" and "bottom face" will be used to refer to these upper and lower flat regions of the lattice respectively.

---

[1] Signed distance function with resolution $dx/r = 0.125$ (see Chapter 5, § 5.2.1).

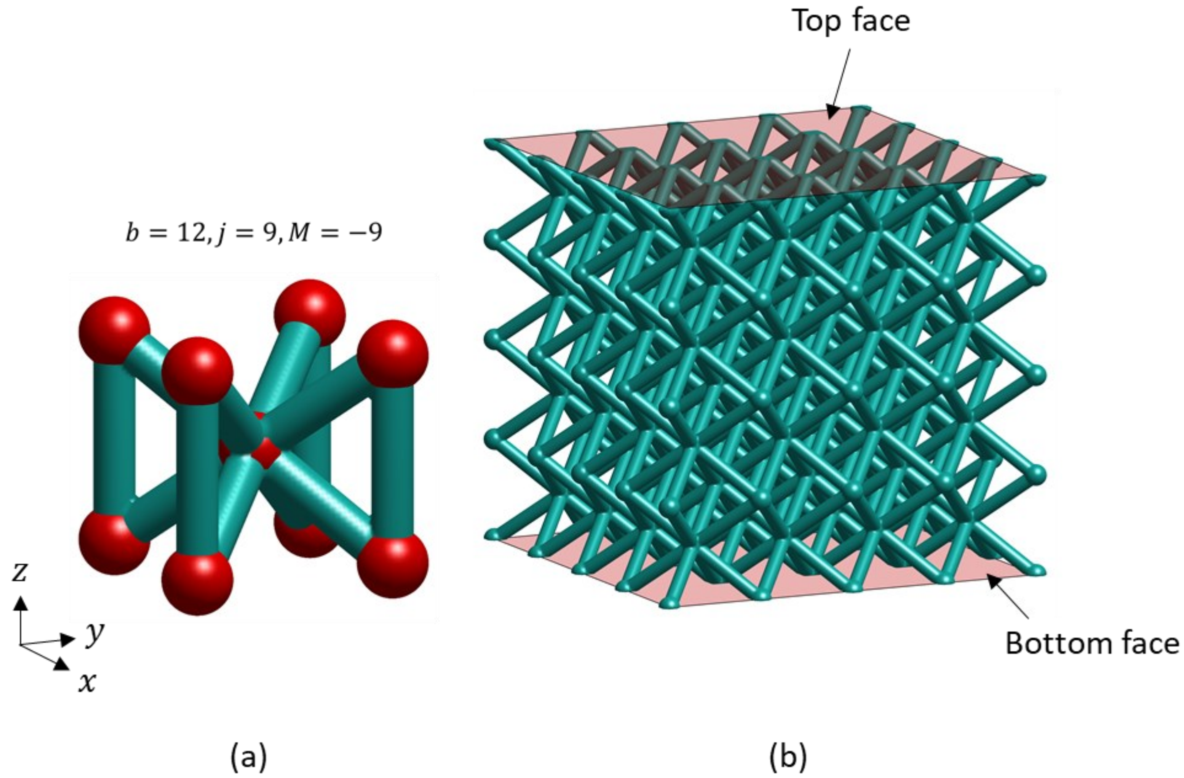

Figure 3.2. BCCZ lattice structure, the design selected for manufacture. (a) BCCZ unit cell. (b) Example model of the BCCZ lattice structure.

STL files of the lattice structures were generated using an open-source function from the MATLAB File Exchange, “stlwrite.m” [152] (note that an official MATLAB function for creating STL files has now been made available, from MATLAB version 2018b onwards). The lattice structure samples were manufactured using the ReaLizer laser powder bed fusion system with Ti6Al4V powder, an example is shown in Figure 3.3. The Realizer has a maximum build volume of approximately (40 x 40 x 40) mm which must include the substrate to which the samples are fused; the volume is approximate because the substrate thickness can vary. Five lattice samples were produced on the ReaLizer using the following process parameters:

- Laser voltage: 25 V
- Laser current: 3300 µA
- Hatch distance: 90 µm
- Point distance: 20 µm

- Exposure time: 20 μs
- Layer thickness: 40 μm

These parameters were selected by in-house technicians.

The samples were oriented such that the bottom face and top face were parallel to the build bed. Post-manufacture, the samples were manually cut from the substrate and the remaining support structures were manually smoothed, using a belt sander.

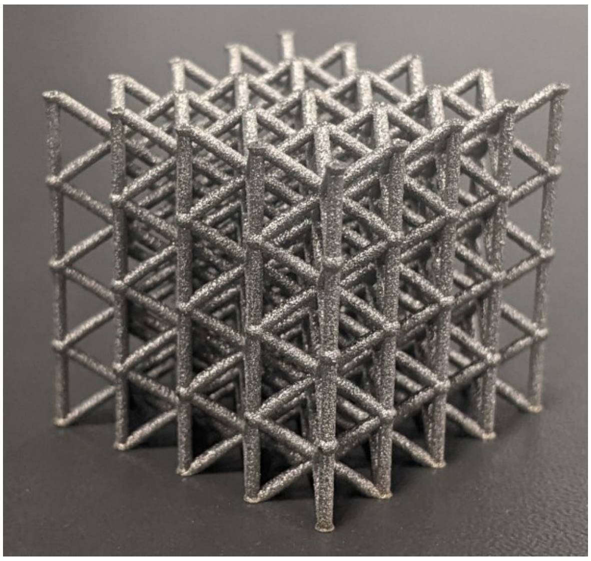

Figure 3.3. 4 x 4 x 4 BCCZ lattice manufactured by laser powder bed fusion.

3.3 Measurement

The measurement stage of the methodology consists of three sub-stages: X-ray computed tomography (XCT), data processing and dimensional analysis. The XCT stage (§ 3.3.1) is the actual measurement procedure, which outputs raw greyscale data. The data processing stage (§ 3.3.2) converts the raw data in point clouds of individual struts, suitable for dimensional analysis (§ 3.3.3), which is the final stage.

3.3.1 X-ray computed tomography

XCT measurement and reconstruction was performed externally by industrial sponsor (The Manufacturing Technology Centre). The XCT measurement was performed using the diondo d2 XCT system. The settings of the diondo d2 system were as follows (see Appendix A for full settings):

- Voltage: 130 kV
- Current: 90 μA
- Filter: Aluminium 1 mm thickness
- Number of projections: 3500
- Exposure time: 750 ms
- Images per projection: 1
- Magnification: 8.571

These parameters yielded a voxel size of 16 μm. Approximate scan time of 45 minutes. Reconstruction was performed on the reconstruction software diControl. Default reconstruction settings were used, apart from additional beam hardening correction (“setting 3”).

3.3.2 Data processing

As shown in Figure 3.4, the data processing stage consists of six stages which are used convert the raw greyscale data from the XCT measurement into point cloud data of the individual strut in the lattice structure. Each of these stages will now be explained.

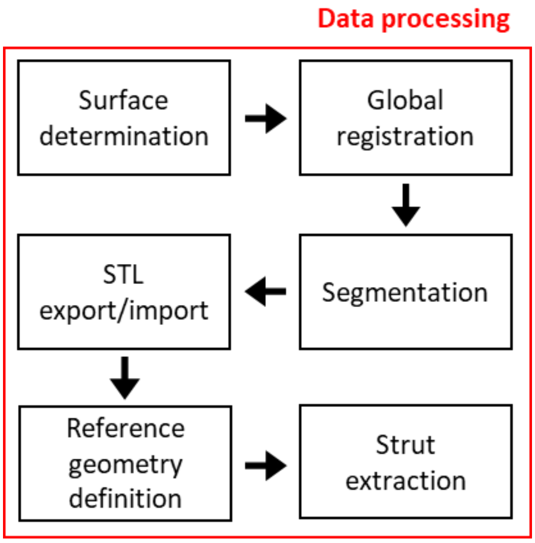
Data processing
Surface determination
Global registration
Segmentation
STL export/import
Reference geometry definition
Strut extraction

Figure 3.4. Flowchart of the XCT data processing stages.

Surface determination

Surface determination was performed using XCT data processing software VG Studio MAX 3.0. The “advanced mode” (a local thresholding method) was used with the following settings:

- Starting contour: as defined in histogram
- Search distance: 4 voxels
- Void and particle removal

“Starting contour” refers to the initial surface that is extracted from the grey-scale data which is then modified to produce a final determined surface. The initial surface is “as defined by histogram”, which means that the ISO50 value was used. The starting contour is then iteratively modified by evaluating the grey-values within a “search distance” of the starting contour i.e. four voxels perpendicular to the surface. Figure 3.5 shows an example of a starting contour and modified contour based off grey scale data. The search distance is indicated by the perpendicular lines..

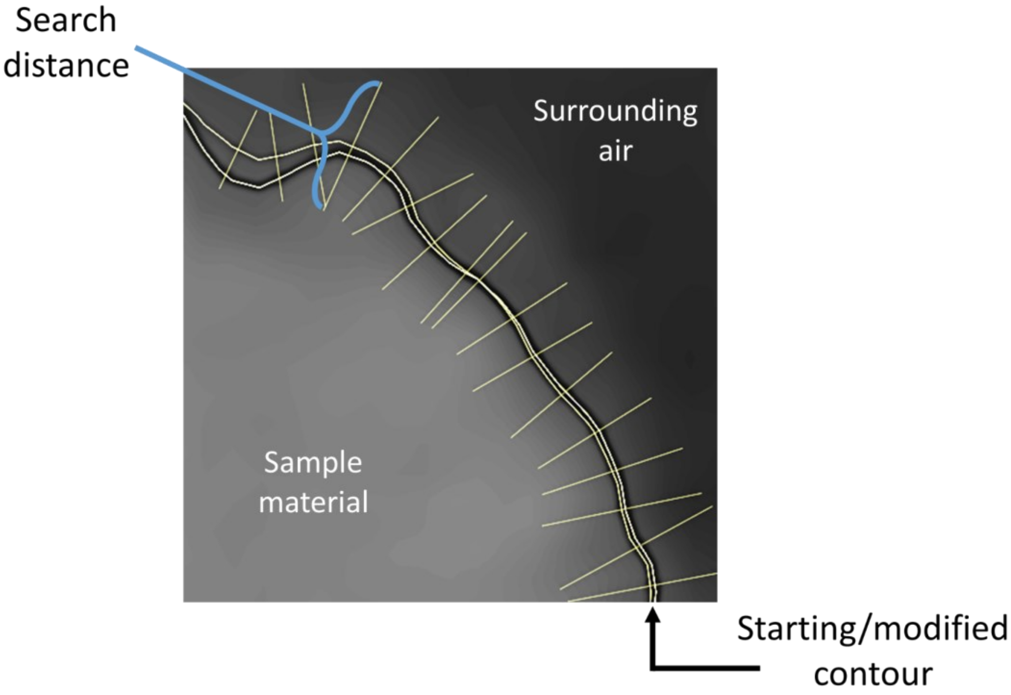

Figure 3.5. Illustration of surface determination. The starting contour is modified according to the grey value data found within the search distance.

Global registration

Global registration is used to take an arbitrarily oriented surface and reorient into a position favourable for analysis. In this case, the surface is repositioned into an upright position such that the top and bottom faces are parallel with the xy plane. A "3-2-1 registration" method was used, which requires the fitting of three "geometry elements": a plane, a line, and a single point. The name "3-2-1" corresponds to the minimum number of points required to define a plane, line and point respectively. The plane was defined by manually selecting three fit points on the top face of the surface. Each of the two points used to define the line were defined as the intersection between the fitted plane and the centre of a cylinder fitted to a strut perpendicular to the top face, as shown in Figure 3.6. To fit the cylinders, ten points were manually selected. The 3-2-1 registration was then performed using the plane, the line connecting the two points, and any of the two single points (this was arbitrarily selected).

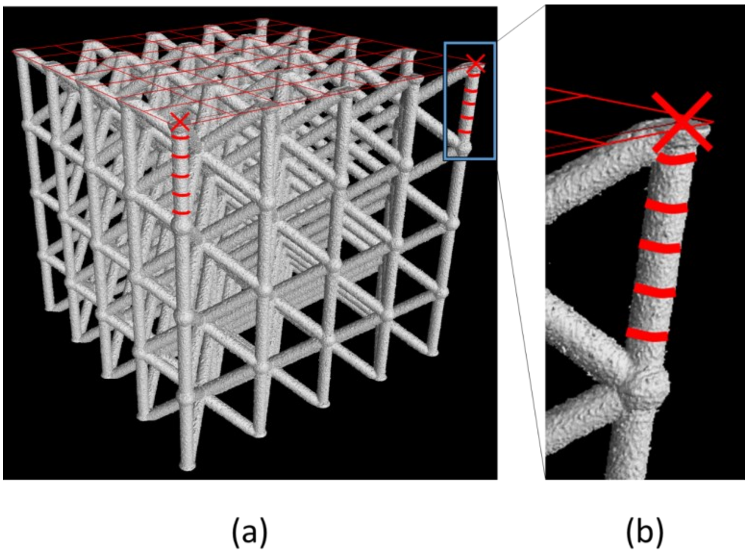
(a) (b)

Figure 3.6. Fitting of geometry elements to determined surface. (a) Example lattice in VG Studio MAX with geometry elements fitted. (b) Close-up of one strut. 'x' marks the intersection of the fitted cylinder and the plane.

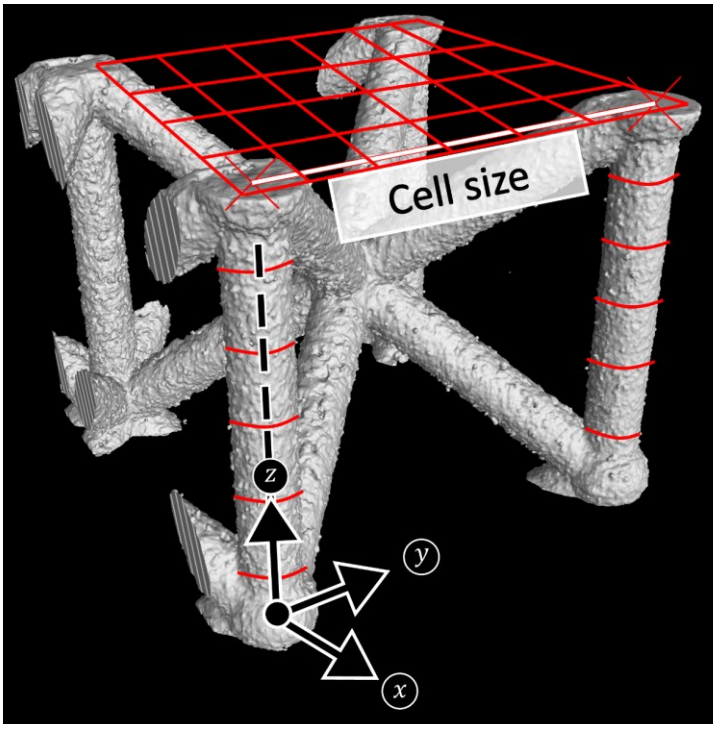

Figure 3.7. A unit cell ROI. Geometry elements are fitted to the ROI: cylinders to the vertical struts; a plane to the top face; two points—marked 'x'—at the intersection of the centre of each cylinder and the plane. Cell size is calculated as the distance between the two points marked 'x'. The 3-2-1 registration is configured such that the bottom face is coincident with the xy plane and the centre of the fitted cylinder of one vertical strut is coincident with the origin.

Segmentation

The determined surface was segmented in order to extract specific regions of interest (ROIs) for analysis. Due to the manual nature of this method, four unit cells were arbitrarily selected as ROIs from each of the five samples – two from the top and bottom layers of each lattice. A 3-2-1 registration was performed again on each ROI, using the same settings as in the global registration. This secondary registration is performed so that the bottom face is coincident with the xy plane and the centre of the fitted cylinder of one vertical strut is coincident with the origin of the coordinate system (Figure 3.7), this becomes useful for the later stage when the reference geometry is defined. Lastly, the cell size of each unit cell is calculated; the cell size is given as the distance between the two points which are defined by the intersection between the plane and the two fitted cylinders (Figure 3.7). The cell size of all unit cells is estimated by calculating the average of all the cell sizes calculated in each ROI.

STL export/import

The ROIs were exported from VG Studio MAX 3.0 as STL files using the following settings:

- Preset: Normal
- Surface definition: use determined surface
- Resampling: normal
- No mesh simplification

The STL files of each unit cell were imported into MATLAB using an open-source function from the MATLAB File Exchange, "stlread.m" [153] (note that an official MATLAB function for reading STL files has now been made available, from MATLAB version 2018b onwards). The STL was then converted into a point cloud by discarding the triangulation and only saving the coordinates of each point.

Reference geometry definition

Before the point clouds of each strut can be extracted, a method is required for uniquely identifying each strut in the point cloud. A reference line segment is defined for each strut, where this line segment is analogous to the medial axis of the strut. Given that the point cloud inherits the coordinate system from the segmentation stage, the point cloud is positioned at the origin in the same way as the ROI was positioned. Therefore, the coordinates of each reference line segment were derived from the cell size calculated in the Segmentation section.

Strut extraction

To extract each individual strut from the unit cell point cloud, the distance between each point and all the reference line segments in the unit cell is calculated and used to divide the point cloud into groups, where each group shares the property of being closest to the same reference line segment. Figure 3.8a-c shows examples of a two struts being extracted from the unit cell. Note that Figure 3.8b actually shows a pair of inclined struts (separated by a central node), whose medial axes lie on the same line. Such pairs of struts are treated as a single strut for this analysis.

Lastly, the cylindrical section of each strut in the point cloud is extracted, removing the points at the nodes. To extract the cylindrical sections a parameter called the intersection ratio t is used as a threshold value which filters out points based on where they are positioned along the strut[2]. For the vertical struts, the threshold value $t_{vertical}$ is used to retain the points whose t value satisfies the following condition

$$t_{vertical} < t < 1 - t_{vertical}\ . \tag{3.1}$$

For inclined struts, the threshold value $t_{inclined}$ is used to retain the points which satisfy the criteria

$$\begin{gathered} t_{inclined} < t < 0.5 - t_{inclined} \\ or \\ 0.5 + \ t_{inclined} < t < 1 - t_{inclined}. \end{gathered} \tag{3.2}$$

Figure 3.9 illustrates how the struts are filtered using Eq. (3.1) and Eq. (3.2); the nodes in the vertical struts are located at t values of 0 and 1; the nodes in the inclined struts are located at t values of $0, 0.5$ and 1.

---

[2] The reader is referred to Eq. (4.14) where intersection ratio is defined thoroughly.

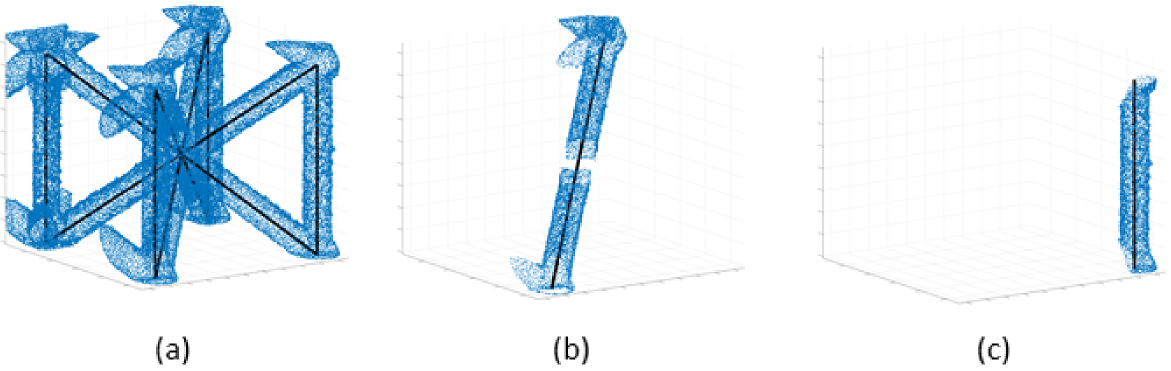

Figure 3.8. Extraction of individual struts from point cloud data. (a) point cloud of unit cell with reference line segments (b) extracted inclined strut (c) extracted vertical strut.

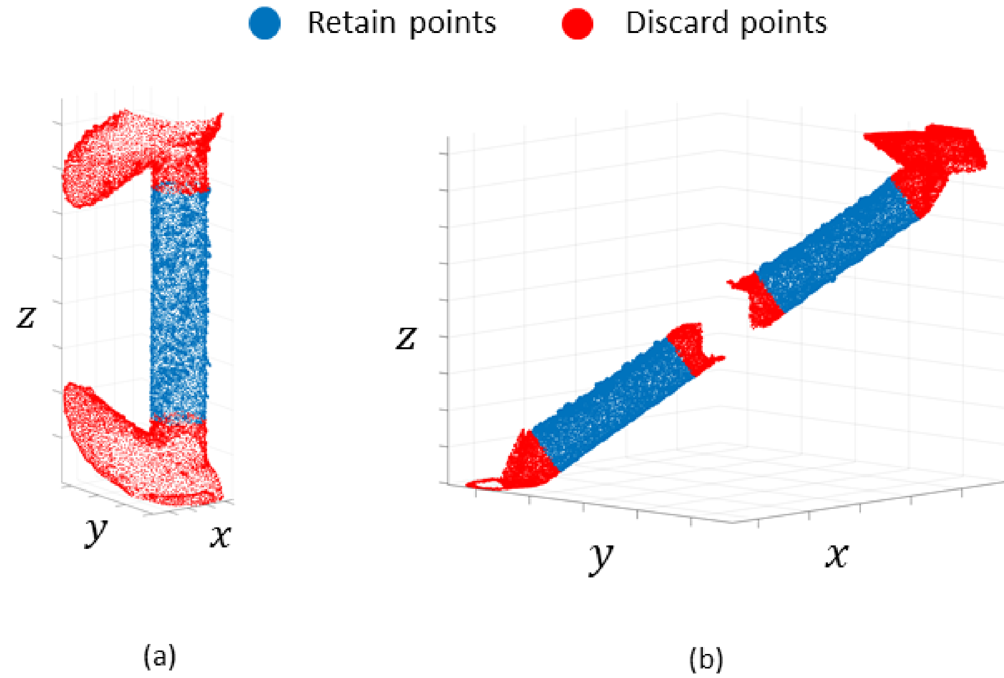

Figure 3.9. Examples of extraction of the cylindrical section inclined and vertical struts.

For explanation on the implementation in MATLAB of stages from STL import until strut extraction, the reader is referred to Appendix B, Figure B.1, Figure B.2 and Figure B.6.

3.3.3 Dimensional analysis

This section describes four methods of dimensional analysis: cross section analysis, convergence analysis, texture bias analysis and surface unwrapping. These analyses were developed using MATLAB in order to maintain full control of the dataset, as opposed to using proprietary software (e.g. VGSTUDIO). These particular deviations were selected due to their relevance lattices, demonstrated by their prevalence in the literature.

Cross section analysis

To perform cross section analysis on the strut point cloud, a transformation is applied, if required, in order to orient the point clouds such that the reference line segment (as defined in the “reference geometry definition” stage in Section 3.3.2) is perpendicular to the xy plane. The reference line segment is used to calculate the angles of rotation. Cross sections of the point cloud were then extracted by isolating a set of points whose z coordinate is within a given slice depth (Figure 3.10a). The slice depth is defined by the layer thickness used in the manufacturing of the samples, that is, 40 μm. After extracting the point cloud, a circle is fitted to each cross section (Figure 3.10b) using a least squares method. This circle is defined by centre coordinates (x, y) and radius r. For a given point cloud of a strut, the vector $\boldsymbol{R}_{ptcloud}$ stores the radius values of all cross sections as

$$\boldsymbol{R}_{ptcloud} = [r_1, r_2, \dots, r_n] \tag{3.3}$$

where n is the number of cross sections. $\boldsymbol{R}_{ptcloud}$ gives insight into the radius variation in a given strut. The matrix $\boldsymbol{X}_{ptcloud}$ stores the x, y coordinates of the centre of each of the cross sections

$$\boldsymbol{X}_{ptcloud} = \begin{bmatrix} \vec{X}_1 \\ \vec{X}_2 \\ \vdots \\ \vec{X}_n \end{bmatrix} = \begin{bmatrix} x_1 & y_1 \\ x_2 & y_2 \\ \vdots & \vdots \\ x_n & y_n \end{bmatrix}. \tag{3.4}$$

The coordinates of average centre $\vec{c}$ of all the fitted circles are determined by calculating the mean x, y coordinates from $\boldsymbol{X}_{ptcloud}$. Insight into the waviness in a given strut can be achieved by calculating the distance between the centre of a given slice $\vec{X}_i$ and the average centre $\vec{c}$ of all the cross sections of that strut. The distance between $\vec{X}_i$ and $\vec{c}$ is termed the *offset* and stored in the vector $\boldsymbol{O}_{ptcloud}$

$$\boldsymbol{O}_{ptcloud} = \begin{bmatrix} o_1 \\ o_2 \\ \vdots \\ o_n \end{bmatrix} = \begin{bmatrix} |\vec{X}_1 - \vec{c}| \\ |\vec{X}_2 - \vec{c}| \\ \vdots \\ |\vec{X}_n - \vec{c}| \end{bmatrix}. \tag{3.5}$$

For information on the cross section analysis implementation in MATLAB, the reader is referred to Appendix B.

Convergence analysis

Convergence analysis is necessary for assessing whether the arbitrary selection of struts from the XCT data is representative of the full measurement dataset. The convergence analysis is performed by calculating the cumulative mean of the radius and offset of the cross sections. For a given set of cross sectional data, the cumulative mean of the radius data $\boldsymbol{R}_{ptcloud}$ is given by $\boldsymbol{R}_\mu$

$$\begin{aligned} \boldsymbol{R}_\mu &= [R_1, R_2, R_3, \dots, R_n] \\ &= \left[\frac{r_1}{1}, \frac{r_1 + r_2}{2}, \frac{r_1 + r_2 + r_3}{3}, \dots, \frac{r_1 + r_2 + r_3 + \cdots + r_n}{n}\right] \end{aligned} \tag{3.6}$$

where n is the number of slices. The percentage change in $\boldsymbol{R}_\mu$ is given by

$$\% = \left[\frac{R_2 - R_1}{R_1}, \frac{R_3 - R_2}{R_2}, \dots, \frac{R_n - R_{n-1}}{R_{n-1}}\right] \times 100. \tag{3.7}$$

The cumulative mean $\boldsymbol{O}_\mu$ of the offset data $\boldsymbol{O}$ and the percentage change can be obtained from Eqs. (3.6) and (3.7) via symmetry.

Texture bias analysis

In the point cloud of a given strut, each point has a Euclidean distance d to its reference line segment and a surface angle α[3]. Plotting d vs α gives insight into the character of the surface as a function of α and can thus be used for texture bias analysis. Figure 3.11 shows a diagram illustrating d and α; this figure shows the local coordinate system $(\vec{x}', \vec{y}')$ which is used to calculate α. The texture bias plots of multiple struts can be averaged by binning the data at a fixed α interval and averaging the distances d within each α interval.

Surface unwrapping

Surface unwrapping can be considered as an extension of texture bias analysis. Texture bias considers two dimensions, d and α; surface unwrapping adds a third dimension t, the intersection ratio. For each strut in the point cloud, plotting the distance d as a function of surface angle α and intersection ratio t unwraps the surface onto a plane, removing the cylindrical form. The unwrapped surface can be averaged by binning the data at fixed intervals for α and t and averaging the distances d within each interval.

---

[3] The reader is referred to Eq. (4.32) where intersection ratio is defined.

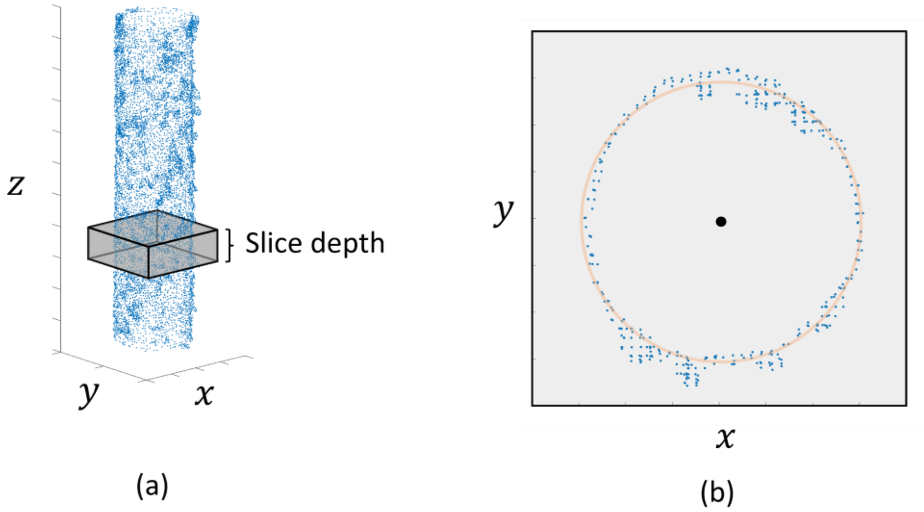

Figure 3.10. Extraction of strut cross sections from point cloud (a) A slice depth is defined for extracting each cross section (b) A circle is fitted to each cross section.

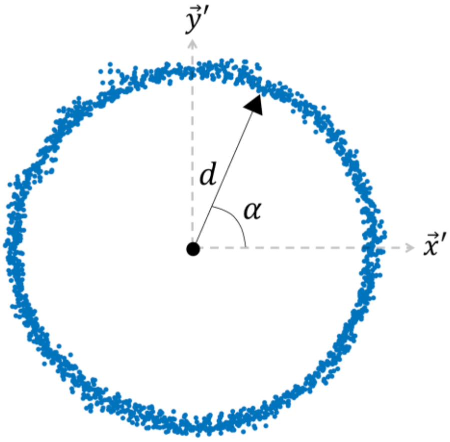

Figure 3.11. Illustration of the definition the parameters used for texture bias analysis , d and α.

3.4 Mechanical testing

Uniaxial compression tests of the lattice structure samples were conducted using an Instron 5969 universal testing machine equipped with a 50 kN load cell. The compressive displacement was applied at a rate of 0.28 mms^{-1}. Strain data was recorded directly from readout provided by the machine's software. Samples were compressed until complete failure was observed in one layer of the lattice. Video of each test was recorded using a Canon EOS 1300D camera at a rate of capture of 30 frames per second. The raw data of each test – Force (N), displacement (mm) – were recorded in a .csv file.

The .csv files were imported into MATLAB for calculation of Young's modulus. The force-displacement data of each test was combined by sampling the force values from each .csv at equally spaced extension values of $0\ mm, 0.01\ mm, 0.02\ mm, \ldots, 7.65\ mm$ using linear interpolation. The sampling spacing of $0.1\ mm$ was chosen as this was the average spacing from all of the test data. The mean and standard deviation of the combined force values was calculated. The mean force-displacement data was converted into stress-strain using the nominal area of the lattice structures, $784\ mm^2$. Young's modulus was determined by arbitrarily selecting two points in the elastic regime of the stress-strain graph and calculating the gradient.

3.5 Incorporation of deviations into model

The XCT data captured in Section 3.3.3 was used to apply geometric deviations to lattice structures generated using signed distance functions. The strut's medial axis is divided into multiple line segments, denoted by the matrix $\boldsymbol{L}$ (Eq. (4.18)). Waviness is modelled by displacing the points in $\boldsymbol{L}$, radius variation is modelled by changing the radius assigned at these points. No modifications are made to the positions of $\vec{l}_1$ and $\vec{l}_N$.

The vectors $\boldsymbol{O}$ (Eq. (3.3)) and $\boldsymbol{R}_{ptcloud}$ (Eq. (3.5)), derived from the XCT data describe the waviness and radius variation in the measured samples. The data in $\boldsymbol{O}$ and $\boldsymbol{R}_{ptcloud}$ was fitted to probability density functions (PDF) using a Kernel density estimation. Waviness was modelled by applying displacements to the points in $\boldsymbol{L}$, where the magnitude a of the displacement is determined from randomly generated values from the PDF fitted to $\boldsymbol{O}$. The displacements are applied to each point in a local plane perpendicular to the medial axis and coincident to each point in its initial position. The local x and y components of the displacement are given by $a\cos(\beta)$ and $a\sin(\beta)$ respectively, where β is a randomly generated number between 0 and 2π radians. Radius variation is modelled by using the PDF fitted to $\boldsymbol{R}_{ptcloud}$ to assign radius values to the points in the strut's medial axis (Eq. (4.23)), using linear interpolation between these values.

The key parameters (dx/r, $maxvol/vol_r$, $radbound/r$) for the generation of the meshes are given in Table 4. These values were selected due to their proven stability and convergence, as described in Chapter 5.

Table 4 Lattice modelling parameters.

dx/r	$maxvol/vol_r$	$radbound/r$
0.0625	0.1	0.05

3.6 Finite element analysis

The tetrahedral meshes were configured for simulation using commercial finite element software, Abaqus. As shown in Figure 3.12, the first step was to configure an .inp file which contained all the necessary information about the mesh and the simulation instructions for Abaqus to execute. Abaqus then performs the simulation by running the .inp file, and then outputs the results to a .dat file. Note that both .inp files and .dat files are text files.

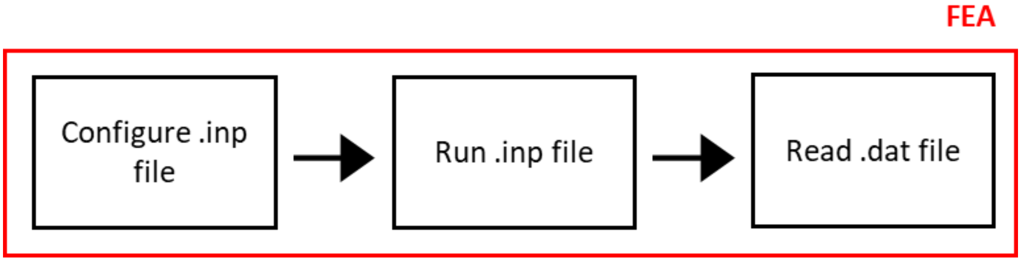

Figure 3.12. Flowchart of FEA stages.

To configure the .inp file for a given tetrahedral mesh, several steps of data processing are required. Firstly, all of the points in a given mesh must be defined by the matrix $\boldsymbol{M}_{mesh}$

$$\boldsymbol{M}_{mesh} = \begin{bmatrix} \vec{M}_1 \\ \vec{M}_2 \\ \vdots \\ \vec{M}_n \end{bmatrix} = \begin{bmatrix} x_1, y_1, z_1 \\ x_2, y_2, z_2 \\ \vdots \\ x_n, y_n, z_n \end{bmatrix}. \tag{3.8}$$

where n is the number of vertices in the mesh. The mesh's indexing matrix $\boldsymbol{I}_{mesh}$ is given by

$$\boldsymbol{I}_{mesh} = \begin{bmatrix} p_1^1, p_2^1, p_3^1, p_4^1 \\ p_1^2, p_2^2, p_3^2, p_4^2 \\ \vdots \\ p_1^m, p_2^m, p_3^m, p_4^m \end{bmatrix}. \tag{3.9}$$

where m is the number of tetrahedra in the mesh. To clarify the notation in Eq. (3.9), each row in $\boldsymbol{I}_{mesh}$ identifies a unique tetrahedron in the mesh and contains four integers, each of which references a row of x, y, z coordinates in $\boldsymbol{M}_{mesh}$. In Eq. (3.9), p_j^i is a positive integer which refers to the jth point of ith tetrahedron in the mesh, that is $\vec{M}_{p_j^i}$.

Next, the vertices in the mesh upon which boundary conditions and initial conditions are to be applied must be identified. As shown in Figure 3.13, two sets of vertices are created, "top node set" and "bottom node set", along with two corresponding indexing matrices $\boldsymbol{I}_{top}$ and $\boldsymbol{I}_{bottom}$. $\boldsymbol{I}_{top}$ is given by

$$\boldsymbol{I}_{top} = \begin{bmatrix} node_1 \\ node_2 \\ \vdots \\ node_k \end{bmatrix}. \tag{3.10}$$

where k is the number of nodes in $\boldsymbol{I}_{top}$. $\boldsymbol{I}_{top}$ is a column vector where each entry identifies a point in the mesh which belongs to "top node set". Every entry in $\boldsymbol{I}_{top}$ is an integer referring to a row in $\boldsymbol{M}_{mesh}$. The definition of indexing matrix $\boldsymbol{I}_{bottom}$ can be determined from Eq. (3.10) by symmetry.

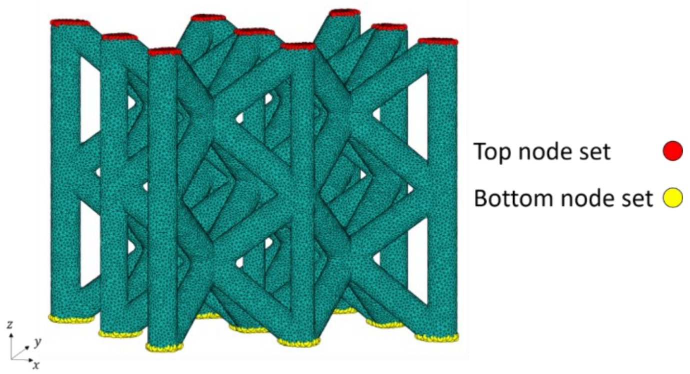

Figure 3.13. Example mesh of a BCCZ lattice with cropped top and bottom faces. The top and bottom node sets have been labelled.

Boundary conditions are applied to the bottom node set by restricting all degrees of freedom (i.e. no translation or rotation) using the "$ENCASTRE$" setting. Initial conditions are applied to the top node set by applying an arbitrary displacement in the negative z direction, the displacement was selected as a hundredth of the lattice height. Two material properties are applied to the mesh: Young's modulus 126 GPa and Poisson ratio 0.32. Lastly, the output variables - the reaction force in the positive z direction – is requested from the top node set.

To configure the .inp file, a MATLAB script was written which creates an .inp file containing all the above information, namely:

- $\boldsymbol{M}_{mesh}$
- $\boldsymbol{I}_{mesh}$, $\boldsymbol{I}_{top}$, $\boldsymbol{I}_{bottom}$
- Boundary conditions i.e. bottom node set $ENCASTRE$
- Initial conditions i.e. displacements on top node set
- Material properties
- Output variables

The simulation is performed by sending the .inp file to abaqus, using the following command: *Abaqus job=filename.*

After simulation, the output .dat file is read in MATLAB and the sum of the reaction forces F at each node in the top set is calculated. The Young's modulus E of the lattice is then calculated using

$$E = \frac{FL}{AU} \tag{3.11}$$

where U is the displacement applied to the top node set and A is the area of the lattice. L is the lattice height.

Chapter 4 – SDF-based modelling of strut-based lattice structures

---

In this chapter an approach for modelling strut-based lattice structures and applying geometric deviations and defects is proposed. A signed distance function (SDF) forms the base of this approach. SDFs are a well-known tool for generating surfaces and this proposed modelling approach applies novel extensions to the SDFs, making them adaptable to any strut-based lattice structure and also capable of replicating a range of geometric deviations observed in the literature.

Section 4.1 introduces the topic of implicit surfaces which provides the foundation necessary for understanding SDFs (§ 4.1.2). Section 4.2 explains the novel extensions applied to the basic SDF, providing intuitive mathematical definitions for strut-based lattice structures and a range of geometric deviations. Section 4.3 discusses the chosen method for conversion of triangulated surface meshes into tetrahedral meshes required for finite element analysis. Discussions and summaries of the chapter are given in Section 4.4 and Section 4.5 respectively.

Note that the extension of the SDF for lattice structures was published in a journal paper, [154].

4.1 Implicit surfaces

To introduce the topic of implicit surfaces, Section 4.1.1 first explains implicit functions, after which Section 4.1.2 discusses a specific implicit function—a signed distance function—and demonstrates its ability to generate complex geometries using implicit definitions.

4.1.1 Implicit functions

Consider a domain Ω in which the unit circle is defined, as shown in Figure 4.1. This circle divides the domain into two regions, Ω^- and Ω^+, which define the regions inside and outside the circle respectively. The circle is the interface between Ω^- and Ω^+, which is denoted by $\partial\Omega$. The unit circle can be defined by the function $\phi(\vec{x})$

$$\phi(\vec{x}) = x^2 + y^2 - 1 = 0. \tag{4.1}$$

Eq. (4.1) is an implicit function in which $\partial\Omega$ is defined by the set of points where $\phi(\vec{x}) = 0$. The term "level set" defines the set of points for which a function yields a constant value. Therefore, in Eq (4.1), the unit circle is a level set of $\phi(\vec{x})$, specifically the zero level set, corresponding to the solution $\phi(\vec{x}) = 0$. Naturally, $\phi(\vec{x}) < 0$ corresponds to the region Ω^-. $\phi(\vec{x}) > 0$ corresponds to the region Ω^+.

Level sets can also be called isocontours or isosurfaces. In Eq. (4.1), $\phi(\vec{x})$ is defined in a two-dimensional domain; the interface $\partial\Omega$ is therefore a one-dimensional isocontour that separates the two-dimensional regions Ω^- and Ω^+. In the case where a function $\phi(\vec{x})$ is defined in three dimensions, the interface $\partial\Omega$ will be two dimensional i.e. an isosurface which separates the three dimensional regions Ω^- and Ω^+.

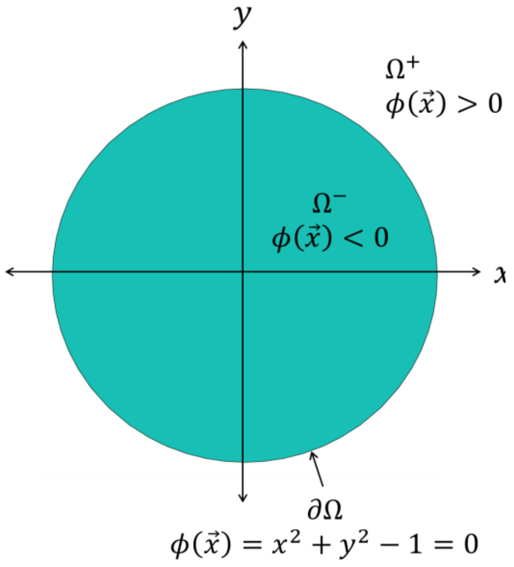

Figure 4.1. The unit circle defined by an implicit function. The unit circle is the interface $\partial\Omega$, separating the inner and outer regions Ω^- and Ω^+ respectively.

4.1.2 Signed distance functions

Continuing with the example of a unit circle, a distance function $d(\vec{x})$, as provided by Osher and Fedkiw [155], is defined as

$$d(\vec{x}) = \min(|\vec{x} - \vec{x}_I|) \qquad \text{for all} \quad \vec{x}_I \in \partial\Omega \tag{4.2}$$

Eq. (4.2) finds the shortest distance between a given point $\vec{x}$ and the interface $\partial\Omega$. As shown in Figure 4.2, if $\vec{x} \in \partial\Omega$ then $d(\vec{x}) = 0$. If $\vec{x} \notin \partial\Omega$ then $\vec{x}_C$ is defined as the point in the interface which is closest to a given point $\vec{x}$ and $d(\vec{x})$ is then given by

$$d(\vec{x}) = |\vec{x} - \vec{x}_C|. \tag{4.3}$$

A signed distance function (SDF) is an implicit function $\phi(\vec{x})$ with the property (provided again by Osher and Fedkiw)

$$|\phi(\vec{x})| = d(\vec{x}). \tag{4.4}$$

In words, Eq. (4.4) states that for a given point $\vec{x}$, an SDF calculates a distance whose magnitude is always equal to $d(\vec{x})$. The distinguishing property of SDFs is that the sign of the distance $\phi(\vec{x})$ denotes whether $\vec{x} \in \Omega^-$ or $\vec{x} \in \Omega^+$. As shown in Figure 4.3, the sign of the SDF $\phi(\vec{x})$ can immediately identify the inner and outer regions Ω^- and

Ω^+; conversely, the distance function $d(\vec{x})$ in Figure 4.2 is ambiguous because $d(\vec{x}) > 0$ in both regions Ω^- and Ω^+.

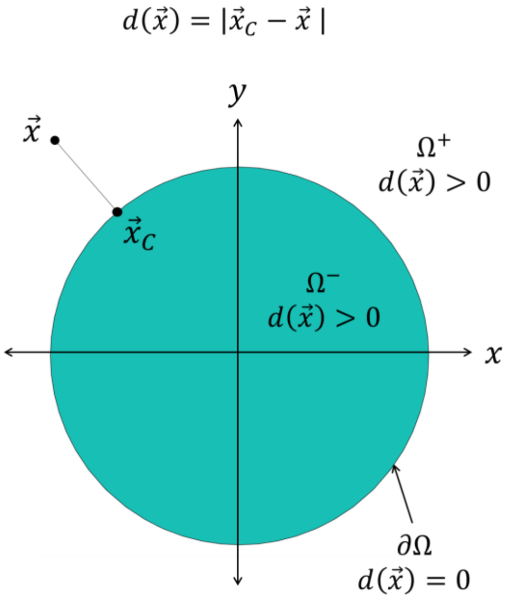
$d(\vec{x}) = |\vec{x}_C - \vec{x}\,|$
y
$\vec{x}$
Ω^+
$d(\vec{x}) > 0$
$\vec{x}_C$
Ω^-
$d(\vec{x}) > 0$
x
$\partial\Omega$
$d(\vec{x}) = 0$

Figure 4.2. An illustration of a distance function. Note that $d(\vec{x}) > 0$ in both Ω^- and Ω^+ which is ambiguous.

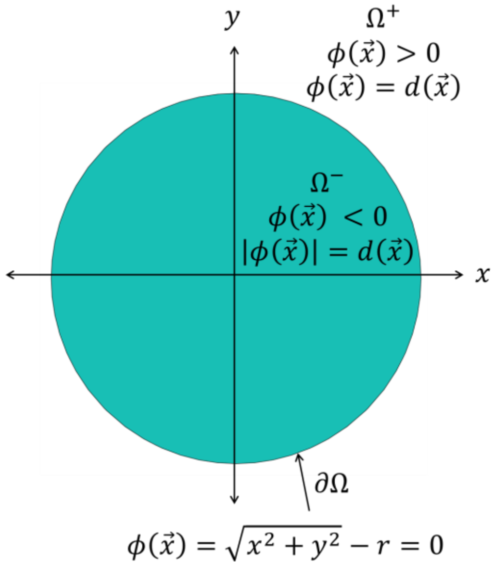
y
Ω^+
$\phi(\vec{x}) > 0$
$\phi(\vec{x}) = d(\vec{x})$
Ω^-
$\phi(\vec{x}) < 0$
$|\phi(\vec{x})| = d(\vec{x})$
x
$\partial\Omega$
$\phi(\vec{x}) = \sqrt{x^2 + y^2} - r = 0$

Figure 4.3. An illustration of a signed distance function. $\partial\Omega$ is well defined, due to the change of sign between Ω^- and Ω^+.

Rearranging Eq. (4.1), the unit circle can be implicitly defined using the SDF

$$\phi(\vec{x}) = \sqrt{x^2 + y^2} - r = 0 \tag{4.5}$$

where $r = 1$. $\phi(\vec{x})$ calculates the signed distance between a given point $\vec{x}$ and the closest point on the interface. The unit circle is represented as the zero level set of $\phi(\vec{x})$.

SDFs can be considered as comprising of two stages: distance calculation and adjustment. In the distance calculation stage, the distance between each point $\vec{x}$ and some predefined boundary (note that this boundary is not the interface $\partial\Omega$) is calculated, creating a distance field. In the adjustment stage, values in the distance field are adjusted such that the interface $\partial\Omega$ is found at the solution $\phi(\vec{x}) = 0$. Inspection of Eq. (4.5) shows that the distance calculation stage is performed by the square root term and the adjustment stage is performed by the subtraction of a constant r. Significant geometric complexity can be obtained by modifying either the distance calculation or adjustment stage. For example, the adjustment stage in Eq. (4.5) is modified by adding an additional term a_i to give

$$\phi(\vec{x}_i) = \sqrt{x_i^2 + y_i^2} - r + a_i = 0 \qquad i = 1, 2, \dots, N \tag{4.6}$$

where N is the number of points in the domain at which the SDF is computed. The subscript i is now introduced to indicate a numerical implementation wherein the SDF is computed iteratively through each point of a discrete domain. Eq. (4.6) adjusts the unit circle into a "petal-like" structure, as shown in Figure 4.4a. a_i is defined as

$$a_i = Bsin(\omega\theta), \tag{4.7}$$

where

$$\theta = arctan2(y_i, x_i) \tag{4.8}$$

and B and ω are the amplitude and angular frequency of the sine function respectively. Simple modification of B and ω can create significant changes to the geometry, as shown in Figure 4.4b-c.

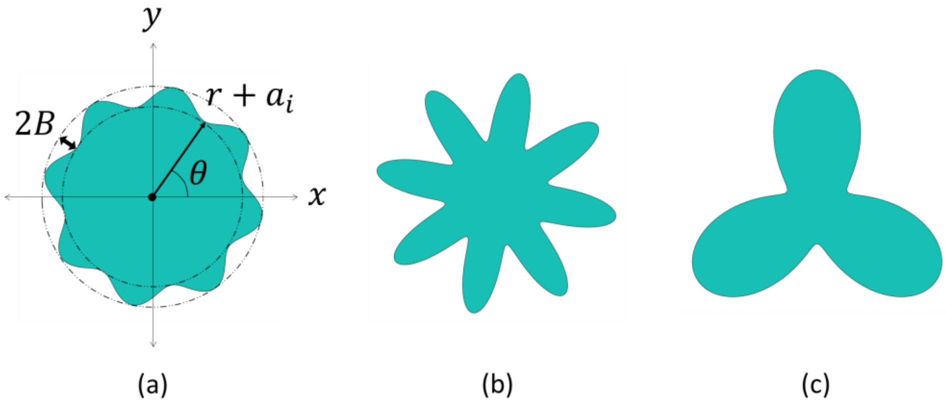

Figure 4.4. An example of modifying the signed distance function of a unit cell to increase geometric complexity, generating a petal-like structure. (a), (b) and (c) show examples where the a_i term has been modified.

Geometric complexity can also be increased by combining multiple distance fields. SDFs are suitable for Boolean operations (unions, additions, subtractions, etc.) which are used in constructive solid geometry tools. As an example, two shapes are generated, ϕ_1 and ϕ_2, based on the SDF defined in Eq. (4.6) and the union of these two shapes is computed by $\min(\phi_1, \phi_2)$, as shown in Figure 4.5. Because negative distance values are used to define Ω^-, computing $\min(\phi_1, \phi_2)$ gives precedence to the negative values and so the result combines the geometries from the two input distance fields.

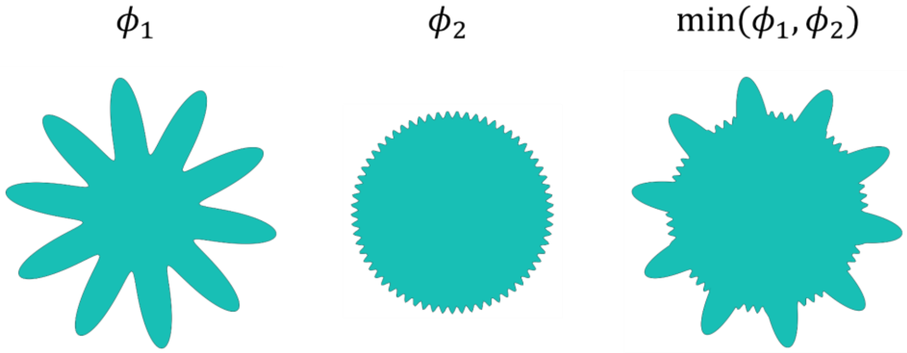

Figure 4.5. A Boolean union of two distance fields. A more complex geometry is created.

Lastly, consideration is given to the numerical implementation of SDFs. As first implied in Eq. (4.6), SDFs are computed over a discretized domain i.e. a Cartesian grid, as illustrated in Figure 4.6a. The interface $\partial\Omega$ is located within the Cartesian grid by calculating the coordinates locating where the SDF $\phi(\vec{x}) = 0$. This calculation is performed by linear interpolation between adjacent points where a sign change is detected in the distance field, as shown in Figure 4.6b.

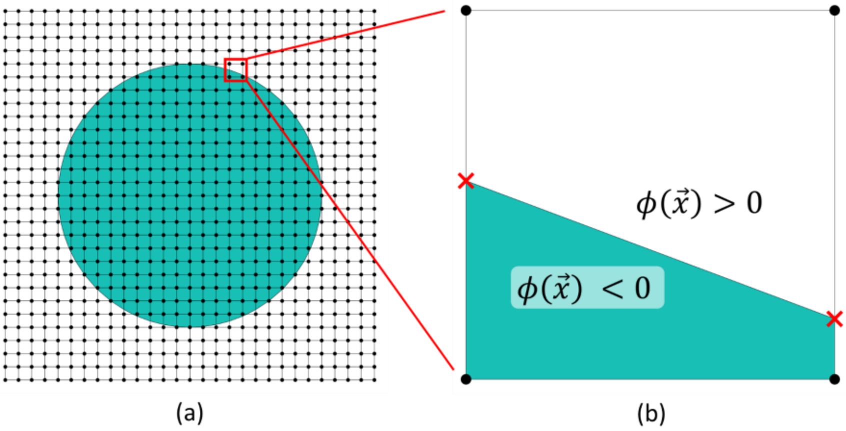

Figure 4.6. Illustration of the locating of $\phi(\vec{x}) = 0$ in a discrete distance field (a) Cartesian grid in which an SDF is computed (b) Enlarged view. Linear interpolation is used to locate the points where $\phi(\vec{x}) = 0$, marked with the red 'x'.

4.2 Surface modelling

This section builds upon the basic theory of SDFs (§ 4.1.2) and explains how SDFs can be used for generating lattice structure geometries. Mathematical definitions will be provided by for modelling lattice struts (§ 4.2.1), unit cells and lattice structures (§ 4.2.2), and geometric deviations/defects (§ 4.2.3).

4.2.1 Lattice strut

The surface of a lattice strut is defined by the set of points at an equal distance r from the strut's medial axis, as shown in Figure 4.7a. The medial axis $\boldsymbol{L}$ is a line segment specified by two points $\vec{l}_1$ and $\vec{l}_2$, that is

$$\boldsymbol{L} = [\vec{l}_1, \vec{l}_2]. \tag{4.9}$$

The lattice strut surface can be modelled as the zero level set of the SDF that calculates the distance between the medial axis and each point $\vec{x}_i$ in a three-dimensional Cartesian grid. The SDF $\phi(\vec{x})$ for the strut is given by

$$\phi(\vec{x}) = |\vec{x}_i - \vec{v}_i| - r = 0 \qquad i = 1,2,\ldots,M \tag{4.10}$$

where M is the total number of points in the three-dimensional Cartesian grid and $\vec{v}_i$ is the point on $\boldsymbol{L}$ which is closest to $\vec{x}_i$. $\vec{v}_i$ is analogous to $\vec{x}_C$ in the distance function given by Eq. (4.3) . Note that all arrow notation (e.g. $\vec{v}_i$) denotes coordinates in three axes, for example

$$\vec{v}_i = \left(x_{\vec{v}_i}, y_{\vec{v}_i}, z_{\vec{v}_i}\right). \tag{4.11}$$

Therefore, in Eq. (4.10),

$$|\vec{x}_i - \vec{v}_i| = \sqrt{(x_{\vec{x}_i} - x_{\vec{v}_i})^2 + (y_{\vec{x}_i} - y_{\vec{v}_i})^2 + (z_{\vec{x}_i} - z_{\vec{v}_i})^2}. \tag{4.12}$$

$\vec{v}_i$ is given by

$$\vec{v}_i = \left[\vec{l}_1 + \left(\vec{l}_2 - \vec{l}_1\right)t_i\right]. \tag{4.13}$$

Eq. (4.13) is simply the vector equation of a line. t_i is termed as the intersection ratio which describes the location of $\vec{v}_i$ within $\boldsymbol{L}$, as a ratio of the vector $\left(\vec{l}_2 - \vec{l}_1\right)$. Thus, $0 \leq t_i \leq 1$ for all points on the line segment. The intersection ratio is calculated using

$$t_i = \frac{\left(\vec{l}_2 - \vec{x}_i\right) \cdot \left(\vec{l}_2 - \vec{l}_1\right)}{\left|\vec{l}_2 - \vec{l}_1\right|^2}. \tag{4.14}$$[4]

In Eq. (4.14) $\vec{l}_2$ and $\vec{l}_1$ define a line of infinite length, therefore, there are some cases where $\vec{x}_i$ is located such that $t_i > 1$ or $t_i < 0$, as shown in Figure 4.7b. Such cases identify when the point $\vec{v}_i$ extends beyond the line segment and to prevent this, the following condition is added

$$t_i = \begin{cases} 0, & \text{for} \quad t_i < 0 \\ 1, & \text{for} \quad t_i > 1 \end{cases}. \tag{4.15}$$

The last term in Eq. (4.10), r, is subtracted from $|\vec{x}_i - \vec{v}_i|$ in order for the lattice strut of radius r to be represented by $\phi(\vec{x}) = 0$.

---

[4] See [165].

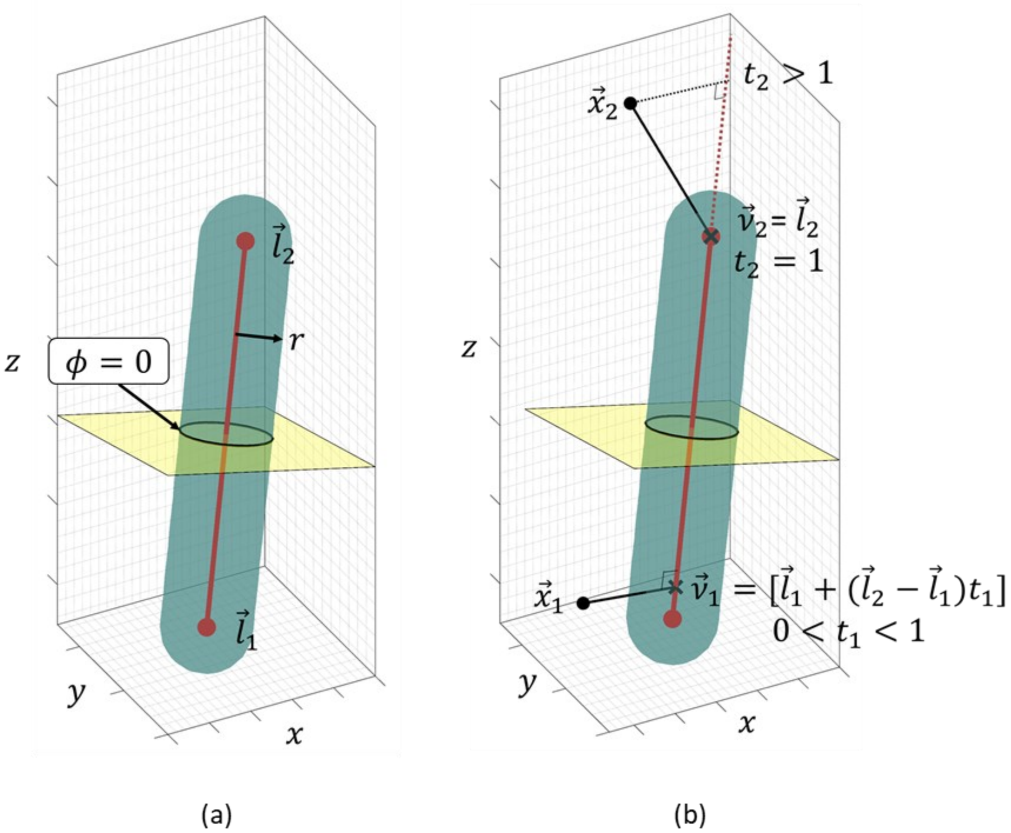

Figure 4.7. A lattice strut generated using a signed distance function. (a) Illustration of a lattice strut modelled as the points at distance r from the line segment $(\vec{l}_2 - \vec{l}_1)$. (b) Illustration of how the intersection ratio, t, is used in the distance calculation. At $\vec{x}_1, \vec{v}_1$ is located in between $\vec{l}_2$ and $\vec{l}_1$ and therefore $0 < t_1 < 1$. At $\vec{x}_2$, a case is shown where the Euclidean distance would naturally cause $\vec{v}_2$ to extend beyond the line segment, t_2 is therefore adjusted.

For further information regarding the numerical implementation of SDFs using MATLAB, the reader is referred to Appendix B, Figure B.3.

4.2.2 Unit cell and lattice structure

Unit cells are modelled by performing a Boolean union on the distance fields of individual struts. The isosurface of a unit cell ϕ_{cell} is defined as

$$\phi_{cell} = \min(\phi_1, \phi_2, \dots, \phi_N) = 0 \tag{4.16}$$

where N is the number of struts in the unit cell. Figure 4.8 shows a BCC unit cell generated using Eq. (4.16); each distance field ϕ for each individual strut is generated using the SDF in Eq. (4.10). Note that, where symmetry applies in the unit cell, struts can be generated by duplicating existing distance fields and performing a rotation, thus saving computational load. For example, ϕ_2, ϕ_3 and ϕ_4 in Figure 4.8 can all be generated by duplicating and rotating ϕ_1.

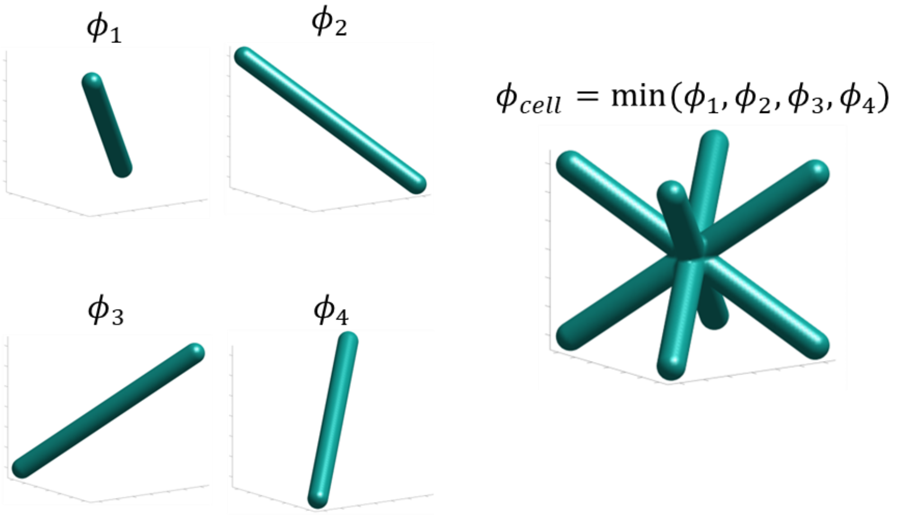

Figure 4.8. Boolean union performed to create the BCC unit cell. The distance field for the first strut ϕ_1 is duplicated and rotated to create three additional struts, ϕ_2, ϕ_3, ϕ_4. The unit cell ϕ_{cell} is created by calculating $\min(\phi_{1,}, \phi_2, \phi_3, \phi_4)$.

Lattice structures are modelled by tessellating the distance field ϕ_{cell} of a given unit cell. Conceptually, the tessellation process is performed by first initialising a distance field that is large enough to store all the unit cells, and then iteratively positioning each unit cell in its correct location. See Appendix B, Figure B.4 for more information on the implementation of the tessellation function, using MATLAB.

After tessellation, a final modification is made to the lattice structure $\phi_{lattice}$ wherein the upper and lower regions of $\phi_{lattice}$ are cropped to create flat surfaces which are parallel to the xy plane, as shown in Figure 4.9a-b. These modifications are necessary for configuring the finite element model, as explained in Section 3.6. Two planes are defined, $z = z_{min}$ and $z = z_{max}$, where z_{min} and z_{max} are defined as the minimum and maximum z coordinates of the medial axis $\boldsymbol{L}$ of the lattice structure respectively, as shown in Figure 4.9c. The regions of $\phi_{lattice}$ which are outside of both planes are cropped out. see Appendix B, Figure B.5 for further explanation of the cropping function, using MATLAB.

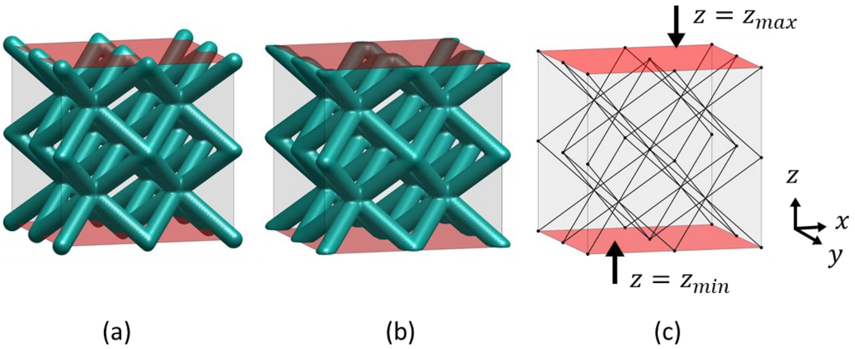

Figure 4.9. Cropped surfaces created on the lattice structure (a) ϕ_{lattice} before cropping (b) ϕ_{lattice} after cropping (c) the two planes used in the cropping, $z = z_{\text{min}}$ and $z = z_{\text{max}}$. z_{min} and z_{max} are defined by the minimum and maximum z coordinates of the medial axis of the lattice structure respectively.

4.2.3 Defects and geometric deviations

The following subsections demonstrate how a range of the geometric deviations and defects observed in lattice structures (see Chapter 2, § 2.4) can be implemented into this SDF-based modelling approach. The following defects are discussed due to their prevalence in the literature: waviness, radius variation, elliptical cross sections, porosity, surface defects. The reader is reminded that an SDF can be considered as comprising of two stages: distance calculation and adjustment (see § 4.1.2).

4.2.3.1 Waviness

To model waviness, the SDF remains similar to Eq. (4.10), however, the distance calculation stage is modified. As shown in Figure 4.10, the medial axis is now partitioned, creating additional vertices used to modify the strut's medial axis. The vertices of the medial axis are now defined as

$$\vec{l}_j = (x_j, y_j, z_j) \qquad j = 1,2, \dots, N+1 \tag{4.17}$$

where N is the number of line segments. Again, the vertices of the medial axis are stored in the matrix $\boldsymbol{L}$

$$\boldsymbol{L} = \begin{bmatrix} L_1 \\ L_2 \\ \vdots \\ L_N \end{bmatrix} = \begin{bmatrix} \vec{l}_1 & \vec{l}_2 \\ \vec{l}_2 & \vec{l}_3 \\ \vdots & \vdots \\ \vec{l}_N & \vec{l}_{N+1} \end{bmatrix}. \tag{4.18}$$

where each line segment in the medial axis is defined by L_j. The SDF now calculates the distance between a given point $\vec{x}_i$ and the closest line segment in $\boldsymbol{L}$. This SDF is given by

$$\phi(\vec{x}) = \min\left(\boldsymbol{D}_{\vec{x}_i}\right) - r = 0 \tag{4.19}$$

where $\min\left(\boldsymbol{D}_{\vec{x}_i}\right)$ is the minimum of the distances between a given point $\vec{x}_i$ and all the line segments in $\boldsymbol{L}$. To clarify, consider again an arbitrary point $\vec{x}_i$ in the Cartesian grid (Figure 4.10). The distance $\boldsymbol{D}_{\vec{x}_i}$ between $\vec{x}_i$ and all the line segments is given by

$$\boldsymbol{D}_{\vec{x}_i} = [d_1, d_2, \ldots, d_N]. \tag{4.20}$$

Computing the $\min\left(\boldsymbol{D}_{\vec{x}_i}\right)$ gives the Euclidean distance to the closest line segment. Once this distance is found, the constant r is subtracted in order for the desired surface to be represented by $\phi = 0$.

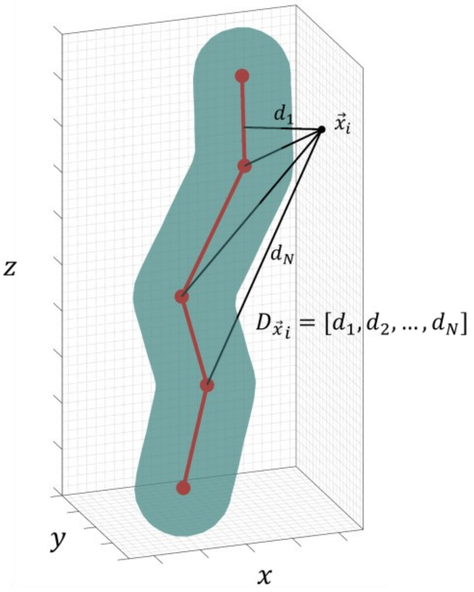

Figure 4.10. Illustration of the signed distance function used for modelling waviness. The strut's medial axis has been modified.

4.2.3.2 Radius variation

To apply radius variation, the SDF will be similar to Eq. (4.19), but the r term must be modified; in other words, the adjustment stage of the SDF must be changed. Eq. (4.19) is modified to

$$\phi(\vec{x}) = \min\left(\boldsymbol{D}_{\vec{x}_i}\right) - r_i = 0 \tag{4.21}$$

where

$$r_i = f(t_i). \tag{4.22}$$

The value of r_i depends on the intersection ratio of the line segment closest to $\vec{x}_i$. The radius of the strut can be made to vary along the strut's medial axis by defining the vector $\boldsymbol{R}$ which assigns a radius value to each point $\vec{l}_j$ in the medial axis $\boldsymbol{L}$

$$\boldsymbol{R} = [R_1, R_2, \dots, R_{N+1}]. \tag{4.23}$$

For every point $\vec{x}_i$ in the domain, after locating the closest line segment L_j, Eq. (4.21) is computed, where

$$r_i = \begin{cases} R_{j,} & if\ t_i = 0\ or\ t_i = 1 \\ \text{interpolate,} & if\ 0 < t_i < 1 \end{cases}. \tag{4.24}$$

Recalling the definition of $\vec{v}_i$ from Eq. (4.13), if $\vec{v}_i$ is coincident with any of the vertices $\vec{l}_j$, then the first condition of Eq. (4.24) will be true and thus the r_i value will equal the value in $\boldsymbol{R}$ assigned to $\vec{l}_j$. In all other cases, r_i is found by interpolating within $\boldsymbol{R}$. An example of Eq. (4.24) is shown in Figure 4.11, where cubic interpolation is used. Lastly, because $0 \leq t_i \leq 1$ for all $\vec{x}_i$, there is currently no way of identifying the line segment to which t_i is associated. Therefore, the following condition is added

$$t_{adjusted} = j - 1 + t_i \tag{4.25}$$

$t_{adjusted}$ is used in Eq. (4.24) instead of t_i, as shown in Figure 4.11.

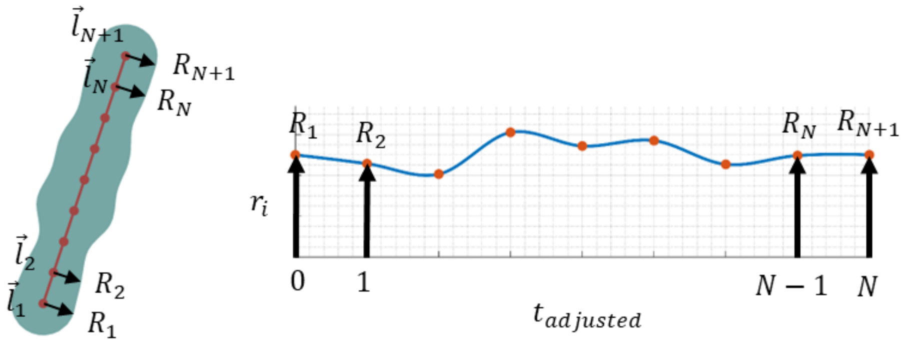

(a) (b)

Figure 4.11. Illustration of how radius variation is applied to the signed distance function. (a) Radius values are assigned to the vertices of the line segments. (b) An example of $\boldsymbol{R}$, which assigns radius values to each point $\vec{l}_j$.

4.2.3.3 Elliptical cross sections

An ellipse is defined as the set of points in the plane which satisfy

$$r_1 + r_2 = a. \tag{4.26}$$

a is the major axis of the ellipse and r_1 and r_2 are the distances between the two points F_1 and F_2 separated at a distance c, where $c < a$, as shown in Figure 4.12a. Eq. (4.26) is used to build an SDF which can model struts with elliptical cross sections

$$\phi(\vec{x}) = \min\left(\boldsymbol{D_1}_{\vec{x}_i}\right) + \min\left(\boldsymbol{D_2}_{\vec{x}_i}\right) - a_i = 0. \tag{4.27}$$

Figure 4.12b shows an example strut with elliptical cross sections; the figure also shows two sets of connected line segments which are parallel to each other. For each point $\vec{x}_i$ in the domain, the distances to each set of line segments is calculated. $\boldsymbol{D_1}_{\vec{x}_i}$ is given by

$$\boldsymbol{D_1}_{\vec{x}_i} = [d_1, d_2, \ldots, d_N]. \tag{4.28}$$

and stores the distances between a given point $\vec{x}_i$ and one set of line segments; $\boldsymbol{D_2}_{\vec{x}_i}$ stores the distances to the second set of line segments can be defined through symmetry from Eq. (4.28). Calculating $\min\left(\boldsymbol{D_1}_{\vec{x}_i}\right)$ and $\min\left(\boldsymbol{D_2}_{\vec{x}_i}\right)$ gives the distance between $\vec{x}_i$ and the closest line segment in each set of line segments. $\min\left(\boldsymbol{D_1}_{\vec{x}_i}\right)$ and $\min\left(\boldsymbol{D_2}_{\vec{x}_i}\right)$ correspond to r_1 and r_2 respectively in Eq. (4.26).

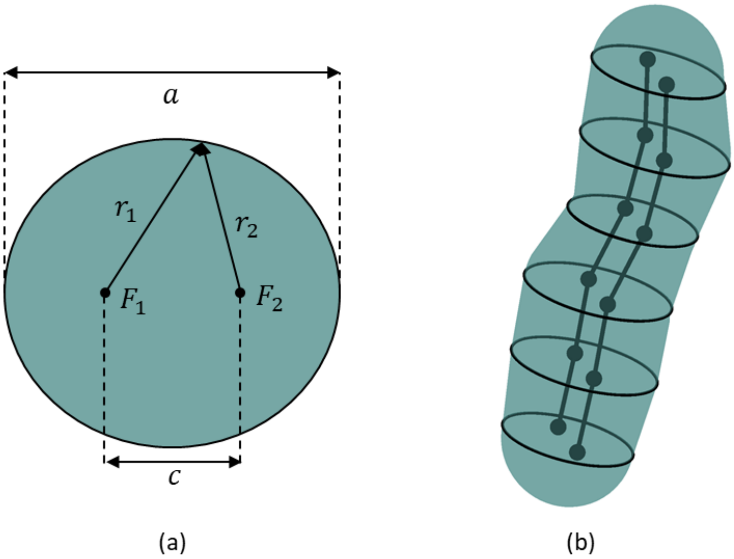

Figure 4.12. Modelling a strut with an elliptical cross section. (a) Diagram of an ellipse with major axis a. (b) Lattice strut with an elliptical cross section.

4.2.3.4 Porosity

SDFs can be used to model porosity, as shown in Figure 4.13. Conceptually, each pore is generated using its own SDF, and then the surfaces of all pores and struts can be combined. To model n spherical pores of equal radius r, each pore is defined by a 3D point $\vec{p}_i$ and stored in $\boldsymbol{P}$

$$\boldsymbol{P} = [\vec{p}_1, \vec{p}_2, \dots, \vec{p}_n]. \tag{4.29}$$

The SDF $\phi(\vec{x})$ is then given by

$$\phi(\vec{x}) = \min(\boldsymbol{D_P}) - r = 0 \tag{4.30}$$

where $\boldsymbol{D_P}$ stores the distances between the point in the Cartesian grid $\vec{x}_i$ and $\boldsymbol{P}$. To model spheres of differing radii—as demonstrated in Figure 4.13— separate sets of spheres must be defined and Eqs. (4.29) and (4.30) must be computed with a different radius for each set.

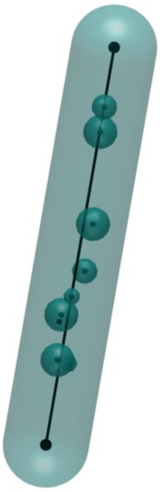

Figure 4.13. Example of modelling porosity. Larger pores have been used to aid visibility.

4.2.3.5 Surface defects

Surface defects can be applied to the model by modifying the surface mesh produced by the SDF. These modifications can be made by applying displacements to specific points on the surface. Before any displacements can be applied, each point on the surface of each strut must be characterised so it can be uniquely identified. Figure 4.14a shows an example of a surface of a lattice strut produced from an SDF. Three parameters are defined which are used to describe any point $\vec{x}_i$ on the surface: overhang angle θ_i, intersection ratio t_i, and surface angle α_i.

Overhang angle θ_i (see Chapter 2, § 2.2) and intersection ratio t_i (Eq. (4.14)) are already familiar terms. To define the surface angle α_i, a local coordinate system must first be defined. For a given point $\vec{x}_i$ a two-dimensional local coordinate system is defined in the strut's cross-sectional plane i.e. a plane perpendicular to the medial axis and coincident with $\vec{x}_i$ (Figure 4.14a). The origin of this local coordinate system is located at the centre of the cross-sectional circle. The base vectors of this local coordinate system are given by $(\vec{x}', \vec{y}')$. As shown in Figure 4.14a, $\vec{y}'$ in global coordinates is given by the vector at the local origin in the direction of the vector $\vec{R}$. $\vec{R}$ is the a reference line in the positive z direction starting at the lower point of the medial axis. $(\vec{x}', \vec{y}')$ are transformed into local coordinates, where $\vec{y}' = (0, 1, 0)$ and $\vec{x}' = (1, 0, 0)$, as shown in

Figure 4.14b. The surface normal $\vec{n}_i$ of any point $\vec{x}_i$ is transformed into local coordinates $\vec{n}_i'$, where

$$\vec{n}_i' = (x_i', y_i', 0). \tag{4.31}$$

Lastly, to define the surface angle α_i, α_i is defined in degrees as the *anti-clockwise* angle between $\vec{n}_i'$ and $\vec{x}'$, given by

$$\alpha_i = \begin{cases} arctan2(y_i', x_i') & if\ y_i' \geq 0 \\ 360 + arctan2(y_i', x_i') & if\ y_i' < 0 \end{cases}. \tag{4.32}$$

α_i has a range $0° \leq \alpha_i \leq 360°$ and describes whether the point $\vec{x}_i$ is up-skin or down-skin. Up-skin and down-skin values of α_i are given by the ranges

$$\text{Up-skin: } 0° \leq \alpha_i \leq 180°. \tag{4.33}$$

$$\text{Down-skin: } 180° < \alpha_i < 360°. \tag{4.34}$$

The most up-skin point is given by $\alpha_i = 90°$, which can also be considered as the angle for which the y' component of $\vec{n}_i'$ is maximum. Similarly, the most down-skin point is given by $\alpha_i = 270°$, which can be considered as the angle for which the y' component of $\vec{n}_i'$ is minimum. Note that when $\theta = 0°$ or $\theta = 90°$ the global coordinates of $(\vec{x}', \vec{y}')$ cannot be determined via the relationship between the local origin and the vector $\vec{R}$. When $\theta = 0°$, the local origin is coincident with $\vec{R}$ and therefore $\vec{y}'$ is automatically defined in both global and local coordinates as $(0, 1, 0)$. When $\theta = 90°$, $\vec{y}'$ in *global* coordinates is parallel to $\vec{R}$, therefore, $\vec{y}'$ is automatically defined in global coordinates as $(0, 0, 1)$ which is transformed into local coordinates $(0, 1, 0)$.

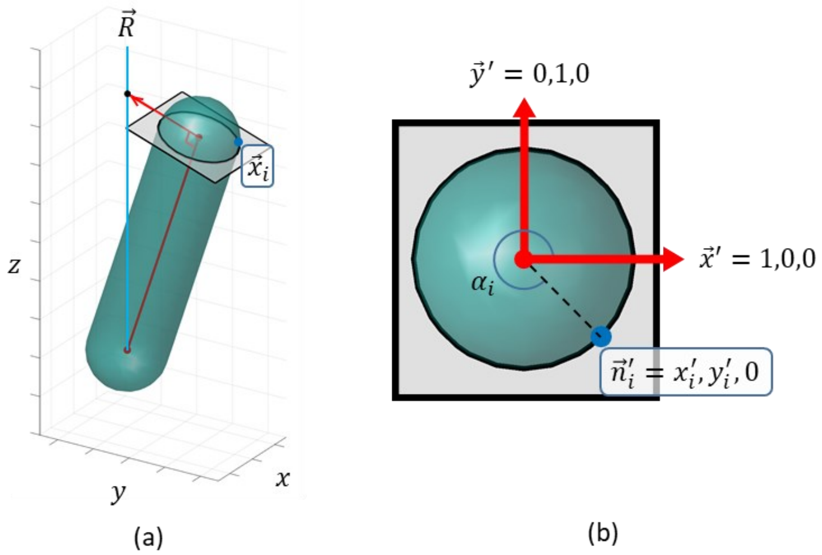

(a) (b)

Figure 4.14. Diagram showing how the surface angle is defined. (a) A strut showing how the local coordinate is first defined. (b) Local coordinate system in which α is calculated.

The three parameters θ, t, α can now be used to apply surface defects. The reader is referred to Appendix B, Figure B.6, for further information on the how MATLAB was used to derive these parameters.

Figure 4.15a shows an example for values of θ, t, α for different points on the surface of a BCCZ unit cell. To apply surface defects to the surface geometry, a function must be defined that displaces each point $\vec{x}_i$ by an amount δ_i in the direction of its surface normal $\vec{n}_i$ according to a given criteria defined by θ, t, α. Figure 4.15b shows an example of a unit cell to which displacements have been applied to model texture bias. For further discussion on the building of functions for modelling texture bias, the reader is referred to Appendix C.

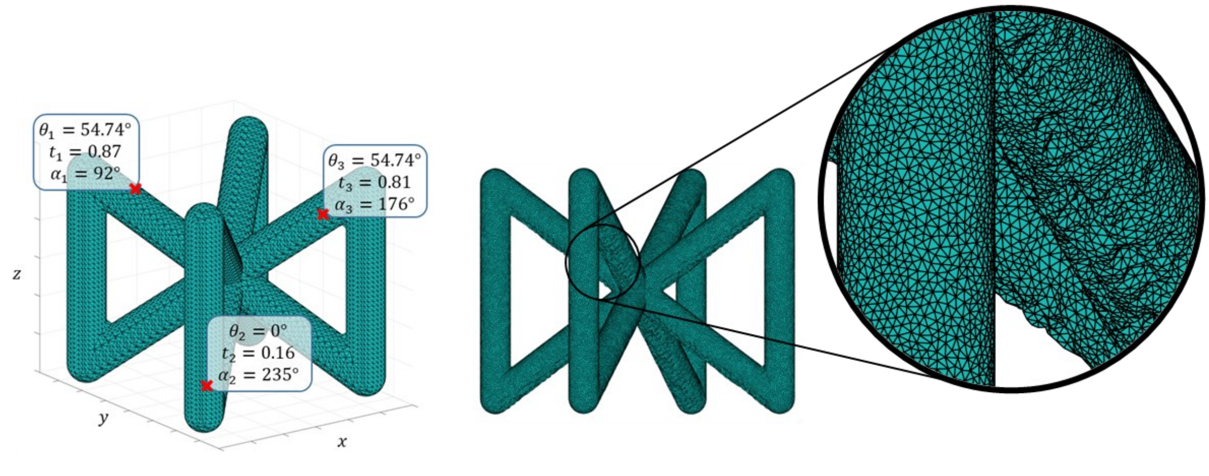

(a) (b)

Figure 4.15. Derivation of surface parameters and application of surface defects (a) Examples of overhang angle θ, intersection ratio t and surface angle α for points on a BCCZ unit cell. (b) Example surface with texture bias applied.

4.3 Tetrahedral modelling

This section discusses the open source MATLAB meshing software, Iso2mesh [156], which was used to create the tetrahedral meshes, necessary for finite element (FE) modelling. Iso2mesh is a toolbox of functions used for generating tetrahedral meshes from triangulated surfaces, as well as 3D binary and 3D grey-scale volumetric images [157].

Tetrahedral meshes were generated using one function from Iso2mesh, *CGALS2M*. Note that *CGALS2M* is developed by the Computational Geometry Algorithms Library (CGAL) [158]. CGALS2M converts a triangulated surface into a tetrahedral mesh using a restricted Delaunay tetrahedralisation (RDT). An example of the conversion from surface mesh to tetrahedral mesh is shown in Figure 4.16.

The CGAL documentation [159] describes the RDT algorithm in two main stages. In the first stage, a set of sample points are generated on the input triangulated surface and an initial tetrahedral mesh is generated using these sample points. The second stage iteratively modifies the initial tetrahedral mesh until a given mesh criteria on the size and shape of the mesh elements is satisfied.

The terms “surface elements” and “body elements” will now be defined to make a distinction between elements with a face on the surface of a mesh and elements with all faces beneath the surface, respectively. Additionally, the term “surface triangle” refers to the one face (out of four) of a surface element that is located on the surface of a mesh.

The mesh criteria is defined by several parameters controlling either the shape or size of the tetrahedral elements in the mesh. The parameters which control the surface triangles are named as follows:

- Angular bound
- Radius bound
- Distance bound

“Angular bound” is a shape parameter which specifies the lower bound (in degrees) for the internal angles of the surface triangles. “Radius bound” is a size parameter which defines the upper bound of the radius of the circumcircle of the surface triangles. “Distance bound” is a size parameter which define the upper bound for the distance between the circumcentre of all surface triangles and the centre of their associated circumsphere.

The parameters which control all tetrahedra are named as follows:

- Radius-edge bound
- Max volume

“Radius-edge bound” is a shape parameter which defines the upper bound for the ratio between the radius of the tetrahedron’s circumsphere and the shortest edge in the tetrahedron. “Max volume” is an upper bound on the radius of the tetrahedron’s circumsphere. For the work in this thesis, two parameters are used to optimise the meshes of lattice structures:

- Radius bound
- Max volume

Illustrations of these two parameters are shown in Figure 4.16. Hereafter, "radius bound" and "max volume" will be referred to as $radbound$ and $maxvol$ respectively. The combination of these two parameters allows for the generation of graded meshes, where smaller surface elements can be generated by modifying $radbound$, and larger body elements can be generated within the rest of the mesh by modifying $maxvol$. Smaller surface elements must be used in order to provide a good approximation of the input geometry, however, reducing the size of the body elements can help to optimise computational load. The shape parameters were kept at default values, in order to prevent from detrimentally effecting element shape, particularly given the limited CGAL documentation. Further discussion on the effects of $radbound$ and $maxvol$ on tetrahedral meshes is provided in Chapter 5

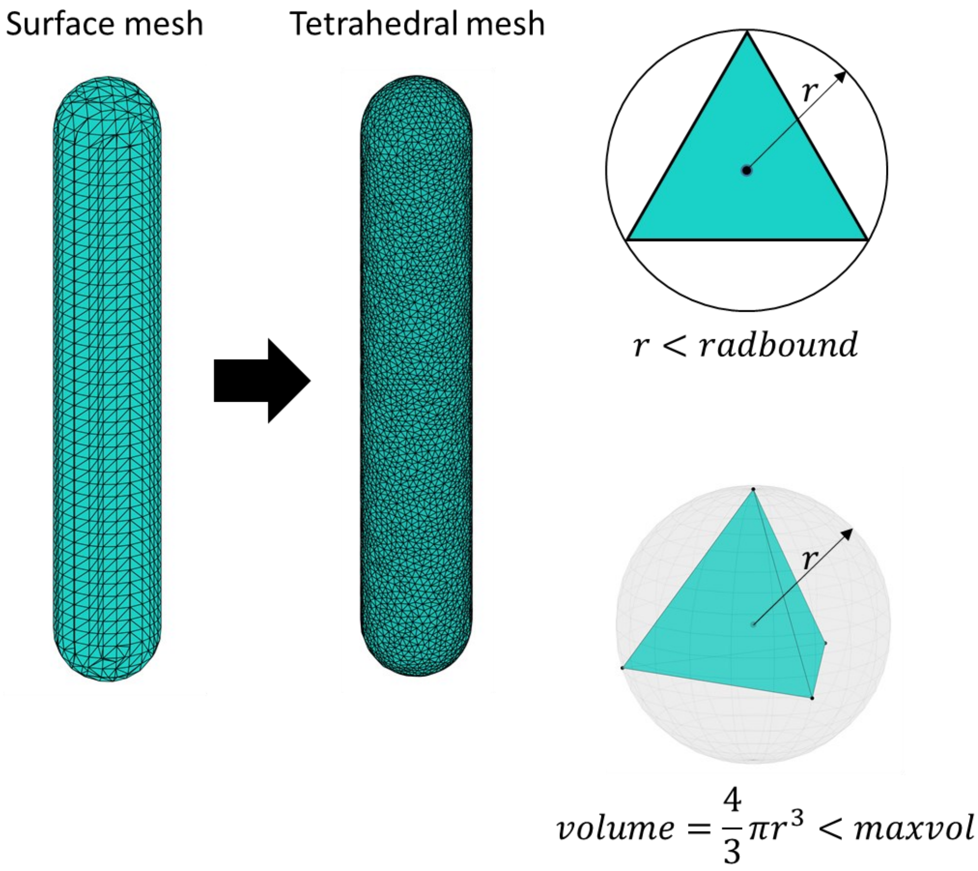

Figure 4.16. Example conversion from surface mesh to tetrahedral mesh . Also shown (right): illustrations of meshing parameters radbound and $maxvol$.

4.4 Discussion and conclusion

This chapter has described an SDF-based approach for modelling a range of defects in strut-based lattice structures. Figure 4.17 shows a flowchart which summarises the modelling approach defined in this chapter. As shown in Figure 4.17, there are three main stages, each with its own set of inputs and outputs. The first stage in the flowchart is the SDF, which produces triangulated surface meshes of strut, unit cell, and lattice geometries. These lattice geometries are defined by a medial axis and a radius; geometric deviations and porosity can be modelled by modifying the medial axis and/or SDF. The second stage is the surface defects function which modifies the triangulated surface mesh by applying displacements defined by the displacement function δ. The modified triangulated surface mesh is passed to the third stage—the meshing function—which produces the tetrahedral mesh. Naturally, combinations of defects can also be applied to these lattice geometries. For example, the SDF can first apply form defects to the struts, after which texture bias can be applied to the surface.

As demonstrated, this modelling approach is highly versatile and easily modifiable. Since the medial axes can be easily reconfigured, this approach is capable easily adapting to any strut-based lattice structure design. Additionally, the capability to model a range of common defects has been well demonstrated. Modelling geometric deviations via modification of the SDF is particularly effective and applicable to other defects not yet demonstrated. For example, a surface protrusion (see § 2.4.1) could easily be modelled by simply defining its own medial axis.

The trade-off that must be considered with this modelling approach is its computational requirements; SDFs can generate significant computational load when domains are discretised at high resolution. In particular, porosity modelling would require extremely high resolution, as this defect occurs at a significantly smaller scale than other lattice features. Additionally, the chosen tetrahedral modelling approach is significantly more computationally expensive in comparison to beam element modelling (as discussed in Chapter 2, § 2.8). However, beam elements are not suitable for the range of geometric complexity demonstrated with this SDF-based approach.

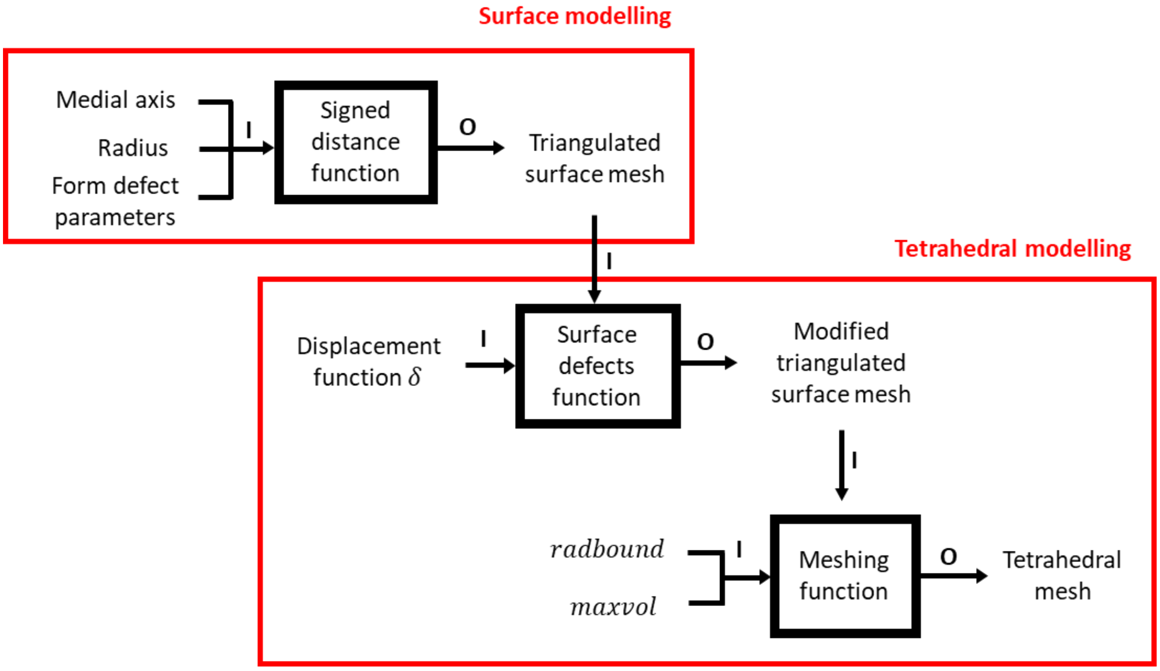
Surface modelling
Medial axis
Radius
Form defect parameters
I
Signed distance function
O
Triangulated surface mesh
I
Tetrahedral modelling
Displacement function δ
I
Surface defects function
O
Modified triangulated surface mesh
I
$radbound$
$maxvol$
I
Meshing function
O
Tetrahedral mesh

Figure 4.17. Summary of the proposed modelling approach. I/O corresponds to inputs/outputs.

4.5 Summary

This chapter has described the SDF-based approach which is used in this thesis for the modelling of strut-based lattice structures with the inclusion of a range of defects. Firstly, the topic of implicit functions was discussed as this is the basis upon which SDFs are built. Next, novel extensions to basic SDFs were demonstrated, showing how the mathematical definitions of basic SDF can be intuitively extended for modelling strut-based lattice structures and a range defects. Following this, an overview was provided of the selected tetrahedral meshing process, Iso2mesh, an open-source meshing toolbox.

Chapter 5 – Sensitivity study of the proposed modelling approach

---

The proposed modelling approach in the previous chapter is controlled by a range of parameters, each of which will have an effect on the geometries being generated. The aim of this chapter is to perform a sensitivity study of the proposed modelling approach, determining the behaviour of each of the parameters on the outputs of the modelling functions and locating regions of both stability and instability. This sensitivity study is necessary because the proposed model cannot be confidently used without first understanding how the selection of parameters impacts the integrity of the output.

Section 5.1 defines the outputs of the modelling approach, namely SDF error, meshing error and mesh quality which will be used to assess sensitivity. Section 5.2 defines all the inputs of the modelling approach; these values will be varied to observe their impact on the sensitivity of the model's outputs. Section 5.3 to Section 5.5 contain the results of the three sensitivity studies, corresponding to the three outputs defined in Section 5.1. Concluding discussions and summaries are provided in Section 5.6 and Section 5.7 respectively.

5.1 Outputs

This section defines the set of outputs which will be used to assess the sensitivity of the SDF and the meshing function. This sensitivity study is performed by considering three separate areas: SDF error sensitivity, meshing error sensitivity and mesh quality sensitivity. The following paragraphs will explain how SDF error, meshing error and mesh quality are calculated.

SDF error

The error in an SDF can be considered as the discrepancy between the output triangulated surface mesh and the input geometry defined by the SDF's geometrical input parameters. This error can be quantified by comparing the volume of the output triangulated surface mesh to the volume of the input geometry defined by the geometrical input parameters. This discrepancy is quantified as a percentage error, SDF error, ϵ_{SDF}

$$\epsilon_{SDF} = \frac{V_{SDF}^{i} - V_{SDF}^{o}}{V_{SDF}^{i}} \times 100. \tag{5.1}$$

where V_{SDF}^{i} and V_{SDF}^{o} are the volumes of the SDF input geometry and output geometry respectively. V_{SDF}^{i} must be determined analytically for whichever input geometry is being used (see Appendix D). V_{SDF}^{o} is given by

$$V_{SDF}^{o} = \textstyle\sum_{j=1}^{m} V_j \tag{5.2}$$

where m is the total number of triangular faces in the surface mesh [160]. For each triangle in the surface mesh, V_j denotes the signed volume of the tetrahedron defined by the connecting the jth triangle $\vec{a}_j, \vec{b}_j, \vec{c}_j$ to the origin, that is

$$V_j = \frac{1}{6}\vec{a}_j \cdot \left(\vec{b}_j \times \vec{c}_j\right) \tag{5.3}$$

as shown in Figure 5.1. The sign of V_j is determined by

$$\vec{a}_j \cdot \vec{n}_j \tag{5.4}$$

where $\vec{n}_j$ is the surface normal of the triangle; the convention requires $\vec{n}_j$ to be in the direction pointing away from the volume being calculated. A positive value for $\vec{a}_j \cdot \vec{n}_j$ yields a positive signed volume, and vice versa.

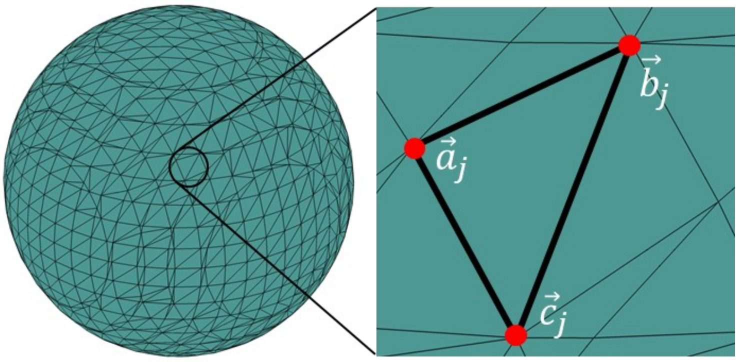

Figure 5.1. Triangulated surface mesh of a sphere geometry. An example of $\vec{a}_j, \vec{b}_j, \vec{c}_j$ which is used in calculating the volume of a triangulated surface.

Meshing error

The error in the meshing function can be considered in two ways, depending on whether surface defects are present in the geometry. Firstly, if there are no surface defects in the geometry, the error ϵ_{mesh} in the meshing function can be considered using a similar method as the SDF error ϵ_{SDF}. The meshing error ϵ_{mesh} can be quantified by comparing the volume of the output tetrahedral mesh to the volume of the input triangulated surface mesh. This discrepancy is quantified as a percentage error, ϵ_{mesh}

$$\epsilon_{mesh} = \frac{V^i_{mesh} - V^o_{mesh}}{V^i_{mesh}} \times 100. \tag{5.5}$$

Eq. (5.5) for the meshing error ϵ_{mesh} is similar to Eq. (5.1) for ϵ_{SDF}, however, in Eq. (5.5) both V^i_{mesh} and V^o_{mesh} are determined using Eq. (5.2), as both the input and output geometries are triangulated surfaces.

Secondly, if surface defects are present in the geometry, the error ϵ'_{mesh} in the meshing function can be considered by comparing the points on the surface of the tetrahedral mesh to their corresponding values in the input displacement function δ. For each point on the output tetrahedral mesh to which surface defects have been applied, there is a discrepancy between the actual displacement δ' on the surface of the tetrahedral mesh and the corresponding displacement value δ in the input displacement function. This discrepancy is expressed as an absolute difference $|\delta - \delta'|$. Therefore,

$$\mu = \frac{\sum_{i=1}^{n} \frac{|\delta_i - \delta_i'|}{\delta_i}}{n} \times 100 \tag{5.6}$$

denotes the mean error between the surface of the tetrahedral mesh and the input displacement function and n is the total number of points on the surface. The standard deviation is given by

$$\sigma = \frac{\sqrt{\frac{\sum_{i=1}^{n}(\delta_i - \mu\,)}{n-1}}}{\mu} \times 100 \tag{5.7}$$

which is expressed as a percentage of the mean. Therefore, meshing error ϵ_{mesh}' when surface defects are applied is given by

$$\epsilon_{mesh}' = \mu \pm \sigma. \tag{5.8}$$

Mesh quality

Mesh quality can be quantified by calculating shape properties of the elements in the tetrahedral mesh; mesh quality is not quantified by comparing inputs and outputs of the meshing function. Calculating mesh quality analysis is an important analysis step because finite element analysis can be negatively affected by the shape of the mesh's tetrahedral elements. The results produced in FE analysis are affected by the shape of the elements and may be erroneous if the mesh elements' edge lengths vary drastically. Additionally, an element with zero volume will cause simulation failure. As shown in Figure 5.2, the quality q_k of an element can be considered by comparing the volume $V_{element}^k$ of the element to the volume V_{equil}^k of the equilateral tetrahedron derived from the element's circumsphere, that is

$$q_k = \frac{V_{element}^k}{V_{equil}^k} \quad k = 1,2, \dots, m \tag{5.9}$$

where m denotes the total number of elements in the mesh and

$$0 \leq q_k \leq 1. \tag{5.10}$$

Figure 5.2 shows an example tetrahedral element, from which the equilateral tetrahedron has been derived. If $q_k = 1$ then $V_{element}^k = V_{equil}^k$ which is the most ideal result. If $q_k = 0$ then $V_{element}^k = 0$ which means that the points in the element lie in the same plane or line, therefore the tetrahedron is undefined and this is a failure. Mesh quality is therefore defined by the vector $\boldsymbol{q}$ which stores all the mesh quality values for the elements in a mesh

$$\boldsymbol{q} = [q_1, q_2, \dots, q_m]. \tag{5.11}$$

The equilateral tetrahedral is the most desirable shape for an element in a mesh as its edge lengths are of equal length.

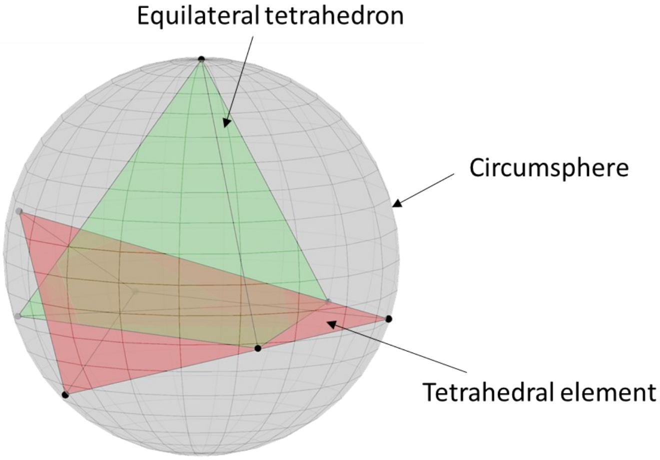

Figure 5.2. Illustration of mesh quality calculation. Every tetrahedral element can be compared to the equilateral tetrahedron derived from the element's circumsphere.

5.2 Inputs

This section defines all the inputs used in this sensitivity study. Figure 5.3 shows an expanded version of the flowchart in Figure 4.17, listing all the parameters which serve as inputs to the proposed modelling approach. The expanded flowchart in Figure 5.3 has several differences. Firstly, the inputs are now notated as **I_F** and **I_G**, corresponding to "functional input parameters" and "geometrical input parameters", respectively. Functional input parameters describe parameters which must always be configured each time a function is used; functional input parameters exist independent of the geometry being modelled. Geometrical input parameters are parameters which are dependent on the geometry being modelled. The second change in the expanded flowchart is the introduction of dx. dx is a functional input parameter that defines the resolution of the Cartesian grid over which a signed distance function is computed; dx is simply the edge length of a voxel in a Cartesian grid.

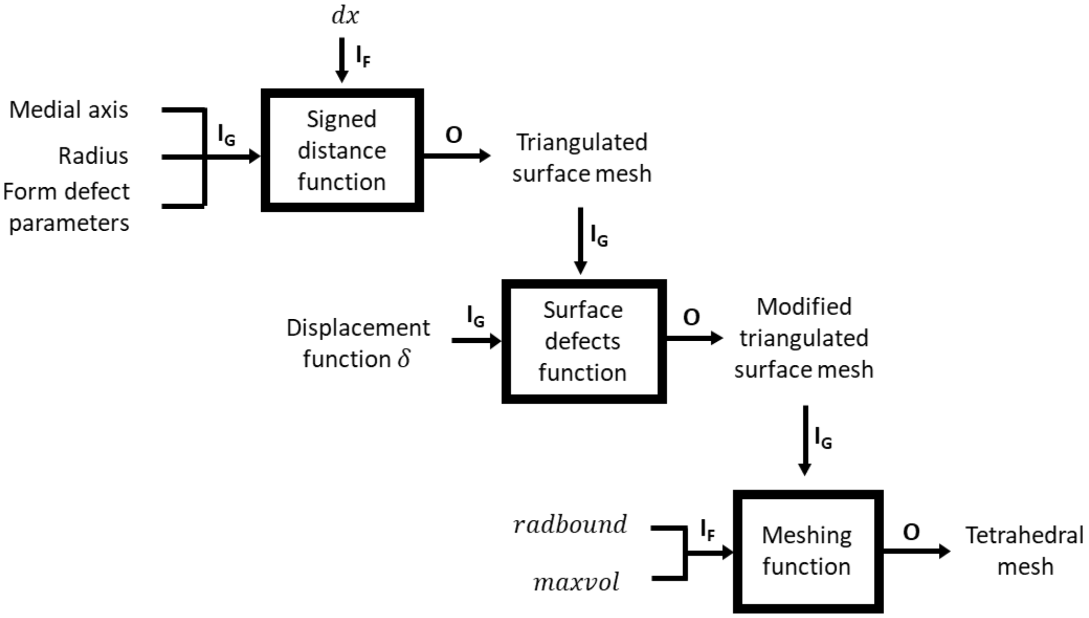
dx
IF
Medial axis
Radius
Form defect parameters
IG
Signed distance function
O
Triangulated surface mesh
IG
Displacement function δ
IG
Surface defects function
O
Modified triangulated surface mesh
IG
radbound
maxvol
IF
Meshing function
O
Tetrahedral mesh

Figure 5.3. Expanded flowchart of proposed modelling approach.

5.2.1 Functional input parameters

The SDF has one functional input parameter, dx, which controls the resolution of the Cartesian grid over which the function is computed. For a given fixed set of geometrical input parameters, modifying dx will produce surfaces with varying SDF error. Figure 5.4 shows the surface of a sphere generated from an SDF using different dx values. Visual inspection of Figure 5.4 illustrates the intuitive trend that decreasing the dx/r value produces a geometry which more accurately resembles a true sphere.

Note the use of the term dx/r, as dx has been normalised to the radius r. dx/r will be referenced extensively in the remaining sections.

The meshing function has two functional input parameters, $radbound$ and $maxvol$. $radbound$ defines the upper bound of the circumcircle of surface triangles, $maxvol$ defines the upper bound of the volume of the circumsphere of all elements. Consider a strut of radius r and volume vol_r. The terms $radbound/r$ and $maxvol/vol_r$ are used to normalise $radbound$ and $maxvol$ to the sphere radius and volume of a sphere with radius r, respectively. Figure 5.6 shows the effect of $radbound/r$ and $maxvol/vol_r$ on an example mesh. Again, by visual inspection, Figure 5.5 shows that decreasing $radbound/r$ creates geometries which more closely resemble a true sphere and therefore reduces the meshing error. Figure 5.6 shows how decreasing $maxvol/vol_r$ reduces the size and shape of the elements and therefore is closely related to mesh quality.

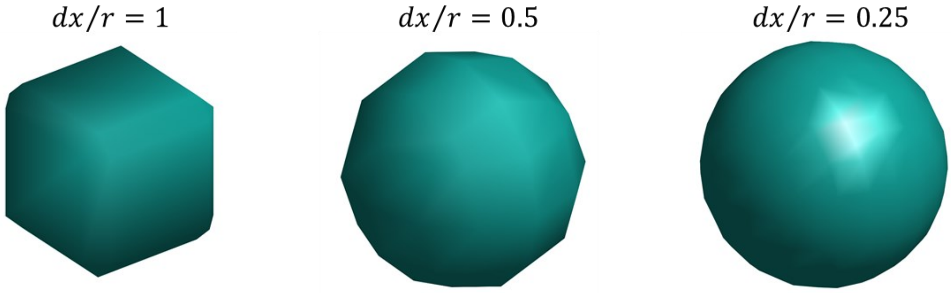

Figure 5.4. Spheres generated from signed distance functions using different resolutions. As dx/r decreases the geometry can be seen to more closely resemble a true sphere.

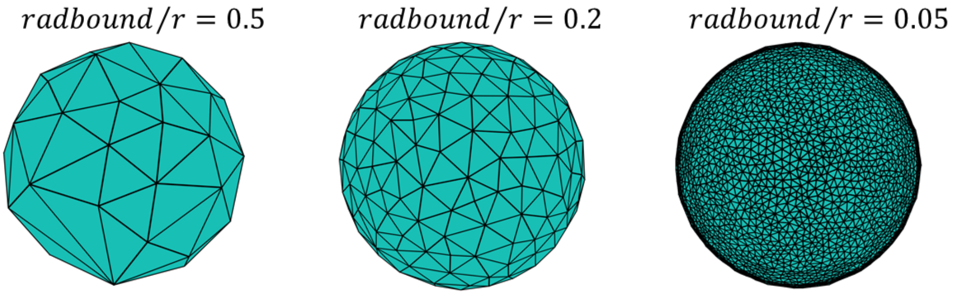

Figure 5.5. Examples of the effects of $radbound$ on the mesh of a sphere. As $radbound/r$ decreases the geometry can be seen to more closely resemble a true sphere.

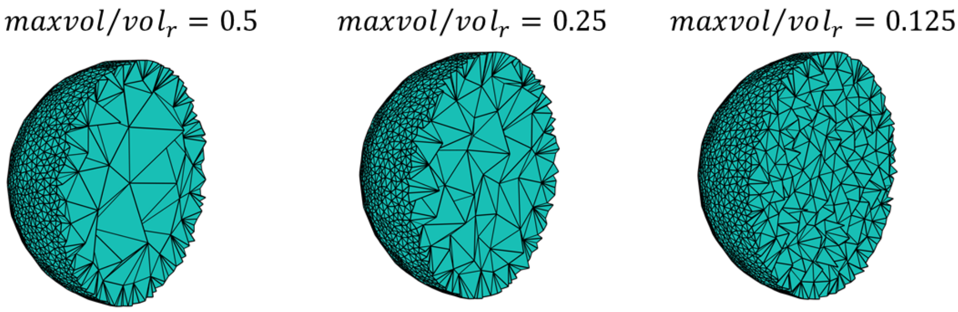

Figure 5.6. Examples of the effect of the $maxvol$ parameter on the mesh of a sphere. The images show the cross section of the sphere; the surface elements remain the same size and the body elements change size, thus impacting mesh quality.

5.2.2 Geometrical input parameters

Any given lattice structure may require a unique set of geometrical input parameters, depending on the design of the lattice structure and the presence of form and surface defects. Therefore, the sensitivity studies in this chapter require a simplified, finite set of geometrical input parameters which can still be considered as representative of all modelling scenarios for strut-based lattice structures in this thesis. Figure 5.7 shows a set of four geometries which have been selected and considered as representative of all modelling scenarios in this thesis: a sphere, a strut, a strut intersection and a radius deviation. This section will explain the geometrical input parameters which define these geometries, followed by justifying why this set has been considered as representative of lattice structures and the modelling scenarios in this thesis.

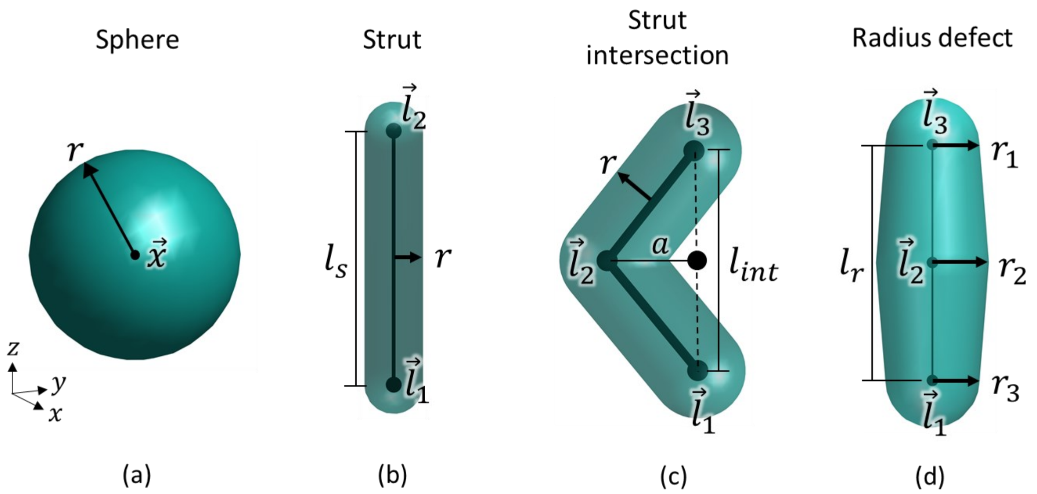
Sphere
Strut
Strut intersection
Radius defect
r
$\vec{x}$
z
y
x
$\vec{l}_2$
l_s
r
$\vec{l}_1$
$\vec{l}_3$
r
$\vec{l}_2$
a
l_{int}
$\vec{l}_1$
$\vec{l}_3$
r_1
l_r
$\vec{l}_2$
r_2
r_3
$\vec{l}_1$
(a)
(b)
(c)
(d)

Figure 5.7. Geometries considered representative of strut-based lattice structures and geometric deviations. (a) sphere (b) strut (c) strut intersection/waviness (d) radius variation.

The sphere (Figure 5.7a) is defined by a centre point $\vec{x}$ and radius r; the only parameter which modifies its geometry is the radius r. The strut (Figure 5.7b) is defined by medial axis $\boldsymbol{L} = [L_1] = [\vec{l}_1 \quad \vec{l}_2]$ and radius r. The strut geometry can be altered by modifying the radius r and the length l_s of the strut, given by $l_s = |\vec{l}_1 - \vec{l}_2|$; the term l_s/r denotes strut length normalised to its radius. The strut intersection (Figure 5.7c) is defined by medial axis

$$\boldsymbol{L} = \begin{bmatrix} L_1 \\ L_2 \end{bmatrix} = \begin{bmatrix} \vec{l}_1 & \vec{l}_2 \\ \vec{l}_2 & \vec{l}_3 \end{bmatrix}. \tag{5.12}$$

and radius r. The line segments in the strut intersection are of equal length, that is $|\vec{l}_1 - \vec{l}_2| = |\vec{l}_2 - \vec{l}_3|$. As shown in Figure 5.7, there are two parameters, l_{int} and a which are derived from the medial axis coordinates $\vec{l}_1$, $\vec{l}_2$, and $\vec{l}_3$. l_{int} is the length of the strut intersection; a is the “offset” and defined as the distance between $\vec{l}_2$ and the line connecting $\vec{l}_1$ and $\vec{l}_3$. l_{int} and a are given by

$$l_{int} = |\vec{l}_3 - \vec{l}_1|. \tag{5.13}$$

and

$$a = \sqrt{\left|\vec{l}_2 - \vec{l}_3\right|^2 - \left(\frac{l_{int}}{2}\right)^2}. \tag{5.14}$$

respectively. Note that $\left|\vec{l}_1 - \vec{l}_2\right|$ can be used in place of $\left|\vec{l}_2 - \vec{l}_3\right|$ in Eq. (5.14). Modifying l_{int} or a will alter the geometry of the strut intersection. The terms l_{int}/r and a/r denote strut length and offset normalised to its radius. Additionally, the term β can be used in the strut intersection to describe the angle created between the two line segments which meet at $\vec{l}_2$. β can be considered as twice the size of the angle between the line a and either of the line segments, that is

$$\beta = 2\tan^{-1}\left(\frac{l_{int}}{2a}\right) \qquad for\ a > 0\ and\ l_{int} > 0. \tag{5.15}$$

Therefore,

$$0° < \beta < 180°. \tag{5.16}$$

β will be referred to as the intersection angle. The radius deviation (Figure 5.7d) is defined by the same medial axis in Eq. (5.12), however, the points $\vec{l}_1$, $\vec{l}_2$, and $\vec{l}_3$ lie on the same line and are each assigned a radius r_1, r_2 and r_3.

A fixed radius r is applied to r_1 and r_3, that is

$$r_1 = r_3 = r \tag{5.17}$$

and the radius r_2 can be modified, thus altering the geometry of the radius deviation. The term r_2/r denotes normalisation to the original radius r.

The justification for the selection of these geometries is as follows. The sphere and strut were selected because a sphere is a simple three-dimensional shape which naturally extends into a lattice strut, which is the foundational geometry of all strut-based lattice structures. The strut intersection was selected because it is representative of two lattice features. Firstly, any lattice structure will consist of multiple pairs of struts which meet at lattice nodes, hereafter referred to as a "strut connection" in this chapter. Therefore, the strut intersection in Figure 5.7c is a simplified case of a single strut connection; the parameters l_{int} and a can be modified to match any pair of intersecting struts in a lattice structure. For example, Figure 5.8 shows a BCCZ unit cell, highlighting different strut intersections; if a cell size equal to unity is assumed, the highlighted strut intersection in Figure 5.8a has a length $l_{int} = 1$, each line segment has a length of $\sqrt{3}/2$ and thus $a = \sqrt{\left(\sqrt{3}/2\right)^2 - (1/2)^2} = 0.707$, and $\beta = 70.5°$, from Eqs. (5.14) and (5.15) respectively.

The second reason for selecting the strut intersection is because it is also representative of one of the form deviations, waviness. Waviness is modelled by dividing the medial axis of a strut into multiple line segments and applying displacements to the additional points which have been generated. Therefore, the simplest geometry representative of form deviations can be defined by using only two line segments. Figure 5.9a further illustrates how the strut intersection can be considered representative of waviness.

Distinguishing between these two features can be achieved by considered the scale of the parameters l_{int} and a. Using the terms l_{int}/r and a/r to normalise the strut intersection parameters to its radius, visual inspection of Figure 5.8 and Figure 5.9 confirms that in the case of modelling struts meeting at nodes (Figure 5.8) l_{int}/r and a/r are significantly larger than in the case of modelling waviness (Figure 5.9a). For clarity, the following convention is defined for making an approximate distinction between strut connections and the waviness deviation:

$$0 < l_{int}/r < 1, a/r < 1 \qquad \text{waviness deviation} \tag{5.18}$$

$$l_{int}/r \geq 1, a/r > 1 \qquad \text{strut connection.} \tag{5.19}$$

Furthermore, in the case where the strut intersection is representative of waviness, the length l_{int} can be shown to relate to Eq. (4.18) which defines how form deviations are modelled in the general case. From Eq. (4.18), the term l' is now used to define the distance between any two points in the medial axis which are separated by a single point, that is

$$l' = \left|\vec{l}_i - \vec{l}_{i+2}\right|. \tag{5.20}$$

The length l_{int} in the strut intersection is analogous to l' in the generalised case of modelling form deviations, as illustrated in Figure 5.9a. In Eq. (4.18), as the medial axis is divided into more line segments, l' will decrease; this is analogous to decreasing l_{int} in the strut intersection, and vice versa.

Lastly, the radius deviation (Figure 5.7d) is selected because it can be considered as representative of the second form deviation, radius variation. Similar to waviness, radius variation is modelled by increasing the number of line segments defining the strut's medial axis.

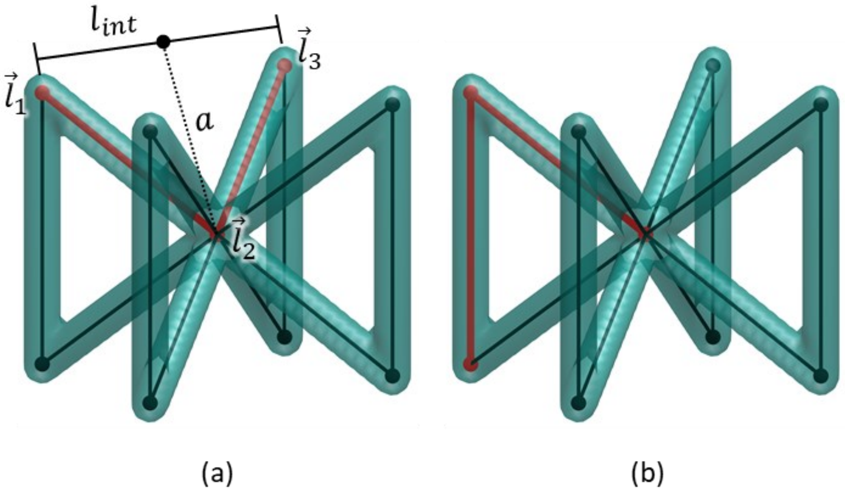

Figure 5.8. BCCZ unit cell showing examples of strut connections.

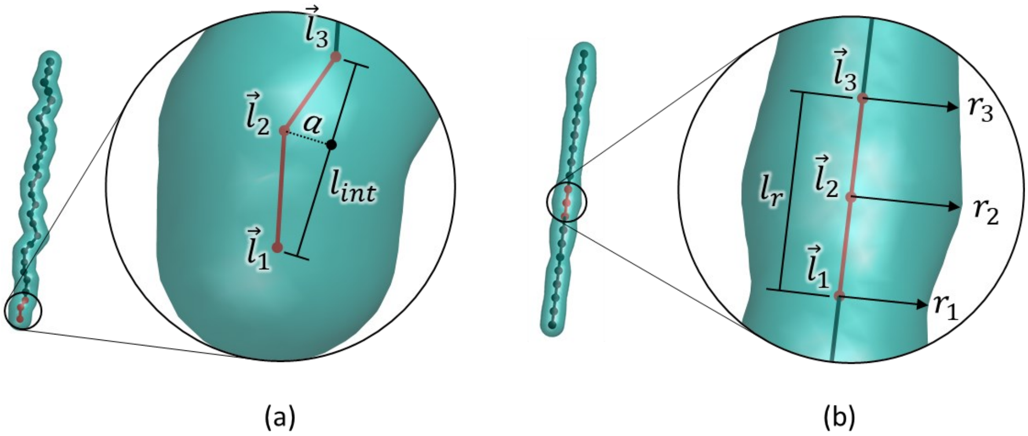

Figure 5.9. Illustrations of a strut intersection and radius deviation. (a) The strut intersection relates to waviness (b) an example of the radius deviation geometry within a strut.

5.2.3 Surface defect parameters

Surface defects are modelled by defining a displacement function δ which modifies the surface geometry produced by the SDF. For the purposes of this chapter, a basic displacement function δ is defined for applying peaks and troughs of varying frequency and amplitude to lattice surfaces. This displacement function is given by

$$\delta = A\sin(\omega_t t_i)\sin(\omega_\alpha \alpha_i). \tag{5.21}$$

The key parameters of this function are the amplitude A, and the frequencies ω_t and ω_α in the t and α axes respectively. The reader is reminded that t and α define the intersection ratio and surface angle respectively, as defined in Eq. (4.14) and Eq. (4.32) respectively. The term A/r is used to normalise the amplitude to the strut radius r. The frequency terms can be expressed in terms of normalised wavelengths. Firstly, the frequencies ω_t and ω_α can be expressed in terms of wavelengths λ_t and λ_α respectively. λ_t is given by

$$\lambda_t = l/\omega_t \tag{5.22}$$

where l is the strut length. Similarly, for the frequency ω_α in the α axis is given by

$$\lambda_\alpha = C/\omega_\alpha \tag{5.23}$$

where C is the circumference of the strut, defined by $2\pi r$. The terms λ_t/l and λ_α/C are used to normalise the wavelengths to the strut length and circumference respectively.

5.2.4 Summary

Table 5 lists all the input parameters which have been defined in previous sections and will be used in the subsequent sensitivity studies. In line with the following sections, the parameters are expressed in their normalised forms. Parameters are normalised to strut radius r, sphere (of radius r) volume vol_r, strut length l; strut circumference C.

Table 5. Summary of input parameters used in the sensitivity studies.

	Parameter (normalised)	**Definition**
Functional input parameters	dx/r	Cartesian grid resolution; edge length of a voxel.
	$radbound/r$	Upper bound of the circumcircle of surface triangles in a mesh.
	$maxvol/vol_r$	Upper bound of the volume of the circumsphere of all elements in a mesh
Geometrical input parameters	l_s/r	Strut length (when modelling no defects)
	l_{int}/r	Length of the strut intersection
	a/r	Offset of strut intersection
	l_r/r	Strut length (when modelling radius deviations)
	r_2/r	Modified radius
	A/r	Amplitude of displacement function
	λ_t/l	Wavelength of displacement function in t-axis
	λ_α/C	Wavelength of displacement function in α-axis

5.3 Study #1: SDF error sensitivity

This section assesses how the SDF error ϵ_{SDF} is affected by dx and the geometries which are representative of lattice structures and geometric deviations. The following geometrical input parameters are investigated:

- Sphere: centre $\vec{x}$, radius r
- Strut: length l_s, radius r
- Strut intersection: length l_{int}, offset a
- Radius deviation: length l_r, original radius r, modified radius r_2

As explained in Section 5.1, ϵ_{SDF} is calculated by comparing the volumes of the input and output geometries. The volumes of the input geometries must be determined analytically; these derivations are provided in Appendix D. Each geometry is tested with a fixed radius r; the variables in all tests will be expressed normalised to the radius r of their respective geometries.

The notation used for volume and error calculations in Section 5.1 will be expanded on in order to clarify which type of geometry is being referred to. Note the following: $\epsilon_{SDF,sphere}$, $\epsilon_{SDF,strut}$, $\epsilon_{SDF,int}$, $\epsilon_{SDF,rad}$ refer to the SDF error specifically for spheres, struts, strut intersections and radius deviations respectively, all of which are calculated using Eq. (5.1).

5.3.1 Sphere

To gain insight into the SDF error for sphere surfaces, $\epsilon_{SDF,sphere}$, multiple spheres were generated at range of resolutions, dx. Each sphere was generated with a fixed centre $\vec{x} = 0,0,0$. As shown in Figure 5.10, the relationship between $\epsilon_{SDF,sphere}$ and dx/r is an intuitive result, demonstrating that the error $\epsilon_{SDF,sphere}$ reduces upon reducing dx/r. Regarding stability, the results suggest that $dx/r \leq 0.125$ is a stable region as at $dx/r \leq 0.125$, $\epsilon_{SDF,sphere}$ begins to strongly converge to less than 1%.

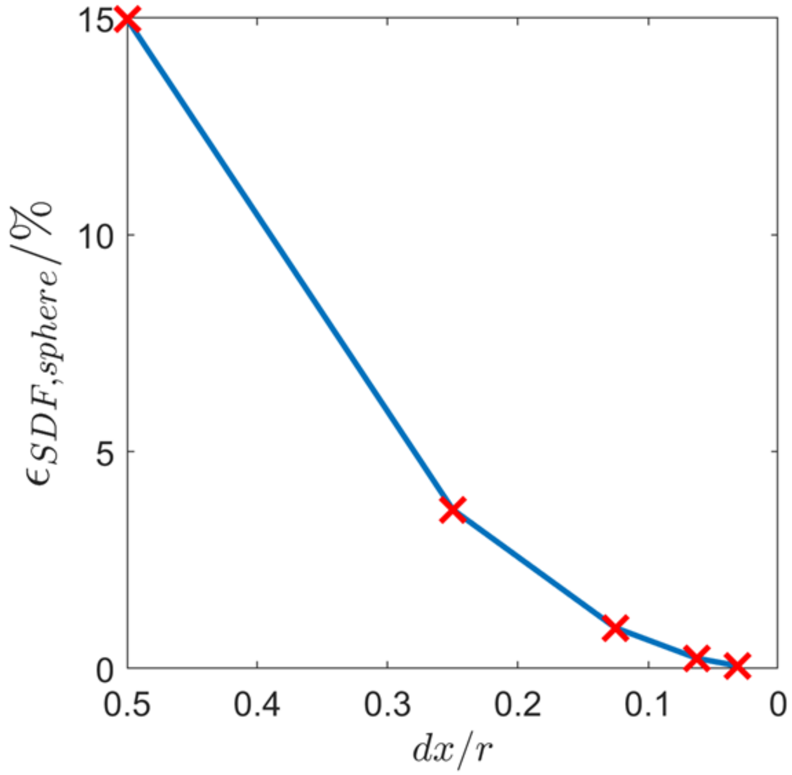

dx/r	0.5	0.25	0.125	0.0625	0.03125
$\epsilon_{SDF,sphere}/\%$	14.97	3.66	0.93	0.23	0.06

Figure 5.10. Relationship between SDF error for a sphere and the domain resolution. Plot shows $\epsilon_{SDF,sphere}$ vs dx/r.**Strut**

To investigate the SDF error for strut surfaces, $\epsilon_{SDF,strut}$, multiple strut surfaces were generated with different strut lengths l_s/r, using a range of domain resolutions dx/r. The medial axis of each strut was defined by $\vec{l}_1 = (0,0,0)$ and $\vec{l}_2 = (0,0,l_s)$. Figure 5.11 shows the results of calculating the SDF error $\epsilon_{SDF,strut}$ for the range of strut lengths l and the domain resolutions dx.

The first observation is that the output $\epsilon_{SDF,strut}$ consistently increases in stability as l_s/r increases, and the point of stability is reached earlier for higher values of dx/r. For each dx/r plot, $\epsilon_{SDF,strut}$ decreases upon increasing l_s/r and displays a converging behaviour. The decrease in error upon increasing l_s/r may be due to the increasing size of the cylindrical section of the geometry, which possesses zero curvature in its longitudinal direction. Because linear interpolation is used to extract the geometries in SDFs, increasing l_s/r creates a greater portion of the geometry which possesses zero curvature – which is ideal for the linear interpolation – and thus $\epsilon_{SDF_{strut}}$ decreases with increasing l_s/r. This reasoning is further supported by the fact that the maximum error in each plot is found at $l_s/r = 0$, which represents a sphere; a sphere possesses curvature in all directions and therefore produces the greatest error. At higher values of l_s/r, $\epsilon_{SDF_{strut}}$ converges towards the minimum error possible for a given dx/r. The second observation is that at values of $dx/r \leq 0.125$, the error $\epsilon_{SDF_{strut}}$ is less than 1% and is near constant for all l_s/r, suggesting that $dx/r \leq 0.125$ produces low error strut surfaces.

SDFs with domain resolution $dx/r \leq 0.125$ have now been shown to be stable and low error for both spheres and struts ($\epsilon_{SDF_{sphere}} \leq 0.93\%$ and $\epsilon_{SDF_{strut}} < 0.68\%$ respectively). Therefore, for all following tests of the SDF, a fixed value of $dx/r = 0.125$ is used.

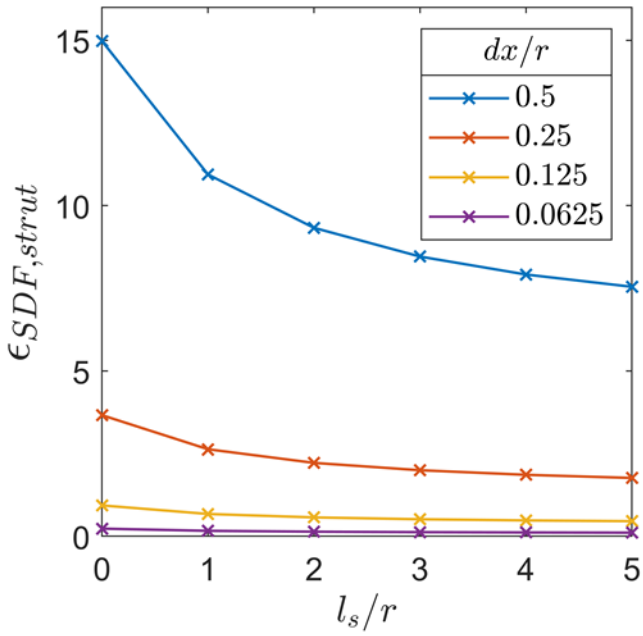

		l_s/r					
		0	**1**	**2**	**3**	**4**	**5**
dx/r	**0.5**	14.97	10.94	9.33	8.46	7.92	7.55
	0.25	3.66	2.63	2.22	2.00	1.86	1.76
	0.125	0.93	0.68	0.57	0.52	0.48	0.46
	0.0625	0.23	0.17	0.14	0.13	0.12	0.11

Figure 5.11. Relationship between SDF error for a strut and domain resolution Plot shows $\epsilon_{SDF_{strute}}$ vs l_s/r, for differing values of dx/r.

In Figure 5.11, the trend of decreasing error for fixed values of dx/r suggests that the SDF error for a strut ($l_s/r > 0$), is always less than the SDF error for a sphere ($l_s/r = 0$), that is

$$\epsilon_{SDF,sphere} > \epsilon_{SDF,strut} \tag{5.24}$$

Since the results in Figure 5.11 were generated using a strut of fixed orientation, namely $\vec{l}_1 = (0,0,0)$ and $\vec{l}_2 = (0,0,l)$, Monte Carlo simulation (MCS) can be used to generate a high number of randomly positioned struts and, for each strut, compare the SDF error in the strut $\epsilon_{SDF,strut}$ to the SDF error of a sphere $\epsilon_{SDF,sphere}$. The flowchart in Figure 5.12 describes the implementation of the MCS; the flowchart is split into two stages: initialisation and iteration. The initialisation stage is as follows:

- Define the value of the first iteration $i = 1$ and the total number of iterations n i.e. the total number of randomly positioned struts.
- Define the fixed parameters r and dx/r which will be constant for all SDFs in the MCS.
- Calculate $\epsilon_{SDF,sphere}$. Because r and dx/r are fixed, $\epsilon_{SDF,sphere}$ is a constant and does not need to be calculated for each iteration.

The iteration stage is as follows:

- Randomly position a strut by generating random values for $\vec{l}_1$ and $\vec{l}_2$.
- Compute the SDF for this randomly oriented strut.
- Calculate $\epsilon_{SDF,strut}$. Because $\vec{l}_1$ and $\vec{l}_2$ are *not* fixed, $\epsilon_{SDF,strut}$ will change with every iteration.
- Compare the current value of $\epsilon_{SDF,strut}$ to the value of $\epsilon_{SDF,strut}$ in all previous iterations. If the current iteration of $\epsilon_{SDF,strut}$ is larger than all previous iterations, store the current value in $\max(\epsilon_{SDF,strut})$.
- If $i = n$ then end the MCS, otherwise, increment i and repeat the iteration.

The following parameters were used for the MCS: $n = 5000, r = 1, dx/r = 0.125$. n and r were arbitrarily selected, $dx/r = 0.125$ was selected as this value was observed to produce low error for spheres and struts (Figure 5.10, Figure 5.11). Figure 5.13 shows a plot of the results. Figure 5.13 suggests that the value of $\max(\epsilon_{SDF,strut})$ converges to a value less than the constant $\epsilon_{SDF,sphere}$, that is

$$\epsilon_{SDF,sphere} > \max(\epsilon_{SDF,strut}). \tag{5.25}$$

The value of $\max(\epsilon_{SDF,strut})$ is determined from all the iterations of randomly positioned struts in the MCS. The strong convergence of $\max(\epsilon_{SDF,strut})$ to a value less than $\epsilon_{SDF,sphere}$ suggests that the assertion in Eq. (5.24) remains true for a strut in any orientation.

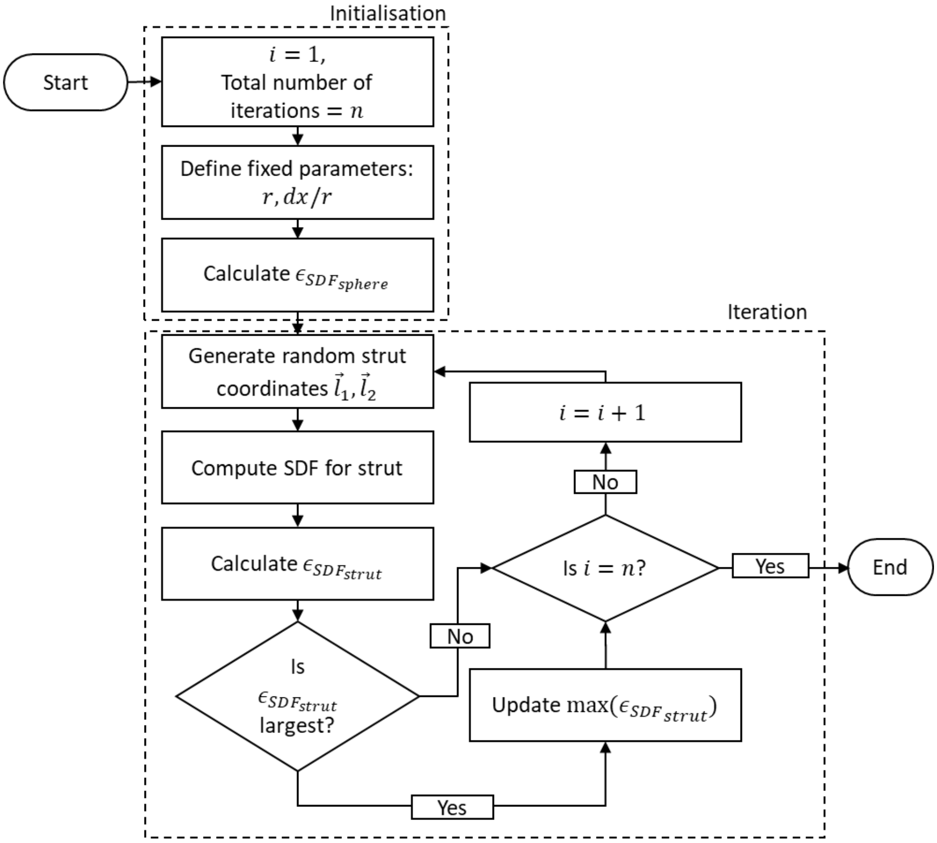
Initialisation
Start
$i = 1$,
Total number of iterations = n
Define fixed parameters: $r, dx/r$
Calculate $\epsilon_{SDF_{sphere}}$
Iteration
Generate random strut coordinates $\vec{l}_1, \vec{l}_2$
Compute SDF for strut
Calculate $\epsilon_{SDF_{strut}}$
Is $\epsilon_{SDF_{strut}}$ largest?
Yes
No
Update max($\epsilon_{SDF_{strut}}$)
Is $i = n$?
No
Yes
$i = i + 1$
End

Figure 5.12. Flowchart of Monte Carlo simulation steps.

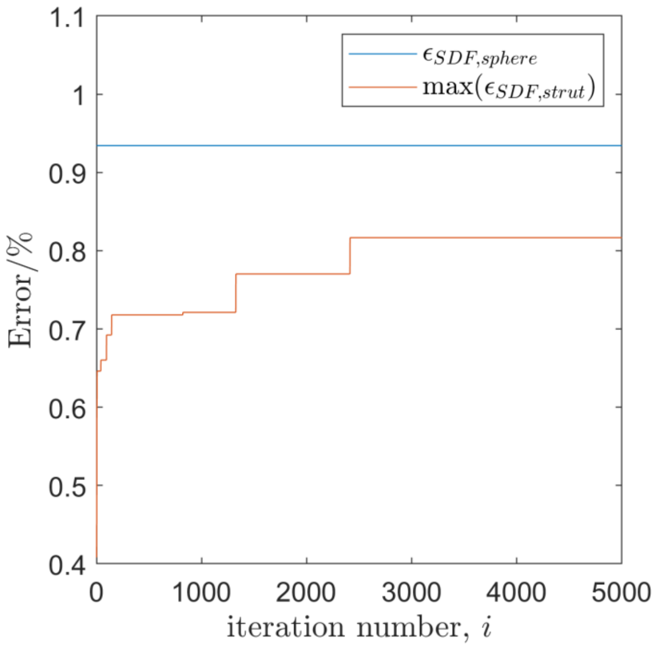

Figure 5.13. Results of the Monte Carlo simulation.

5.3.3 Strut intersection

To gain insight into the SDF error for strut intersections, $\epsilon_{SDF,int}$, multiple strut intersections were generated using a range of values for a/r and l_{int}/r. The medial axis of each strut intersection was defined by $\vec{l}_1 = (0, 0, 0), \vec{l}_2 = (a, 0, l_{int}/2), \vec{l}_3 = (0, 0, l_{int})$. The range of values for a/r and l_{int}/r were selected such that the strut intersection would model scenarios of both lattice features (strut connection and waviness). A new term is introduced, dx/l_{int}, which normalises the fixed domain resolution ($dx/r = 0.125$) to the length l_{int} of the strut intersection and is useful for interpreting the results in Figure 5.14.

The first observation from the results in Figure 5.14a is that, upon increasing a/r, $\epsilon_{SDF,int}$ is very unstable in the plots where $dx/l_{int} \geq 0.5$; the maximum error reaches over 500%. Although Figure 5.14a may initially suggest that results have no structure, further inspection proves insightful. Figure 5.14b and Figure 5.14c show zoomed in versions of the results, which reveal a clear structure. In Figure 5.14c, at $a/r = 0$, $\epsilon_{SDF,int}$ increases systematically (although only a small amount) upon increasing dx/l_{int}. The second observation in Figure 5.14c is that increasing a/r eventually causes instability in $\epsilon_{SDF,int}$, where that instability occurs earlier as l_{int}/dx decreases. This instability is characterised by a rapid 'decrease' in the error $\epsilon_{SDF,int}$, however, this decrease is not indicative of increased accuracy, as convergence is not observed.

The behaviour highlighted in Figure 5.14c is intuitive, namely, that the SDF error for any geometry can only be low if the resolution dx of the domain is several times smaller than the dimensions of the geometry being generated. Secondly, increasing a/r creates an increasingly large discontinuity in the surface of the strut intersection that can only be stably generated at low dx/l_{int}. A region of stability $dx/l_{int} < 0.167$ has been determined for modelling strut intersections.

The limits of stability shown in Figure 5.14c are useful for informing how strut intersections can be used practically for modelling lattice structures; the reader is reminded of the approximate ranges defined for waviness and strut connections in Eqs. (5.18) and (5.19) respectively. When waviness is being modelled ($0 < l_{int}/r < 1$,

$a/r < 1$ Eq. (5.18)), only small displacments a/r are permitted before the SDF becomes unstable. If l_{int}/r is reduced significantly, dx should also be reduced in order to maintain stability. When a strut connection is being modelled ($l_{int}/r \geq 1, a/r > 1$ Eq. (5.19)), much larger displacements a/r are permitted before the SDF becomes unstable.

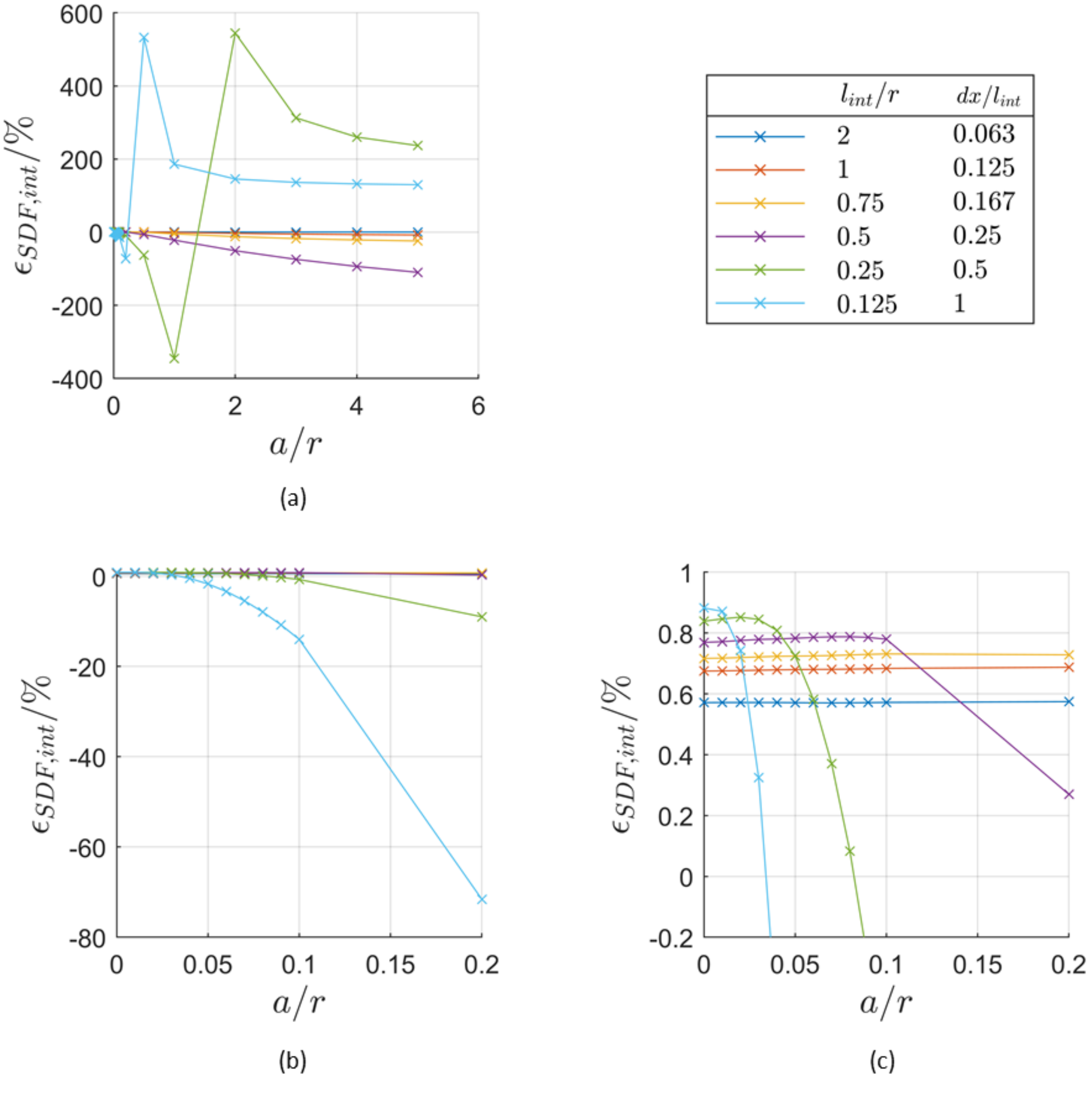

(a)

(b)

(c)

Figure 5.14. Relationship between the SDF error and the displacement applied to the strut intersection. Plot shows $\epsilon_{SDF,int}$ vs a/r, plotted for different values of l_{int}/r (which is also expressed in terms of dx/l_{int}.

5.3.4 Radius deviation

To understand the sensitivity of the SDF error for radius deviations $\epsilon_{SDF,rad}$, multiple radius deviations were generated using a range of values for r_2/r and l_r/r. The medial axis of each radius deviation was defined by $\vec{l}_1 = (0,0,0), \vec{l}_2 = (0,0,l_r/2), \vec{l}_3 = (0,0,l_r)$.

Figure 5.15 shows the results; the term dx/l_r is provided and useful for interpreting the results. The first observation from Figure 5.15a is that, for $dx/l_r \leq 0.5$, the results are very stable; increasing the radius variation r_2/r causes negligible change to $\epsilon_{SDF,rad}$ as the error remains below 1%. This negligible change is more clearly observed in Figure 5.15b which shows a zoomed in portion of Figure 5.15a. The second observation from Figure 5.15a is that, at $dx/l_r > 0.5$, the error $\epsilon_{SDF,rad}$ becomes unstable and increases rapidly, from approximately 1% to nearly 6% upon increasing r_2/r.

The trend in Figure 5.15 is again intuitive and similar to the results for the strut intersection in Section 5.3.3. Low error is only possible when the SDF domain resolution dx is several times smaller than dimensions of the geometry being generated. For the radius deviation, a stable modelling region of $dx/l_r \leq 0.5$ has been located.

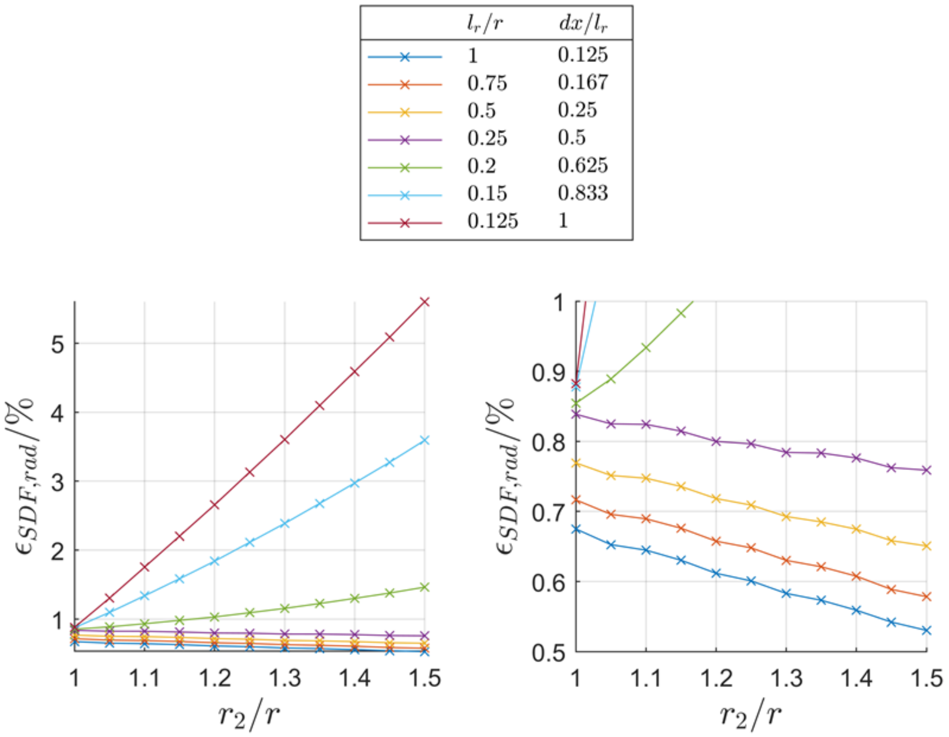

(a) (b)

Figure 5.15. Relationship between the SDF error and the varied radius applied to the radius deviation. Plot shows $\epsilon_{SDF,rad}$ vs r_2/r, plotted at different values of l_r/r (which is also be expressed as dx/l_r).

5.3.5 Key findings

This section provides a summary of the key findings from the SDF error analysis tests conducted in Sections 5.3.1-5.3.4:

- $dx/r = 0.125$ to was found to be a suitable resolution for the sphere and strut geometries, producing stable errors less than 1%.
- Strut error $\epsilon_{SDF,strut}$ initially reduces and then converges upon increasing strut length l_s/r.
- $\epsilon_{SDF,strut} > \epsilon_{SDF,sphere}$ for all strut orientations.
- For strut intersections, a region of stability $dx/l_{int} < 0.167$ has been determined for modelling strut intersections.
- For radius deviations, a region of stability of $dx/l_r \leq 0.5$ has been located

5.4 Study #2: Meshing error sensitivity

The aim of this section is to investigate how the meshing error ϵ_{mesh} is affected by the functional input parameter $radbound$ and the geometries considered representative of lattice structures, form deviations and surface defects. The following geometrical input parameters are investigated:

- Sphere: centre $\vec{x}$, radius r
- Strut: length l_s, radius r
- Strut intersection: length l_{int}, offset a
- Radius deviation: length l_r, original radius r, modified radius r_2/r
- Displacement function: amplitude A/r, wavelengths λ_t/l and λ_α/C

In this section, all input geometries for the meshing function are produced by a SDF using a fixed resolution $dx/r = 0.125$, as Section 5.3 has demonstrated that this produces stable, low error, geometries for spheres and struts. The medial axis of each geometry is defined in the same way as the corresponding geometry used for the SDF error analysis in Section 5.3. Again, modifications to meshing error notation first introduced in Section 5.1 will be made here to clarify the meshing error associated to a specific geometry (e.g. $\epsilon_{mesh,strut}$).

5.4.1 Sphere

Figure 5.16 displays the relationship between $\epsilon_{mesh,sphere}$ and $radbound/r$. The results in Figure 5.16 show an intuitive result: $\epsilon_{mesh,sphere}$ reduces as $radbound/r$ decreases because smaller surface elements are being used in the tetrahedral mesh, this will better approximate the input surface. The region of stability can be seen at $radbound/r \leq 0.05$, the error $\epsilon_{mesh,sphere}$ is very low and is less than 1%.

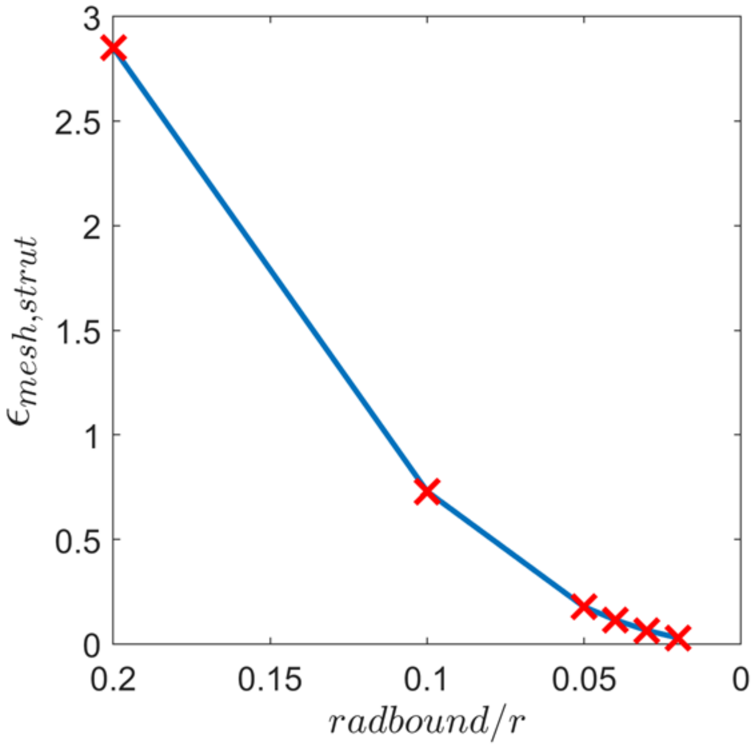

$radbound/r$	0.2	0.1	0.05	0.04	0.03	0.02
$\epsilon_{mesh,sphere}/\%$	2.85	0.73	0.18	0.12	0.07	0.03

Figure 5.16. Relationship between the meshing error for a sphere and$radbound$. Plot shows $\epsilon_{mesh,sphere}$ vs $radbound/r$.

5.4.2 Strut

Figure 5.17 displays the relationship between $\epsilon_{mesh,strut}$ and the normalised length of the strut l_s/r for several values of $radbound/r$.

The first observation of the results is that the pattern is very similar to the results for $\epsilon_{mesh,strut}$ in Section 5.3.2; the error $\epsilon_{mesh,strut}$ is greatest for the sphere ($l_s/r = 0$) and becomes stable upon increasing l_s/r. Naturally, this behaviour may be due to the same reasons described in Section 5.3.2, namely that increasing l_s/r creates a greater region with zero curvature in the strut's longitudinal axis and is therefore easier for the meshing function to generate. Also observed in these results is that when $radbound/r \leq 0.05$, the value of l_s/r has little effect on the error when $radbound/r \leq 0.05$ and, although slight convergence is observed, the error is near constant and is very stable. At $radbound/r \leq 0.05$, the output meshes possess very small surface elements which approximate the input geometry with very low error.

The parameter $radbound/r$ has now been shown to produce very stable and low meshing error for both sphere and struts. Therefore, for all following tests of the meshing function, a fixed value of $radbound/r = 0.05$ is used.

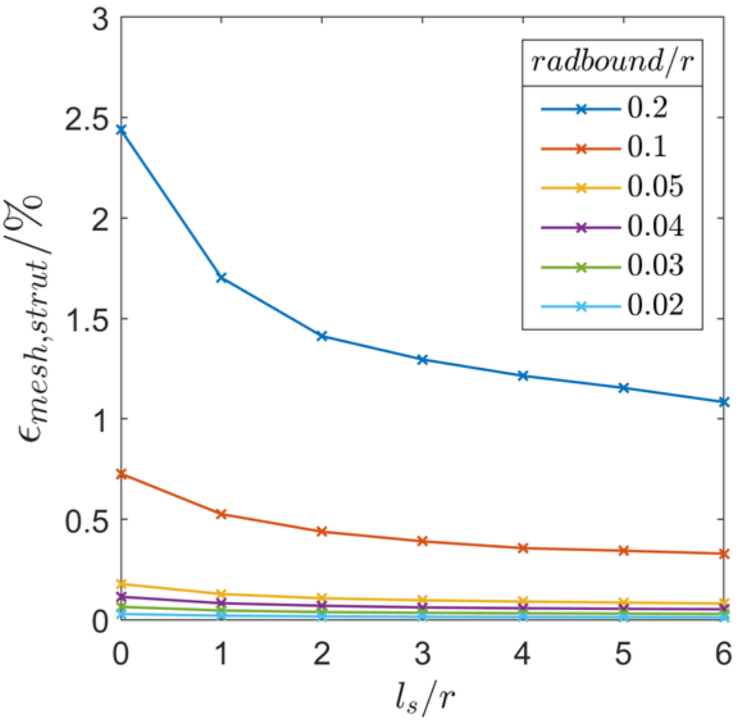

	l_s/r						
$radbound/r$	**0**	**1**	**2**	**3**	**4**	**5**	**6**
0.2	2.44	1.70	1.41	1.30	1.21	1.15	1.08
0.1	0.73	0.53	0.44	0.39	0.36	0.34	0.33
0.05	0.18	0.13	0.11	0.10	0.09	0.09	0.08
0.04	0.11	0.08	0.07	0.06	0.06	0.06	0.05
0.03	0.06	0.05	0.04	0.04	0.03	0.03	0.03
0.02	0.03	0.02	0.02	0.02	0.01	0.01	0.01

Figure 5.17. Relationship between the meshing error and the strut length, plotted at different values of $radbound$. Plot shows $\epsilon_{mesh,strut}$ vs l_s/r, plotted at different values for $radbound/r$.

5.4.3 Strut intersection

Figure 5.18, displays the relationship between $\epsilon_{mesh,int}$ and a/r and l_{int}/r, with fixed parameter $radbound/r = 0.05$. The first observation from Figure 5.18 is the general decrease in the error $\epsilon_{mesh,int}$ upon increasing a/r It must be noted that the error is very low for all plots; maximum error is approximately 0.17%. The decrease in error may again be due to the increased cylindrical section which is better preserved by the meshing function. Figure 5.18b shows that the initial increase in a/r appears to have negligible effect on the error for each l_{int}/r plot. The small fluctuations shown in Figure 5.18b may be due to the inherent variations in the meshing function (the meshing function does not produce identical geometries for constant input parameters). It can also be observed that decreasing l_{int}/r produces a systematic, small increase in the error. The consistent convergence which can be observed in Figure 5.18 implies that the meshing error becomes more stable as a/r increases, however, given the very low values of error it may also suggest that the entire plot is generally stable.

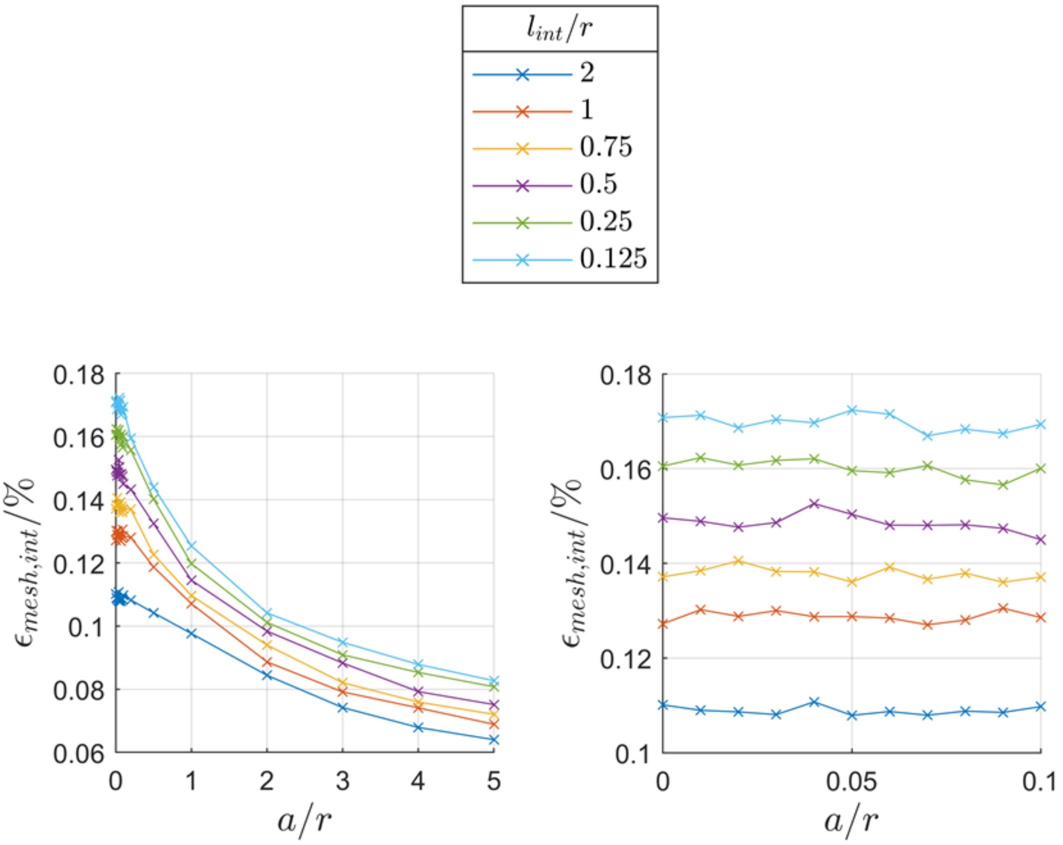

(a) (b)

Figure 5.18. Relationship between the meshing error and the displacement a applied to the strut intersection. Plot shows $\epsilon_{mesh,int}$ vs a/r, plotted at different values of l_{int}/r.

5.4.4 Radius deviation

Figure 5.19 shows how the meshing error $\epsilon_{mesh,rad}$ is affected by l_r/r and r_2/r. The behaviour in Figure 5.19 is unclear, with no obvious trend. Firstly, when $l_r/r > 0.5$, increasing r_2/r has negligible effect on the error. However, at $0.25 \leq l_r/r \leq 0.5$, increasing r_2/r causes the error to diverge. Lastly, at $l_r/r < 0.15$, r_2/r appears to again have negligible effect on the error. It is unclear what may be causing the meshing function to exhibit this behaviour. The unstable behaviour at $0.25 \leq l_r/r \leq 0.5$ requires further investigation. Overall, the error is still low, with a maximum error of approximately 0.3% found in the $l_r/r = 0.25$ plot at $r_2/r = 1.5$.

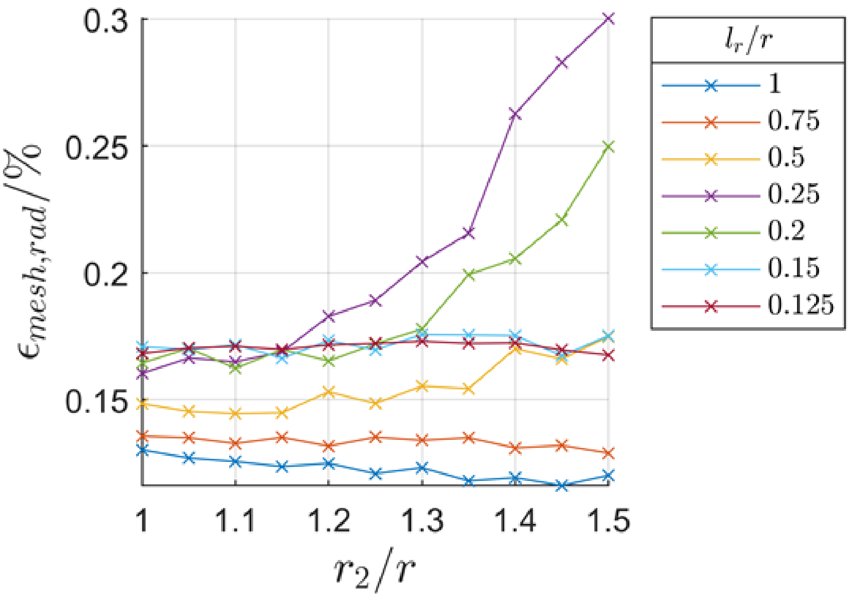

Figure 5.19. Relationship between the meshing error and the varied radius applied to the radius deviation Plot shows $\epsilon_{mesh,rad}$ vs r_2/r, plotted at different values for l_r/r.

5.4.5 Surface defects

To investigate the effect of surface defects on meshing error, two parameters of the displacement function—amplitude A/r and wavelengths λ_α/C—were varied and the meshing error ϵ'_{mesh} was calculated for each of the generated meshes. For simplicity, and ease-of-plotting, the wavelength λ_t in the t axis is kept constant and fixed at $\lambda_t/l = 1$.

Figure 5.20a shows the results for the mean μ of the error ϵ'_{mesh}. The general trend in Figure 5.20a shows the mean error μ to rise as the amplitude increases. At $A/r = 0$, where no surface defects are applied, the mean error μ is approximately 0.2%; as the wavelength λ_α/C reduces, the mean error increases at a higher rate. At maximum amplitude $A/r = 0.5$, the mean error at $\lambda_\alpha/C = 1$ increases to approximately 1%, however, the mean error increases to approximately 4.5% at low wavelength $\lambda_\alpha/C = 0.1$. This trend is intuitive, as increasing the amplitude and decreasing the wavelength of the displacement function creates increased distortion to the surface which will be harder for the meshing function to preserve.

Figure 5.20b shows the plot of the standard deviation σ of the error ϵ'_{mesh}, which is expressed as a percentage of the mean μ. Initially at $A/r = 0$, where no surface defects are applied, the standard deviation σ is approximately 46%. Between $0 \leq A/r \leq 0.1$, σ can be seen to rise sharply to approximately 75% for all λ_α/C. At $A/r > 0.1$, σ rises at a slower rate, to a maximum of approximately 90% for $\lambda_\alpha/C = 1$. The rapid increase in σ suggests that some specific points on the surface may possess large errors at $A/r > 0.1$.

Regarding stability, Figure 5.20a suggests that the meshing error is generally unstable in response to modifications via the surface defects function. Further analysis, in which the errors are not averaged, may be necessary.

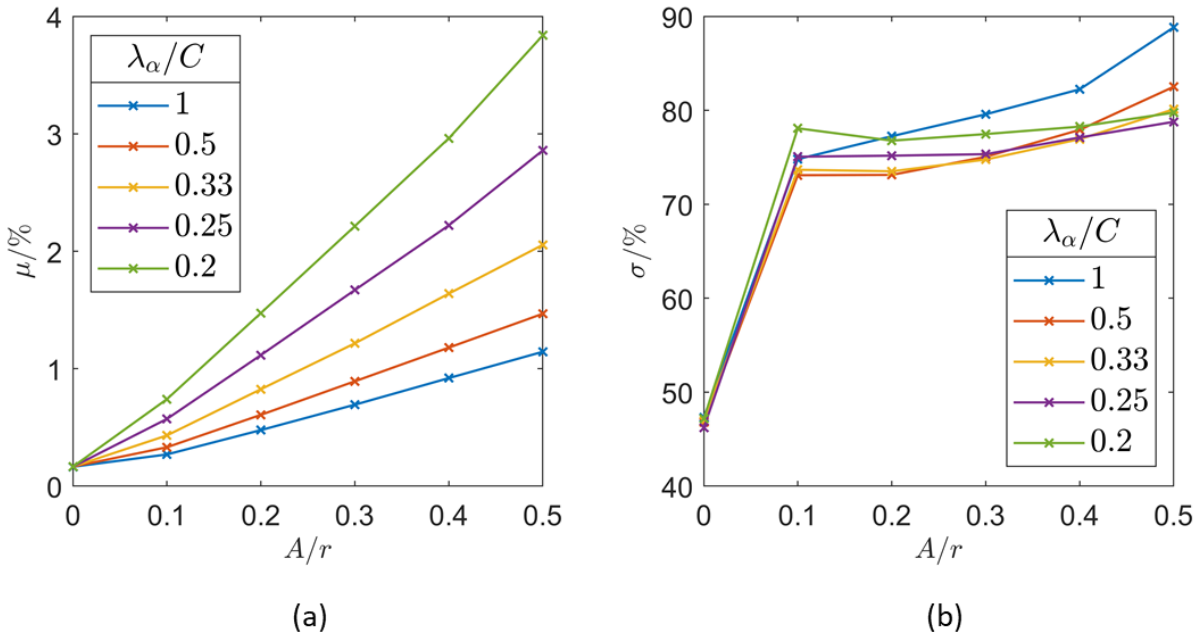

Figure 5.20. Relationship between the meshing error and the parameters of the surface defects function The plots show how the mean error μ and standard deviation σ are affected by varying the amplitude A/r and wavelength λ_α/C.

5.4.6 Key findings

This section provides a summary of the key findings from the sensitivity study of meshing error conducted in Sections 5.4.1-5.4.5:

- The sphere error $\epsilon_{mesh,sphere}$ is stable and converges to less than 1% at $radbound/r \leq 0.05$.
- The strut error $\epsilon_{mesh,strut}$ converges upon increasing l/r; it is very stable and is close to constant, for $radbound/r \leq 0.05$.
- The very low error values for $\epsilon_{mesh,int}$ could suggest that it is stable through all the tested values. However, the visual trend does show that $\epsilon_{mesh,int}$ initially decreases as a/r is increased, followed by converging.
- The relationship between $\epsilon_{mesh,rad}$ and l_{int}/r and r_2/r is unclear and presents no obvious trend.
- The mean μ of the meshing error ϵ'_{mesh} for surface defects increases systematically upon increasing A/r and λ_α/C
- The standard deviation σ of the meshing error ϵ'_{mesh} for surface defects behaves similarly for all wavelengths λ_α/C; an initial rapid increase in σ is followed by a relative plateau.
- The meshing error is generally unstable in response to modifications via the surface defects function

5.5 Study #3: Mesh quality sensitivity

The aim of this section is to investigate how the quality $\boldsymbol{q}$ of a mesh is affected by modifying the parameters which define all the geometries defined in Section 5.2.2. All of the meshes generated in the section are produced by an SDF with fixed resolution $dx/r = 0.125$ and are meshed with fixed surface element size $radbound/r = 0.05$. These fixed parameters have been shown to generate surfaces with stable SDF error and stable meshing error for spheres and struts.

An additional parameter is introduced, d, denoting the distance between an element's centroid and the medial axis of the geometry from which the mesh is generated. For a sphere or strut of radius r, d/r denotes the normalised distance between an element's centroid and the medial axis. Values of d/r near to unity indicate an element on the surface of the mesh; values of d/r near zero indicate an element very close to the medial axis. d/r is useful for identifying the location of elements within the mesh.

5.5.1 Sphere

For the sphere geometry, Figure 5.21 shows histograms of the mesh quality $\boldsymbol{q}$ for selected values of $maxvol/vol_r$, including the chosen minimum and maximum of $maxvol/vol_r = 0.05$ and $maxvol/vol_r = 0.2$ respectively.

Firstly, in Figure 5.21a, at $maxvol/vol_r = 0.2$, the histogram shows a low quality distribution of q values; the mesh mainly consists of surface elements of low quality – most elements have a quality value q near 0.2. As $maxvol/vol_r$ decreases, the histogram of mesh quality improves. At $maxvol/vol_r = 0.1$ (Figure 5.21b) the mesh still consists predominantly of surface elements, but the distribution of values has improved and most elements have a quality value q near 0.4. At $maxvol/vol_r = 0.05$ (Figure 5.21c) the distribution improves significantly; most elements have a quality value q near 0.7. Decreasing the $maxvol/vol_r$ beyond 0.05 was found not to change the histogram distribution; the mesh quality can be considered stable at $maxvol/vol_r \leq 0.05$.

The trend shown in Figure 5.21 is intuitive and is due to the relationship between $maxvol$ and $radbound$. Note that $radbound$ has been fixed at $radbound/r = 0.05$ and, therefore, the surface triangles of the surface elements are of relatively small size. At higher values of $maxvol$, the meshing function is permitted to generate meshes with elements of higher volumes, therefore, surface elements possess large discrepancies in their edge lengths, resulting in low quality. As $maxvol$ reduces, the volume of each element must be smaller, thus reducing the discrepancies between edge lengths. Naturally, decreasing $maxvol$ increases the total number of elements in a mesh.

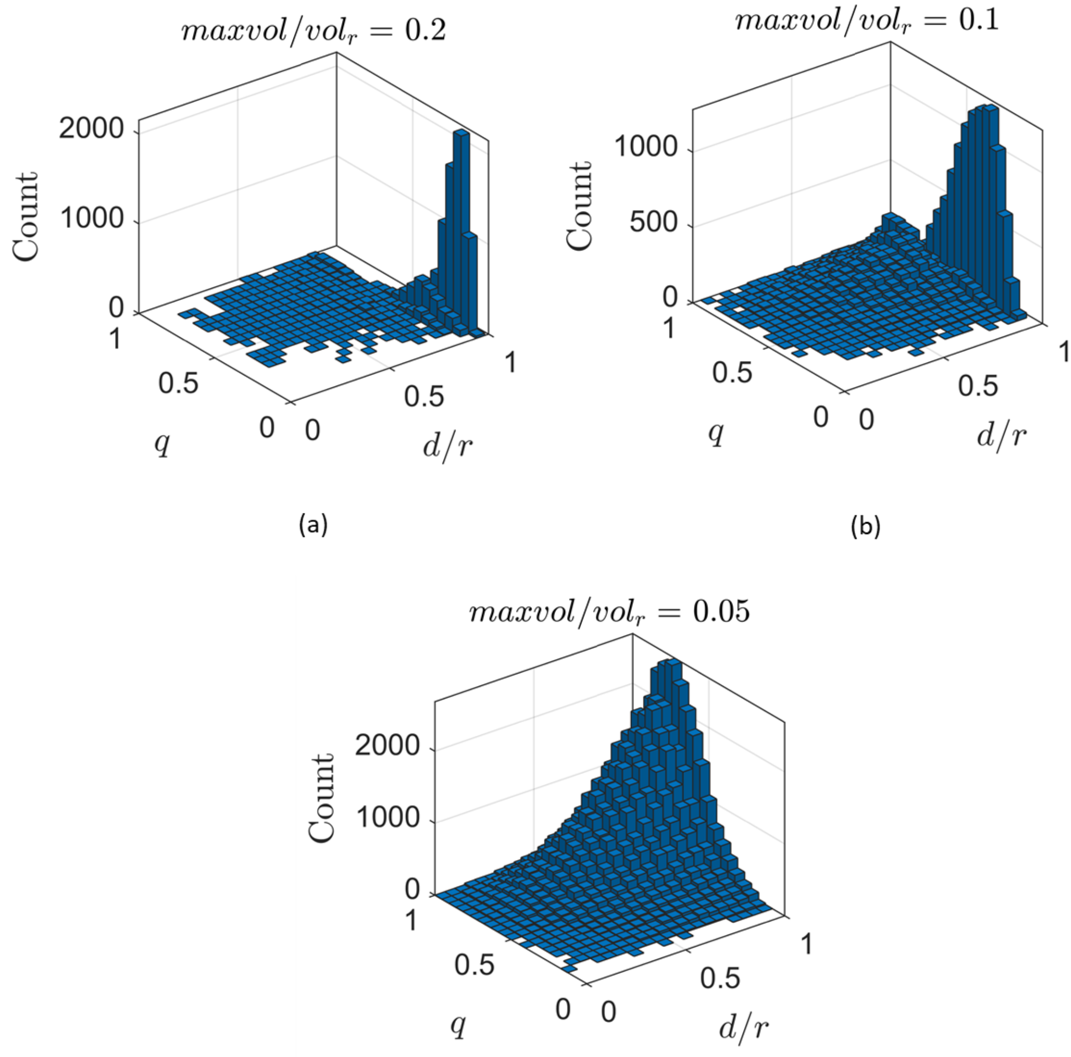

(a) (b)

(c)

Figure 5.21. Histogram showing how mesh quality is impacted by the parameter controlling element size , $maxvol$.

5.5.2 Strut

For the strut geometry, Figure 5.22 shows histograms of the mesh quality $\boldsymbol{q}$ for selected values of strut length l_s/r. Using the results from the previous section, $maxvol$ is now fixed at $maxvol/r = 0.05$.

As shown in Figure 5.22, modifying l_s/r is shown to produce no change to the distribution of quality values in the mesh; mesh quality is stable. Most elements have quality values near 0.7. This result is expected; increasing the strut length only increases the cylindrical section of the strut and does not present any geometrical change for the meshing function.

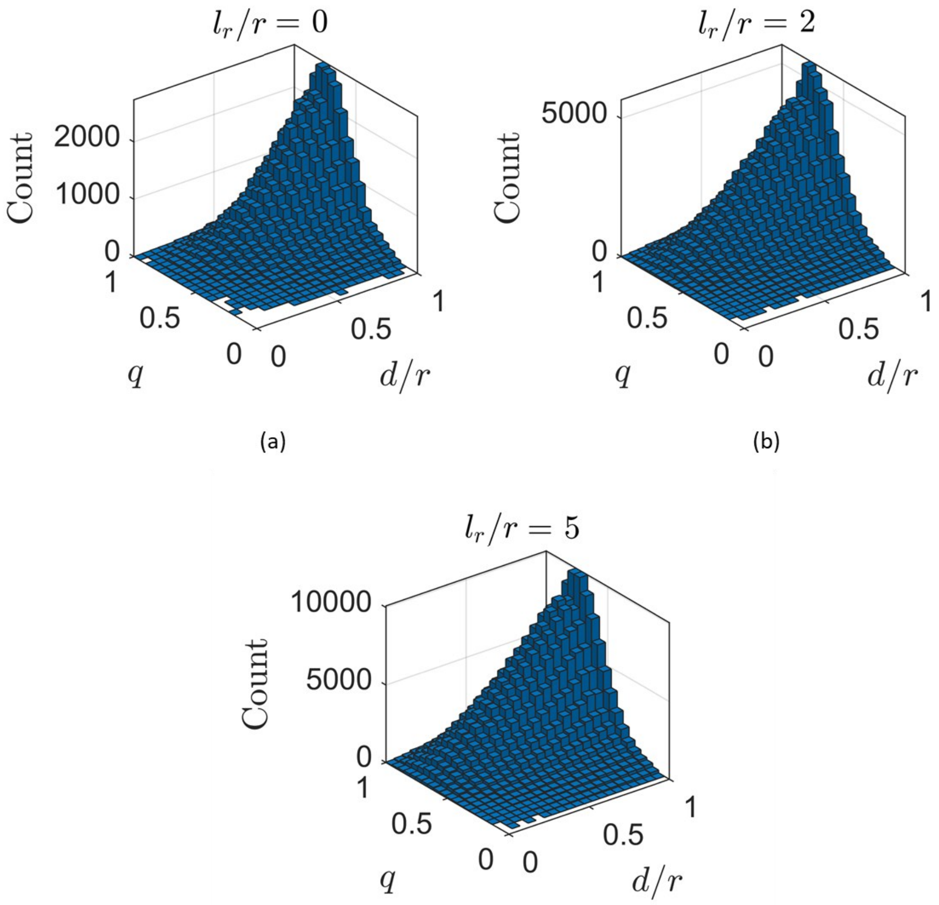

(a)

(b)

(c)

Figure 5.22. Histogram showing how mesh quality is impacted by strut length, l/r.

5.5.3 Strut intersection

To gain insight into the mesh quality for the strut intersection, a simplified study was performed in which the lengths of the line segments of the strut intersection were fixed, and only the intersection angle β was varied. A local analysis was employed, where mesh quality was only calculated for surface elements within a distance $0.2r$ of the strut intersection's plane of symmetry (as illustrated in Figure 5.23), where r is the strut radius. This local analysis is used because the actual points of intersection in a strut intersection only constitute a small area of its surface. The results in Figure 5.23 suggest that mesh quality is not impacted by strut intersection angle β, as the general distribution of the mesh quality does not change as β is varied; the mesh quality remains stable. Most elements are of high quality and near $q = 0.7$. One explanation for these results may be that the meshing algorithm prioritises mesh quality over mesh accuracy; mesh quality may be unchanged at low β because the meshes being produced have been modified in such a way as to maintain mesh quality, to the detriment of mesh accuracy.

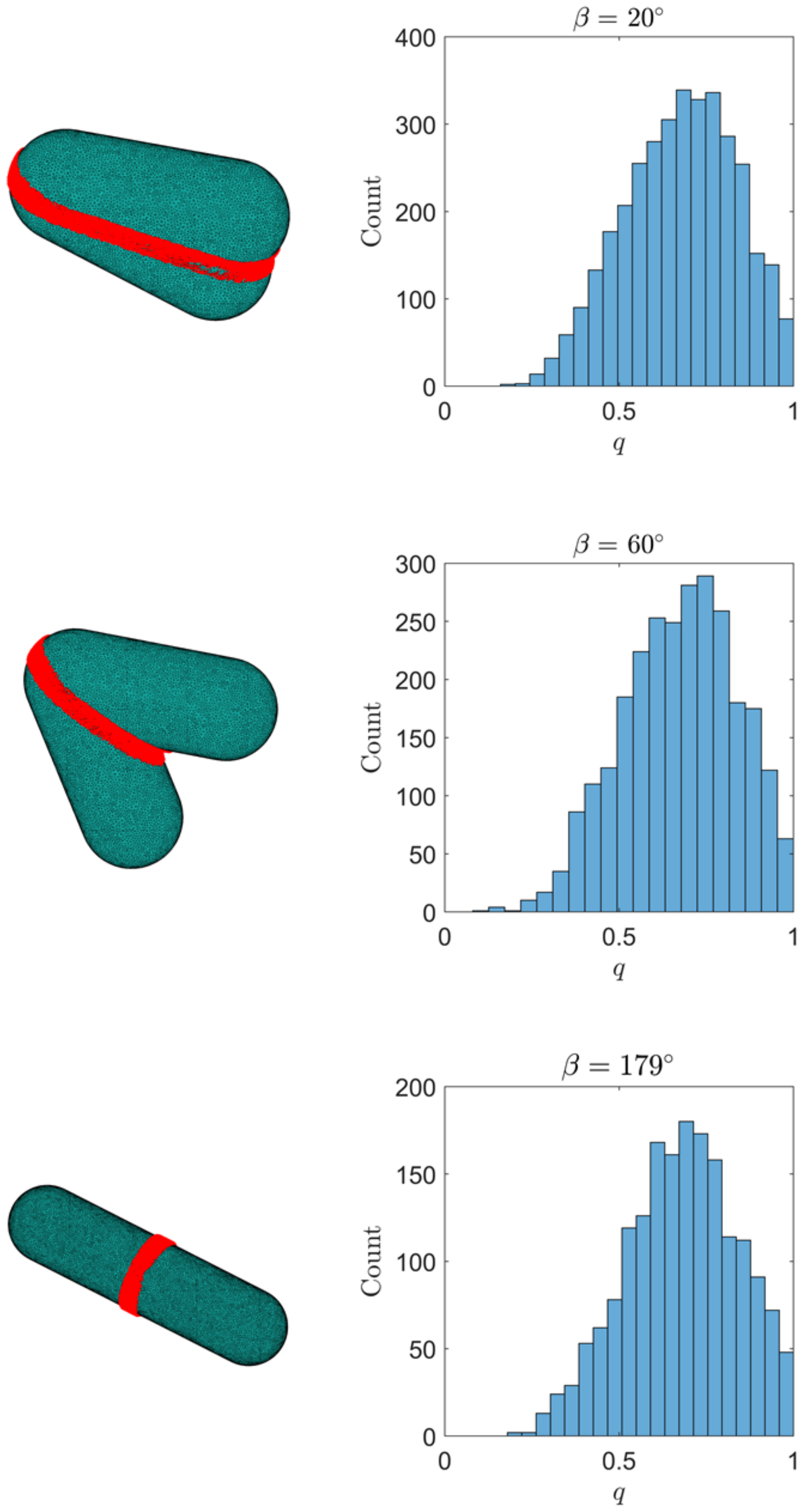

Figure 5.23. Histogram showing how mesh quality is impacted by intersection angle , β.

5.5.4 Radius deviation

Figure 5.24 shows how mesh quality for the radius deviation is affected by r_2/r. For simplicity, the length l_r of the radius deviation is fixed at $l_r/r = 0.5$. The results in Figure 5.24 show that, upon increasing r_2/r, an increase in body elements is observed, but there appears to be no change in the distribution of the quality. The quality of both surface and body elements is high, with most near $q = 0.7$. Mesh quality remains stable.

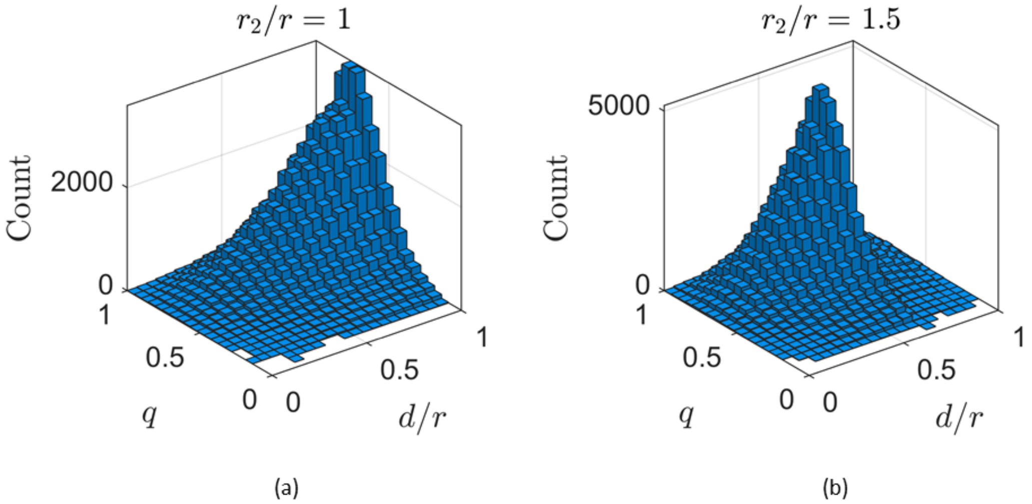

Figure 5.24. Histogram showing how mesh quality is impacted by the radius in the radius deviation , r_2/r.

5.5.5 Surface defects

To investigate the effect of surface defects on mesh quality, two parameters of the displacement function δ - amplitude A and wavelength λ_α – were varied and the mesh quality $\boldsymbol{q}$ was calculated for each of the generated meshes. As in Section 5.4.5, for simplicity, and ease-of-plotting, the wavelength λ_t in the t axis is kept constant and fixed at $\lambda_t/l = 1$. For each test, the quality values of each mesh were separated into body and surface elements and the mean μ and standard deviation σ of the mesh quality $\boldsymbol{q}$ of each group was calculated. σ is expressed as a percentage of the mean.

Figure 5.25 shows the results. For the body elements (Figure 5.25a-b), modifying the amplitude A/r and wavelength λ_α/C has no clear effect on the mean and standard deviation of the mesh quality. For all λ_α/C, as the amplitude is increasing, small fluctuations in the mean between approximately 0.67 and 0.68 are observed; the standard deviation fluctuates between approximately 23.5% and 25.0%.

For the surface elements (Figure 5.25c-d), modifying A/r and λ_α/C has a more significant effect. Initially, upon increasing the amplitude at high wavelength $\lambda_\alpha/C = 1$, a change to the mean quality of the surface elements is not clearly observed. However, as λ_α/C is decreased, the mean quality of the surface elements decreases as A/r is increased; the lowest mean quality of approximately 0.665 is observed at $\lambda_\alpha/C = 0.2$ and $A/r = 0.5$. The maximum change in mean quality of surface elements is observed at $\lambda_\alpha/C = 0.2$, where the mean quality changes from 0.6802 to 0.6641 upon increasing A/r from 0 to 0.5; this is a 2.4% change in mesh quality.

Similarly for the standard deviation, at high wavelengths, increasing the amplitude bears little effect. However, as λ_α/C is decreased, the standard deviation of the mesh quality of the surface elements also steadily increases; the maximum standard deviation of approximately 25% is observed at maximum amplitude $A/r = 0.5$ and minimum wavelength $\lambda_\alpha/C = 0.2$.

The maximum change in standard deviation of the quality of surface elements is observed at $\lambda_\alpha/C = 0.33$, where the mean quality changes from 22.75% to 24.40% upon increasing A/r from 0 to 0.5; this is a 6.7% change in standard deviation.

The results observed for body elements and surface elements in Figure 5.25 are intuitive. The body elements are not on the surface of the mesh, therefore, body elements are unaffected by changes to the displacement function and remain stable. The fluctuations in Figure 5.25a-b are likely due to the inherent variations in the meshing function. The reader is reminded that the meshing function generates meshes using an algorithm that iteratively modifies the mesh until a criteria (defined by functional input parameters) is satisfied. The meshes are not unique solutions and, therefore, slight variation can exist between meshes generated using the same criteria. Surface elements, however, are affected by variations in surface defects. Decreasing the wavelength λ_α/C and increasing the amplitude A/r increases the distortion being apply to the surface and thus requires smaller surface elements to maintain quality.

Since *radbound* is fixed in this study, a decrease in mesh quality of the surface elements is observed. The mesh quality of surface elements can be considered increasingly unstable as wavelength decreases and amplitude increases.

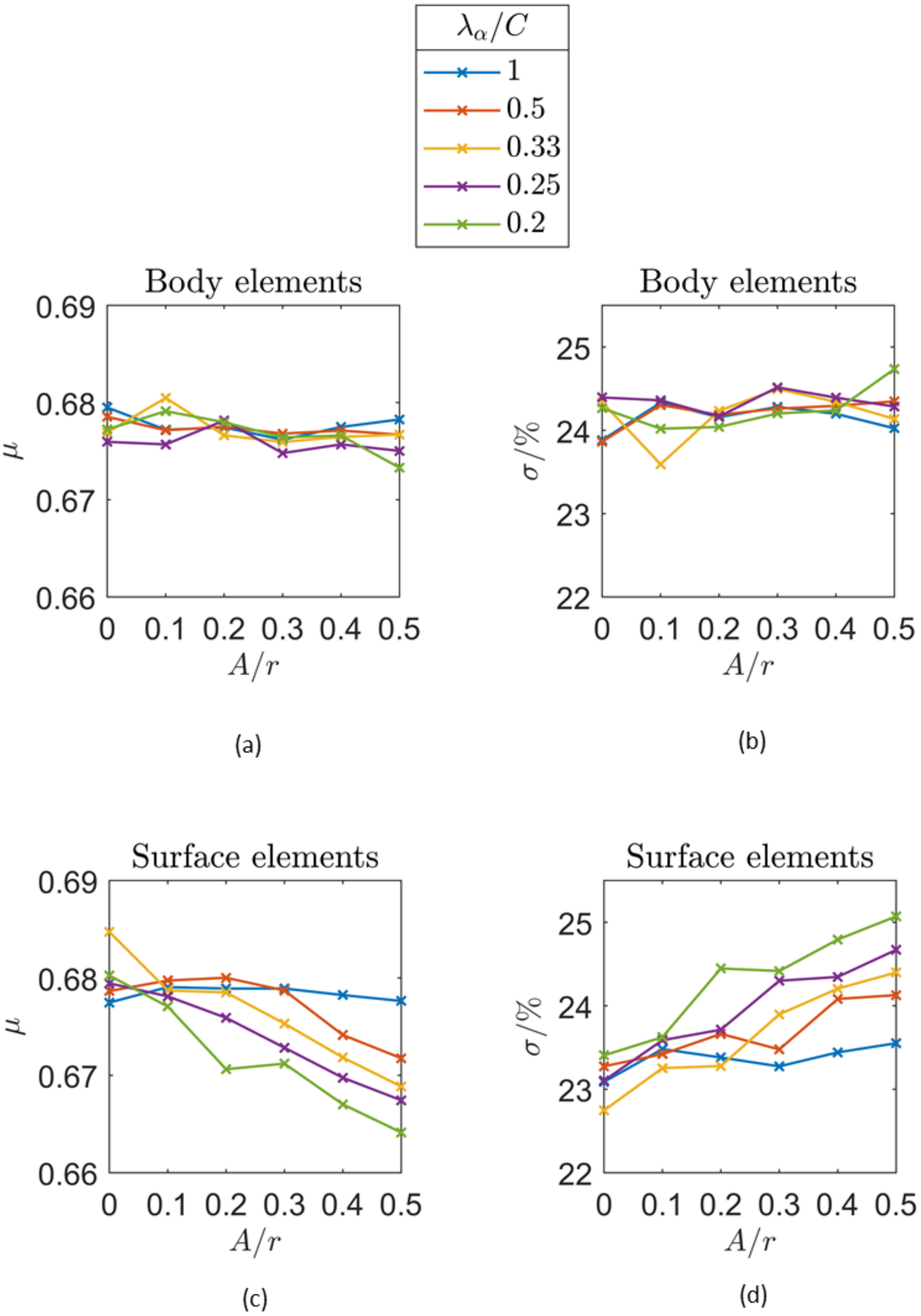

(a) (b)

(c) (d)

Figure 5.25. Influence of surface defects on the mesh quality of body and surface elements. Mean quality of body elements and surface elements shown in (a) and (c) respectively. Standard deviation of quality of body elements shown in (b) and (d) respectively.

5.5.6 Key findings

This section provides a summary of the key findings from the analysis of the impact of deviations on SDF error and meshing error, Sections 5.5.1-5.5.5.

- After optimising $radbound$ for reducing mesh error (Section 5.4), $maxvol$ can be optimised to improve mesh quality.
- For the sphere geometry, fixing the mesh parameters at $radbound/r = 0.05$ and $maxvol/vol_r \leq 0.05$ produces a high-quality mesh, with most mesh quality values approximately 0.7.
- Strut length l_s/r, strut intersection angle β, and radius deviation r_2/r appear to have no effect on mesh quality; mesh quality remains stable.
- Modifying the displacement function δ does not affect the mesh quality of body elements, they remain stable.
- The mesh quality of surface elements can be considered increasingly unstable as wavelength decreases and amplitude increases.

5.6 Discussion and conclusion

This chapter is important for understanding the limitations of the modelling approach and for selecting appropriate parameters which will produce stable outputs. The three selected outputs—SDF error, meshing error and mesh quality—enable the sensitivity study to cover the full scope of the modelling approach and thus all the model's inputs have been studied.

The SDF error study revealed key regions of stability for the function's parameters. For an ideal geometry, $dx/r \leq 0.125$ was observed to be a sufficient value for stability, producing converged errors less than 1%. However, in the case of modelling form deviations, where there are scenarios in which there are other dimensions shorter than the radius, the ranges $dx/l_{int} < 0.167$ and $dx/l_r \leq 0.5$ were found as suitable constraints. These values of dx highlight the significant computational load associated with this approach; significant amounts of memory may be required to produce stable geometries, if modelling small features. To potentially counteract the computational load, however, the values of dx which have been identified can also be used for creating a Cartesian grid of variable resolution which would increase computational efficiency.

The meshing error study provided mixed results. In some cases, the trends are intuitive. However, the behaviour of the strut intersection and radius deviation is unclear; ability to comment on this behaviour is hindered due to the limited information on the meshing function.

The studies in this chapter illustrate that some values for the input parameters may produce stable, converged error values in the meshes, but the error values themselves are not low. In such scenarios, the mesh remains undesirable for a different reason: the mesh is a poor representation of the 'real' geometry defined by its geometrical input parameters. In short, the error must be both low and stable in order to be suitable for further uses such as conversion to an STL before manufacturing, or FE analysis. The results of this chapter provide users of the proposed modelling approach a means of ensuring that the parameter selection meets theses constraints.

The mesh quality analysis revealed the relationship between $radbound$ and $maxvol$ with regards to the quality of surface and body elements. Mesh quality appears unaffected by strut, strut intersection and radius deviation geometries. For surface defects, a relationship between the displacement function δ and the quality of the surface elements was observed; body elements appeared unaffected. These results are useful for optimising mesh quality for FE analysis.

5.7 Summary

This chapter has performed a sensitivity study for the modelling approach proposed in Chapter 4. Firstly, all of the inputs and outputs of the modelling approach were listed. Next, three outputs—SDF error, meshing error and mesh quality—were defined which could be used to measure the model's sensitivity to its inputs. The input parameters were categorised as either functional input parameters and geometrical input parameters. For the geometrical input parameters, justification for their selected was provided, since a simplified set of parameters was used. Next, the results of three sensitivity studies—SDF error sensitivity, meshing error sensitivity and mesh quality sensitivity—were provided, identifying the regions of stability and the corresponding values of the input parameters.

Chapter 6 – Results: XCT, experiments, modelling and simulations

This chapter discusses the results of the X-ray computed tomography (XCT) measurement of lattice structures and the use of the XCT data to model lattice structures with geometric deviations. Section 6.1 shares the XCT results, Section 6.2 shows the compression test results and Section 6.3 shows the FEA.

6.1 XCT

6.1.1 Cross sectional analysis

Figure 6.1 and Figure 6.2 show histograms of the radius $\boldsymbol{R}_{ptcloud}$ and offset $\boldsymbol{O}_{ptcloud}$ vectors obtained from the cross sectional data of the vertical and inclined struts. Superscripts v and i have been used to refer to the vertical set and inclined sets respectively.

For the vertical struts, the histogram of the radius (Figure 6.1a), $\boldsymbol{R}_{ptcloud}^{v}$, shows that the most frequent radius value is approximately 0.49 mm, which indicates that the vertical struts are generally slightly undersized. The histogram of the offset of the vertical struts (Figure 6.1b), $\boldsymbol{O}_{ptcloud}^{v}$, shows a very small offset, the most frequent offset is approximately 0.01 mm.

For the inclined struts, the histogram of the radius (Figure 6.2a), $\boldsymbol{R}_{ptcloud}^{i}$, shows the most frequent radius value to be around 0.52 mm, implying that the radius of the inclined struts is generally oversized. The histogram of the offset of the inclined struts (Figure 6.2b), $\boldsymbol{O}_{ptcloud}^{i}$, shows the most frequent offset to be near 0.03 mm.

Comparing the radius histograms for the vertical and inclined struts, $\boldsymbol{R}_{ptcloud}^{v}$ (Figure 6.1a) displays multiple peaks, located on both sides of the nominal radius 0.5 mm, implying that the deviations in the radius of the vertical struts are not strongly biased towards oversizing or undersizing. In comparison, the histogram of $\boldsymbol{R}_{ptcloud}^{i}$ (Figure 6.2a) contains only one strong peak implying a strong bias of the inclined struts towards oversizing. The differences in the shapes of the plots in Figure 6.1 and Figure 6.2 may be because the 0° overhang angle in the vertical struts applies no bias to the deviations in radius, whereas the overhang angle in the inclined struts applies a bias towards oversizing, caused by overheating due to contact with supporting powder material.

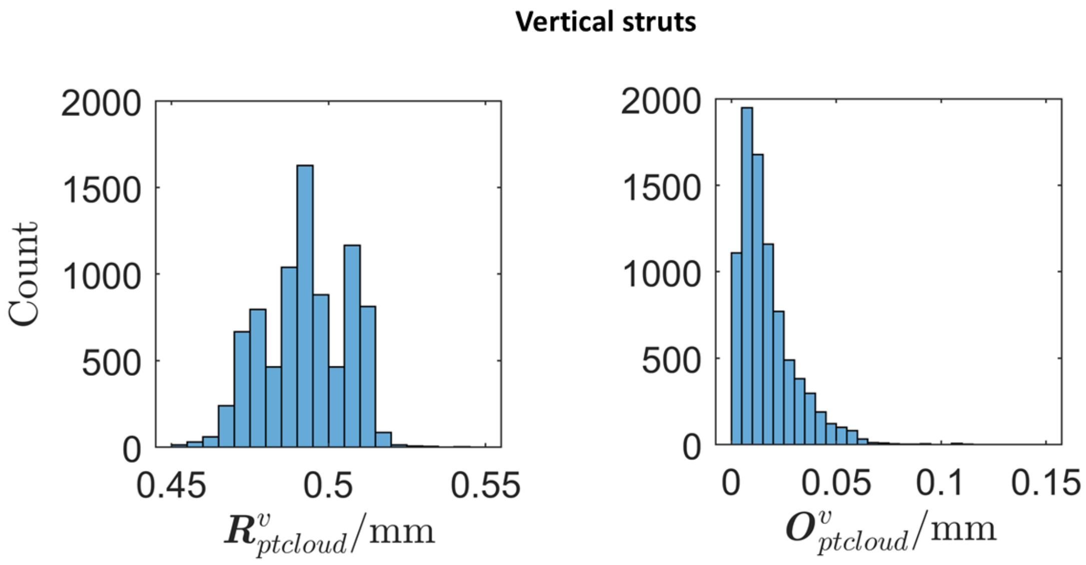

(a) (b)

Figure 6.1. XCT cross section results for the vertical struts. Histograms of the (a) radius of the cross sections of vertical struts (b) offset of the cross sections of vertical struts.

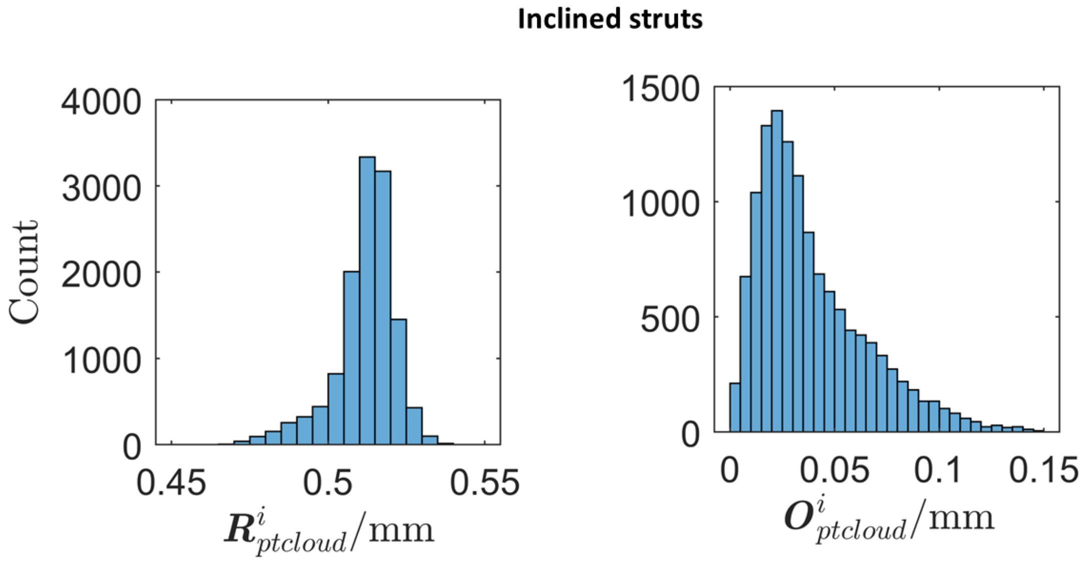

(a) (b)

Figure 6.2. XCT cross section results for the inclined struts. Histograms of the (a) radius of the cross sections of inclined struts (b) offset of the cross sections of inclined struts.

Comparing the offset histograms for the vertical and inclined struts, the distributions of $\boldsymbol{O}^{v}_{ptcloud}$ (Figure 6.1b) and $\boldsymbol{O}^{v}_{ptcloud}$ (Figure 6.2b) possess very similar shapes. The fact that these distributions are very similar may imply that, to some degree, the offset in vertical and inclined struts is caused by the same error source, a systematic error within the laser, for example. Additionally, the increased offset in the inclined struts implies that the error source produces stronger effects in inclined struts. There is a significant disparity between the location of the peak offset for the inclined and vertical struts, showing that the offset is generally greater in the inclined struts. Additionally, the increased offset in Figure 6.2b may be due to the aforementioned overheating effects of inclined struts.

6.1.2 Texture bias and surface unwrapping

Figure 6.3 shows plots of the average texture bias in the vertical and inclined struts, where the data was binned at α intervals of 1°. The texture bias plot for the vertical struts (Figure 6.3a) shows d to be a minimum of approximately 0.47 mm, at approximately $\alpha = 180°$. On either side of this minimum d value, $d \approx 0.5$ which corresponds to the nominal radius of 0.5 mm. The undersizing observered in Figure 6.3a corresponds to the undersizing observed in Figure 6.1. Although α typically is used to identify up-skin or down-skin surfaces, the vertical struts do not possess up-skin/down-skin surfaces, due to their overhang angle $\theta = 0°$. Therefore, the strong bias implied in Figure 6.3a must be revealing a different type of bias, which is not yet accounted for. Again, this bias may be related to a systematic error within the alignment of the laser beam.

The texture bias plots for the inclined struts (Figure 6.3b) consistently show a different trend, displaying a sinusoidal behaviour. When $\alpha < 180$, d is generally less than 0.5 mm, with a minimum observed at approximately 90°. When $\alpha > 180$, d is generally greater than 0.5 mm, with a maximum observed at approximately 270°. Given that the inclined struts do possess up-skin and down-skin surfaces (due to the overhang angle $\theta = 54.7°$), the results in Figure 6.3b clearly display undersizing and oversizing in the up-skin surfaces ($0° \leq \alpha \leq 180°$) and down-skin surfaces ($180° < \alpha < 360°$) respectively. The location of these minimum and maximum d values are found at approximately $\alpha = 90°$ and $\alpha = 270°$, which are the most up-skin and down-skin angles in the strut (as described in Section 4.2.3.4).

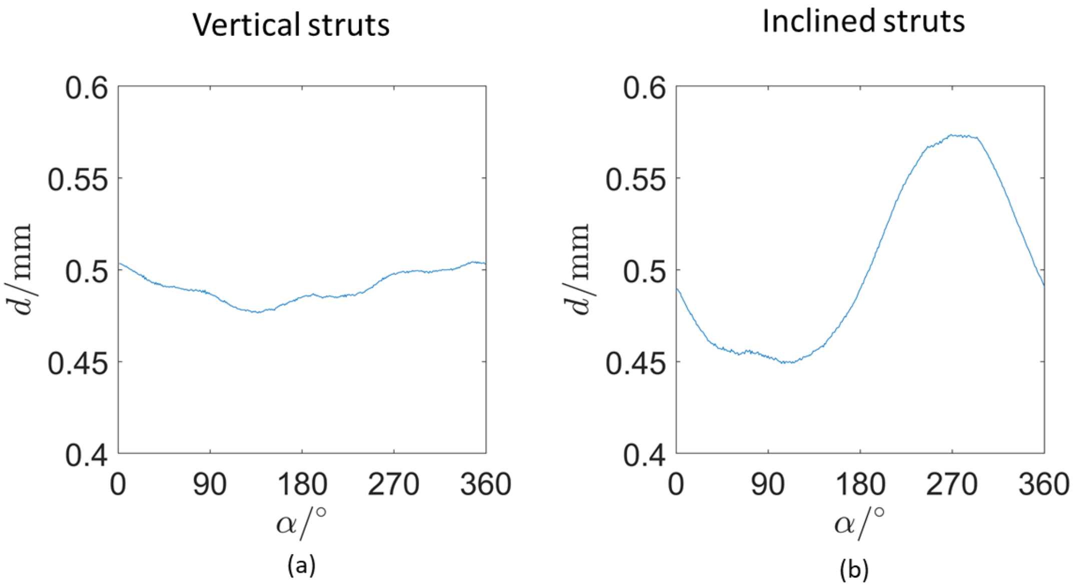

Figure 6.3. Plots of the average texture bias for vertical and inclined struts.

Figure 6.4 shows the results of the surface unwrapping, displaying the average of all unwrapped surfaces for the vertical and inclined struts. The data was binned at α intervals of 1° and t intervals of 0.01. The addition of the t axis shows the average distances d along the entire length of the struts. For the vertical struts (Figure 6.4a), again, slight undersizing can generally be observed throughout the plot near $\alpha = 180°$. However, for any value of t, the values d changes seemingly randomly. The randomness in the vertical struts is again likely due to the overhang angle $\theta = 0°$. In comparison, the inclined struts (Figure 6.4b) have a very strong trend which is consistent for all values of t; the most severe oversizing and undersizing is observed for at approximately $\alpha = 270°$ and $\alpha = 90°$ respectively.

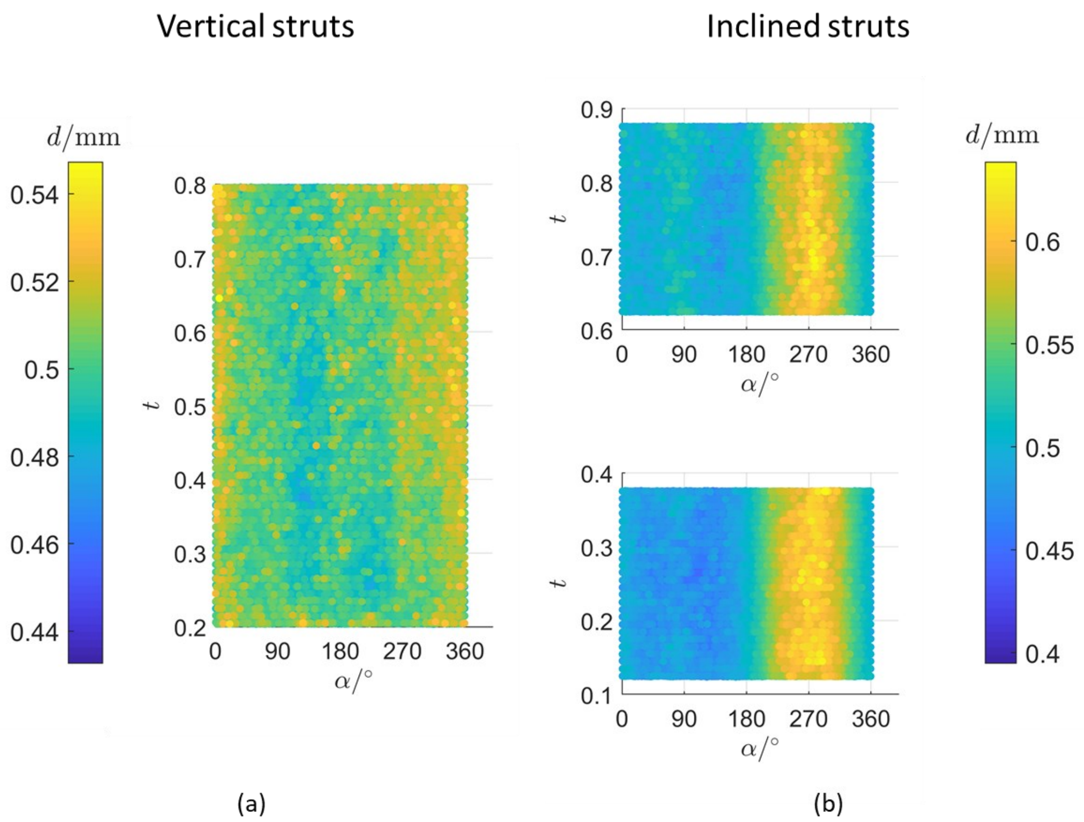

Figure 6.4. Results of the average unwrapped surface of the vertical and inclined struts (a) vertical struts, scale shown left (b) inclined struts, scale shown right.

6.1.3 Influence factors

As mentioned in Section 2.6.5, XCT measurements are potentially affected by a large number of influence factors. Referring to Table 3, an introductory consideration is given to the following influence factors: surface generation and measurement strategy.

To consider the effects of surface generation, Figure 6.5 shows average texture bias plots produced using different settings for point cloud generation in the XCT software, VG Studio MAX. The selected settings are named “fast”, “default” and “precise”, all of which take increasing amounts of time to generate point clouds from the data. The plots in Figure 6.5 also plot the standard deviation above and below the mean d in each 1° bin. These results are accompanied by Table 6 which shows the minimum and maximum d in each of the point clouds, notated as d_{min} and d_{max} respectively. Figure

6.5 shows a smoothing effect to occur between the "fast" and "precise" point cloud generation settings, most clearly observed in the plots of the standard deviations. Table 6 shows that as the settings are changed from "fast" through to "precise", d_{min} increases and d_{max} decreases, which may be caused by the removal of points being considered as erroneous. Comparing only the "fast" and "precise" results, for the vertical struts, d_{min} increases by 9.2% from 0.420 mm to 0.459 mm; d_{max} decreases by 5.7% from 0.558 mm to 0.526 mm. For the inclined struts, d_{min} increases by 11.3% from 0.380 mm to 0.423 mm; d_{max} decreases by 1.4% from 0.642 mm to 0.633 mm. Given the voxel size of 0.016 μm, the differences between the "fast" and "precise" methods more confidently suggest a significant, detectable change; comparisons to "default" are less significant and therefore less confident.

To consider the effects of an element of the measurement strategy, Figure 6.6 and Figure 6.7 show the results of the convergence analysis of the radius $\boldsymbol{R}_\mu$ and offset $\boldsymbol{O}_\mu$ data. The superscripts v and i are used to differentiate between the vertical and inclined struts respectively. For the vertical struts, the plot of cumulative mean of the radius data $\boldsymbol{R}_\mu^v$ (Figure 6.6a) implies convergence to $\boldsymbol{R}_\mu^v \approx 0.495$ mm after approximately 2000 slices, before which the plot is characterised by rapid fluctuations. The percentage change becomes negligible beyond slice numbers greater than approximately 1000. The cumulative mean of the offset data $\boldsymbol{O}_\mu^v$ (Figure 6.6b) shows $\boldsymbol{O}_\mu^v$ to converge near 0.017 mm after approximately 4000 slices

Figure 6.7a shows the convergence of the cumulative mean $\boldsymbol{R}_\mu^i$ of the radius of the inclined struts, suggesting convergence at approximately 2000 slices. Figure 6.7b shows the convergence of the cumulative mean of the offset of the inclined struts, $\boldsymbol{O}_\mu^i$, suggesting convergence at approximately 6000 slices, which is the largest amount of slices required for convergence from all plots in Figure 6.6 and Figure 6.7.

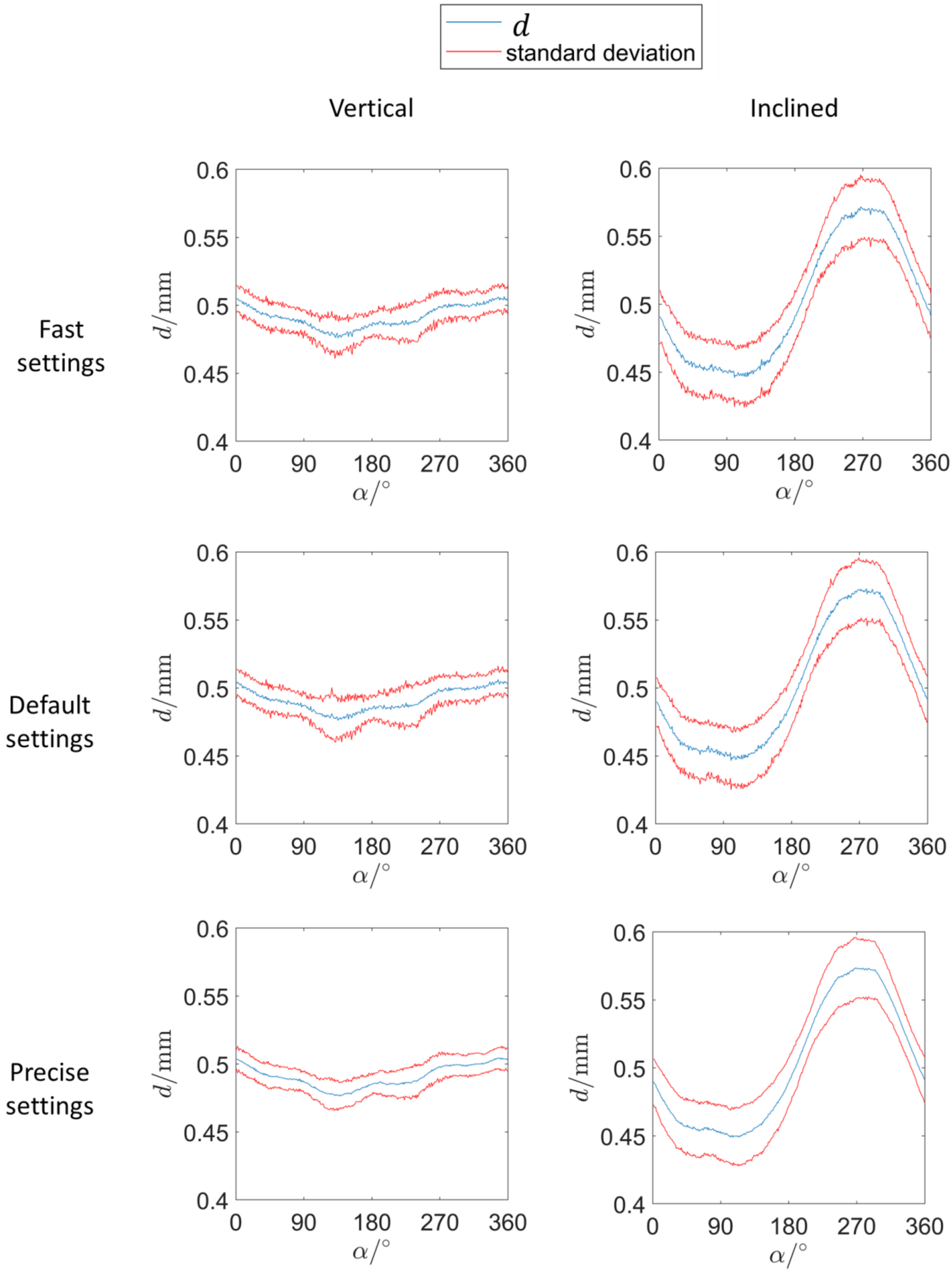

Figure 6.5. Texture bias plots using different settings for point cloud generation.

Table 6. Minimum and maximum distances d for different settings used for point cloud generation.

	Vertical struts			**Inclined struts**		
	d_{min} **(mm)**	d_{max} **(mm)**	**Range (mm)**	d_{min} **(mm)**	d_{max} **(mm)**	**Range (mm)**
Fast	0.420	0.558	0.138	0.380	0.642	0.262
Default	0.433	0.547	0.114	0.395	0.638	0.243
Precise	0.459	0.526	0.067	0.423	0.633	0.210

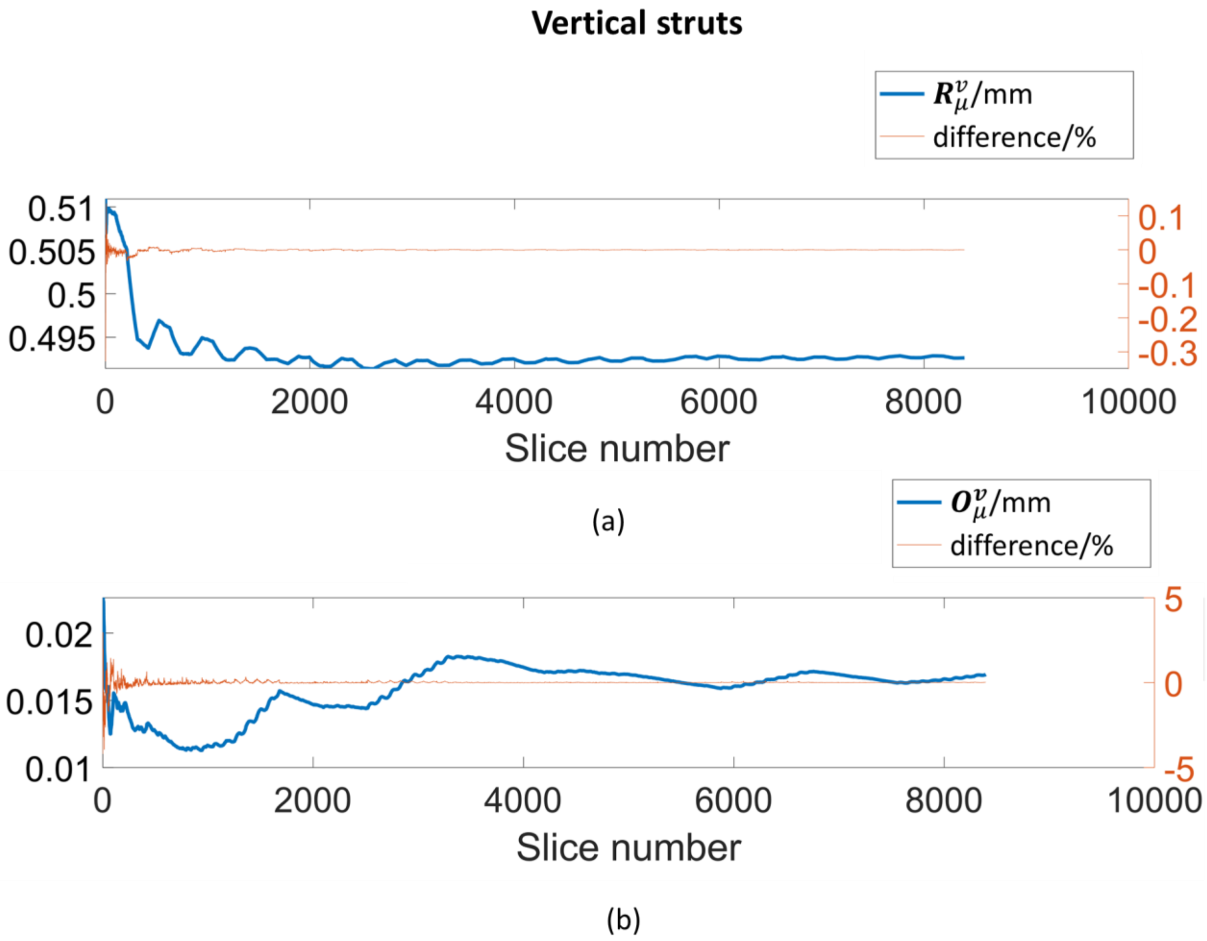

Figure 6.6. Convergence analysis for the vertical struts. (a) Convergence of the cumulative average of the radius $\boldsymbol{R}_\mu^v$ of the cross sections. (b) Convergence of the cumulative average of the offset $\boldsymbol{O}_\mu^v$ of the cross sections.

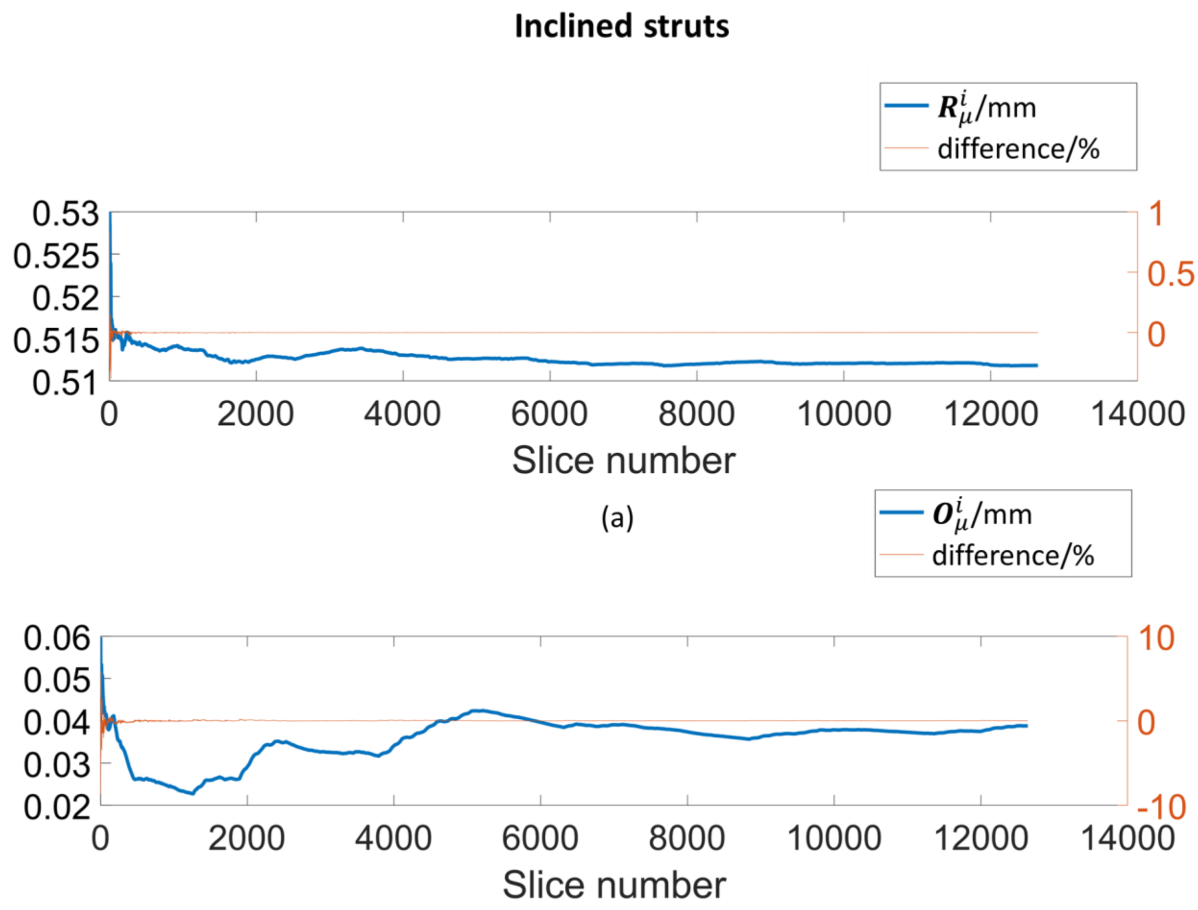

(a)

(b)

Figure 6.7. Convergence analysis for the inclined struts. (a) Convergence of the cumulative average of the radius $\boldsymbol{R}^i_\mu$ of the cross sections. (b) Convergence of the cumulative average of the offset of the cross sections $\boldsymbol{O}^i_\mu$.

6.2 Compression testing

Figure 6.8 shows a plot of the average stress-strain data from the five compression tests of the lattice samples, accompanied by images of the samples during different stages of the test. Figure 6.9 to Figure 6.13 show the individual results from the five compression tests.

The averaged results show an elastic response approximately for strain values ≤ 0.05. From this elastic region, the Young's modulus was calculated as 984.1 MPa. At near 0.05 strain, the struts begin to fail at peak stress of approximately 30 MPa. Figure 6.8c shows the initial buckling in the struts, this is followed by rapid decrease in stress due to failure by buckling in the first layer of unit cells in the lattice (Figure 6.8d). A local peak in stress is observed at 0.15 strain, which is likely due a random configuration of the failed struts temporarily becoming more load-bearing. At 0.25 strain, the stress begins to rise significantly, indicating that full failure has occurred in the first layer and the remaining layers have become load-bearing again.

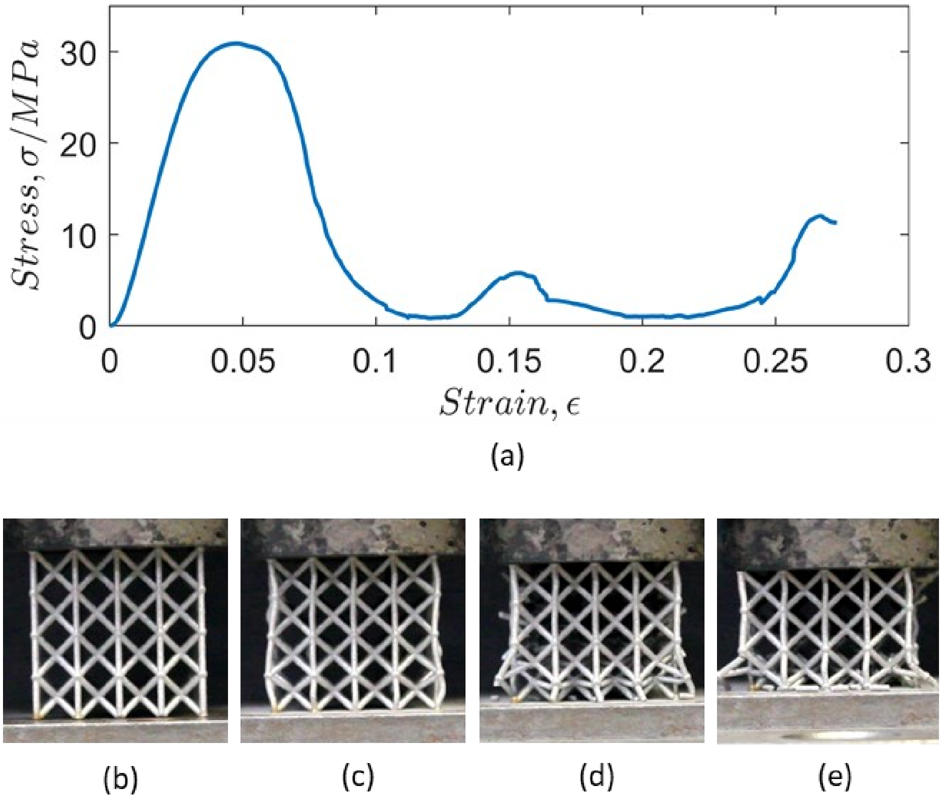

(a)

(b) (c) (d) (e)

Figure 6.8. Average results from the compression tests. (a) Average stress strain results of lattice samples (b)-(e) images of compressive failure developing in the samples.

The following graphs show the data for each of the individual compression tests.

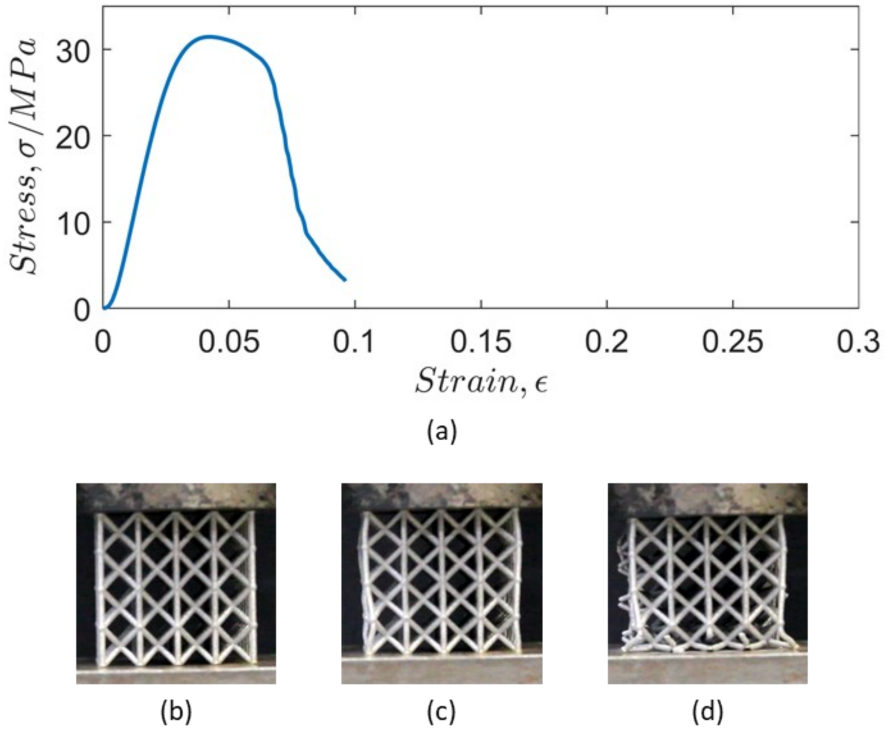

(a)

(b) (c) (d)

Figure 6.9. Compression test results of sample 1.

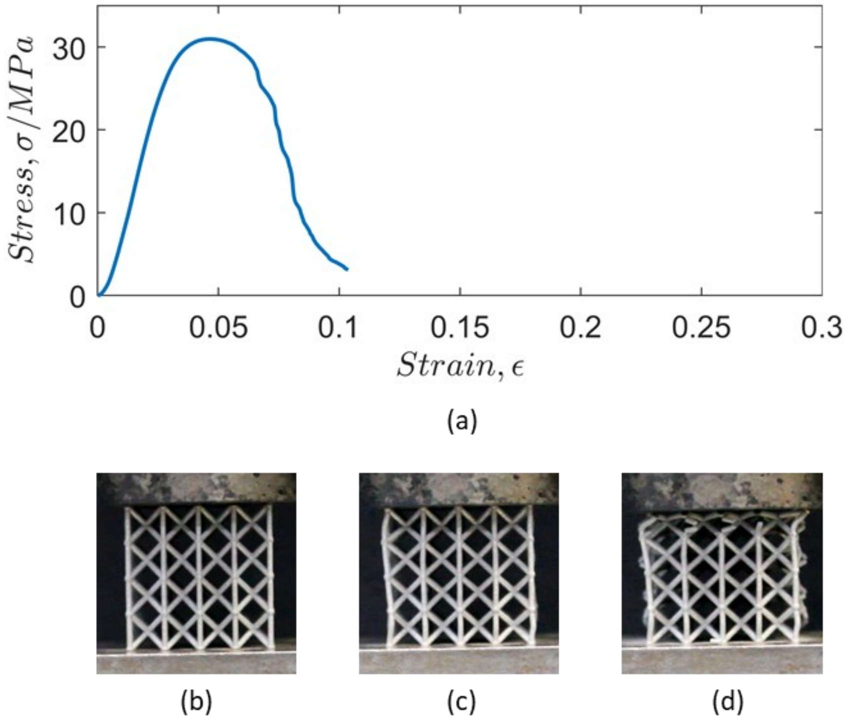

(a)

(b) (c) (d)

Figure 6.10. Compression test results of sample 2.

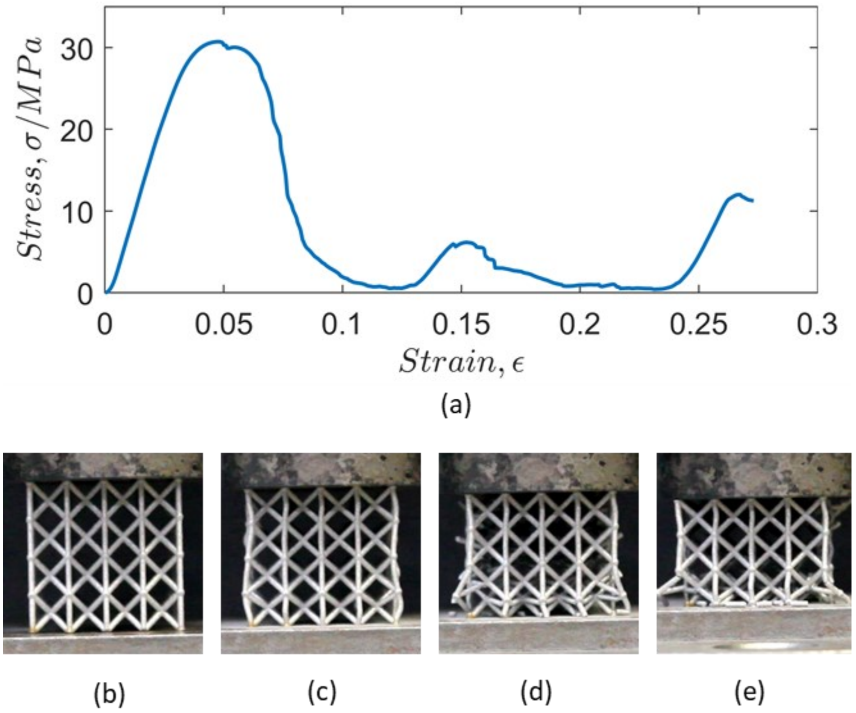

Figure 6.11. Compression test results of sample 3.

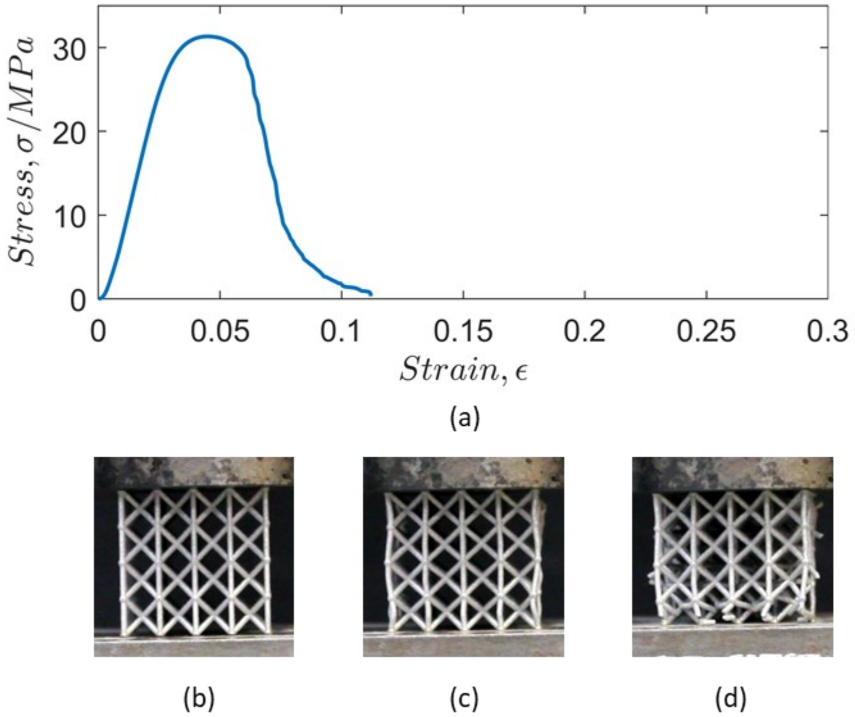

Figure 6.12. Compression test results of sample 4.

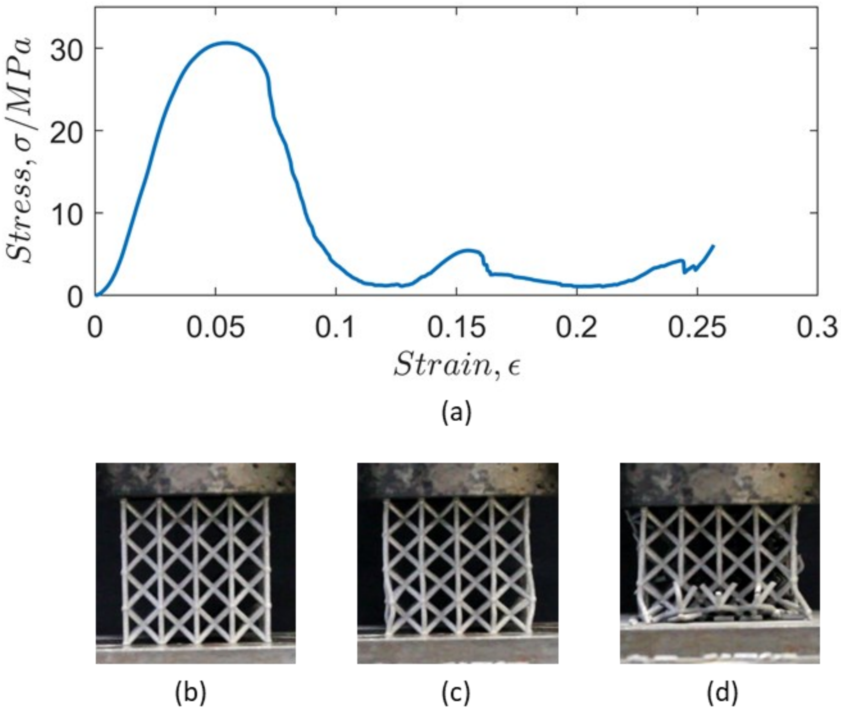

Figure 6.13. Compression test results of sample 5.

6.3 FEA

6.3.1 Modelling of geometric deviations

The probability density functions fitted to the cross sectional data in Section 6.1 (using a Kernel density estimation) were used to generate simulated cross sectional data for the radius and offset of vertical and inclined struts, as shown in Figure 6.14, where each histogram contains 50 000 values. The similarity between the XCT cross section data (Figure 6.1 and Figure 6.2) and the histograms in Figure 6.14 demonstrate the suitability of Kernel density estimations for fitting probability density functions to the XCT data.

The histograms in Figure 6.14 show the maximum offset and radius values to be 0.15 mm and 0.54 mm respectively. These maximum values can be related to the parameters a and r_2 to help understand how the signed distance function (SDF) can be configured for modelling deviations using the data shown in Figure 6.14. The reader is reminded of the parameters a/r and r_2/r which define the strut intersection and radius deviation, which are part of the simplified set of geometrical input parameters in Section 5.2.2, used for waviness and radius variation respectively. The lattice structures in this study have a radius $r = 0.5$ mm, therefore $a/r = 0.15/0.5 = 0.3$ and $r_2/r = 0.54/0.5 = 1.08$. From Figure 5.14, $a/r = 0.3$ can be stably generated if $dx/l_{int} \leq 0.25$.; from Figure 5.15, $r_2/r = 1.06$ can be stably generated if $dx/l_r \leq 0.5$. Therefore, dx/l_{int} is the more constraining parameter for the SDF, given that dx/l_{int} must be lower than dx/l_r.

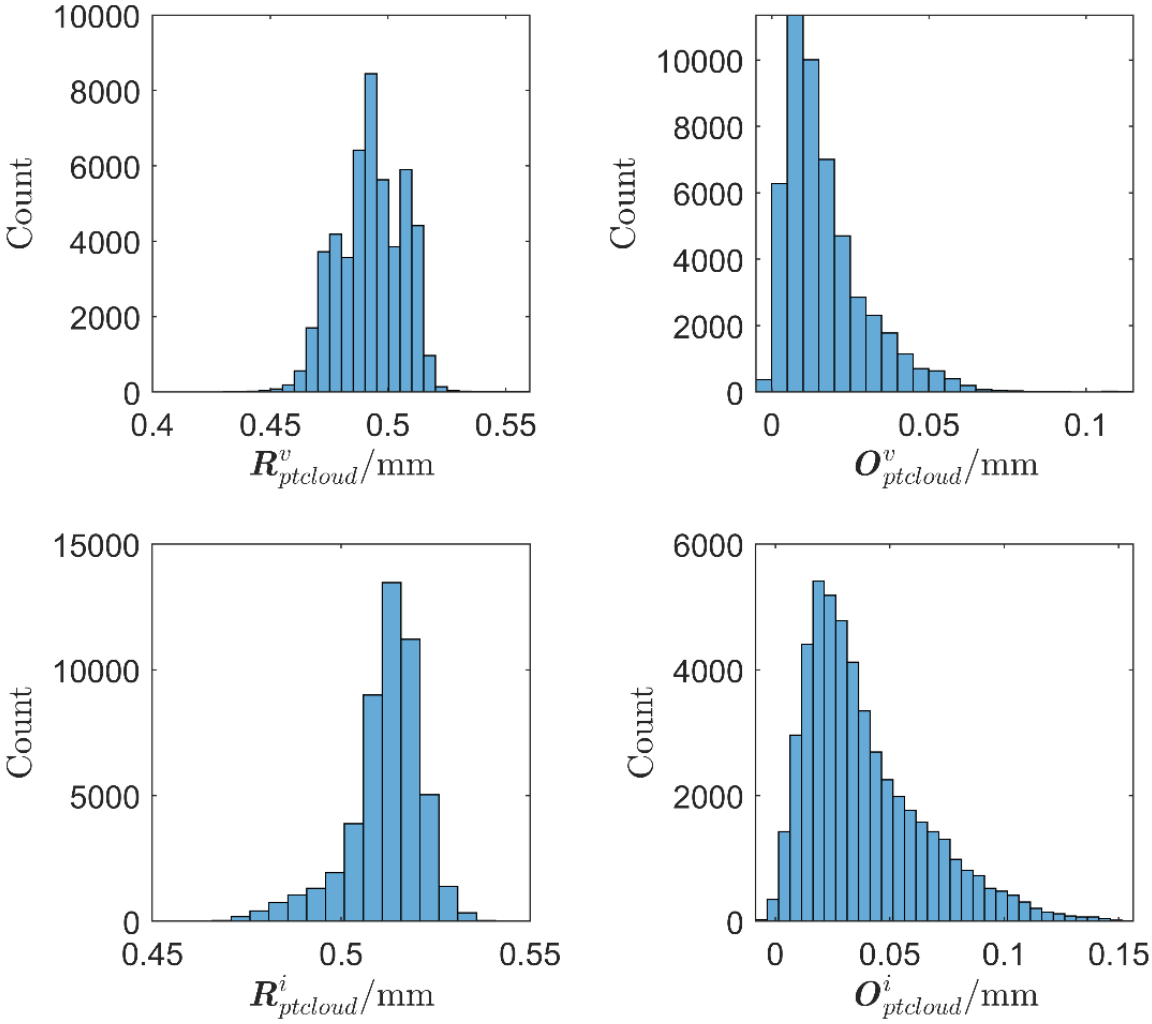

Figure 6.14 Simulated cross sectional data for the radius and offset of vertical and inclined struts, using probability density functions fitted to the XCT data.

Figure 6.15 shows examples of surfaces generated by the SDF, where waviness and radius variation deviations have been applied using the probability density functions fitted to the XCT data. Since the SDF was computed with resolution $dx/r =$

0.0625 mm, the constraint $dx/l_{int} \leq 0.25$ (defined in the previous paragraph) corresponds to $l_{int} \geq 0.0625/0.25 = 0.25$ mm. As described in Eq. (5.20), l_{int} is analogous to the distance l' between any two points in the medial axis which are separated by a single point, therefore, the length of a single line segment is given by $l'/2$ and is subject to the constraint $l'/2 \geq 0.125$ mm. Figure 6.15 also shows the effect of increasing the number of line segments in the underlying medial axis of each strut, thus decreasing line segment length $l'/2$.

Table 7 shows the results of the FE simulations. Two simulations were performed, firstly a lattice without deviations, followed by a lattice with both radius variation and waviness. For the lattice with deviations, the line segment length was defined as $l'/2 = 0.7$ which complies to the constraint in the above paragraph, as well as being high enough to perform stably when applying waviness deviations (see § 5.3.3). The results in Table 7 show that the inclusion of the geometric deviations resulted in a reduction in the stiffness of the lattice, however, both results have significantly overestimated the stiffness, in comparison to the experimentally determined value of 948.1 MPa (see § 6.2). This overestimation may be due to the values of Young's modulus and Poisson's ratio used in the material model for the simulations; these values were not obtained via tensile tests of specimens manufactured from the same powder supply as used for the lattice structures.

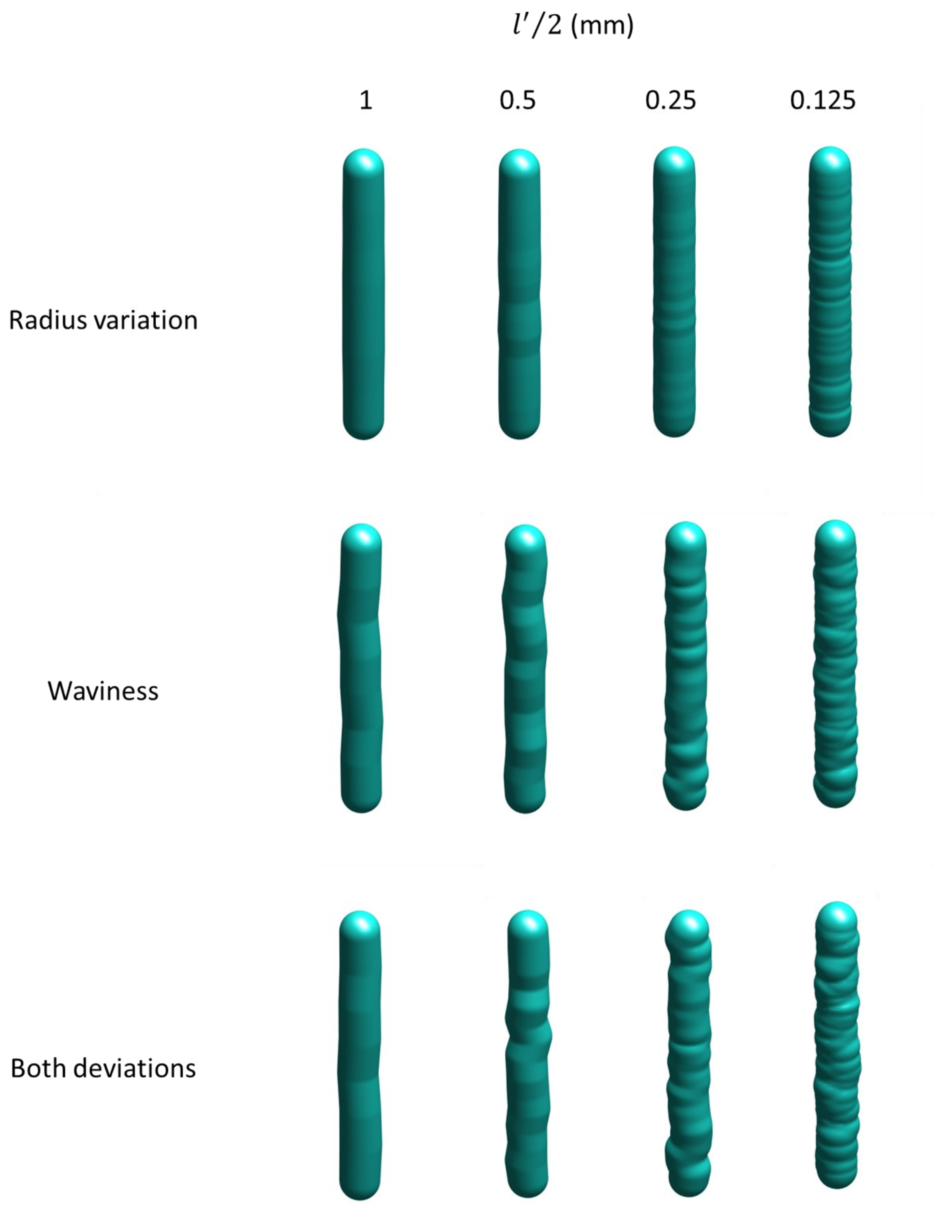
$l'/2$ (mm)
1
0.5
0.25
0.125
Radius variation
Waviness
Both deviations

Figure 6.15. Example struts generated with deviations defined from probability density function fitted to XCT cross sectional data.

Table 7 FEA results.

	Young's Modulus (MPa)
Ideal lattice	4148
Lattice with radius variation and waviness	4023

6.4 Conclusion

This chapter has displayed the results of this thesis, namely XCT measurements, compression testing and FEA.

The XCT results showed the inclined struts to be significantly more prone to geometric deviations; radius variation, waviness and texture bias all showed greater deviations in the inclined struts. The consistency between the results obtained from each measurement approach, and their agreement to trends in the literature, confirms the suitability of each technique. As for the investigation in the effects of the settings for point cloud generation, using 'precise' settings does appear to remove noise from the results, however, this may not be significant for this application because the noise is of very high spatial frequency.

The FEA results suggest that the inclusion of geometric deviations will decrease lattice stiffness. Further simulations should be performed wherein the PDFs are resampled in order to generate new sets of geometric deviation data. This is important since the PDFs must be sampled many times before they become representative of the XCT data on which they're defined.

Chapter 7 – Discussions, conclusions and future work

This chapter provides a summary of the work presented in the thesis, providing a critical discussion of each chapter and concluding with considerations for future work.

7.1 Thesis summary

The following paragraphs summarise the content within all previous chapters of the thesis.

Chapter 1 introduced the motivations for this work, namely that lattice structures are an incredibly versatile design with features which can encourage the formation of defects and geometric deviations. The application of lattice structures for vibration isolation was also explained, which is the context in which this thesis' aim and objectives were defined. As a reminder, the objectives of the thesis were as follows:

1. Develop an approach for modelling lattice structure defects/geometric deviations and performing simulations via finite element (FE) modelling.
2. Perform a sensitivity study on the developed modelling approach to define limits on its underlying parameters.
3. Use X-ray computed tomography (XCT) to quantify manufacturing defects/geometric deviations in lattice structures and extract defect parameters which can be applied to the FE model.
4. Perform mechanical testing and validate the developed model using the experimental data.

Chapter 2 reviewed the relevant literature, demonstrating significant popularity of lattice structures and additive manufacturing (AM), the range of observed defects and geometric deviations which can form, and the measurement and modelling tools used to examine their impact. X-ray computed tomography (XCT) was identified as the most used measurement technique for imaging lattice structures. FE modelling is the most used modelling approach for lattice structures, modelling with either beam elements of tetrahedral elements. Reviewing the literature helped identify the need for exploring versatile modelling approaches which are suitable not only to the modelling of defects and geometric deviations, but also suitable for modelling highly configurable lattice structure designs.

Chapter 3 explained the methodology designed for meeting the thesis' objectives. The foundation of the work is a signed distance function (SDF) based modelling approach, from which triangulated surfaces of lattice structures can be converted into tetrahedral meshes. In addition to the modelling, XCT is used for capturing geometric deviation data from a BCCZ lattice, which is then imported back into the model, for comparison between experimentally determined and simulated lattice stiffness.

Chapter 4 explained the SDF-based modelling approach in detail. An intuitive set of mathematical functions were defined for creating surface meshes of strut-based lattice structures with the inclusion of geometric deviations and surface defects. Signed distance functions (SDFs) were used to first model ideal lattice struts before being extended to apply geometric deviations via modification of the medial axis and/or distance calculation. Surface defects were applied by defining a displacement function δ which modified the surface produced by the SDF. The surface meshes were then converted into tetrahedral meshes via open-source MATLAB toolbox, iso2mesh.

Chapter 5, performed a sensitivity study of the SDF-based modelling approach. Three quantities were defined for the assessment of the model's stability, namely SDF error, meshing error and mesh quality. A simplified, finite set of parameters were defined for use in each analysis method, this set was considered representative of the lattice geometries. Intuitive relationships between the resolution of the domain and the model's stability were demonstrated. Additionally, regions of stability for the geometrical input parameters were identified; these regions are less intuitive. This chapter was crucial for determining a method for identifying modelling parameters which can be proven to produce stable outputs, and these results were used for subsequent simulations.

Chapter 6 displayed results of the XCT measurement, compression testing, FE modelling and simulation. The XCT measurement results showed clear differences between the geometric deviations and texture bias in the vertical and inclined struts. In the cross section analysis, the radius of the vertical struts showed no strong bias towards oversizing or undersizing, conversely, the radius of the inclined struts showed a strong bias towards oversizing. Similarly, the offset of the cross sections of the vertical struts was significantly less severe than the inclined struts. The texture bias and surface unwrapping results were useful for gaining additional insight on the vertical and inclined struts, revealing that a consistent area of the surface of vertical struts was undersized, potentially indicating a systematic error which may be related to laser misalignment. Additionally, for the inclined struts, the texture bias analysis and surface analysis showed significant oversizing and undersizing in the down-skin and up-skin areas, respectively.

Chapter 6 also contained introductory considerations to the effect of influence factors on the measurement data. Convergence analysis was used to increase confidence on the minimum number of slices which can be considered representative of the full XCT dataset. The effects of point cloud conversion settings were quantified. Lastly, probability density functions (PDFs) were fitted to the extracted XCT data and used to generate models with statistically similar defects. The fitting of PDFs to the measurement data proved effective for generating surfaces of lattice struts with defects.

Lastly, Chapter 6 also compared the experimentally determined lattice structure stiffness to FEA results based on lattice structures with geometric deviations applied using PDFs. The cross sectional data from the XCT measurement was well replicated by the PDFs, allowing for the modelling of lattice struts with statistically equivalent form defects. Each of the compression tests behaved similarly, with failure occurring by the buckling of the vertically reinforcing struts, an intuitive result. However, comparing the experimentally determined lattice structure stiffness to the FE calculations showed a current significant disparity between the FE model and the experimental data. As previously mentioned, a significant improvement may be found by updating the material model with properties obtained via mechanical testing of specimens manufactured from the same powder material. However, this is outside of the time and resource constraints of this work.

7.2 Discussion

For the proposed modelling approach, it must be stated that, although the approach is very geometrically versatile, the approach is also very computationally expensive (as expected and discussed in Chapter 2 as well as elsewhere). As lattice tessellation increases, it becomes harder to find the resources for the modelling and simulations. The use of tetrahedral elements could perhaps be better suited for more localised analysis, the results of which could be transferred into a larger model using beam elements, for example.

Regarding implementation of the SDF-based modelling approach, attempts were made to optimise functions, only when necessary for achieving more practical computation times. Therefore, there are still computational limitations to the SDF implemented in its current form. The SDF operates in a domain of equally spaced points (using the MATLAB function, meshgrid.m), therefore, increasing the resolution results in an exponential increase in the number of points in the domain. More specifically, the total number of points in a three-dimensional Cartesian grid is given by n^3, where n is the number of points in any dimension. To mitigate memory limitations – and reduce the number of points in the distance field –, the distance field could be optimised using an adaptive grid in which the high resolution is only located near the interface in which the level set is location. An example of such an optimisation is the Octree structure, which can recursively subdivide regions of interest in a three-dimensional Cartesian grid (the two-dimensional equivalent is called a quadtree structure). Additional aspects can also be considered to optimise the implementation of the SDF. For example, computing $\boldsymbol{D}_{\vec{x}_i}$ (Eq. (4.20)) can become computationally expensive upon increasing the number of line segments as the medial axis increases.

Considering the XCT measurement results, firstly, further analysis of the effects of influence factors in the XCT measurement process would be valuable. For the point cloud conversion, a wider range of settings could be investigated and their effects on specific stages in the data processing stages (Figure 3.4) could be studied – for example, reference geometry definition which may be sensitive to variations/erroneous points in the XCT point cloud. Analysing many XCT influence factors is difficult, partly because time constraints very limiting; XCT scans can quickly require several hours. The XCT measurements in this thesis were performed by an external company, further increasing the waiting times.

For the XCT surface determination stage, an iterative approach was selected which is well established as superior to a global ISO50 method, however, it may still be valuable to compare the effects of these two methods. As mentioned in Section 2.8, surface determination has been shown to cause greater error in edge-to-edge length measurements over sphere-centre distances [124]. Therefore, from the results in Chapter 6, the offset data (which is calculated using the centre of the circles fitted to the cross sectional data) may be more reliable than all the other measurement results (which can all be considered as edge-to-edge length measurements). Global registration is dependent upon the manual selection of fit points; determining an ideal number of fit points is not straightforward, particularly because the presence of defects displaces the data points from their "true" location. Future considerations could attempt to align the determined surface to a CAD model. The reference geometry definition stage will be significantly dependent upon the accuracy of the global registration stage.

There are several other aspects of the XCT data processing to consider. The data from the surface unwrapping is expressed using the same axes (i.e. t vs α) as the displacement function which models surface defects and therefore can be directly applied into the model. However, to capture the high frequencies in the surface unwrapping data, a very dense surface mesh will be required, which raises potential issues related to the limitations of the domain resolution dx of the SDF. Alternatively, the higher frequencies could be discarded (again, they are likely to have negligible effect on lattice stiffness), for example, through Fourier analysis. An example of using Fourier analysis to remove higher frequencies from XCT lattice structure data is provided by Lei et al. [138], in which a method for smoothing the radius struts was determined. Lastly, it is also worth considering the stages at which arbitrary decisions are made when converting the XCT measurement data into defects used in the model.

For example, waviness is currently modelled by displacing the points in the medial axis in a random direction. Future investigations could consider developing a method which uses the XCT data to determine the direction, perhaps again through the fitting of a PDF.

Lastly, the results of this thesis are now considered in light of the initial objectives. Progress has certainly been made towards the initial project aim of developing a modelling approach for investigating the impact of defects on lattice structures. The objectives have also all been achieved, though some would still benefit from further work, in particular the validation of the model and further investigating the disparity between the experimental and FE results.

A summary of the main points discussed in this section is provided below:

- The proposed modelling approach is geometrically versatile but very computationally expensive. Optimisation options are still available for improving the proposed approach, but at higher lattice tessellations, beam elements are likely a more suitable choice.
- Further analysis of XCT influence factors would be beneficial, in particular the sensitivity of the reference geometry definition to variations in the XCT point cloud.

7.3 Future work

The first place to direct future efforts must be the comparison of the FE modelling results to the experimental data. As previously stated, the Ti6Al4V powder material should first be used for generating specimens for mechanical tests, from which Young's modulus and Poisson's ratio can be determined. These properties should then be used in the FE material model.

To further investigate the utility of the proposed modelling approach, it would be useful to investigate alternative meshing tools which use quadratic tetrahedral elements, given that linear tetrahedral meshes were used for this work. In FEA, the displacement field described by linear tetrahedral elements is often inaccurate (because linear displacements are not representative of complex displacement fields). Additionally, quadratic tetrahedral elements may be better suited for describing the displacement field of bending-dominated lattice structures, as opposed to stretch dominated. A comparison between using linear and quadratic tetrahedral elements for stretch-dominated and bending-dominated structures would be useful for understanding which element types are more appropriate for FEA of strut-based lattice structures. Comparisons to beam element modelling methods should also be made, to determine when this more computationally efficient approach can be utilised.

Additional geometric deviations and defects should be investigated, to determine which ones have a crucial impact on lattice properties. Alternative methods for determining lattice structure mechanical properties may need to be considered. Homogenisation methods could be used, these methods operate by performing simulations on individual unit cells and using the derived properties to infer mechanical properties of the lattice structure ([64,161]). Homogenisation techniques have an advantage of reducing computational load. Other alternative methods include the finite cell method ([162,163]), an imaged-based method which converts XCT voxel data into meshes for FEA.

The MATLAB-based method which was implemented for the dimensional analysis proved sufficient for capturing geometric deviations which are in line with similar observations in the literature, however, this method should be compared to established XCT software tools such as VGSTUDIO. Such a comparison will be helpful for determining if there is any significant detail being missed by the MATLAB-based approach. Further investigation into the effects of the XCT data during conversion from volume data through to STL would be valuable. However, this may be challenging do to the restrictions on proprietary software.

Given the large data files produced for XCT, a future study could be performed to investigate the impact on parameters such as number of projections on file size.

As for the manufacturing of the samples, further investigation into the effects of process parameters on geometric deviations should be studied. For example, the impact of hatch spacing and layer thickness of radius deviation and waviness.

A summary of the main points discussed in this section is provided below:

- The material model for the FEA must be updated using properties obtained from the powder used for sample manufacture.
- The performance of other mesh types—quadratic tetrahedral elements; beam elements—should be performed.
- Homogenization methods should be considered for increasing the proposed approach’s computational efficiency.
- The bespoke XCT data processing algorithms written for this work should be compared to any similar functions available in commercial software alternatives, such as VGSTUDIO.

References

[1] L.J. Gibson, M.F. Ashby, Cellular Solids: Structure and properties, 2nd ed., Cambridge University Press, Cambridge, 1997.

[2] P. Köhnen, C. Haase, J. Bültmann, S. Ziegler, J.H. Schleifenbaum, W. Bleck, Mechanical properties and deformation behavior of additively manufactured lattice structures of stainless steel, Mater. Des. 145 (2018) 205–217. https://doi.org/10.1016/j.matdes.2018.02.062.

[3] T. Tancogne-Dejean, D. Mohr, Stiffness and specific energy absorption of additively-manufactured metallic BCC metamaterials composed of tapered beams, Int. J. Mech. Sci. 141 (2018) 101–116. https://doi.org/10.1016/j.ijmecsci.2018.03.027.

[4] I. Maskery, A. Hussey, A. Panesar, A. Aremu, C. Tuck, I. Ashcroft, R. Hague, An investigation into reinforced and functionally graded lattice structures, J. Cell. Plast. 53 (2017) 151–165. https://doi.org/10.1177/0021955X16639035.

[5] Q.Y. Jin, J.H. Yu, K.S. Ha, W.J. Lee, S.H. Park, Multi-dimensional lattices design for ultrahigh specific strength metallic structure in additive manufacturing, Mater. Des. 201 (2021) 109479. https://doi.org/10.1016/j.matdes.2021.109479.

[6] S.-Y. Park, K.-S. Kim, B. AlMangour, D. Grzesiak, K.-A. Lee, Effect of unit cell topology on the tensile loading responses of additive manufactured CoCrMo triply periodic minimal surface sheet lattices, Mater. Des. 206 (2021) 109778. https://doi.org/10.1016/j.matdes.2021.109778.

[7] Z. Alomar, F. Concli, Compressive behavior assessment of a newly developed circular cell-based lattice structure, Mater. Des. 205 (2021) 109716. https://doi.org/10.1016/j.matdes.2021.109716.

[8] S. Ma, Q. Tang, X. Han, Q. Feng, J. Song, R. Setchi, Y. Liu, Y. Liu, A. Goulas, D.S. Engstrøm, Y.Y. Tse, N. Zhen, Manufacturability, Mechanical Properties, Mass-Transport Properties and Biocompatibility of Triply Periodic Minimal Surface (TPMS) Porous Scaffolds Fabricated by Selective Laser Melting, Mater. Des. 195 (2020) 1–15. https://doi.org/10.1016/j.matdes.2020.109034.

[9] N. Taniguchi, S. Fujibayashi, M. Takemoto, K. Sasaki, B. Otsuki, T. Nakamura, T. Matsushita, T. Kokubo, S. Matsuda, Effect of pore size on bone ingrowth into porous titanium implants fabricated by additive manufacturing: An in vivo experiment, Mater. Sci. Eng. C. 59 (2016) 690–701. https://doi.org/10.1016/j.msec.2015.10.069.

[10] D. Carluccio, C. Xu, J. Venezuela, Y. Cao, D. Kent, M. Bermingham, A.G. Demir, B. Previtali, Q. Ye, M. Dargusch, Additively manufactured iron-manganese for

biodegradable porous load-bearing bone scaffold applications, Acta Biomater. 103 (2020) 346–360. https://doi.org/10.1016/j.actbio.2019.12.018.

[11] Y. Zheng, Q. Han, D. Li, F. Sheng, Z. Song, J. Wang, Promotion of tendon growth into implant through pore-size design of a Ti-6Al-4 V porous scaffold prepared by 3D printing, Mater. Des. 197 (2021) 109219. https://doi.org/10.1016/j.matdes.2020.109219.

[12] N. Tatar, M. Tuzlalı, E. Bahçe, Investigation of the Lattice Production of Removable Dental Prostheses with CoCr Alloy Using Additive Manufacturing, J. Mater. Eng. Perform. 30 (2021) 6722–6731. https://doi.org/10.1007/s11665-021-05972-1.

[13] S. Catchpole-Smith, R.R.J. Sélo, A.W. Davis, I.A. Ashcroft, C.J. Tuck, A. Clare, Thermal conductivity of TPMS lattice structures manufactured via laser powder bed fusion, Addit. Manuf. 30 (2019) 100846. https://doi.org/10.1016/j.addma.2019.100846.

[14] A. Chaudhari, P. Ekade, S. Krishnan, Experimental investigation of heat transfer and fluid flow in octet-truss lattice geometry, Int. J. Therm. Sci. 143 (2019) 64–75. https://doi.org/10.1016/j.ijthermalsci.2019.05.003.

[15] B.S. Lazarov, O. Sigmund, K.E. Meyer, J. Alexandersen, Experimental validation of additively manufactured optimized shapes for passive cooling, Appl. Energy. 226 (2018) 330–339. https://doi.org/10.1016/j.apenergy.2018.05.106.

[16] I. Kaur, P. Singh, Critical evaluation of additively manufactured metal lattices for viability in advanced heat exchangers, Int. J. Heat Mass Transf. 168 (2021) 120858. https://doi.org/10.1016/j.ijheatmasstransfer.2020.120858.

[17] A. Beharic, R. Rodriguez Egui, L. Yang, Drop-weight impact characteristics of additively manufactured sandwich structures with different cellular designs, Mater. Des. 145 (2018) 122–134. https://doi.org/10.1016/j.matdes.2018.02.066.

[18] R.A.W. Mines, S. Tsopanos, Y. Shen, R. Hasan, S.T. McKown, Drop weight impact behaviour of sandwich panels with metallic micro lattice cores, Int. J. Impact Eng. 60 (2013) 120–132. https://doi.org/10.1016/j.ijimpeng.2013.04.007.

[19] F. Warmuth, M. Wormser, C. Körner, Single phase 3D phononic band gap material, Sci. Rep. 7 (2017) 3843. https://doi.org/10.1038/s41598-017-04235-1.

[20] M. Wormser, F. Warmuth, C. Körner, Evolution of full phononic band gaps in periodic cellular structures, Appl. Phys. A Mater. Sci. Process. 123 (2017) 661. https://doi.org/10.1007/s00339-017-1278-6.

[21] F. Lucklum, M.J. Vellekoop, Design and fabrication challenges for millimeter-scale three-dimensional phononic crystals, Crystals. 7 (2017). https://doi.org/10.3390/cryst7110348.

[22] W. Elmadih, Additively manufactured lattice structures for vibration attenuation, University of Nottingham, 2019. http://eprints.nottingham.ac.uk/id/eprint/60383.

[23] W. Elmadih, D. Chronopoulos, W.P. Syam, I. Maskery, H. Meng, R.K. Leach, Three-dimensional resonating metamaterials for low-frequency vibration attenuation, Sci. Rep. 9 (2019) 1–8. https://doi.org/10.1038/s41598-019-47644-0.

[24] A. Bauereiß, T. Scharowsky, C. Körner, Defect generation and propagation mechanism during additive manufacturing by selective beam melting, J. Mater. Process. Technol. 214 (2014) 2522–2528. https://doi.org/10.1016/j.jmatprotec.2014.05.002.

[25] A. Moussa, D. Melancon, A. El Elmi, D. Pasini, Topology optimization of imperfect lattice materials built with process-induced defects via Powder Bed Fusion, Addit. Manuf. (2020) 101608. https://doi.org/10.1016/j.addma.2020.101608.

[26] M. Grasso, B.M. Colosimo, Process defects and in situ monitoring methods in metal powder bed fusion: a review, Meas. Sci. Technol. 28 (2017) 044005. https://doi.org/10.1088/1361-6501/aa5c4f.

[27] E. Hernández-Nava, C.J. Smith, F. Derguti, S. Tammas-Williams, F. Leonard, P.J. Withers, I. Todd, R. Goodall, The effect of defects on the mechanical response of Ti-6Al-4V cubic lattice structures fabricated by electron beam melting, Acta Mater. 108 (2016) 279–292. https://doi.org/10.1016/j.actamat.2016.02.029.

[28] B. Lozanovski, M. Leary, P. Tran, D. Shidid, M. Qian, P. Choong, M. Brandt, Computational modelling of strut defects in SLM manufactured lattice structures, Mater. Des. 171 (2019) 107671. https://doi.org/10.1016/j.matdes.2019.107671.

[29] A. El Elmi, D. Melancon, M. Asgari, L. Liu, D. Pasini, Experimental and numerical investigation of selective laser melting-induced defects in Ti-6Al-4V octet truss lattice material: The role of material microstructure and morphological variations, J. Mater. Res. (2020) 1–13. https://doi.org/10.1557/jmr.2020.75.

[30] I. Echeta, X. Feng, B. Dutton, R. Leach, S. Piano, Review of defects in lattice structures manufactured by powder bed fusion, Int. J. Adv. Manuf. Technol. 106 (2019) 2649–2668. https://doi.org/10.1007/s00170-019-04753-4.

[31] W. Elmadih, W.P. Syam, I. Maskery, D. Chronopoulos, R. Leach, Mechanical vibration bandgaps in surface-based lattices, Addit. Manuf. 25 (2019) 421–429. https://doi.org/10.1016/j.addma.2018.11.011.

[32] W. Elmadih, W.P. Syam, I. Maskery, D. Chronopoulos, R. Leach, Multidimensional phononic bandgaps in three-dimensional lattices for additive

manufacturing, Materials (Basel). 12 (2019) 1–16. https://doi.org/10.3390/ma12111878.

[33] Y. Amani, S. Dancette, P. Delroisse, A. Simar, E. Maire, Compression behavior of lattice structures produced by selective laser melting: X-ray tomography based experimental and finite element approaches, Acta Mater. 159 (2018) 395–407. https://doi.org/10.1016/j.actamat.2018.08.030.

[34] A. du Plessis, I. Yadroitsava, I. Yadroitsev, Ti6Al4V lightweight lattice structures manufactured by laser powder bed fusion for load-bearing applications, Opt. Laser Technol. 108 (2018) 521–528. https://doi.org/10.1016/j.optlastec.2018.07.050.

[35] S. Van Bael, G. Kerckhofs, M. Moesen, G. Pyka, J. Schrooten, J.P. Kruth, Micro-CT-based improvement of geometrical and mechanical controllability of selective laser melted Ti6Al4V porous structures, Mater. Sci. Eng. A. 528 (2011) 7423–7431. https://doi.org/10.1016/j.msea.2011.06.045.

[36] H.N.G. Wadley, K.P. Dharmasena, M.Y. He, R.M. McMeeking, A.G. Evans, T. Bui-Thanh, R. Radovitzky, An active concept for limiting injuries caused by air blasts, Int. J. Impact Eng. 37 (2010) 317–323. https://doi.org/10.1016/j.ijimpeng.2009.06.006.

[37] A. Panesar, M. Abdi, D. Hickman, I. Ashcroft, Strategies for functionally graded lattice structures derived using topology optimisation for Additive Manufacturing, Addit. Manuf. 19 (2018) 81–94. https://doi.org/10.1016/J.ADDMA.2017.11.008.

[38] M.F. Ashby, The properties of foams and lattices, Philos. Trans. R. Soc. A Math. Phys. Eng. Sci. 364 (2006) 15–30. https://doi.org/10.1098/rsta.2005.1678.

[39] J.C. Maxwell, L. On the calculation of the equilibrium and stiffness of frames, London, Edinburgh, Dublin Philos. Mag. J. Sci. 27 (1864) 294–299. https://doi.org/10.1080/14786446408643668.

[40] H.I. Choi, C.Y. Han, Chapter 19 - The Medial Axis Transform, in: G. Farin, J. Hoschek, M.-S.B.T.-H. of C.A.G.D. Kim (Eds.), North-Holland, Amsterdam, 2002: pp. 451–471. https://doi.org/https://doi.org/10.1016/B978-044451104-1/50020-4.

[41] ISO, Additive manufacturing — General principles — Terminology, (2017).

[42] A. Nazir, K.M. Abate, A. Kumar, J.-Y. Jeng, A state-of-the-art review on types, design, optimization, and additive manufacturing of cellular structures, Int. J. Adv. Manuf. Technol. 104 (2019) 3489–3510. https://doi.org/10.1007/s00170-019-04085-3.

[43] M. Helou, S. Kara, Design, analysis and manufacturing of lattice structures: An

overview, Int. J. Comput. Integr. Manuf. 31 (2018) 243–261. https://doi.org/10.1080/0951192X.2017.1407456.

[44] I. Gibson, D.W. Rosen, B. Stucker, Additive Manufacturing Technologies, Springer, 2010.

[45] L.N. Carter, X. Wang, N. Read, R. Khan, M. Aristizabal, K. Essa, M.M. Attallah, Process optimisation of selective laser melting using energy density model for nickel based superalloys, Mater. Sci. Technol. 0836 (2015) 1–5. https://doi.org/10.1179/1743284715y.0000000108.

[46] H. Gong, K. Rafi, H. Gu, T. Starr, B. Stucker, Analysis of defect generation in Ti-6Al-4V parts made using powder bed fusion additive manufacturing processes, Addit. Manuf. 1 (2014) 87–98. https://doi.org/10.1016/j.addma.2014.08.002.

[47] S. Tammas-Williams, H. Zhao, F. Léonard, F. Derguti, I. Todd, P.B. Prangnell, XCT analysis of the influence of melt strategies on defect population in Ti-6Al-4V components manufactured by Selective Electron Beam Melting, Mater. Charact. 102 (2015) 47–61. https://doi.org/10.1016/j.matchar.2015.02.008.

[48] B. Zhang, Y. Li, Q. Bai, Defect formation mechanisms in selective laser melting: a review, Chinese J. Mech. Eng. 30 (2017) 515–527. https://doi.org/10.1007/s10033-017-0121-5.

[49] M. Grasso, B.M. Colosimo, Process defects and in situ monitoring methods in metal powder bed fusion: a review, Meas. Sci. Technol. 28 (2017). https://doi.org/10.1088/1361-6501/aa5c4f.

[50] P. Mercelis, J.P. Kruth, Residual stresses in selective laser sintering and selective laser melting, Rapid Prototyp. J. 12 (2006) 254–265. https://doi.org/10.1108/13552540610707013.

[51] S. Sun, M. Brandt, M. Easton, Powder bed fusion processes: An overview, Elsevier Ltd, 2016. https://doi.org/10.1016/B978-0-08-100433-3.00002-6.

[52] X. He, D. Kong, Y. Zhou, L. Wang, X. Ni, L. Zhang, W. Wu, R. Li, X. Li, C. Dong, Powder recycling effects on porosity development and mechanical properties of Hastelloy X alloy during laser powder bed fusion process, Addit. Manuf. 55 (2022) 102840. https://doi.org/10.1016/j.addma.2022.102840.

[53] F. Ahmed, U. Ali, D. Sarker, E. Marzbanrad, K. Choi, Y. Mahmoodkhani, E. Toyserkani, Study of powder recycling and its effect on printed parts during laser powder-bed fusion of 17-4 PH stainless steel, J. Mater. Process. Technol. 278 (2020) 116522. https://doi.org/10.1016/j.jmatprotec.2019.116522.

[54] L. Thijs, F. Verhaeghe, T. Craeghs, J. Van Humbeeck, J.P. Kruth, A study of the microstructural evolution during selective laser melting of Ti-6Al-4V, Acta Mater. 58 (2010) 3303–3312. https://doi.org/10.1016/j.actamat.2010.02.004.

[55] M. Seifi, A. Salem, J. Beuth, O. Harrysson, J.J. Lewandowski, Overview of Materials Qualification Needs for Metal Additive Manufacturing, Jom. 68 (2016) 747–764. https://doi.org/10.1007/s11837-015-1810-0.

[56] R. Li, J. Liu, Y. Shi, L. Wang, W. Jiang, Balling behavior of stainless steel and nickel powder during selective laser melting process, Int. J. Adv. Manuf. Technol. 59 (2012) 1025–1035. https://doi.org/10.1007/s00170-011-3566-1.

[57] D. Wang, S. Wu, F. Fu, S. Mai, Y. Yang, Y. Liu, C. Song, Mechanisms and characteristics of spatter generation in SLM processing and its effect on the properties, Mater. Des. 117 (2017) 121–130. https://doi.org/10.1016/j.matdes.2016.12.060.

[58] A. Cuadrado, A. Yánez, O. Martel, S. Deviaene, D. Monopoli, Influence of load orientation and of types of loads on the mechanical properties of porous Ti6Al4V biomaterials, Mater. Des. 135 (2017) 309–318. https://doi.org/10.1016/j.matdes.2017.09.045.

[59] S. Arabnejad, R. Burnett Johnston, J.A. Pura, B. Singh, M. Tanzer, D. Pasini, High-strength porous biomaterials for bone replacement: A strategy to assess the interplay between cell morphology, mechanical properties, bone ingrowth and manufacturing constraints, Acta Biomater. 30 (2016) 345–356. https://doi.org/10.1016/j.actbio.2015.10.048.

[60] L. Zhang, S. Feih, S. Daynes, S. Chang, M.Y. Wang, J. Wei, W.F. Lu, Energy absorption characteristics of metallic triply periodic minimal surface sheet structures under compressive loading, Addit. Manuf. 23 (2018) 505–515. https://doi.org/10.1016/j.addma.2018.08.007.

[61] B. Lozanovski, D. Downing, P. Tran, D. Shidid, M. Qian, P. Choong, M. Brandt, M. Leary, A Monte Carlo simulation-based approach to realistic modelling of additively manufactured lattice structures, Addit. Manuf. 32 (2020) 101092. https://doi.org/10.1016/j.addma.2020.101092.

[62] T.B. Sercombe, X. Xu, V.J. Challis, R. Green, S. Yue, Z. Zhang, P.D. Lee, Failure modes in high strength and stiffness to weight scaffolds produced by Selective Laser Melting, Mater. Des. 67 (2015) 501–508. https://doi.org/10.1016/j.matdes.2014.10.063.

[63] D. Melancon, Z.S. Bagheri, R.B. Johnston, L. Liu, M. Tanzer, D. Pasini, Mechanical characterization of structurally porous biomaterials built via additive manufacturing: experiments, predictive models, and design maps for load-bearing bone replacement implants, Acta Biomater. 63 (2017) 350–368. https://doi.org/10.1016/j.actbio.2017.09.013.

[64] L. Liu, P. Kamm, F. García-Moreno, J. Banhart, D. Pasini, Elastic and failure response of imperfect three-dimensional metallic lattices: the role of geometric

defects induced by Selective Laser Melting, J. Mech. Phys. Solids. 107 (2017) 160–184. https://doi.org/10.1016/j.jmps.2017.07.003.

[65] Z. Dong, Y. Liu, W. Li, J. Liang, Orientation dependency for microstructure, geometric accuracy and mechanical properties of selective laser melting AlSi10Mg lattices, J. Alloys Compd. 791 (2019) 490–500. https://doi.org/10.1016/j.jallcom.2019.03.344.

[66] M. Dallago, B. Winiarski, F. Zanini, S. Carmignato, M. Benedetti, On the effect of geometrical imperfections and defects on the fatigue strength of cellular lattice structures additively manufactured via Selective Laser Melting, Int. J. Fatigue. 124 (2019) 348–360. https://doi.org/10.1016/j.ijfatigue.2019.03.019.

[67] S.Y. Choy, C.N. Sun, K.F. Leong, J. Wei, Compressive properties of Ti-6Al-4V lattice structures fabricated by selective laser melting: Design, orientation and density, Addit. Manuf. 16 (2017) 213–224. https://doi.org/10.1016/j.addma.2017.06.012.

[68] R. Gümrük, R.A.W. Mines, S. Karadeniz, Static mechanical behaviours of stainless steel micro-lattice structures under different loading conditions, Mater. Sci. Eng. A. 586 (2013) 392–406. https://doi.org/10.1016/j.msea.2013.07.070.

[69] S. Li, H. Hassanin, M.M. Attallah, N.J.E. Adkins, K. Essa, The development of TiNi-based negative Poisson's ratio structure using selective laser melting, Acta Mater. 105 (2016) 75–83. https://doi.org/10.1016/j.actamat.2015.12.017.

[70] O. Al-Ketan, R. Rowshan, R.K. Abu Al-Rub, Topology-mechanical property relationship of 3D printed strut, skeletal, and sheet based periodic metallic cellular materials, Addit. Manuf. 19 (2018) 167–183. https://doi.org/10.1016/j.addma.2017.12.006.

[71] T. Tancogne-Dejean, A.B. Spierings, D. Mohr, Additively-manufactured metallic micro-lattice materials for high specific energy absorption under static and dynamic loading, Acta Mater. 116 (2016) 14–28. https://doi.org/10.1016/j.actamat.2016.05.054.

[72] M. Leary, M. Mazur, J. Elambasseril, M. McMillan, T. Chirent, Y. Sun, M. Qian, M. Easton, M. Brandt, Selective laser melting (SLM) of AlSi12Mg lattice structures, Mater. Des. 98 (2016) 344–357. https://doi.org/10.1016/j.matdes.2016.02.127.

[73] D.A. Hollander, M. Von Walter, T. Wirtz, R. Sellei, B. Schmidt-Rohlfing, O. Paar, H.J. Erli, Structural, mechanical and in vitro characterization of individually structured Ti-6Al-4V produced by direct laser forming, Biomaterials. 27 (2006) 955–963. https://doi.org/10.1016/j.biomaterials.2005.07.041.

[74] C.-Y. Lin, T. Wirtz, F. LaMarca, S.J. Hollister, Structural and mechanical evaluations of a topology optimized titanium interbody fusion cage fabricated

by selective laser melting process, J. Biomed. Mater. Res. Part A. 83A (2007) 272–279. https://doi.org/10.1002/jbm.a.31231.

[75] S.L. Sing, W.Y. Yeong, F.E. Wiria, B.Y. Tay, Characterization of titanium lattice structures fabricated by selective laser melting using an adapted compressive test method, Exp. Mech. 56 (2016) 735–748. https://doi.org/10.1007/s11340-015-0117-y.

[76] S.Y. Choy, C.N. Sun, K.F. Leong, J. Wei, Compressive properties of functionally graded lattice structures manufactured by selective laser melting, Mater. Des. 131 (2017) 112–120. https://doi.org/10.1016/j.matdes.2017.06.006.

[77] F. Calignano, Design optimization of supports for overhanging structures in aluminum and titanium alloys by selective laser melting, Mater. Des. 64 (2014) 203–213. https://doi.org/10.1016/j.matdes.2014.07.043.

[78] G. Kerckhofs, G. Pyka, M. Moesen, J. Schrooten, High-resolution micro-CT as a tool for 3D surface roughness measurement of 3D additive manufactured porous structures, Proc. ICT. (2012) 77–83. https://doi.org/10.1002/adem.201200156.

[79] K. Lietaert, A. Cutolo, D. Boey, B. Van Hooreweder, Fatigue life of additively manufactured Ti6Al4V scaffolds under tension-tension, tension-compression and compression-compression fatigue load, Sci. Rep. 8 (2018) 1–9. https://doi.org/10.1038/s41598-018-23414-2.

[80] G. Pyka, G. Kerckhofs, I. Papantoniou, M. Speirs, J. Schrooten, M. Wevers, Surface roughness and morphology customization of additive manufactured open porous Ti6Al4V structures, Materials (Basel). 6 (2013) 4737–4757. https://doi.org/10.3390/ma6104737.

[81] ISO, Geometrical Product Specifications (GPS) — Surface texture: Profile method — Terms, definitions and surface texture parameters (Corr 2), (2005).

[82] A. Townsend, N. Senin, L. Blunt, R.K. Leach, J.S. Taylor, Surface texture metrology for metal additive manufacturing: a review, Precis. Eng. 46 (2016) 34–47. https://doi.org/10.1016/j.precisioneng.2016.06.001.

[83] ISO 25178-2: Geometrical Product Specifications (GPS) – Surface Texture: Areal – Part 2: Terms, Definitions and Surface Texture Parameters, (2012).

[84] A. Thompson, N. Senin, I. Maskery, L. Körner, S. Lawes, R.K. Leach, Internal surface measurement of metal powder bed fusion parts, Addit. Manuf. 20 (2018) 126–133. https://doi.org/10.1016/j.addma.2018.01.003.

[85] X.Y. Cheng, S.J. Li, L.E. Murr, Z.B. Zhang, Y.L. Hao, R. Yang, F. Medina, R.B. Wicker, Compression deformation behavior of Ti–6Al–4V alloy with cellular structures fabricated by electron beam melting, J. Mech. Behav. Biomed. Mater.

16 (2012) 153–162. https://doi.org/10.1016/j.jmbbm.2012.10.005.

[86] P. Heinl, C. Körner, R.F. Singer, Selective electron beam melting of cellular titanium: mechanical properties, Adv. Eng. Mater. 10 (2008) 882–888. https://doi.org/10.1002/adem.200800137.

[87] N.W. Hrabe, P. Heinl, B. Flinn, C. Körner, R.K. Bordia, Compression-compression fatigue of selective electron beam melted cellular titanium (Ti-6Al-4V), J. Biomed. Mater. Res. - Part B Appl. Biomater. 99 B (2011) 313–320. https://doi.org/10.1002/jbm.b.31901.

[88] X. Li, Y.-F. Feng, C.-T. Wang, G.-C. Li, W. Lei, Z.-Y. Zhang, L. Wang, Evaluation of biological properties of electron beam melted Ti6Al4V implant with biomimetic coating in vitro and in vivo, PLoS One. 7 (2012) e52049. https://doi.org/10.1371/journal.pone.0052049.

[89] M.R.K. Ravari, S.N. Esfahani, M.T. Andani, M. Kadkhodaei, A. Ghaei, H. Karaca, M. Elahinia, On the effects of geometry, defects, and material asymmetry on the mechanical response of shape memory alloy cellular lattice structures, Smart Mater. Struct. 25 (2016) 025008. https://doi.org/10.1088/0964-1726/25/2/025008.

[90] C. Han, C. Yan, S. Wen, T. Xu, S. Li, J. Liu, Q. Wei, Y. Shi, Effects of the unit cell topology on the compression properties of porous Co-Cr scaffolds fabricated via selective laser melting, Rapid Prototyp. J. 23 (2017) 16–27. https://doi.org/10.1108/RPJ-08-2015-0114.

[91] M. Dallago, V. Fontanari, E. Torresani, M. Leoni, C. Pederzolli, C. Potrich, M. Benedetti, Fatigue and biological properties of Ti-6Al-4V ELI cellular structures with variously arranged cubic cells made by selective laser melting, J. Mech. Behav. Biomed. Mater. 78 (2018) 381–394. https://doi.org/10.1016/j.jmbbm.2017.11.044.

[92] J. Parthasarathy, B. Starly, S. Raman, A. Christensen, Mechanical evaluation of porous titanium (Ti6Al4V) structures with electron beam melting (EBM), J. Mech. Behav. Biomed. Mater. 3 (2010) 249–259. https://doi.org/10.1016/j.jmbbm.2009.10.006.

[93] C. Yan, L. Hao, A. Hussein, P. Young, Ti–6Al–4V triply periodic minimal surface structures for bone implants fabricated via selective laser melting, J. Mech. Behav. Biomed. Mater. 51 (2015) 61–73. https://doi.org/10.1016/j.jmbbm.2015.06.024.

[94] C. Qiu, S. Yue, N.J.E. Adkins, M. Ward, H. Hassanin, P.D. Lee, P.J. Withers, M.M. Attallah, Influence of processing conditions on strut structure and compressive properties of cellular lattice structures fabricated by selective laser melting, Mater. Sci. Eng. A. 628 (2015) 188–197.

https://doi.org/10.1016/j.msea.2015.01.031.

[95] C. Han, Y. Li, Q. Wang, S. Wen, Q. Wei, C. Yan, L. Hao, J. Liu, Y. Shi, Continuous functionally graded porous titanium scaffolds manufactured by selective laser melting for bone implants, J. Mech. Behav. Biomed. Mater. 80 (2018) 119–127. https://doi.org/10.1016/j.jmbbm.2018.01.013.

[96] E. Sallica-Leva, A.L. Jardini, J.B. Fogagnolo, Microstructure and mechanical behavior of porous Ti-6Al-4V parts obtained by selective laser melting, J. Mech. Behav. Biomed. Mater. 26 (2013) 98–108. https://doi.org/10.1016/j.jmbbm.2013.05.011.

[97] D. Wang, Y. Yang, R. Liu, D. Xiao, J. Sun, Study on the designing rules and processability of porous structure based on selective laser melting (SLM), J. Mater. Process. Technol. 213 (2013) 1734–1742. https://doi.org/10.1016/j.jmatprotec.2013.05.001.

[98] Y. Shen, W. Cantwell, R. Mines, Y. Li, Low-velocity impact performance of lattice structure core based sandwich panels, J. Compos. Mater. 48 (2014) 3153–3167. https://doi.org/10.1177/0021998313507616.

[99] C. Yan, L. Hao, A. Hussein, D. Raymont, Evaluations of cellular lattice structures manufactured using selective laser melting, Int. J. Mach. Tools Manuf. 62 (2012) 32–38. https://doi.org/10.1016/j.ijmachtools.2012.06.002.

[100] C. de Formanoir, M. Suard, R. Dendievel, G. Martin, S. Godet, Improving the mechanical efficiency of electron beam melted titanium lattice structures by chemical etching, Addit. Manuf. 11 (2016) 71–76. https://doi.org/10.1016/j.addma.2016.05.001.

[101] P. Lhuissier, C. de Formanoir, G. Martin, R. Dendievel, S. Godet, Geometrical control of lattice structures produced by EBM through chemical etching: Investigations at the scale of individual struts, Mater. Des. 110 (2016) 485–493. https://doi.org/10.1016/j.matdes.2016.08.029.

[102] M.K. Agarwala, D.L. Bourell, J.J. Beaman, Densification of selective laser sintered metal parts by hot isotatic pressing, Proc. SFF Symp. (1994) 65–73.

[103] M. Agarwala, D. Bourell, J. Beaman, H. Marcus, J. Barlow, Post-processing of selective laser sintered metal parts, Rapid Prototyp. J. 1 (1995) 36–44. https://doi.org/10.1108/13552549510086853.

[104] P. Li, D.H. Warner, J.W. Pegues, M.D. Roach, N. Shamsaei, N. Phan, Investigation of the mechanisms by which hot isostatic pressing improves the fatigue performance of powder bed fused Ti-6Al-4V, Int. J. Fatigue. 120 (2019) 342–352. https://doi.org/10.1016/j.ijfatigue.2018.10.015.

[105] M.W. Wu, J.K. Chen, B.H. Lin, P.H. Chiang, Improved fatigue endurance ratio

of additive manufactured Ti-6Al-4V lattice by hot isostatic pressing, Mater. Des. 134 (2017) 163–170. https://doi.org/10.1016/j.matdes.2017.08.048.

[106] B. Dutton, W. Vesga, Waller, S. James, M. Seifi, Metal Additive Manufacturing Defect Formation and NDE Detectability, STP1620 ASTM Symp. Struct. Integr. Addit. Manuf. Parts. (2019) 1–36.

[107] B. Van Hooreweder, Y. Apers, K. Lietaert, J.P. Kruth, Improving the fatigue performance of porous metallic biomaterials produced by Selective Laser Melting, Acta Biomater. 47 (2017) 193–202. https://doi.org/10.1016/j.actbio.2016.10.005.

[108] S. Van Bael, G. Kerckhofs, M. Moesen, G. Pyka, J. Schrooten, J.P. Kruth, Micro-CT-based improvement of geometrical and mechanical controllability of selective laser melted Ti6Al4V porous structures, Mater. Sci. Eng. A. 528 (2011) 7423–7431. https://doi.org/10.1016/j.msea.2011.06.045.

[109] S. Van Bael, Y.C. Chai, S. Truscello, M. Moesen, G. Kerckhofs, H. Van Oosterwyck, J.P. Kruth, J. Schrooten, The effect of pore geometry on the in vitro biological behavior of human periosteum-derived cells seeded on selective laser-melted Ti6Al4V bone scaffolds, Acta Biomater. 8 (2012) 2824–2834. https://doi.org/10.1016/j.actbio.2012.04.001.

[110] P.H. Warnke, E. Sherry, S.T. Becker, J. Wiltfang, Rapid prototyping: porous titanium alloy scaffolds produced by selective laser melting for bone tissue engineering, Tissue Eng. Part C Methods. 15 (2009) 115–124. https://doi.org/10.1089/ten.tec.2008.0288.

[111] W. van Grunsven, E. Hernandez-Nava, G. Reilly, R. Goodall, Fabrication and mechanical characterisation of titanium lattices with graded porosity, Metals (Basel). 4 (2014) 401–409. https://doi.org/10.3390/met4030401.

[112] L. Xiao, W. Song, C. Wang, H. Tang, Q. Fan, N. Liu, J. Wang, Mechanical properties of open-cell rhombic dodecahedron titanium alloy lattice structure manufactured using electron beam melting under dynamic loading, Int. J. Impact Eng. 100 (2017) 75–89. https://doi.org/10.1016/j.ijimpeng.2016.10.006.

[113] X. Li, C.-T. Wang, W.-G. Zhang, Y.-C. Li, Properties of a porous Ti—6Al—4V implant with a low stiffness for biomedical application, Proc. Inst. Mech. Eng. Part H J. Eng. Med. 223 (2009) 173–178. https://doi.org/10.1243/09544119JEIM466.

[114] S.L. Sing, F.E. Wiria, W.Y. Yeong, Selective laser melting of lattice structures: a statistical approach to manufacturability and mechanical behavior, Robot. Comput. Integr. Manuf. 49 (2018) 170–180. https://doi.org/10.1016/j.rcim.2017.06.006.

[115] C. Yan, L. Hao, A. Hussein, P. Young, D. Raymont, Advanced lightweight 316L

stainless steel cellular lattice structures fabricated via selective laser melting, Mater. Des. 55 (2014) 533–541. https://doi.org/10.1016/j.matdes.2013.10.027.

[116] L. Yang, O. Harrysson, D. Cormier, H. West, H. Gong, B. Stucker, Additive manufacturing of metal cellular structures: design and fabrication, JOM. 67 (2015) 608–615. https://doi.org/10.1007/s11837-015-1322-y.

[117] D.S.J. Al-Saedi, S.H. Masood, M. Faizan-Ur-Rab, A. Alomarah, P. Ponnusamy, Mechanical properties and energy absorption capability of functionally graded F2BCC lattice fabricated by SLM, Mater. Des. 144 (2018) 32–44. https://doi.org/10.1016/j.matdes.2018.01.059.

[118] X. Li, C. Wang, W. Zhang, Y. Li, Fabrication and characterization of porous Ti6Al4V parts for biomedical applications using electron beam melting process, Mater. Lett. 63 (2009) 403–405. https://doi.org/10.1016/j.matlet.2008.10.065.

[119] J. Wieding, A. Jonitz, R. Bader, The effect of structural design on mechanical properties and cellular response of additive manufactured titanium scaffolds, Materials (Basel). 5 (2012) 1336–1347. https://doi.org/10.3390/ma5081336.

[120] R. Wauthle, S.M. Ahmadi, S. Amin Yavari, M. Mulier, A.A. Zadpoor, H. Weinans, J. Van Humbeeck, J.P. Kruth, J. Schrooten, Revival of pure titanium for dynamically loaded porous implants using additive manufacturing, Mater. Sci. Eng. C. 54 (2015) 94–100. https://doi.org/10.1016/j.msec.2015.05.001.

[121] P. Delroisse, P.J. Jacques, E. Maire, O. Rigo, A. Simar, Effect of strut orientation on the microstructure heterogeneities in AlSi10Mg lattices processed by selective laser melting, Scr. Mater. 141 (2017) 32–35. https://doi.org/10.1016/j.scriptamat.2017.07.020.

[122] S. Amin Yavari, R. Wauthle, J. Van Der Stok, A.C. Riemslag, M. Janssen, M. Mulier, J.P. Kruth, J. Schrooten, H. Weinans, A.A. Zadpoor, Fatigue behavior of porous biomaterials manufactured using selective laser melting, Mater. Sci. Eng. C. 33 (2013) 4849–4858. https://doi.org/10.1016/j.msec.2013.08.006.

[123] S. Amin Yavari, S.M. Ahmadi, R. Wauthle, B. Pouran, J. Schrooten, H. Weinans, A.A. Zadpoor, Relationship between unit cell type and porosity and the fatigue behavior of selective laser melted meta-biomaterials, J. Mech. Behav. Biomed. Mater. 43 (2015) 91–100. https://doi.org/10.1016/j.jmbbm.2014.12.015.

[124] S. Carmignato, W. Dewulf, R.K. Leach, Industrial X-Ray Computed Tomography, Springer International Publishing, 2017. https://books.google.co.uk/books?id=KLo6DwAAQBAJ.

[125] A. Thompson, I. Maskery, R.K. Leach, A. Thompson, I. Maskery, R.K. Leach, X-ray computed tomography for additive manufacturing: a review, 27 (2016). http://eprints.nottingham.ac.uk/33856/3/X-ray computed tomography for%0Ahttp://eprints.nottingham.ac.uk/end_user_agreement.pdf.

[126] I. Maskery, N.T. Aboulkhair, M.R. Corfield, C. Tuck, A.T. Clare, R.K. Leach, R.D. Wildman, I.A. Ashcroft, R.J.M. Hague, Quantification and characterisation of porosity in selectively laser melted Al-Si10-Mg using X-ray computed tomography, Mater. Charact. 111 (2016) 193–204. https://doi.org/10.1016/j.matchar.2015.12.001.

[127] R.C. Roche, R.A. Abel, K.G. Johnson, C.T. Perry, Quantification of porosity in Acropora pulchra (Brook 1891) using X-ray micro-computed tomography techniques, J. Exp. Mar. Bio. Ecol. 396 (2010) 1–9. https://doi.org/10.1016/j.jembe.2010.10.006.

[128] JCGM, International vocabulary of metrology – Basic and general concepts and associated terms (VIM), (2008).

[129] VDI/VDE, 2630-1.2 Influencing variables on measurement results and recommendations for computed-tomography dimensional measurements, (2010).

[130] A. Stolfi, L. De Chiffre, S. Kasperl, Error Sources - Industrial X-Ray Computed Tomography, in: S. Carmignato, W. Dewulf, R. Leach (Eds.), Springer International Publishing, Cham, 2018: pp. 143–184. https://doi.org/10.1007/978-3-319-59573-3_5.

[131] P. Müller, J. Hiller, Y. Dai, J.L. Andreasen, H.N. Hansen, L. De Chiffre, Estimation of measurement uncertainties in X-ray computed tomography metrology using the substitution method, CIRP J. Manuf. Sci. Technol. 7 (2014) 222–232. https://doi.org/10.1016/j.cirpj.2014.04.002.

[132] J.J. Lifton, A.A. Malcolm, J.W. McBride, An experimental study on the influence of scatter and beam hardening in x-ray CT for dimensional metrology, in: 5th Conf. Ind. Comput. Tomogr. Austria, 2014. https://doi.org/10.1088/0957-0233/27/1/015007.

[133] A. Townsend, L. Pagani, L. Blunt, P.J. Scott, X. Jiang, Factors affecting the accuracy of areal surface texture data extraction from X-ray CT, CIRP Ann. - Manuf. Technol. 66 (2017) 547–550. https://doi.org/10.1016/j.cirp.2017.04.074.

[134] A. Tawfik, L. Blunt, C. Dawson, R. Racasan, D. Bacheva, P. Bills, Optimization of surface determination to improve the accuracy of detecting unfused powder in AM Aluminium component, 9th Conf. Ind. Comput. Tomogr. (2019) 1–7.

[135] G. Dong, Y. Tang, Y.F. Zhao, A Survey of Modeling of Lattice Structures Fabricated by Additive Manufacturing, J. Mech. Des. 139 (2017) 100906. https://doi.org/10.1115/1.4037305.

[136] M. Suard, P. Lhuissier, R. Dendievel, J.-J. Blandin, F. Vignat, F. Villeneuve, Towards stiffness prediction of cellular structures made by electron beam melting (EBM), Powder Metall. 57 (2014) 190–195.

https://doi.org/10.1179/1743290114Y.0000000093.

[137] X. Cao, Y. Jiang, T. Zhao, P. Wang, Y. Wang, Z. Chen, Y. Li, D. Xiao, D. Fang, Compression experiment and numerical evaluation on mechanical responses of the lattice structures with stochastic geometric defects originated from additive-manufacturing, Compos. Part B Eng. 194 (2020) 108030. https://doi.org/10.1016/j.compositesb.2020.108030.

[138] H. Lei, C. Li, J. Meng, H. Zhou, Y. Liu, X. Zhang, P. Wang, D. Fang, Evaluation of compressive properties of SLM-fabricated multi-layer lattice structures by experimental test and μ-CT-based finite element analysis, Mater. Des. 169 (2019) 107685. https://doi.org/10.1016/j.matdes.2019.107685.

[139] G. Campoli, M.S. Borleffs, S. Amin Yavari, R. Wauthle, H. Weinans, A.A. Zadpoor, Mechanical properties of open-cell metallic biomaterials manufactured using additive manufacturing, Mater. Des. 49 (2013) 957–965. https://doi.org/10.1016/j.matdes.2013.01.071.

[140] M. Smith, Z. Guan, W.J. Cantwell, Finite element modelling of the compressive response of lattice structures manufactured using the selective laser melting technique, Int. J. Mech. Sci. 67 (2013) 28–41. https://doi.org/10.1016/j.ijmecsci.2012.12.004.

[141] A.S. Bhuwal, T. Liu, I. Ashcroft, W. Sun, Localization and coalescence of imperfect planar FCC truss lattice metamaterials under multiaxial loadings, Mech. Mater. 160 (2021) 103996. https://doi.org/https://doi.org/10.1016/j.mechmat.2021.103996.

[142] S.H. Li, P. Kumar, S. Chandra, U. Ramamurty, Directed energy deposition of metals: processing, microstructures, and mechanical properties, Int. Mater. Rev. (2022) 1–43. https://doi.org/10.1080/09506608.2022.2097411.

[143] T.F. Babuska, B.A. Krick, D.F. Susan, A.B. Kustas, Comparison of powder bed fusion and directed energy deposition for tailoring mechanical properties of traditionally brittle alloys, Manuf. Lett. 28 (2021) 30–34. https://doi.org/10.1016/j.mfglet.2021.02.003.

[144] Bathe K J., Finite Element Procedures, 2nd ed., Prentice Hall, 1996.

[145] D.G. Pavlou, Beams, in: Essentials Finite Elem. Method, Academic Press, 2015: pp. 135–212. https://doi.org/10.1016/b978-0-12-802386-0.00006-2.

[146] D.G. Pavlou, Trusses, in: Essentials Finite Elem. Method, Academic Press, 2015: pp. 81–133. https://doi.org/10.1016/B978-0-12-802386-0.00005-0.

[147] O.C. Zienkiewicz, R.L. Taylor, J.Z. Zhu, Shape Functions, Derivatives, and Integration, in: Finite Elem. Method Its Basis Fundam., Butterworth–Heinemann, 2013: pp. 151–209. https://doi.org/10.1016/b978-1-85617-633-

0.00006-x.

[148] O.C. Zienkiewicz, R.L. Taylor, J.Z. Zhu, Elasticity: Two- and Three-Dimensional Finite Elements, in: Finite Elem. Method Its Basis Fundam., Butterworth–Heinemann, 2013: pp. 211–255. https://doi.org/10.1016/b978-1-85617-633-0.00007-1.

[149] Bathe, Formulation of the Finite Element Method-Linear Analysis in Solid and Structural Mechanics, in: Finite Elem. Proced., Prentice Hall, 1996: pp. 148–337.

[150] O.C. Zienkiewicz, R.L. Taylor, J.Z. Zhu, The Standard Discrete System and Origins of the Finite Element Method, in: Finite Elem. Method Its Basis Fundam., Butterworth–Heinemann, Oxford, 2013: pp. 1–20. https://doi.org/10.1016/b978-1-85617-633-0.00001-0.

[151] D.G. Pavlou, An Overview of the Finite Element Method, in: Essentials Finite Elem. Method, Academic Press, 2015: pp. 1–18. https://doi.org/10.1016/b978-0-12-802386-0.00001-3.

[152] S. Holcombe, stlwrite - write ASCII or Binary STL files, (2018). https://uk.mathworks.com/matlabcentral/fileexchange/20922-stlwrite-write-ascii-or-binary-stl-files.

[153] E. Johnson, STL File Reader, (2011). https://uk.mathworks.com/matlabcentral/fileexchange/22409-stl-file-reader.

[154] I. Echeta, B. Dutton, R.K. Leach, S. Piano, Finite element modelling of defects in additively manufactured strut-based lattice structures, Addit. Manuf. 47 (2021) 102301. https://doi.org/10.1016/j.addma.2021.102301.

[155] S. Osher, R. Fedkiw, Level Set Methods and Dynamic Implicit Surfaces, Springer New York, 2002. https://books.google.co.uk/books?id=sOuvKm9sMCEC.

[156] Q. Fang, iso2mesh, (n.d.). http://iso2mesh.sourceforge.net/cgi-bin/index.cgi?Home.

[157] Q. Fang, D.A. Boas, Tetrahedral mesh generation from volumetric binary and grayscale images, 2009 IEEE Int. Symp. Biomed. Imaging. (2009) 1142–1145. https://doi.org/10.1109/ISBI.2009.5193259.

[158] The CGAL Project, CGAL, Computational Geometry Algorithms Library, (2020). https://www.cgal.org (accessed March 16, 2020).

[159] CGAL, 3D Mesh Generation, (n.d.). https://doc.cgal.org/Manual/3.5/doc_html/cgal_manual/Mesh_3/Chapter_main.html.

[160] C. Zhang, T. Chen, Efficient feature extraction for 2D/3D objects in mesh representation, in: Proc. 2001 Int. Conf. Image Process. (Cat. No.01CH37205),

2001: pp. 935–938 vol.3. https://doi.org/10.1109/ICIP.2001.958278.

[161] B. Hassani, E. Hinton, A review of homogenization and topology optimization I - Homogenization theory for media with periodic structure, Comput. Struct. 69 (1998) 707–717. https://doi.org/10.1016/S0045-7949(98)00131-X.

[162] N. Korshunova, G. Alaimo, S.B. Hosseini, M. Carraturo, A. Reali, J. Niiranen, F. Auricchio, E. Rank, S. Kollmannsberger, Image-based numerical characterization and experimental validation of tensile behavior of octet-truss lattice structures, Addit. Manuf. 41 (2021) 101949. https://doi.org/10.1016/j.addma.2021.101949.

[163] L. Geng, B. Zhang, Y. Lian, R. Gao, D. Fang, An image-based multi-level hp FCM for predicting elastoplastic behavior of imperfect lattice structure by SLM, Comput. Mech. (2022). https://doi.org/10.1007/s00466-022-02158-x.

[164] I. The MathWorks, meshgrid, (2022). https://uk.mathworks.com/help/matlab/ref/meshgrid.html.

[165] E.W. Weisstein, Point-Line Distance--3-Dimensional, MathWorld--A Wolfram Web Resour. (n.d.). https://mathworld.wolfram.com/Point-LineDistance3-Dimensional.html.

[166] I. The MathWorks, lsqnonlin, (2022). https://uk.mathworks.com/help/optim/ug/lsqnonlin.html.

List of publications and presentations

A list of publications and conference presentations by the author are given here in one place for ease of reference.

Journal papers

Echeta, I., Dutton, B., Leach, R. K. & Piano, S. 2021 Finite element modelling of defects in additively manufactured strut-based lattice structures. Addit. Manuf. 102301. 10.1016/j.addma.2021.102301

Echeta, I., Feng, X., Dutton, B., Leach, R. & Piano, S. 2019 Review of defects in lattice structures manufactured by powder bed fusion. Int. J. Adv. Manuf. Technol. **106**, 2649–2668. 10.1007/s00170-019-04753-4

Conference presentations

Echeta I., 2021 Finite element modelling of defects in additively manufactured strut-based lattice structures. Annual International Solid Freeform Fabrication Symposium (SFF)

Echeta I., 2020 Analysis of defects in additively manufactured lattice structures. Image-Based Simulation for Industry (IBSim-4i)

Appendix A – XCT settings

X-ray parameter

Voltage (kV)	130
Current (µA)	90
Power (W)	11.7
Filter	Aluminium, 1 mm

Detector parameter

Columns (pixels)	3000
Columns (mm)	417
Rows (pixels)	300
Rows (mm)	417
Pixel binning	1:1
Integration time (ms)	750
Framebinning	1
Capacity (pF)	1x1 1
Pitch (mm)	0.139

Scan parameter

Mode:	CtMode
Number of projections	3500
StopAndGo	Off
Scan Field Extension Vertical	Off
Scan Field Extension Horizontal	Off
Rotation Mode	Continuous Mode
Image Type	RAW
Scan time (HH:MM:SS)	00:44:07

Recon parameter

Projection Tilt A	0
Projection Tilt B	0

Projection Tilt C	0
Recon mode	FovExtOff
Detector offset X (mm)	-0.744
Voxel size X (mm)	0.016
Voxel size Y (mm)	0.016
Voxel size Z (mm)	0.016
Dimension X (pixels)	3008
Dimension Y (pixels)	3008
Dimension Z (pixels)	2360
Median	Off
Volume Size X	48.672
Volume Size Y	48.672
Volume Size Z	48.672
Cubic voxel	On
Opt. Volume Height	On
Optimize	On
Image Type	RAW
Beam Hardening	3

Manipulator parameter	
FOD (mm)	140.000
FDD (mm)	1199.989
Height (mm)	402.499
Magnification	8.571

Appendix B – MATLAB code

This appendix provides information on the MATLAB code which has been referred to in previous chapters of the thesis. A mixture of both functions and scripts are described in this appendix. Pseudocode has been used, to help readers gain a high-level understanding of the code. Raw code is available for viewing at this GitHub repository.

In the pseudocode in this appendix, all inputs, outputs, and variable names are given in ***bold italic***. MATLAB built-in functions are referred to with an asterisk (*).

Importing point cloud and segmentation

- Import STL file of BCC unit cell and extract the point cloud
- Define medial axes for each strut represented in the point cloud. Assume nominal positions for the medial axes, 8 in total (i.e. assume that the STL file has been correctly configured before import)
- Using *surfaceanalysis.m*, calculate the following information for each point on the STL surface: overhang angle; surface angle; intersection ratio t; distances to each medial axis
- Segment the point cloud into individual struts (in practise this is performed using logical indexing). Extract cylindrical sections by discarding points outside of a predefined range of values for the intersection ratio

```
for $i$ = 1 to number of points:
    if $i$th point is closest to 1st medial axis
        • Put $i$th point into group 1
    if $i$th point is closest to 2nd medial axis
        • Put $i$th point into group 2
                    ⋮
                    ⋮
    if $i$th point is closest to 8th medial axis
        • Put $i$th point into group 8
    if $t_i$ < predefined lower $t$ boundary OR $t_i$ > predefined upper $t$ boundary
        • Remove the $i$th point from its group
```

Figure B.1. Pseudocode describing the point cloud import and segmentation script.

Cross section analysis

```
• Enter layer thickness
• Import point cloud of cylindrical section of strut
  if the strut overhang angle (using nominal medial axis) $\neq 0$:
      • Use the nominal medial axis to calculate rotation matrices
      • Perform rotations on point cloud such that its overhang angle $= 0$
• Using the layer thickness, calculate the number of slices present in the point cloud and the
  $z$-coordinates bounding each slice
  for $\boldsymbol{i} = 1$ to number of slices:
      • Use logical indexing to extract the points bounded by the $\boldsymbol{i}$th slice
        if number of points in slice $< 10$:
            • Discard this slice
            • continue
      • Fit a circle ($x, y$ coordinates and radius) to the slice, using non-linear least squares
        (lsqnonlin.m*, [166])
• Calculate the mean $x, y$ coordinates of the fitted circles
  for $\boldsymbol{i} = 1$ to number of fitted circles:
      • Calculate $x$ and $y$ offset
• Fit PDF to offset and radii data, using kernel density estimation
```

Figure B.2. Pseudocode describing the cross section analysis script.

Signed distance function

Inputs

n = the number of points in the medial axis

$\boldsymbol{x}, \boldsymbol{y}, \boldsymbol{z}$	$\boldsymbol{x}, \boldsymbol{y}, \boldsymbol{z}$ are 3D matrices representing the x, y and z-coordinates of the Cartesian grid over which the distance field is computed. Generated using *meshgrid.m**(see [164]).
$\boldsymbol{vertices}$	Matrix storing the vertices of the medial axis. Size $n \times 3$.
$\boldsymbol{segments}$	An indexing matrix, size $(n-1) \times 2$, used for assigning vertices to line segments. For example, first row in $\boldsymbol{segments}$ is [1 2], corresponding to the line segment defined by the first and second rows in $\boldsymbol{vertices}$. The second row is [2 3], etc.
$\boldsymbol{radii}$	Column vector, of length n, storing the radius value assigned to each vertex in the medial axis. If no radius variation is being applied to the strut, all the values of $\boldsymbol{radii}$ will be equal

Outputs

$\boldsymbol{d}$	Distance field of the given geometry

```
[$\boldsymbol{d}$] = sdf($\boldsymbol{x}, \boldsymbol{y}, \boldsymbol{z}, \boldsymbol{vertices}, \boldsymbol{segments}, \boldsymbol{radii}$)
    • Create array $\boldsymbol{d}$ with size equal to $\boldsymbol{x}$, with values initialised to infinity
    • Create column vectors $\boldsymbol{dmedial}$ and $\boldsymbol{tmedial}$, with number of rows equal to number of
      rows in $\boldsymbol{vertices}$, with values initialised to zero
      for $\boldsymbol{i}$ = 1 to the number of elements in $\boldsymbol{d}$:
          • $\boldsymbol{x_0} = \boldsymbol{x}(\boldsymbol{i}), \boldsymbol{y}(\boldsymbol{i}), \boldsymbol{z}(\boldsymbol{i})$
          for $\boldsymbol{j}$ = 1 to the number of line segments:
              • For the $\boldsymbol{j}$th line segment, i.e. $\boldsymbol{vertices}(\boldsymbol{j}{:}\boldsymbol{j}+\boldsymbol{1}, :)$, firstly calculate $\boldsymbol{v_i}$ and $\boldsymbol{t_i}$, then
                calculate the Euclidean distance $\boldsymbol{d_j}$ between $\boldsymbol{x_0}$ and the $\boldsymbol{j}$th line segment.
              • $\boldsymbol{dmedial}(\boldsymbol{j}) = \boldsymbol{d_j}$
              • $\boldsymbol{tmedial}(\boldsymbol{j}) = \boldsymbol{t}$
          • Calculate $\boldsymbol{dmin} = \min(\boldsymbol{dmedial})$ to find the smallest of the Euclidean distances
            between $\boldsymbol{x_0}$ and all line segments; store the index of this smallest value in the
            variable $\boldsymbol{k}$
          • $\boldsymbol{r_{max}} = \max(\boldsymbol{radii})$
          if $|\boldsymbol{dmin} - \boldsymbol{r_{max}}| \,/\, \boldsymbol{r_{max}} > 1$:
              • continue ($\boldsymbol{x_0}$ is not near the interface.)
          if no radius variation:
              • $\boldsymbol{r} = \boldsymbol{radii}(\boldsymbol{1})$
          else:
              • Find the value of $\boldsymbol{t}$ used for calculating $\boldsymbol{dmin}$ i.e. $\boldsymbol{tmedial}(\boldsymbol{k})$
              if $\boldsymbol{t} = 0$:
                  • $\boldsymbol{r} = \boldsymbol{radii}(\boldsymbol{k})$
              if $\boldsymbol{t} = 1$:
                  • $\boldsymbol{r} = \boldsymbol{radii}(\boldsymbol{k}+\boldsymbol{1})$
              else:
                  • $\boldsymbol{r}$ = interpolation between $\boldsymbol{radii}(\boldsymbol{k})$ and $\boldsymbol{radii}(\boldsymbol{k}+\boldsymbol{1})$
          • $\boldsymbol{d}(\boldsymbol{i}) = \boldsymbol{dmin} - \boldsymbol{r}$
```

Figure B.3. Pseudocode describing the signed distance function.

Tessellation

Inputs

$\boldsymbol{d}$	Distance field of the unit cell to be tessellated
$\boldsymbol{cs}$	Cell size
$\boldsymbol{radius}$	Strut radius
$\boldsymbol{n}$	3 × 1 row vector defining the number of repeated unit cells x, y and z
$\boldsymbol{z}$	See the $\boldsymbol{z}$ input for sdf.m
$\boldsymbol{dx}$	The value of the spacing between adjacent points in the Cartesian grid

Outputs

$\boldsymbol{tvolume}$	A tessellated volume of the distance field of the lattice structure
$\boldsymbol{x1}, \boldsymbol{y1}, \boldsymbol{z1}$	$\boldsymbol{x1}, \boldsymbol{y1}, \boldsymbol{z1}$ are 3D matrices representing the x, y and z-coordinates of the Cartesian grid over which the distance field is computed for the lattice structure. Generated using *meshgrid.m**(see [164]).

```
[$\boldsymbol{tvolume}, \boldsymbol{x1}, \boldsymbol{y1}, \boldsymbol{z1}$] = tessellate($\boldsymbol{d}, \boldsymbol{cs}, \boldsymbol{radius}, \boldsymbol{n}, \boldsymbol{z}, \boldsymbol{dx}$)
    • $\boldsymbol{cell_{count}} = \boldsymbol{n}(\boldsymbol{1}) \times \boldsymbol{n}(\boldsymbol{2}) \times \boldsymbol{n}(\boldsymbol{3})$
    • Create array $\boldsymbol{tvolume}$ of size equal to a tessellated version (according to $\boldsymbol{n}$) of $\boldsymbol{d}$ and initialise values to infinity
    • Using z and $\boldsymbol{cs}$, calculate the index of the third dimension of z corresponding to the z-coordinate of the highest point in the unit cell's medial axis. Assign this value to the variable $\boldsymbol{index1}$
    • Using z and $\boldsymbol{cs}$, calculate the index of the third dimension of z corresponding to the z-coordinate of the lowest point in the unit cell's medial axis. Assign this value to the variable $\boldsymbol{index2}$
    • $\boldsymbol{shift} = \boldsymbol{index2} - \boldsymbol{index1}$. $\boldsymbol{shift}$ expresses the cell size of the unit cell in terms of indices.
    • Using $\boldsymbol{shift}$ and $\boldsymbol{n}$, find the indices corresponding to the locations of all the unit cells that will be positioned into $\boldsymbol{tvolume}$
      for $\boldsymbol{i}$ = 1 to $\boldsymbol{cell_{count}}$
          • Iterate through the regions of $\boldsymbol{tvolume}$ corresponding to the locations of each unit cell. Perform a Boolean union between this region of $\boldsymbol{tvolume}$ and $\boldsymbol{d}$
    • Use meshgrid.m* to generate Cartesian grid $\boldsymbol{x1}, \boldsymbol{y1}, \boldsymbol{z1}$ for $\boldsymbol{tvolume}$
```

Figure B.4. Pseudocode describing the tessellation function.

Lattice cropping

Inputs

$\boldsymbol{u}$	Distance field of the unit cell/lattice structure to be cropped
$\boldsymbol{z_{max}}$	A constant, defining the plane $z = z_{max}$ (see § 4.2.2)
$\boldsymbol{z_{min}}$	A constant, defining the plane $z = z_{min}$ (see § 4.2.2)
$\boldsymbol{z}$	3D matrix representing the z-coordinates of the Cartesian grid over which the $\boldsymbol{u}$ is computed (i.e. the [~,~,z] output of the *meshgrid.m**(see [164]))

Outputs

$\boldsymbol{u_{crop}}$	Distance field of the cropped unit cell/lattice structure

```
[$\boldsymbol{u_{crop}}$] = cropvolume($\boldsymbol{u}$, $\boldsymbol{z_{max}}$, $\boldsymbol{z_{min}}$, $\boldsymbol{z}$)
    • Using z calculate the index of the third dimension of z corresponding to $\boldsymbol{z_{max}}$. Assign this value to the variable $\boldsymbol{index1}$
    • Using z calculate the index of the third dimension of z corresponding to $\boldsymbol{z_{min}}$. Assign this value to the variable $\boldsymbol{index2}$
    • Create an array $\boldsymbol{crop}$ of size equal to $\boldsymbol{u}$ and initialise values to infinity
    • Assign the value of zero to all elements in $\boldsymbol{crop}$ with a third-dimension index $\leq \boldsymbol{index1}$ or $\geq \boldsymbol{index2}$
    • $\boldsymbol{u_{crop}} = \min(-\boldsymbol{u}, \boldsymbol{crop})$. This performs the Boolean subtraction
```

Figure B.5. Pseudocode describing the cropping function.

Surface analysis

Inputs

n = the number of points on the surface. m = number of strut medial axes

$\boldsymbol{surfaceVertices}$	n x 3 matrix of surface points
$\boldsymbol{strutVertices}$	3 x 2m matrix of strut start/end points. For example, columns 1 and 2 store the start/end points of one medial axis, then columns 3 and 4 store another strut etc.
$\boldsymbol{strutID}$	Row binary vector showing which pairs of adjacent columns strutVertices should be used for the medial axis

Outputs

n = the number of points on the surface

$\boldsymbol{surfaceNormals}$	n x 3 matrix of surface normals
$\boldsymbol{strutAngle}$	n x 1 vector of overhang angle θ (in degrees) of the strut that each point on the surface is associated to
$\boldsymbol{skinAngle}$	n x 1 vector of surface angle α (in degrees) between surface normal and reference vector (normalRef). Angular range of 0-180 degrees
$\boldsymbol{t}$	n x 1 vector of intersection ratios of all points (these values are modified where necessary so that t is never < 0 or > 1)
$\boldsymbol{normalRef}$	n x 3 matrix of reference vectors used for calculating surface angle for each point
$\boldsymbol{vargout}\{\mathbf{1}\}$	n x 1 vector of distances between surface points and closest strut
$\boldsymbol{vargout}\{\mathbf{2}\}$	n x 1 vector of integers used to indicate which medial axis is closest to the n-th point. The numbering convention for the integers is arbitrary
$\boldsymbol{vargout}\{\mathbf{3}\}$	n x 1 vector of surface angles α, but with angular range between 0-360°

```
[$\boldsymbol{surfaceNormals}$, $\boldsymbol{strutAngle}$, $\boldsymbol{skinAngle}$, $\boldsymbol{t}$, $\boldsymbol{normalRef}$, $\boldsymbol{vargout}$] = …
                    surfaceanalysis($\boldsymbol{surfaceVertices}$, $\boldsymbol{strutVertices}$, $\boldsymbol{strutID}$)

    • $\boldsymbol{numOfPoints}$ = the number of rows in $\boldsymbol{surfaceVertices}$
    • $\boldsymbol{top_{surf}}$ = maximum $z$-coordinate of $\boldsymbol{surfaceVertices}$
    • $\boldsymbol{bottom_{surf}}$ = minimum $z$-coordinate of $\boldsymbol{surfaceVertices}$
      for $\boldsymbol{i}$ = 1 to $\boldsymbol{numOfPoints}$:
          • $\boldsymbol{x_0}$ = the $\boldsymbol{i}$th row in $\boldsymbol{surfaceVertices}$
          • Calculate the distances between $\boldsymbol{x_0}$ and all the medial axes in $\boldsymbol{strutVertices}$
          • Store the minimum distance in $\boldsymbol{vargout}\{\mathbf{1}\}$.
          • Store the integer corresponding to the closest medial axis in $\boldsymbol{vargout}\{\mathbf{2}\}$.
          • Calculate the reference vector for the closest medial axis, used for calculating surface
            angle $\alpha$
          • Calculate the surface normal at $\boldsymbol{x_0}$
          • Calculate surface angle $\alpha$ and store in $\boldsymbol{vargout}\{\mathbf{3}\}$
```

Figure B.6. Pseudocode describing the surface analysis script.

Appendix C – Texture bias functions

This appendix discusses the approaches which were considered for applying displacements to lattice surfaces, for the modelling of texture bias. Two methods have been considered: an implicit definition and an explicit definition.

With an implicit definition, the displacement δ_i is applied to the point $\vec{x}_i$ on the surface, where δ_i is randomly selected from a normal distribution, that is

$$\delta_i = \mu \pm \sigma_i \tag{C.1}$$

with mean $\mu = 0$ and standard deviation σ_i. The mean of the normal distribution should be zero because $\mu < 0$ would cause the average strut surface to be less than nominal, and vice versa for $\mu > 0$. The standard deviation in Eq. (C.1) is given by

$$\sigma_i = f(\alpha_i, \theta_i). \tag{C.2}$$

If $\sigma_i > 0$, a non-zero displacement is applied to $\vec{x}_i$ and will modify the surface to introduce some irregularities into the surface. Therefore, Eq. (C.2) can be used to model texture bias by increasing σ_i for down-skin points and for overhanging struts. Note that t_i is not included in Eq. (C.2) because the random selection of values inherently varies δ_i across the strut's length. Figure C.**1**a shows an example of Eq. (C.2) applying texture bias to the strut in Figure C.**1**b.

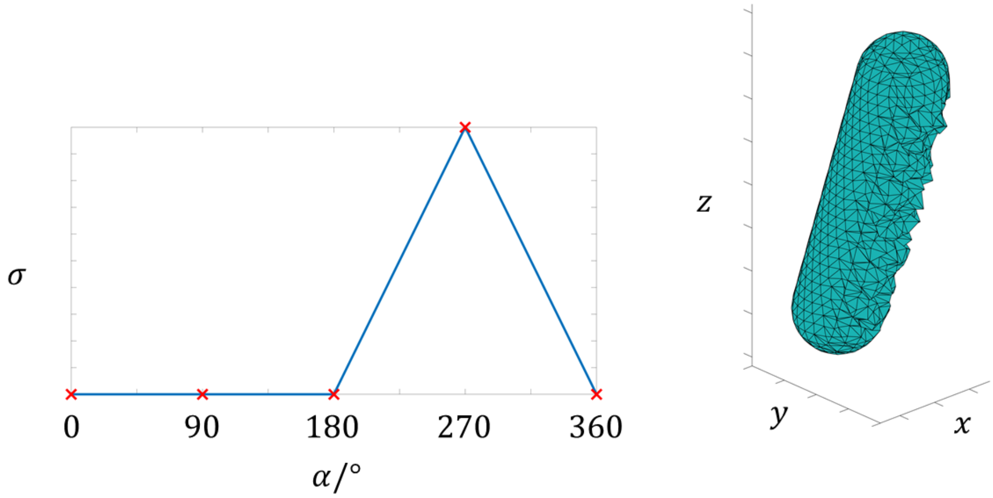

(a) (b)

Figure C.1. Example of using pseudorandom displacements used to apply texture bias. (a) Example function which defines the standard deviation of the distribution from which displacements are applied to a strut surface. (b) An example strut after texture bias applied.

The approach of pseudorandom displacements is useful for fast generation of texture bias in strut surfaces, as Eq. (C.1) uses the normal distribution to define displacements implicitly, allowing for a simple definition of the surface texture which doesn't require explicitly predefining specific displacements on the surface. One drawback, however, is that having no control over the exact values of the displacements can result in highly different displacements being applied to adjacent points – this can adversely affect the quality of the surface and create tetrahedral meshing issues (note that the likelihood of this problem occurring reduces at lower σ values and can become negligible).

The second approach is an explicit approach which defines all the displacements that will be applied to all the points on the surface. Explicitly defining the displacements provides greater control and allows for the modelling of surface defects whilst guaranteeing a locally smooth surface (i.e. no sudden changes to adjacent points).

The function δ_i which explicitly defines the displacement is given by

$$\delta_i = \psi \times \chi \times \Delta \tag{C. 3}$$

where

$$\psi = f(\alpha_i, t_i), \qquad \chi = f(\alpha_i), \qquad \Delta = f(\theta). \tag{C.4}$$

The three functions ψ, χ, Δ enable the surface of a lattice structure to be modified depending on the intersection ratio t the surface angle α and the overhang angle θ. ψ is a base surface which describes the general distribution of peaks to be applied to all the struts. χ then modified specific areas of ψ, depending on the surface angle α_i which allows for the application of texture bias. Δ is a scaling function, which applies equal amplification/dampening to all the points on the surface, depending on overhang angle, allowing for texture bias to be stronger/weaker in struts with greater/smaller overhang angle. Examples of ψ, χ, Δ are shown in Figure C.2. The base surface ψ in Figure C.2a is given by

$$\psi = f(\alpha_i, t_i) = \sin(\omega_\alpha \alpha_i) \sin(\omega_t t_i). \tag{C.5}$$

In Eq. (C.5), the two sine terms create peaks of frequency ω_α, ω_t in the α_i and t_i axes, respectively.

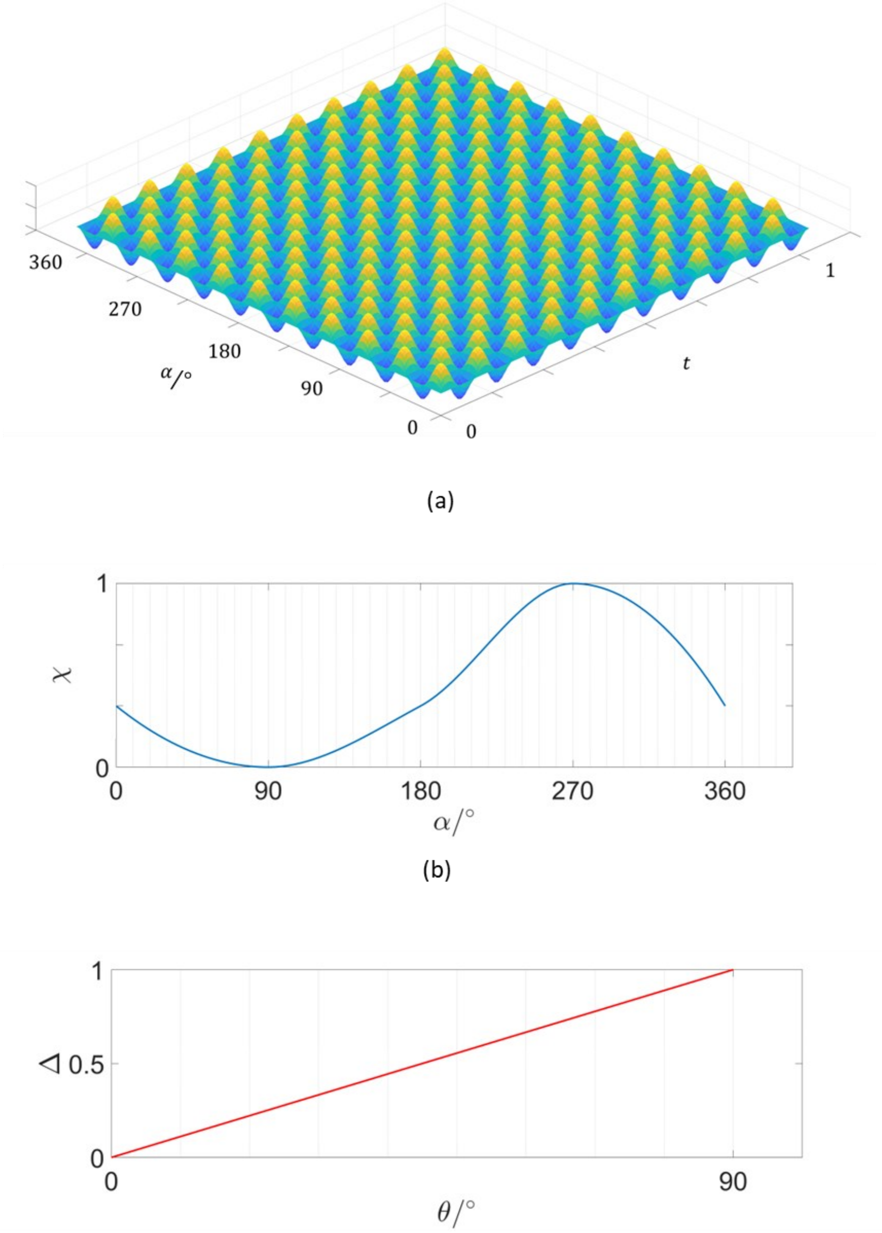

(a)

(b)

(c)

Figure C.2. Examples of functions used to explicitly define the displacements applied to model surface defects. (a) Base surface ψ.(b) χ applies texture bias by modifying the amplitudes of specific areas of ψ, depending on surface angle α. (c) Δ modifies all peaks in ψ using a multiplier that is dependent on overhang angle θ.

Appendix D – Analytical calculation of lattice volumes

This appendix provides the equations used for determining V_{SDF}^{i} for the four geometries defined in Chapter 5, Section 5.2.2, (Figure 5.7).

$V_{SDF,sphere}^{i}$ is simply given by

$$V_{SDF,sphere}^{i} = \frac{4}{3}\pi r^3. \tag{D.1}$$

$V_{SDF,strut}^{i}$ can be considered as the sum of the volumes of a cylinder and the volumes of two half-spheres (i.e. one sphere), that is

$$V_{SDF,strut}^{i} = \pi r^2 l + \tfrac{4}{3}\pi r^3 = \pi r^2 (l + \tfrac{4}{3} r). \tag{D.2}$$

To calculate $V_{SDF,rad}^{i}$, the radius defect geometry (Figure D.1a) must first positioned such that its medial axis is coincident with the y-axis and $\vec{l}_2$ is coincident with the origin (Figure D.1b). Then, after splitting the geometry in half at the xz plane (Figure D.1c), $V_{SDF,rad}^{i}$ can be considered as

$$V_{SDF,rad}^{i} = 2 \times (A_{rad} + B_{rad}) \tag{D.3}$$

where A_{rad} and B_{rad} are the volumes shown in Figure D.1c, given by

$$A_{rad} = \frac{2}{3}\pi r^3 \tag{D.4}$$

$$\begin{aligned} B_{rad} &= \int_{0}^{|\vec{l}_2 - \vec{l}_3|} \pi \left(\frac{r_2 - r_3}{|\vec{l}_2 - \vec{l}_3|} y + r_3 \right)^2 dy \\ &= \frac{\pi}{3} |\vec{l}_2 - \vec{l}_3| (r_2^2 + r_3 r_2 + r_3^2) \end{aligned} \tag{D.5}$$

To calculate $V_{SDF,int}^{i}$, the strut intersection (Figure D.2a) must first be positioned such that $\vec{l}_2$ is coincident with the origin and the medial axis is parallel to the xy plane.

Next, the strut intersection is split in the xz plane (Figure D.2b), this plane can be defined by the vector $\vec{n} = (a, b, c)$ which is located at the origin $\vec{o} = (0, 0, 0)$, Next, a rotation of θ (in degrees) is applied in the z axis, such that the medial axis (disregarding the part of the medial axis that was split off) is coincident with the y axis (Figure D.2c). As shown in Figure D.2d, $V^{i}_{SDF,int}$ can then be considered as

$$V^{i}_{SDF,int} = 2 \times (A_{int} + B_{int} + C_{int} + D_{int}) \tag{D.6}$$

where

$$A_{int} = \frac{\pi}{2} r^2 \left|\vec{l}_2 - \vec{l}_3\right| \tag{D.7}$$

$$B_{int} = \frac{2}{3}\pi r^3 \tag{D.8}$$

$$C_{int} = \frac{4}{3}\pi r^3 \times \left(\frac{\theta}{360}\right) \tag{D.9}$$

$$D_{int} = \int_{y_1}^{y_2} \int_{z_1}^{z_2} \int_{x_1}^{x_2} 1\, dx\, dz\, dy \tag{D.10}$$

where $x_1 = 0, x_2 = r, z_1 = -\sqrt{r^2 - x^2}, z_2 = \sqrt{r^2 - x^2}, y_2 = \left|\vec{l}_2 - \vec{l}_3\right|$ and y_1 is the plane defined by the vector $\vec{n} = (a, b, c)$ located at the origin. Therefore,

$$y_1 = ax + by + cz + d \tag{D.11}$$

which simplifies to

$$y_1 = ax + by \tag{D.12}$$

because $d = \vec{n} \cdot \vec{o} = 0$, and $c = 0$ (as $\vec{n}$ is in the xy plane).

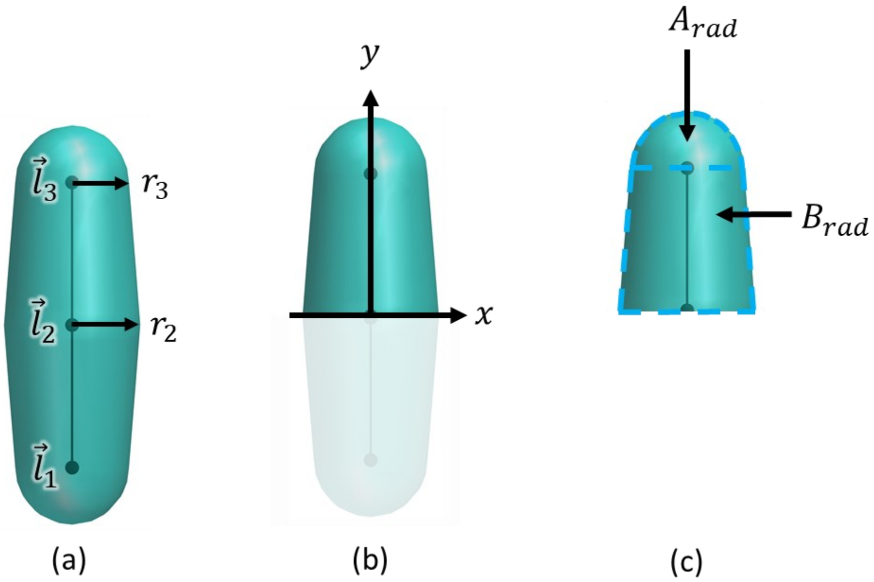
$\vec{l}_3$
r_3
$\vec{l}_2$
r_2
$\vec{l}_1$
y
x
A_{rad}
B_{rad}
(a)
(b)
(c)

Figure D.1. Volume calculation for the radius defect. The initial geometry (a) is divided into two sections (b) from which the volumes of A_{rad} and B_{rad} can be derived.

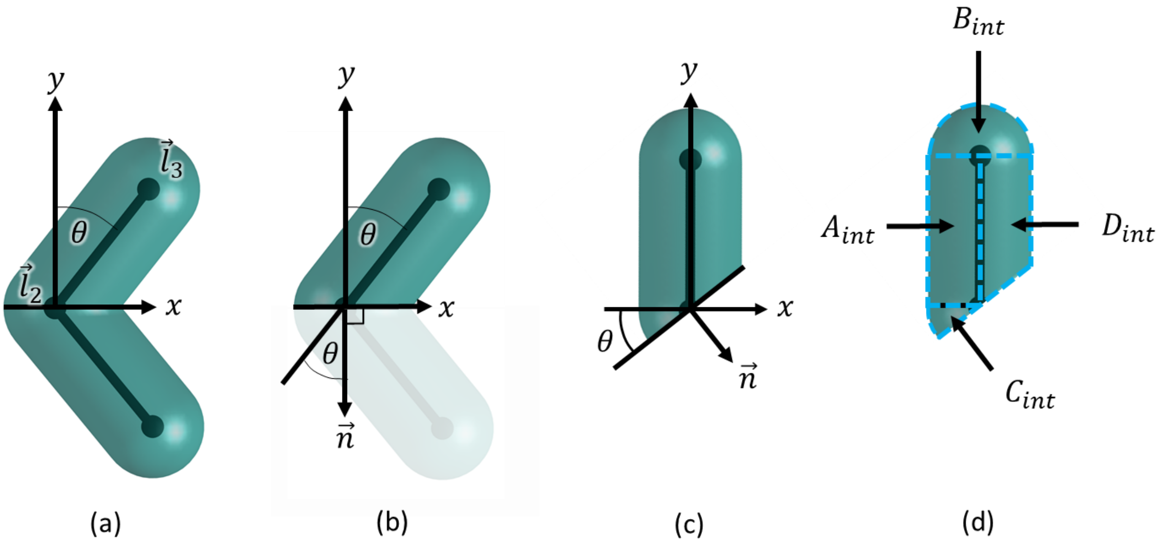
y
$\vec{l}_3$
θ
$\vec{l}_2$
x
y
θ
x
θ
$\vec{n}$
y
x
θ
$\vec{n}$
B_{int}
A_{int}
D_{int}
C_{int}
(a)
(b)
(c)
(d)

Figure D.2. Volume calculation for the strut intersection. The initial geometry (a) is divided into two sections (b) and repositioned in the coordinate system (c), after which the volumes of A_{int}, B_{int}, C_{int} and D_{int} can be derived.